Australian Government
Geoscience Australia

An assessment of the uranium and geothermal prospectivity of the southern Northern Territory

Edited by A. Schofield

Record
2012/51

GeoCat #
74118

With contributions by R.G. Chopping, D.P. Connolly, R.G. Gallagher, E.J. Gerner, D.L. Huston, B. Lewis, A.J. Meixner, T.P. Mernagh, A. Schofield, R.D. Weber and J.A. Whelan

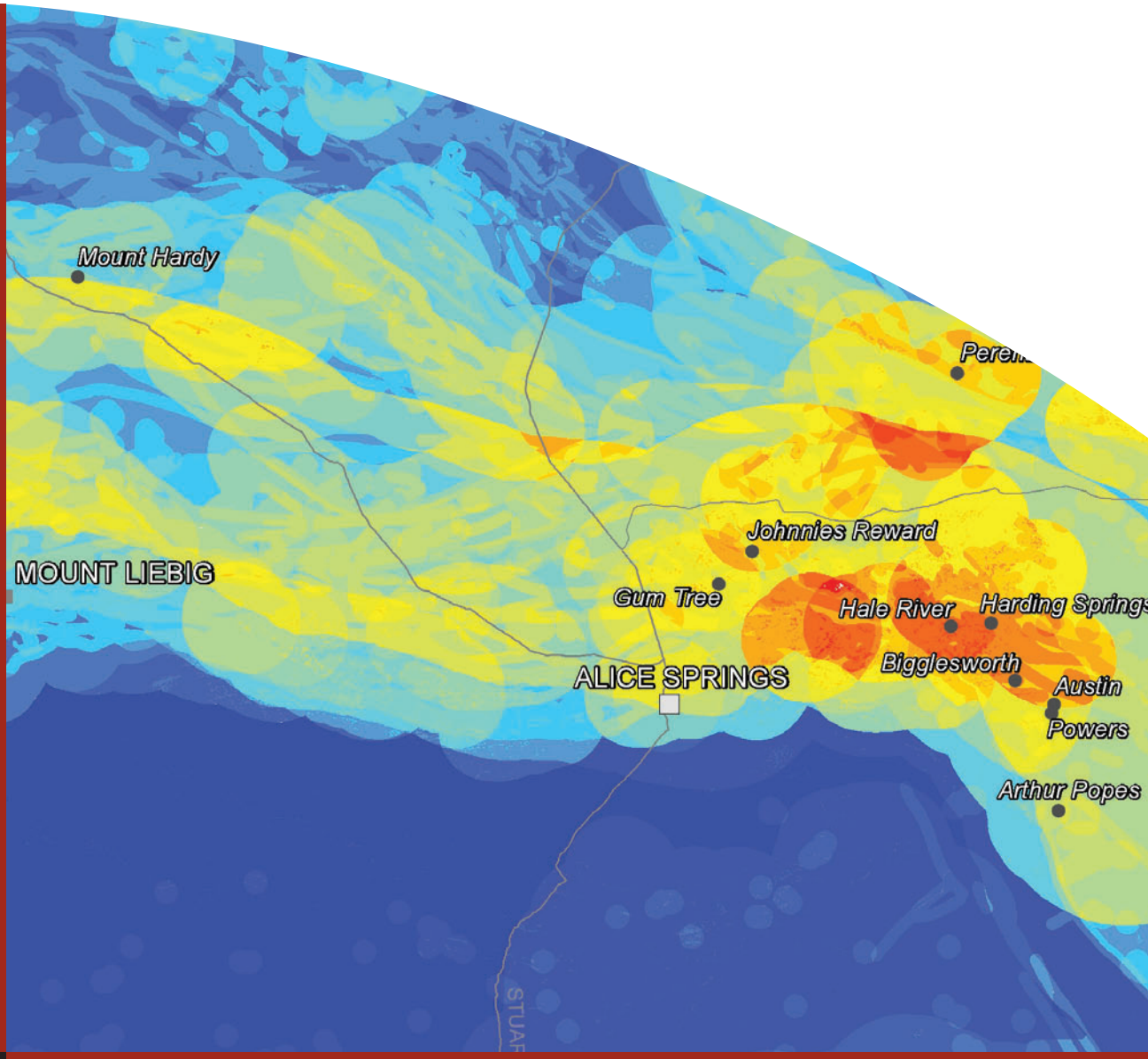

An assessment of the uranium and geothermal prospectivity of the southern Northern Territory

GEOSCIENCE AUSTRALIA
RECORD 2012/51

Edited by

A. Schofield[1]

With contributions by R.G. Chopping[1], D.P. Connolly[1], R.G. Gallagher[1], E.J. Gerner[2], D.L. Huston[1], B. Lewis[1], A.J. Meixner[1], T.P. Mernagh[1], A. Schofield[1], R.D. Weber[2] and J.A. Whelan[3]

Australian Government
Geoscience Australia

Northern Territory Government

1. Minerals and Natural Hazards Division, Geoscience Australia, GPO Box 378, Canberra ACT, 2601
2. Energy Division, Geoscience Australia, Geoscience Australia, GPO Box 378, Canberra ACT, 2601
3. Northern Territory Geological Survey, PO Box 3000, Darwin, Northern Territory 0801

Department of Resources, Energy and Tourism
Minister for Resources, Energy and Tourism: The Hon. Martin Ferguson, AM MP
Secretary: Mr Drew Clarke

Geoscience Australia
Chief Executive Officer: Dr Chris Pigram

This paper is published with the permission of the CEO, Geoscience Australia

ISSN 1448-2177
ISBN 978-1-922103-53-6 (web)
978-1-922103-54-3 (DVD)
978-1-922103-55-0 (print)

GeoCat # 74118

Bibliographic reference: Schofield, A. (ed.), 2012. An assessment of the uranium and geothermal prospectivity of the southern Northern Territory. Record 2012/51. Geoscience Australia: Canberra.

Contents

Executive summary

Recent acquisition of deep crustal seismic and magnetotelluric data in the southern Northern Territory, in conjunction with current and previously completed studies, has led to an increased knowledge of the geological and geodynamic framework of the region. This improved understanding has been used to assess the potential for the presence of uranium and geothermal energy systems within the southern Northern Territory.

Four uranium mineral systems were considered: sandstone-hosted, uranium-rich iron oxide-copper-gold, unconformity-related and magmatic-related. The analysis for uranium systems was undertaken in a 2D, GIS-based environment and employed a mineral systems approach consisting of four key components: 1) sources of metals, fluids and ligands, 2) drivers of fluid flow, 3) fluid-flow pathways and architecture, and 4) depositional sites and mechanisms. Potential for sandstone-hosted uranium systems is highest in the Amadeus and Ngalia basins, which host known sandstone-hosted uranium mineralisation. The portion of the Georgina Basin contained within the study area also exhibits elevated potential, although this is lower than that for the Amadeus and Ngalia basins. Potential for uranium-rich iron oxide-copper-gold mineralisation is elevated along an east-west-trending belt in the southern Aileron Province, and is highest in the Harts Range region. Although unconformity-related uranium deposits are not known within the study area, the results of this assessment suggest potential exists along the northern Amadeus Basin, in the Georgina Basin, and along the margin of the Eromanga Basin. The assessment for magmatic-related uranium systems suggests that potential is highest in the Aileron Province. The assessment particularly highlights granites along the northern margin of the Ngalia Basin, along the southern Aileron Province and into the Warumpi Province, and in the Davenport Province in the northeast of the study area.

Two geothermal systems were assessed: hot rock geothermal and hot sedimentary aquifer. For the hot rock geothermal system assessment, temperatures at depth were predicted in 3D using the 3D GeoModeller software package. Hot sedimentary aquifer potential was assessed using the modelled temperature at the basal contact of sedimentary basins containing favourable aquifer units. Hot rock geothermal potential in the study area is low to moderate, with maximum modelled temperatures of 134^{o}C at four kilometres depth. The highest modelled potential for hot rock geothermal systems occurs in the vicinity of the Ngalia and Eromanga basins. Modelled potential for hot sedimentary aquifer systems is spatially limited to the southeast of the study area, and reaches a maximum temperature of 111^{o}C at the base of the Pedirka Basin.

1. Introduction

Under the recently-completed Onshore Energy Security Program (OESP), Geoscience Australia (GA), in collaboration with State and Territory geoscience agencies, has undertaken regional geological framework studies in order to better understand the geodynamic and architectural controls on major energy systems. These regional studies have been based around the acquisition of deep crustal seismic and magnetotelluric data. In conjunction with these data, a range of complimentary datasets and derivative products have also been generated, including 3D geophysical and geological models, geochemical and geochronological data, geodynamic syntheses and models, and assessments of uranium and geothermal energy potential.

This report provides a prospectivity assessment of the southern Northern Territory for uranium and geothermal energy systems. There are two main goals of the assessment:

1. Identify regions of unknown or previously unrecognised uranium and geothermal energy potential using a systems-based approach in order to enhance the prospectivity of the area; and
2. Provide an indication of regions where follow-up geoscientific investigations may be undertaken to assess the validity of the hypothesised uranium and geothermal potential.

The study area for the assessment is framed by a box extending from 131°10' to 135°55' longitude and 26° S to 21°50' S latitude (Figure 1.1). This area incorporates part of the recently-acquired 08GA-OM1 (Gawler-Officer-Musgrave-Amadeus) and the 09GA-GA1 (Georgina-Arunta-Amadeus) seismic lines (Korsch and Kositcin, 2010; Korsch *et al*., 2011), and extends from the South Australia border in the south to the northern Aileron and Davenport provinces in the north (Figure 1.1). As well as being investigated under the OESP, the study area has also been the focus of investigation for current and previous GA and Northern Territory Geological Survey (NTGS) projects (e.g., Lyons and Huston, 2006; Beyer *et al*., 2010; Beyer *et al*., 2012; Whelan *et al*., 2011; Whelan *et al*., 2012). Together, this work has built a foundation of geoscientific data which provides the basis for the analysis described in this report.

2. Overview of regional geology and energy systems

A. Schofield and D.L. Huston

2.1. REGIONAL GEOLOGY

A number of distinct basement and basin geological provinces occur within the study area (Figure 1.1). The geology of the Northern Territory has recently been comprehensively described by the NTGS (Ahmad, M. and Munson, T.J., *in press*) and, as such, this section will only briefly review the main geological elements within the study area in order to establish the basic geological framework for the uranium and geothermal energy systems assessments. For the purposes of this assessment, two solid geology datasets were produced to represent the geology of the basement and basins in the study area (Figures 2.1.1 and 2.1.2; see Appendix 1 for further information).

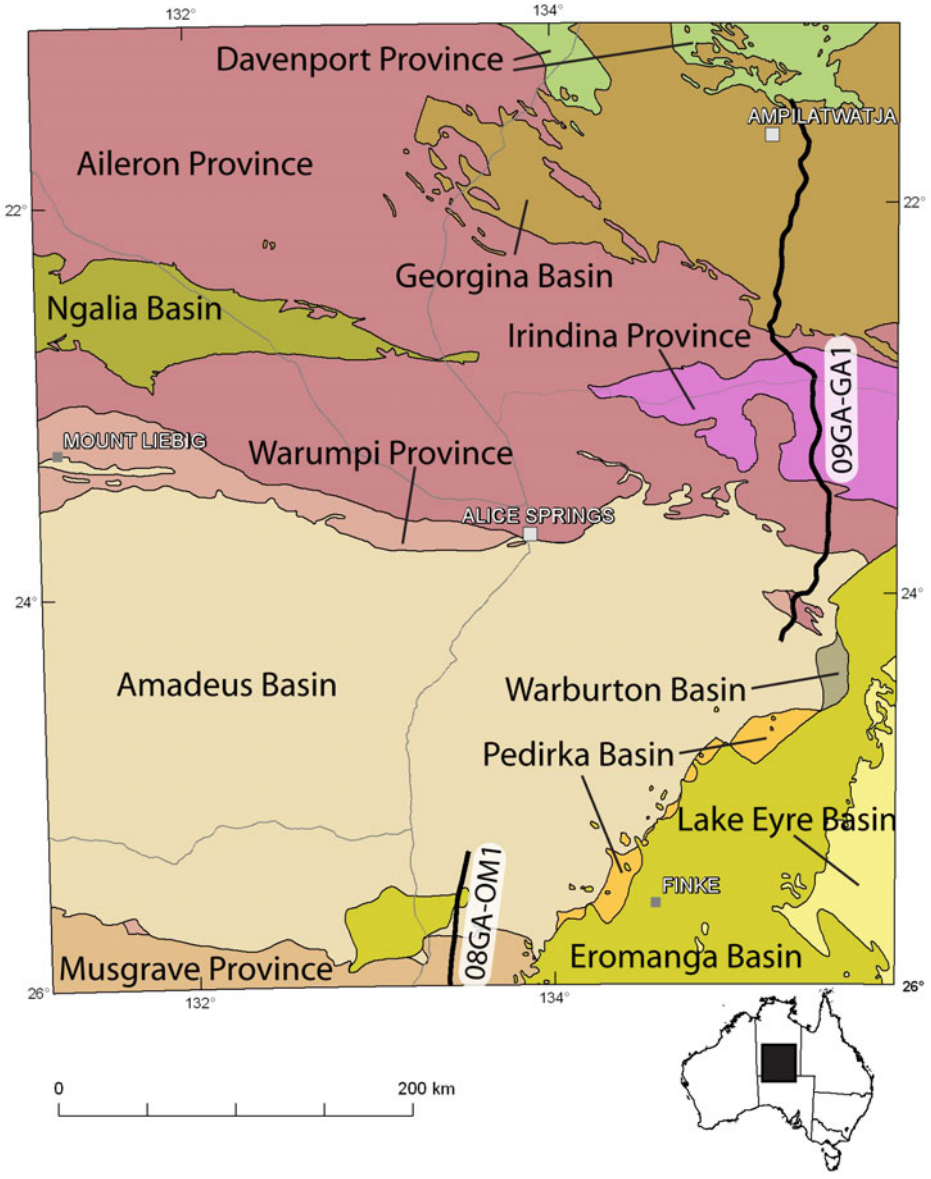

Figure 1.1: *Location of study area, showing major geological elements.*

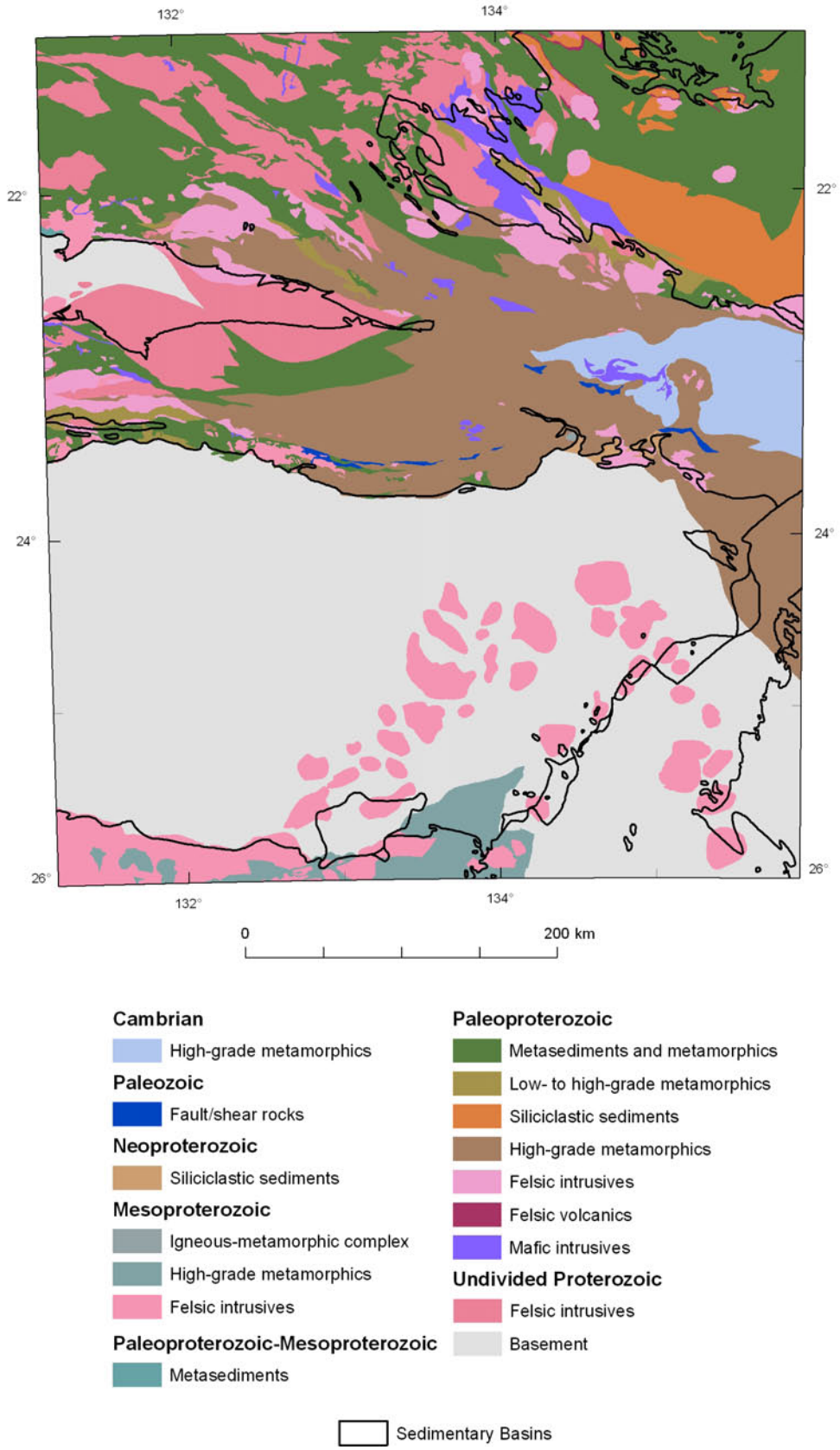

Figure 2.1.1: *Simplified basement solid geology of the study area (see Appendix 1 for details).*

2.1.1 Basement provinces

2.1.1.1 Davenport Province

The Paleoproterozoic Davenport Province forms part of the Tennant Region, and occurs in the northeast of the study area (Figure 1.1; 2.1.1). The stratigraphy consists of deformed sedimentary and volcanic rocks of the Ooradidgee and Hatches Creek groups, 1820–1810 Ma granites (including the Barrow Creek Granite Complex) and 1720–1710 Ma lamprophyres and intrusive rocks of the Devils Suite (see Claoué-Long, 2007; Scrimgeour and Close, 2011, and references therein). Korsch *et al*. (2011) interpret the Atuckera Fault to represent the boundary between the Davenport and Aileron provinces (not shown on Figures 1.1 and 2.1.1).

2.1.1.2 Arunta Region

The Arunta Region dominates the northern half of the study area (Figure 1.1; 2.1.1). It has a long-lived history, and has been subdivided into three provinces based on differences in protolith ages and geological histories (Scrimgeour, 2003): the 1860–1700 Ma Aileron Province, the 1690–1600 Ma Warumpi Province and the Neoproterozoic to Cambrian Irindina Province. A number of metamorphic and thermal events have affected the Arunta Region. These include the 1810–1790 Ma Stafford Event, the 1780–1770 Ma Yambah Event, the 1735–1690 Ma Strangways Event, the 1640–1630 Ma Liebig Orogeny, the 1590–1560 Ma Chewings Orogeny, the 1150–1130 Ma Teapot Event, the 480–460 Ma Larapinta Event, and the 450–300 Ma Alice Springs Orogeny (Scrimgeour, *in press* a, b, c, and references therein).

The Aileron Province consists of variably metamorphosed sedimentary and igneous rocks. The oldest known rocks in the Aileron Province are represented by widely distributed metasedimentary rocks deposited between 1860–1830 Ma in the northern and western Aileron Province. These are dominated by the Lander Rock Formation and its correlatives (see Claoué-Long, 2007; Scrimgeour, *in press* a, and references therein). An additional succession of metasedimentary rocks, deposited between 1810–1790 Ma, is widespread across the Aileron Province, and includes protoliths of the Strangways Metamorphic Complex and Reynolds Range Group and their correlatives (Scrimgeour, *in press* a).

Magmatism occurred in several recognised phases between 1820–1600 Ma. Of particular significance are 1730–1710 Ma granites in the Jinka Domain, which correspond to the high-heat producing suite of Zhao and McCulloch (1995), and 1650–1600 Ma magmatism which includes radiogenic granites in the Ennugan Mountains (Beyer *et al*., 2012; Scrimgeour, *in press* a). Other magmatic events include the 1570–1530 Ma Southwark Suite and alkaline magmas of the 1133 ± 5 Ma (Claoué-Long and Hoatson, 2005) Mordor Igneous Complex and the ~730 Ma (Black and Gulson, 1978) Mud Tank Carbonatite.

The Warumpi Province is interpreted to have accreted to the southern margin of the Aileron Province at around 1640 Ma (Scrimgeour *et al*., 2005), which is reflected in the 1640–1630 Ma Liebig Orogeny (Close *et al*., 2003; Scrimgeour *et al*., 2005). The northern boundary with the Aileron Province occurs along a series of faults, representing the Central Australia Suture (Close *et al*., 2005). The southern boundary is interpreted to be the Woodroffe Thrust (Korsch *et al*., 2010), which juxtaposes the Warumpi Province with the Musgrave Province. The Warumpi Province includes metasedimentary rocks dated at 1660–1640 Ma and 1640–1600 Ma and magmatic suites at 1680–1660 Ma, 1640–1630 Ma and 1610–1600 Ma (Scrimgeour, *in press* b). Further significant magmatism occurred in association with the 1150–1130 Ma Teapot Event, resulting in the emplacement of the uranium-rich Teapot Granite Complex (Scrimgeour, *in press* b).

The Irindina Province is significantly younger than both the Aileron and Warumpi provinces, and consists of highly metamorphosed Neoproterozoic to Cambrian sedimentary and lesser igneous

rocks (Scrimgeour, *in press* c). Sedimentary protoliths of the Harts Range Metamorphic Complex were metamorphosed to upper-amphibolite to granulite facies during the 480–460 Ma Larapinta Event (e.g., Miller *et al*., 1997; Mawby *et al*., 1999), which is synchronous with the deposition of the Larapinta Group in the Amadeus Basin (Scrimgeour, *in press* c, and references therein). The Irindina Province is structurally detached in the middle crust from the underlying Aileron Province (Korsch *et al*., 2011), and was exhumed during the 450–300 Ma Alice Springs Orogeny (Mawby *et al*., 1999; Scrimgeour, *in press* c).

2.1.1.3 Musgrave Province

The Musgrave Province occurs in the south of the study area (Figure 1.1; 2.1.1), and is interpreted to adjoin the Warumpi Province across the Woodroffe Thrust, with docking of the two provinces during the 1590–1560 Ma Chewings Orogeny (Korsch *et al*., 2010). The stratigraphy of the Musgrave Province in the Northern Territory consists of gneisses, voluminous granites of the Pitjantjatjara Supersuite, bimodal rocks emplaced during the Giles Event, and sediments and bimodal volcanics of the Tjauwata Group (see Edgoose *et al*., 2004 and references therein). The evolution of the Musgrave Province has been summarised in four major phases by Edgoose *et al*. (2004):

1. 1600–1540 Ma crust formation, as indicated by protolith ages for Musgravian Gneiss;
2. Pervasive metamorphism, deformation and granitic magmatism during the 1200–1160 Ma Musgrave Orogeny;
3. Bimodal magmatism during the 1080–1040 Ma Giles Event; and
4. Intraplate orogenic activity associated with the 580–530 Ma Petermann Orogeny.

2.1.2 Sedimentary basins

2.1.2.1 Neoproterozoic-Paleozoic basins

Neoproterozoic to Paleozoic sedimentary basins blanket a large proportion of the study area, and include the Amadeus, Georgina and Ngalia basins, and the less well exposed Pedirka and Warburton basins (Figure 1.1; 2.1.2). The Irindina Province, which also consists of Neoproterozoic to Paleozoic sedimentary rocks, has already been described above as part of the Arunta Region. Stratigraphy across a number of these basins has been correlated (e.g., Walter *et al*., 1995; Haines *et al*., 2001), and these are considered to form components of the extensive Centralian Superbasin. The largest basin in the study area is the intracratonic Amadeus Basin, which occupies most of the southern half of the study area (Figure 1.1; 2.1.2). Sedimentation in the Amadeus Basin was initiated during the Neoproterozoic with the deposition of the Heavitree Quartzite, and continued until the Devonian with deposition of the Brewer Conglomerate. The basin was significantly affected by the 580–530 Ma Petermann Orogeny and the 450–300 Ma Alice Springs Orogeny, which is reflected in deformation and syn-orogenic sedimentation (e.g., Korsch and Lindsay, 1989; Haines *et al*., 2001).

The Georgina Basin overlies the Davenport and Aileron provinces in the northeast of the study area (Figure 1.1; 2.1.2). The sedimentary history of the Georgina Basin is summarised by Scrimgeour and Close (2011), and consists of carbonates and clastic sedimentary rocks deposited between the Neoproterozoic and Devonian. Sedimentation in the Ngalia Basin, whilst also commencing during the Neoproterozoic, continued later than in the Amadeus and Georgina basins, with the Mount Eclipse Sandstone deposited during the Devonian to Carboniferous (Wells and Moss, 1983). Both the Georgina and Ngalia basins record syn-orogenic sedimentation corresponding to the Alice Springs Orogeny (Haines *et al*., 2001).

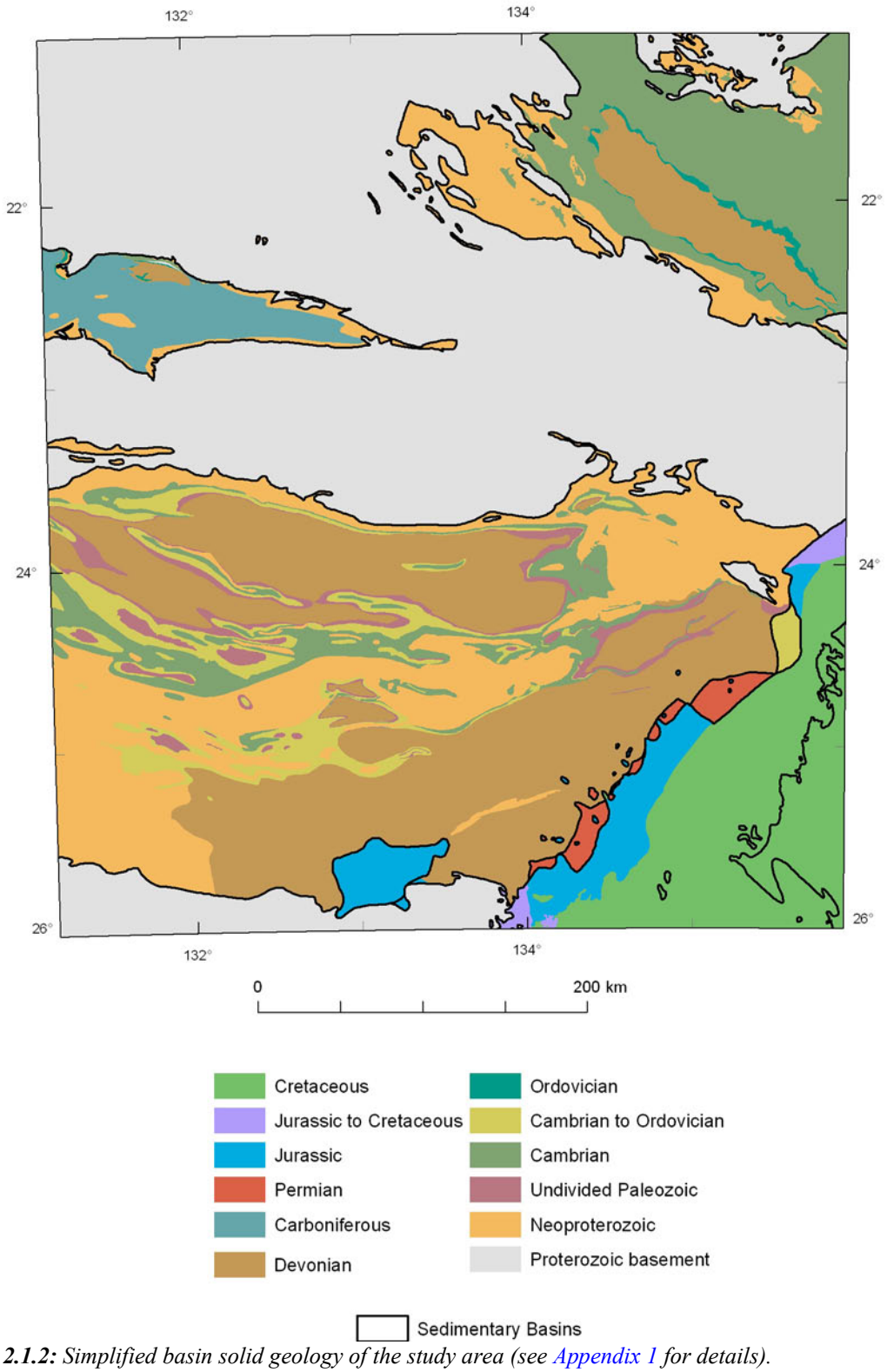

Figure 2.1.2: *Simplified basin solid geology of the study area (see Appendix 1 for details).*

2.1.2.2 Mesozoic to Cenozoic basins

The Mesozoic Eromanga Basin occupies the southeastern part of the study area (Figure 1.1; 2.1.2), and overlies the older Warburton, Pedirka and Amadeus basins. Basin formation was initiated in response to thermal subsidence, followed by marine to fluvial sedimentation (Ambrose, 2006b). Included within the Eromanga Basin are major aquifer systems of the Great Artesian Basin (Radke *et al*., 2000). Cenozoic sedimentary basins are distributed extensively across the study area. Fluvial to lacustrine sedimentary sequences up to 200 m in thickness occur across the study area, including the Hale, Ti-tree, Waite and Aremra basins (Senior *et al*., 1995). Late Paleocene subsidence resulted in the onset of sedimentation in the Lake Eyre Basin (Alley, 1998), which overlies parts of the Eromanga Basin in the southeast of the study area (Figure 1.1; 2.1.2).

2.1.3 Alice Springs Orogeny

The 450–300 Ma Alice Springs Orogeny was a major intraplate orogenic event that has influenced much of the present-day configuration of the central to southern study area. Isotopic evidence and the sedimentary record suggest that, although long-lived, orogenic activity was episodic, with a number of peaks in tectonic activity (Shaw *et al*., 1992; Haines *et al*., 2001). Deformation during the Alice Springs Orogeny was centralised in the eastern Aileron Province, and particularly in the Harts Range area (Scrimgeour and Close, 2011). Uplift resulted in the deposition of syn-orogenic sediments in the Amadeus, Georgina and Ngalia basins, which have been used to delineate discrete ‘movements’ within the Alice Springs Orogeny (Korsch and Lindsay, 1989; Haines *et al*., 2001; Maidment *et al*., 2007). Differing movement names have been assigned within each sedimentary basin, however four main movements can be recognised:

1. The Late Ordovician Rodingan Movement, corresponding to deposition of the Carmichael Sandstone in the Amadeus Basin, the Djagamara Formation in the Ngalia Basin, and the Ethabuka Sandstone in the Georgina Basin;
2. The Devonian Pertnjara Movement, corresponding to deposition of the Pertnjara Group in the Amadeus Basin, the Kerridy Sandstone in the Ngalia Basin, and the Dulcie Sandstone and Craven Peak beds in the Georgina Basin;
3. The Devonian Brewer Movement, corresponding to deposition of the Brewer Conglomerate in the Amadeus Basin. The Brewer Movement is sometimes incorporated into the Pertnjara Movement (e.g., Haines *et al*., 2001; Scrimgeour and Close, 2011); and
4. The Carboniferous Mount Eclipse Movement, corresponding to deposition of the Mount Eclipse Sandstone in the Ngalia Basin.

2.2 MINERAL AND ENERGY SYSTEMS

The study area contains a number of mainly small mineral deposits and occurrences (Figure 2.2.1). Geological evidence suggests that a number of mineral systems may have operated in the past. These systems range in age from Paleoproterozoic to Phanerozoic and include a range of commodities. Despite the numerous prospects and occurrences, there are few ore deposits (*sensu stricto)*. The most significant deposits are described below, and the characteristics of the mineral systems are presented. This discussion is only slightly modified from that given by Huston *et al*. (2011c).

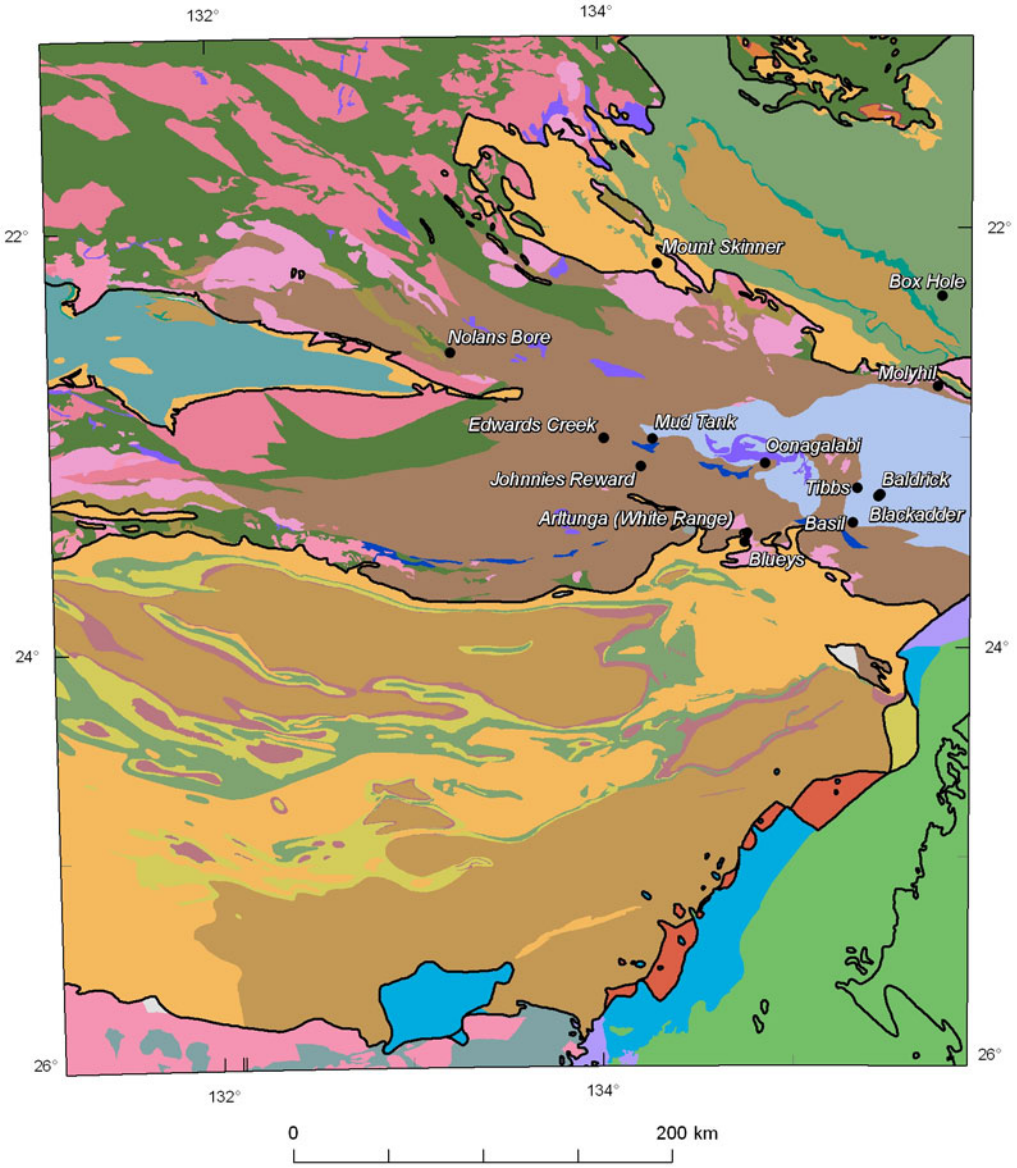

Figure 2.2.1: *Non-uranium mineral deposits and occurrences within the study area. Uranium deposits are shown in Figure 3.1.2. Legend is given in Figures 2.1.1 and 2.1.2.*

2.2.1 Known mineral deposits

The most significant mineral deposits in the area are the White Range lode Au deposit at Arltunga and the Green Parrot Pb-Zn-Ag deposit in the Jervois field (Green Parrot and the Jervois field not shown in Figure 2.2.1; see Section 3.3 for further information). Total Au production from the Arltunga field was 2 355 kg (~76 000 oz), mostly from White Range (Ahmad *et al.,* 2009). Gold deposits in this field are hosted by rocks from both the Paleoproterozoic basement and the Neoproterozoic cover succession (Heavitree Quartzite).

Significant polymetallic prospects in the Irindina Province have recently been identified by Mithril Resources Ltd., including orthomagmatic Ni-Cu ± platinum group element (PGE) (e.g., Blackadder and Baldrick), Cu-Co-rich massive sulfide hosted in the Riddock Amphibolite (e.g., Basil and Manuel) and undefined Au ± W-Cu (e.g., Tibbs) occurrences (McKinnon-Matthews, 2010; Figure 2.2.1). In addition to these new discoveries, the Irindina Province also hosts small hydrothermal

uranium occurrences, and pegmatite-hosted and hydrothermal rare earth element (REE) mineralisation.

The Paleoproterozoic Aileron Province contains small volcanic-hosted massive sulfide deposits (e.g., Edwards Creek and Oonagalabi; Hussey *et al*., 2005), probable iron oxide-copper-gold (IOCG) deposits/prospects (e.g., Johnnies Reward, Jervois and recent discoveries by Mithril Resources; see Section 3.3 for additional information), granite-related W-Mo deposits (e.g., Molyhil), and mafic-hosted V deposits (e.g., Mount Peake). These deposits are probably Paleoproterozoic in age. In addition, the Aileron Province hosts small epigenetic uranium deposits of unknown age and origin, and a major REE-P-U deposit at Nolans Bore. The Nolans Bore deposit consists of a series of massive to brecciated fluorapatite veins. This deposit contains a global resource of 46 Mt grading 2.5% rare earth oxide, 11% P_2O_5 and 186 ppm U_3O_8 (www.arafuraresources.com.au).

The southern Georgina Basin hosts small Mississippi Valley-type Pb-Zn deposits (e.g., Box Hole) and sedimentary phosphorite deposits; both the Amadeus and Georgina basins host Cu prospects (e.g., Blueys) in the lower parts of their successions; and the Amadeus and Ngalia basins contain the sandstone-hosted uranium deposits of Pamela-Angela and Bigrlyi, respectively (described in Section 3.2). Although a significant deposit, Bigrlyi occurs just to the west of the study area.

To the northwest of the study area, there have been important recent discoveries in the Tennant Creek and Rover IOCG fields (not shown in Figure 2.2.1), including the Rover 1 Au-Cu-Bi and the Explorer 108 Pb-Zn deposits. In addition, a small uranium deposit, the Munadgee prospect, is known in the Davenport area (not shown in Figure 2.2.1).

2.2.2 Known or inferred mineral systems

Table 2.2.1 summarises the characteristics of energy (uranium and geothermal) and mineral systems that are known or inferred to have operated in the Tennant, Aileron and the Irindina provinces, and in the Amadeus, Georgina and Ngalia basins.

2.2.2.1 Tennant Creek-Rover iron oxide-copper-gold-uranium system

Seismic data from known IOCG provinces suggests a close association with major boundaries between crustal blocks (Drummond *et al.,* 2006; Korsch *et al.,* 2009a). Goleby *et al.* (2009) identified a major boundary between the Aileron and Tanami provinces approximately 600 km to the northwest of the study area, referred to as the Willowra Suture. Results of the 2009 Georgina-Arunta seismic survey (09GA-GA1) have identified a boundary, the Atuckera Fault, with a similar geometry, which is interpreted as the extension of the Willowra Suture (Korsch *et al.,* 2011). Figure 2.2.2 illustrates the likely extent of this suture based on seismic data, extrapolated along strike using gravity data.

The Rover and Tennant Creek fields are located 50–100 km north of the Willowra Suture. Minerals associated with mineralisation have an Ar-Ar age of approximately 1845 Ma (Fraser *et al.,* 2008), which overlaps the age of the I- to A-type Tennant Creek Supersuite (Budd *et al.,* 2001; Maidment *et al.,* 2006). Granites of similar age are known to the north of this suture from the Tanami Region in the northwest to near the Queensland border. Collectively, these data raise the potential for IOCG deposits associated with ~1850–1845 Ma granites to the north of the suture, along an extensive strike length.

Table 2.2.1: Known and inferred energy and mineral systems in the Irindina, Aileron and Davenport provinces and in the Amadeus, Georgina and Ngalia basins

SYSTEM	COMMODITIES	AGE (MA)	GEODYNAMIC SETTING	KNOWN EXAMPLES	REFERENCES
Tennant Creek-Rover IOCG-U	Au-Cu-Bi-Se-(U-Pb-Zn-Ag)	~1845	Extensional setting (rift and/or back-arc basin) above fertilised mantle	Warrego, Juno, White Devil, Rover 1, Explorer 142, Morning Star	Wedekind *et al*. (1989); Huston *et al*. (1993); Skirrow and Walshe (2002); Fraser *et al*. (2008)
Utnalanama VHMS	Zn-Pb-Cu-(Au-Ag)	1810-1800	Back-arc basin	Edwards Creek, Utnalanama	Hussey *et al*. (2005)
Oonagalabi VHMS	Zn-Pb-Cu-(Au-Ag)	~1765	Back-arc basin	Oonagalabi	Hussey *et al*. (2005)
Yambah IOCG-U	Cu-Au-Bi-Pb-Zn-REE	~1785	Extensional settings (rift and/or back-arc basin) above fertilised mantle	Johnnies Reward, Jervois (Green Parrot)	Hussey *et al*. (2005)
Nolans Bore ?carbonatite	REE-P-U-Th	1560-1240		Nolans Bore	Hussey (2008); Korsch *et al*. (2009b); Huston *et al*. (2011a)
Central Australian Basin U-Cu	U-Cu-(PGE)	850-750 (?)	Ensialic extension; possibly related to Rodinia break-up	Albarta copper, Blueys and Mount Skinner	MODAT[1]
Irindina massive sulfide	Cu-Co	~550 (?)	Extensional setting (rift and/or back-arc basis) with extensive mafic magmatism	Manuel, Basil	www.mithril.com.au
Irindina orthomagmatic Ni-Cu-(PGE)	Ni-Cu-(PGE)	~410	Extensional setting (rifts and/or back-arc basin) with extensive mafic magmatism	Blackadder	www.mithril.com.au
Georgina Zn-Pb-Ag	Zn-Pb-Ag	360 (?)	Marginal to uplift related to basin inversion	Box Hole	Dunster *et al*. (2007)
Arltunga lode Au	Au-(Cu-W?)	322	Intraplate orogenesis	White Range, Winnecke	Ahmad *et al*. (2009)
Sandstone-hosted U	U	<300		Pamela, Angela, Bigrlyi	Borshoff and Faris (1990); Fidler *et al*. (1990)
Paleochannel U	U	< 65	Cenozoic paleochannels	Afghan Swan	www.thundelarra.com.au
Calcrete U	U	< 5	Drainage system with valley and lake calcretes	Napperby	McKay and Miezitis (2001)
Geothermal	Heat	0			Gerner and Holgate (2010)

[1] Mineral Occurrence DATabase, available through the Northern Territory Geological Survey.

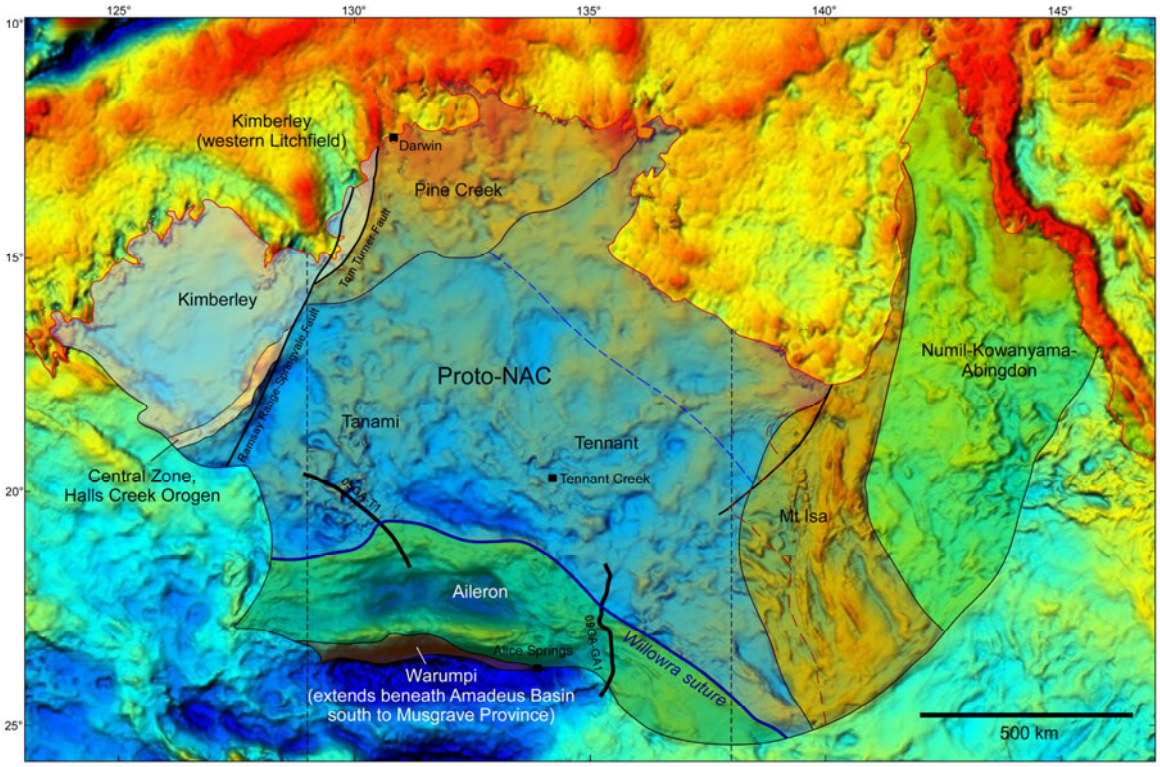

Figure 2.2.2: *Bouger gravity image of the North Australian Craton showing major geological elements, the Willowra Suture and the location of seismic lines 05GA-T1 and 09GA-GA1. Image from Huston et al. (2011c).*

2.2.2.2 Yambah iron oxide-copper-gold-uranium system

The southern to central Aileron Province contains a number of small Cu-Au-(Pb-Zn-Ag) deposits that have been interpreted as IOCG-style mineralisation. Examples include the Johnnies Reward prospect, deposits in the Jervois district and recently-discovered prospects in the eastern and western Arunta Region. Preliminary Pb isotope data suggest ages of between 1795 Ma and 1760 Ma for these deposits (Hussey *et al*., 2005), which overlaps with the Yambah Event. More detailed descriptions of these deposits are presented in Sections 3.3.1.1, 3.3.1.2 and 3.3.1.4.

2.2.2.3 Basin-related (copper)-uranium systems

Sediment-hosted Cu and unconformity-related uranium mineralisation in the Paterson Province (Western Australia) and the Adelaide Rift System (South Australia) is temporally associated with deposition and inversion during the earliest phases of the Centralian Superbasin (Huston *et al.,* 2010; A. Reid, in Drexel, 2008). Several Cu prospects are also known in the eastern part of the Amadeus (e.g., Blueys) and Georgina (e.g., Mount Skinner; Figure 2.2.1) basins, mostly within stratigraphically lower units.

The Albarta and Tourmaline Gorge uranium prospects are hosted in Paleoproterozoic basement and are located at most a few hundred metres below the unconformity with the overlying Heavitree Quartzite of the Amadeus Basin. These potentially represent unconformity-style mineralisation, although the timing and origin of these two prospects remains currently unresolved. Maps of sediment thickness (Wells *et al*., 1970) indicate that the sedimentary pile in the Amadeus Basin may have been sufficient to generate the ~200°C hydrothermal fluids that characterise unconformity-

related deposits (Cuney 2005; Kyser *et al.,* 2000). A more detailed discussion of the potential unconformity-related uranium systems is present in Section 3.4.

2.2.2.4 Sandstone-hosted and paleochannel uranium systems

Significant sandstone-related uranium deposits are known in the Amadeus Basin at Pamela and Angela, and in the Ngalia Basin at the Bigrlyi deposit. These deposits are hosted by fluviatile and feldspathic sandstones deposited in response to uplift during the Alice Springs Orogeny (Borshoff and Faris, 1990; Fidler *et al*., 1990; Haines *et al*., 2001). More recently, Thundelarra Exploration identified uranium within Cenozoic paleochannels overlying the Ngalia Basin at the Afghan Swan prospect. The uranium mineralisation (up to 7 m grading ~1400 eU_3O_8; www.thundelarra.com) has been traced for 15 km along strike, indicating the potential for Frome Embayment-style uranium mineralisation in the study area. Cenozoic basins located within the study area (e.g., Senior *et al*., 1995) must be considered as having potential for a similar style of mineralisation. A more detailed discussion of sandstone-hosted uranium systems is presented in Section 3.2.

2.2.2.5 Calcrete uranium systems

One of the larger uranium deposits in the study area, the Napperby prospect, with a JORC-compliant resource of 9.34 Mt @ 359 ppm U_3O_8 for 3.35 kt U_3O_8 (www.deepyellow.com.au), is interpreted as a calcrete deposit. This deposit occurs three to eight metres below the surface in unconsolidated to semi-consolidated sediments within a paleochannel.

2.2.2.6 Utnalanama and Oonagalabi volcanic-hosted massive sulfide system

The Aileron Province contains a number of volcanic-hosted massive sulfide prospects located in the Strangways Metamorphic Complex and the Oonagalabi 'Tongue' (Warren and Shaw, 1995; Hussey *et al*., 2005). These deposits are thought to have formed in back-arc basins associated with north-dipping subduction along the southern margin of the Aileron Province (e.g., Betts and Giles, 2006; Huston *et al*., 2012) between 1810–1765 Ma (Hussey *et al*., 2005).

2.2.2.7 Mineral systems related to alkaline magmatism

The Nolans Bore deposit is thought to have formed from unusual hydrothermal fluids, possibly associated with alkaline magmatism, at a temperature of ~400^{o}C. The age of mineralisation is constrained to between ~1565 Ma and ~1240 Ma (Huston *et al*., 2011a).

Magmatism associated with the ~1140 Ma Teapot Event is associated with locally significant uranium mineralisation in the Teapot Granite (up to 0.226% U_3O_8; www.panconu.com) and Ni-Cu-PGE mineralisation in ultramafic rocks associated with the Mordor Igneous Complex (Hoatson *et al*., 2005). The Teapot Granite is considered as a probable source of uranium and REE at the nearby Charley Creek sediment-hosted uranium-REE prospect (www.panconu.com).

At this writing, the only operating mine in the study area is the Mud Tank vermiculite mine, which is operated by Imerys Vermiculite and extracts weathered biotite from an alteration zone surrounding the ~732 Ma (Black and Gulson, 1978) Mud Tank Carbonatite (Hussey, 2003) for conversion to vermiculite. The Mud Tank Carbonatite consists of commonly pegmatitic, massive carbonate with less than 10% silicate minerals surrounded by silicate-bearing zones with progressively lower carbonate content.

2.2.2.8 Irindina copper-cobalt massive sulfide system

The Basil and Manuel Cu-Co deposits indicate potential for mafic-hosted massive sulfide deposits within the Harts Range Metamorphic Complex, and particularly the Riddock Amphibolite. Copper-cobalt deposits are apparently structurally controlled, and are situated along structural trends within the Riddock Amphibolite.

2.2.2.9 Georgina Basin zinc-lead-silver system

Several examples of Mississippi Valley-type Pb-Zn mineralisation occur in the southwestern Georgina Basin. The most significant (Box Hole) is hosted by carbonates of the Late Cambrian Arrinthrunga Formation, which constrains the maximum age of mineralisation to ~500 Ma. Leach *et al.* (2005) concluded that Mississippi Valley-type deposits, with the possible exception of the Lennard Shelf deposits in Western Australia, are associated with orogenic forelands produced by Phanerozoic contractional events. Hence, it is possible that the Mississippi Valley-type deposits are associated with uplift associated with the 450–300 Ma Alice Springs Orogeny.

Ar-Ar ages of approximately 360 Ma from structures active during the Alice Springs Orogeny correspond with the inferred timing of Mississippi Valley-type mineralisation in the Canning Basin to the northwest of the study area. These results suggest that the Canning Basin deposits, and probably also the deposits of the Georgina Basin, are related to contractional deformation and uplift, likely during the Devonian Pertnjara Movement. As the orogen associated with the Pertnjara Movement was doubly-vergent (Haines *et al.,* 2001), potential for Mississippi Valley-type mineralisation may also extend southwards into the Amadeus Basin.

2.2.2.10 Arltunga lode gold system

Seismic and other geological studies have indicated the importance of crustal-penetrating shear zones as important, regional-scale controls on lode Au mineralisation (Blewett *et al.,* 2010). In addition, most studied deposits formed at low metamorphic grades (greenschist to sub-greenschist metamorphic conditions; Goldfarb *et al.,* 2005), suggesting that they are deposited in the upper- to mid-crust. The Georgina-Arunta seismic survey has imaged two crust-penetrating shear systems: the Illogwa-Bruna Detachment and the Atnarta Imbricate Fault Zone (Korsch *et al.,* 2011). Deformation of the Irindina Basin was accomplished mainly by thrusting along the Illogwa-Bruna detachment, exhuming the mid-crustal rocks (amphibolite to granulite facies) that dominate the Irindina Province. Even though this structure can be traced to the Moho, it is not likely to be associated with major lode Au deposits, as upper crustal rocks, which would have hosted gold deposits, have been removed. A more favourable structure is the Atnarta Imbricate Fault Zone, which also taps the mantle, but, as it was not the major inversion structure, upper crustal rocks that could host lode Au deposits are more likely to be preserved. The Arltunga goldfield may lie on a west-northwest extension of the Atnarta Imbricate Fault Zone.

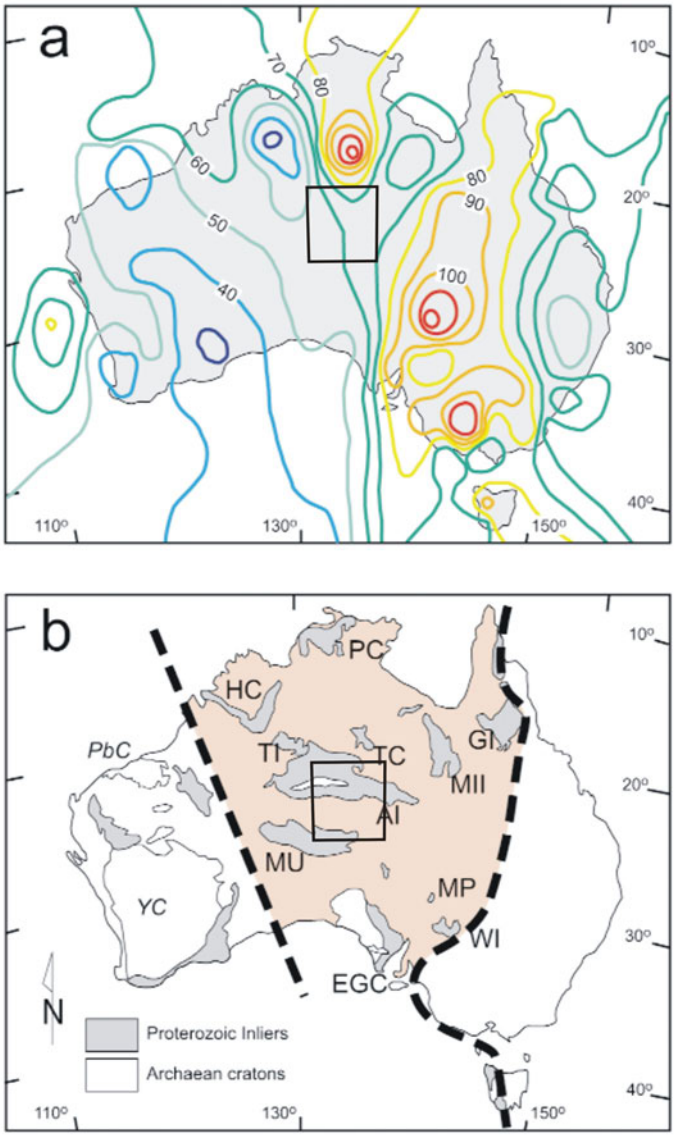

***Figure 2.2.3**: (a) Australian heat-flow field (image from McLaren et al., 2003, after Cull, 1982), with contours in mW/m^2; (b) Location of major Archean to Proterozoic terranes relative to the Central Australian Heat-Flow Province (shaded in tan). Thick dashed lines delineate the Western and Eastern Provinces. HC: Halls Creek Inlier; MII: Mt Isa Inlier; TC: Tennant Creek Inlier; MP: Mt Painter Inlier; AI: Arunta Inlier; TI: Tanami Inlier; WI: Willyama Inlier; MU: Musgrave Block; EGC: Eastern Gawler Craton and Stuart Shelf; PC: Pine Creek Inlier; GI: Georgetown Inlier; YC: Yilgarn Craton; PbC: Pilbara Craton. The location of the study area is shown by the black box.*

2.2.2.11 Geothermal energy systems

The Australian continent is divided into three broad heat-flow provinces: the Western, Central, and the Eastern Heat-Flow Provinces (Sass and Lachenbruch, 1979). The dominantly Archean Western Province, and the dominantly Paleozoic Eastern Province record heat-flow values of 39 ± 8 mW/m^2 and 72 ± 27 mW/m^2 respectively, which are consistent with global average values for terranes of similar ages (McLaren *et al*., 2003). In contrast, the Central Australian Heat-Flow Province shows heat-flow values of 82 ± 25 mW/m^2, which is well above average global values of equivalent-aged Proterozoic terranes (McLaren *et al*., 2003). The Central Australian Heat-Flow Province occupies a broad north-south-trending region across the centre of the Australian continent, as shown in Figure

2.2.3. Data defining these provinces are relatively scarce, with only around 120 values available for the whole continent when major heat-flow synthesis work began to be undertaken in the late 1970s and 1980s, and few additional heat-flow values have been collected since.

Temperatures at five kilometres depth in the study area are suggested by the OZTemp map of Gerner and Holgate (2010). This shows a small thermal anomaly in the Georgina Basin in the northeastern part of the study area. This anomaly is based upon moderately high thermal gradients measured in the MacIntyre 1 and Baldwin 1 petroleum exploration wells located just outside of the study area. Elsewhere in the study area, petroleum wells indicate lower temperature gradients (e.g., 30.1°C/km in the Phillip 2 exploration well). An assessment of geothermal potential of the study area is presented in Section 4.

3. Uranium mineral systems assessment

Uranium mineral deposits have commonly been categorised using the long-established International Atomic Energy Agency (IAEA) scheme, which utilises 15 separate classifications based largely on host rock lithology. In contrast to this more descriptive approach, several workers have proposed classification schema which emphasise genetic aspects, based on the recognition that many of the IAEA categories have common underpinning genetic processes (e.g., Plant *et al*., 1999; Cuney, 2009). This study utilises the genetic classification of Skirrow *et al*. (2009), which approaches classification of uranium deposits using a mineral systems-based perspective. This classification schema consists of three end-member mineralising systems: basin- and surface-related systems, metamorphic-related systems, and magmatic-related systems (Figure 3.1.1). A continuum of deposit styles are predicted between these three end-members, resulting in 'hybrid' uranium systems, which include uranium-rich IOCG systems such as the giant Olympic Dam deposit.

The potential for four different uranium systems has been investigated in this study. These are:
1. Sandstone-hosted (Section 3.2);
2. Uranium-rich IOCG (Section 3.3);
3. Unconformity-related (Section 3.4); and
4. Magmatic-related (includes orthomagmatic and magmatic-hydrothermal; Section 3.5).

A number of known deposits and prospects corresponding to these targeted systems occur within the study area (Figure 3.1.2). The position of these on the classification schema of Skirrow *et al*. (2009) is shown in Figure 3.1.1.

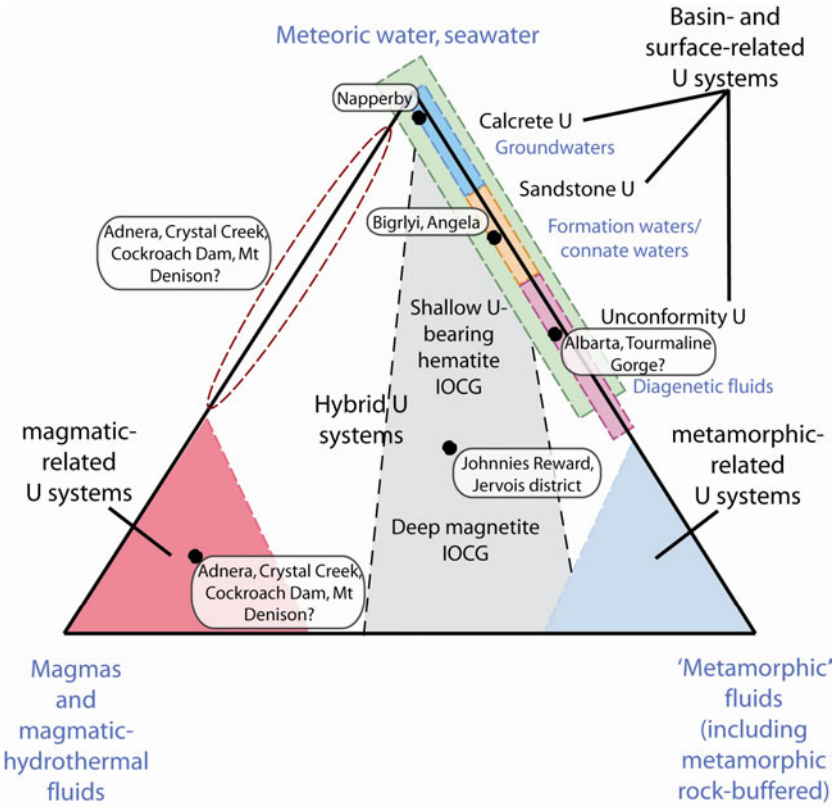

Figure 3.1.1: *Ternary uranium systems classification scheme of Skirrow et al. (2009). Selected deposits and prospects from the study area are plotted.*

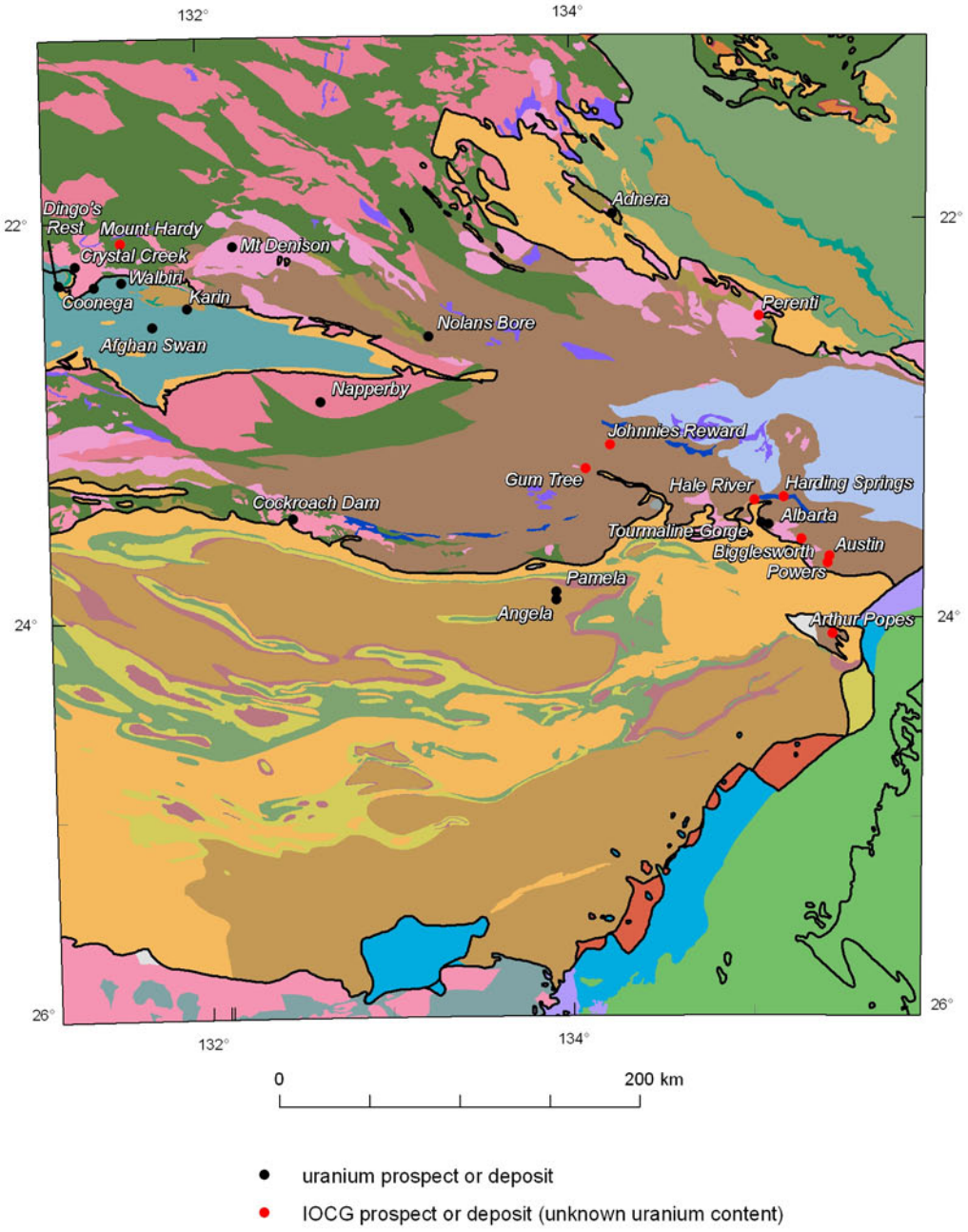

Figure 3.1.2: *Location of significant uranium deposits and prospects within the study area plotted on the combined solid geology. Potential IOCG prospects are also shown. Legend is given in Figures 2.1.1 and 2.1.2.*

3.1 PROSPECTIVITY ANALYSIS METHODOLOGY

The methodology used to assess the potential for uranium mineralisation in this study is only slightly modified from that employed during the assessment for uranium in east-central South Australia, which has been described in Huston and van der Wielen (2011). In the discussion below, portions of this description have been reproduced, while others have been slightly modified.

The formation of mineral deposits is a result of the coincidence of favourable geological conditions within a given spatial setting, constrained by geological time. In a prospectivity analysis, these factors are generally mapped using geological evidence and assigned weightings based on their perceived importance to the mineralising system. The final map of mineral potential is a function of the input evidence maps (Bonham-Carter, 1994). A number of documented approaches exist to integrate the disparate input evidence maps (e.g., see Bonham-Carter, 1994). At the most basic level, these may be subdivided into two broad categories: data-driven methods and knowledge-driven methods (Bonham-Carter, 1994; Knox-Robinson and Wyborn, 1997). Data-driven methods are typically applied in areas where there are numerous known deposits, with criteria development and weightings determined through statistical analysis. With knowledge-driven methods, prospectivity criteria are developed based on a conceptual model (mineral systems model), with criteria weightings assigned subjectively. Due to the mineral systems approach used in this investigation and the relative paucity of known deposits, a knowledge-driven approach has been utilised in this assessment.

Following from the east-central South Australia uranium assessment (Huston and van der Wielen, 2011), a mineral systems model is used consisting of four key system components:

1. Sources of metals, fluids and ligands;
2. Drivers of fluid flow;
3. Fluid-flow pathways and architecture; and
4. Depositional sites and mechanisms.

Using this mineral systems framework, criteria are developed which are interpreted to reflect mineralising processes (see Tables 3.2.1, 3.3.2, 3.4.1, 3.4.2 and 3.5.2). Under each key system component listed above, 'theoretical' conceptual criteria are developed which reflect favourable geological processes for the mineral system. These are in turn translated into mappable geological proxies and assigned weightings. This approach is similar to that described by McCuaig *et al*. (2010). The weighting assigned for each criterion is the product of three factors:

- The importance, which reflects the overall importance of the theoretical criterion to the mineral system;
- The applicability, which reflects the certainty that the mappable geological proxy reflects the desired process given by the theoretical criterion; and
- The confidence, which reflects the confidence in the data source, both in terms of spatial accuracy and overall data quality.

Values for the importance, applicability and confidence are assigned subjectively based on a pre-defined table (Table 3.1.1) in a manner similar to that used in fuzzy logic. Decisions concerning other aspects of the criteria used, such as the selection of buffer distances and assignment of cutoff values, were also made subjectively based on the scientific judgement of the analyst. Further details of these are given in the respective sections for each system. Unlike data-driven methods, criteria are developed without reference to known deposits in order to avoid biasing results to known mineralisation. However, the locations of known deposits are used to verify the results of the assessment.

Following criteria development and the assignment of weightings, mappable criteria are combined into intermediate maps corresponding to each of the four key system components. Each system component represents the sum of the weightings for the input mappable criteria normalised by the number of criteria, and is therefore weighted between zero and one. This ensures that each system component contributes equally to the final assessment regardless of the number of input criteria used. Weightings for the four system components are then added together to generate the final uranium potential map (Figure 3.1.3). This method, which has been custom developed for the east-central South Australia and southern Northern Territory uranium assessments, represents a hybrid of the fuzzy logic and index overlay approaches. The methodology described above is undertaken in a 2D GIS-based environment.

Table 3.1.1: Guide for assigning importance, applicability and confidence values, together with definitions of certainty modified from the Sherman-Kent Scale (see Meyer and Brooker, 1991)

NUMERICAL VALUE	VALUE DESCRIPTION	DEFINITION (CONFIDENCE OF VALUE DESCRIPTION BEING TRUE)
1.0	Total or critical	Proven or definitely true
0.9	Extremely high	Virtually certain or convinced
0.8	Very high	Highly likely
0.7	High	Likely
0.6	Moderately high	Slightly higher than even chance
0.5	Moderate	Even chance
0.4	Moderately low	Slightly lower than even chance
0.3	Low	Unlikely
0.2	Very low	Could be possible, but probably not
0.1	Extremely low	Possible but very doubtful
0	Nil	Proven untrue or impossible

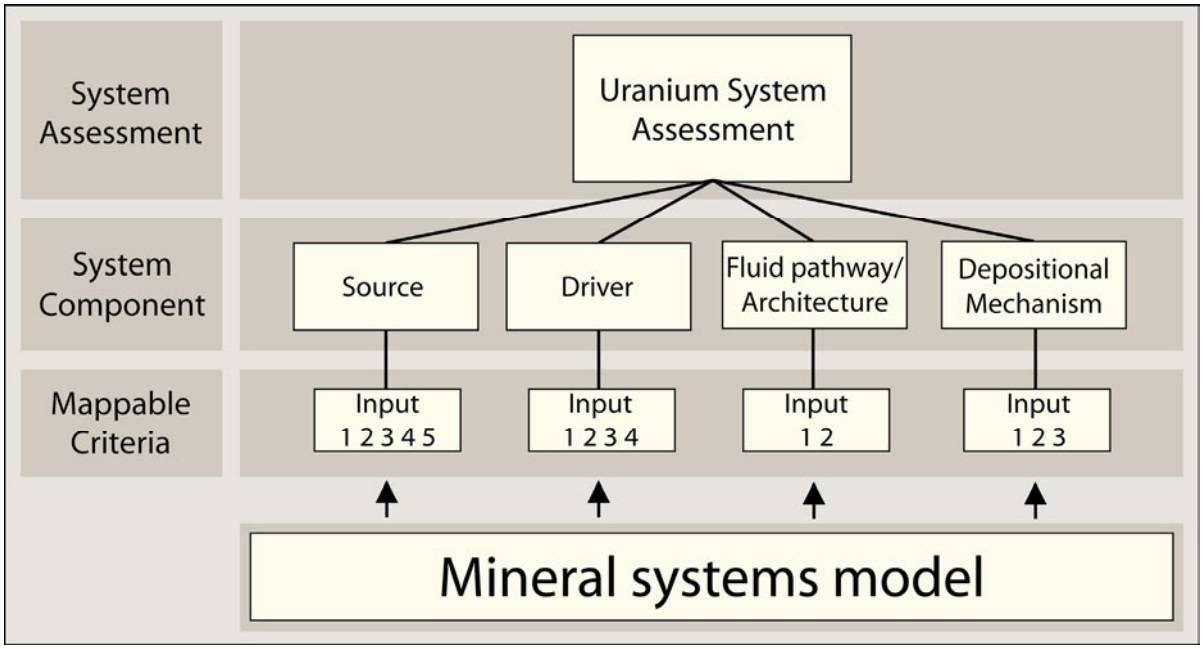

Figure 3.1.3: *Schematic process for developing uranium potential maps.*

3.2. SANDSTONE-HOSTED URANIUM SYSTEMS

A. Schofield and R.G. Gallagher

Sandstone-hosted uranium deposits belong to the basin- and surface-related family of uranium mineral systems of Skirrow *et al*. (2009; Figure 3.1.1). They represent an important subcategory of uranium mineral system, accounting for one quarter of world uranium production and one third of global resources (OECD Nuclear Energy Agency, 2008). Australia currently has two operating mines producing uranium from sandstone-hosted systems, both of which are located in South Australia: Honeymoon and Beverley (including Beverley North). Although uranium is not currently produced from sandstone-hosted deposits within the study area, a number of occurrences of mineralisation are known. These will be briefly described below. Owing to the demonstrated potential for Paleozoic sandstone-hosted uranium systems within the study area, the analysis described below will focus on determining the potential during this era. The potential of Mesozoic basins within the area is also considered.

3.2.1 Sandstone-hosted uranium deposits in the study area

Sandstone-hosted uranium deposits are known within the Ngalia and Amadeus basins, and the Eromanga Basin has also been shown to have potential for sandstone-hosted uranium (van der Wielen *et al*., 2011). One major sandstone-hosted uranium deposit occurs within the study area at Angela (Figure 3.2.1). The Bigrlyi uranium deposit occurs just outside of the study area (Figure 3.2.1), and also represents a major example of sandstone-hosted uranium mineralisation. As well as the major deposits (Bigrlyi and Angela) described below, a number of small prospects also occur within the study area, including Pamela in the Amadeus Basin and Walbiri, Dingo's Rest, Sunberg (not shown in Figure 3.2.1), Coonega and Karin in the Ngalia Basin (Figure 3.2.1; McKay and Miezitis, 2001).

3.2.1.1 Bigrlyi

The Bigrlyi uranium deposit is located within the northern Ngalia Basin approximately 330 km northwest of Alice Springs (Figure 3.2.1). Uranium mineralisation at Bigrlyi was first identified in 1973 during ground radiometric surveys (Fidler *et al*., 1990). Recent figures indicate a resource (Indicated and Inferred JORC categories) of 7.5 Mt at 1283 ppm U_3O_8 for 9600 t of U_3O_8 (Energy Metals Ltd. Australian Stock Exchange (ASX) announcement, 28 June 2011). Mineralisation is contained within seven discontinuous lenses occurring over 11 km strike length in the lower Mount Eclipse Sandstone (Fidler *et al*., 1990; McKay and Miezitis, 2001).

The syn-orogenic Mount Eclipse Sandstone is dominantly an immature medium- to coarse-grained, sub-arkosic sandstone with common carbonate cement deposited in a braided fluvial environment (Wells and Moss, 1983; Fidler *et al*., 1990; Schmid *et al*., 2012). Deposition occurred during the Mount Eclipse Movement of the Alice Springs Orogeny (Haines *et al*., 2001). It is mainly red, although zones of light to dark grey and yellow-brown sand occur locally (Fidler *et al*., 1990). Sedimentary structures are consistent with a source of sediment to the northeast (Fidler *et al*., 1990), possibly within the Paleoproterozoic Carrington Suite (as suggested by Schmid *et al*., 2012) or the uranium-rich Mesoproterozoic Southwark Suite (including the Yarunganyi Granite which hosts the Crystal Creek magmatic-related uranium occurrence; Section 3.5).

Fidler *et al*. (1990) considered uranium mineralisation to be associated with carbonaceous material within the Mount Eclipse Sandstone, principally within the informally named 'Unit C'. Minor uranium also occurs in the adjacent Units B and D, and lower uranium grades have been correlated with a decrease in the abundance of carbonaceous material (Fidler *et al*., 1990). The association between uranium and carbonaceous material has recently been questioned by Schmid *et al*. (2012) on the basis of petrographic investigation of the mineralised Mount Eclipse Sandstone. This has led

those authors to propose a different model for mineralisation at Bigrlyi (see below). However, Wells and Moss (1983) present evidence suggesting at least some of the Mount Eclipse Sandstone has elevated organic carbon content and note the presence of carbonaceous material and plant remains with uranium. Schmid *et al*. (2012) consider uranium mineralisation to have occurred very early, preceding carbonate cementation.

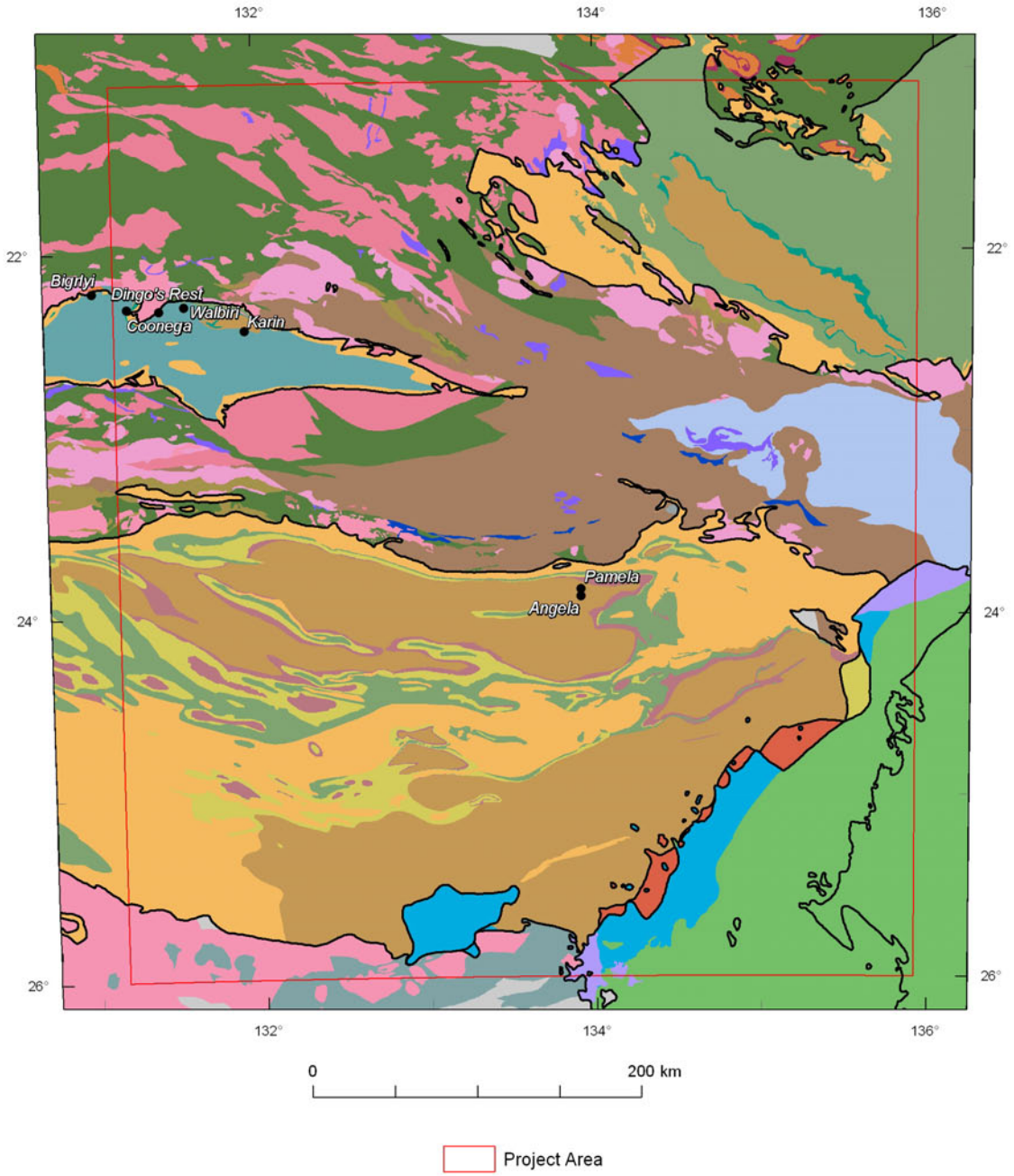

Figure 3.2.1: *Location of known sandstone-hosted uranium mineralisation in the study area (shown by the red box). Legend for geology is given in Figures 2.1.1 and 2.1.2.*

Most primary mineralisation consists of uraninite and montroseite (VO(OH)), with carnotite developed locally above the water table (Fidler *et al*., 1990). High V abundances accompany elevated uranium, and have a correlation of 0.89 R^2 (Schmid and Cleverley, 2011). Mineralised zones also exhibit elevated Bi, Be, Te, Se, Li, W and Ba (Schmid and Cleverley, 2011; Schmid *et al*., 2012). Uranium occurs in association with V-bearing smectite and roscoelite ($K(V,Al,Mg)_2AlSi_3O_{10}(OH)_2$), Fe-Ti oxides, APS (Al-P-S) minerals and biotite. The elemental and mineralogical associations in the mineralised zone have led Schmid *et al*. (2012) to propose a uranium source within pegmatitic or hydrothermal constituents of the granitic source rocks, with primary uranium mineralisation being essentially detrital and uranium deposited in favourable sedimentary environments, followed by secondary remobilisation. In this model, deposition of uranium is controlled by sedimentary facies. However, many of the elemental associations are similar to those found in other sandstone-hosted uranium systems (e.g., Spirakis, 1996; Jaireth *et al*., 2008). Further details are required in order to formulate a mineral systems model based on this interpretation, and hence it is not incorporated in this assessment.

Spores contained within the mineralised sandstone constrain the age of the host unit to the latest Devonian to early Carboniferous (approximately 360 Ma; Fidler *et al*., 1990). This age conflicts with four $^{207}Pb/^{206}Pb$ ages obtained from mineralisation ranging from 576–437 Ma (Pidgeon, 1977). Uranium mineralisation is, however, in radioactive disequilibrium, and there is a deficiency of uranium relative to that expected for the Pb isotope values (Fidler *et al*., 1990). In view of this, it appears that uranium mineralisation must be younger than the early Carboniferous and predate the development of the carbonate cement, the timing of which is as yet undetermined, although it is thought to be early (Schmid *et al*., 2012).

3.2.1.2 Angela

The Angela uranium deposit is located 25 km south of Alice Springs in the Neoproterozoic to Carboniferous Amadeus Basin (Figure 3.2.1). The smaller Pamela prospect is located four kilometres to the north of Angela. Both Angela and Pamela are hosted in sedimentary rocks within a major structural feature known as the Missionary Syncline. A JORC Inferred mineral resource for Angela has been estimated at 10.7 Mt of ore yielding 13,980 t U_3O_8 at a grade of 1310 ppm U_3O_8 (Paladin Energy Annual Report, June 2011). The description below is largely taken from Borshoff and Faris (1990).

Uranium is hosted in syn-orogenic (Haines *et al*., 2001) terrigenous sandstones of the Devonian Undandita Member of the Brewer Conglomerate (Pertnjara Group). Lithologically, it is comprised of fine- to coarse-grained lithic arenite to medium- to coarse-grained lithic arkose and thin mudstone units that were deposited in a braided stream environment. The Undandita Member is generally oxidised. However, reduced horizons within the Undandita Member form a generally planar regional redox boundary with localised uranium mineralisation. In places, this typically planar surface has developed ‘steps’ 30 to 40 m in vertical extent, which may be due to breaches in calcitic aquicludes, facies changes or erosion. Uranium mineralisation is concentrated along the upper redox interface and especially where the redox front is stepped, resulting in a series of stacked mineralised horizons made up of one or more roll fronts (Figure 3.2.2). Four zones characterise the redox boundary, grading from red hematitic sediments to reduced grey-green sands. Mineralisation occurs in a bleached zone associated with the more permeable facies, which likely represents the redox front. Principal reductants in the reduced zone are lithic fragments and clay minerals, and only minor pyrite and organic material.

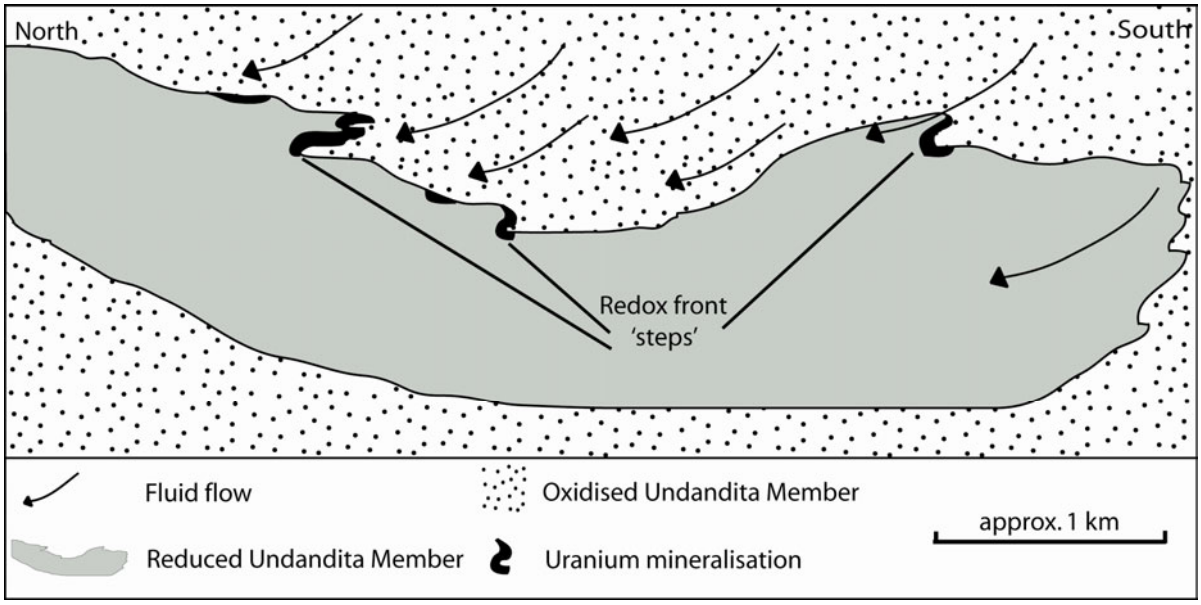

Figure 3.2.2: *Schematic section through the Angela and Pamela deposits in the northern Amadeus Basin. Modified from Borshoff and Faris (1990).*

Primary uranium mineralisation consists mainly of fine-grained to amorphous uraninite, pitchblende and minor coffinite, and occurs as grain coatings, void linings and blebs. A range of secondary uranium minerals have developed within weathering zones. Gangue mineralogy is dominated by hematitic cement. Notably, reductants such as pyrite and organic material are negligible. Vanadium is present in high quantities, grading at values approximately half that of uranium, and anomalous values of Cu, Pb, Se, As and Y have been recorded.

Uranium was likely originally sourced from basement rocks of the Aileron Province, with the uranium-bearing mineralising solutions generated within the sedimentary pile by low-temperature oxidising fluids. The uranium in solution was then precipitated at the regional redox front. Zones of greater permeability within the reducing units are interpreted to have focused the uranium mineralising fluids, and contain the highest uranium grades.

3.2.2 Mineral system model for sandstone-hosted uranium systems

Sandstone-hosted uranium deposits form where oxidised fluids transporting uranium encounter reductants within a basin and precipitate the uranium via the reduction of mobile U^{6+} to immobile U^{4+}. Models for the formation of sandstone-hosted uranium systems have been detailed in previous assessments (van der Wielen, 2010; van der Wielen *et al*., 2011) and, as such, only a brief description will be provided here.

Two main models have been proposed for the formation of sandstone-hosted uranium systems, involving single- or multiple-fluids (Figure 3.2.3a; see Jaireth *et al*., 2008). Single-fluid uranium systems occur in reductant-rich sandstone units, with uranium precipitated from oxidised groundwaters at a redox front via reduction by, for example, organic material. Other sites of uranium deposition may be associated with Fe^{2+}-rich mineralogy (e.g., pyrite, ilmenite), adsorption, or due to bacterially-mediated processes (see Skirrow *et al*., 2009, and references therein). Multiple fluids may explain sandstone-hosted uranium systems where the sandstone lacks significant reducing materials. In such a model, a second reducing fluid, such as hydrocarbons or H_2S, interacts with the oxidised groundwaters along structures, causing uranium deposition (Figure 3.2.3b).

A third alternative, suggested by a recent study of the Bigrlyi uranium deposit (Schmid *et al*., 2012), invokes the deposition of uranium as a detrital phase sourced from hydrothermal mineralisation in the sediment source. Due to uncertainty regarding this model and the clear evidence indicating the involvement of reducing material from other known deposits (e.g., Beverley; Jaireth, 2009 and references therein), this model will not be considered in the assessment.

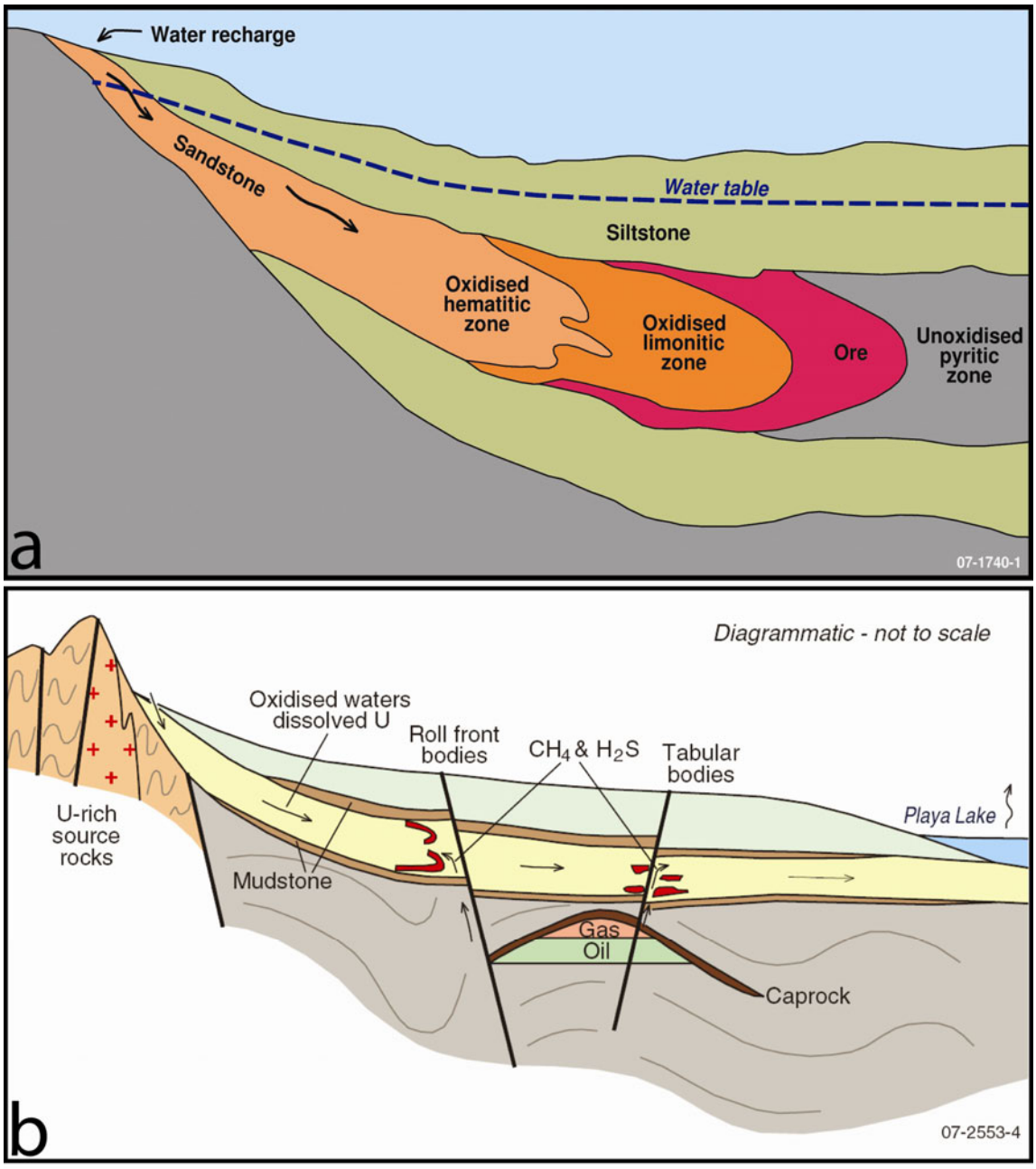

Figure 3.2.3: *Schematic mineral system models for sandstone-hosted uranium systems. a) single-fluid model; b) multiple-fluid model (from Jaireth et al., 2008).*

3.2.3 System components and mappable criteria

The mineral systems model described above has been translated into four key system components that are used to assess the potential for sandstone-hosted uranium systems (see Section 3.1): sources, drivers of fluid flow, fluid-flow pathways and architecture, and depositional mechanisms. Criteria for each of these system components are listed in Table 3.2.1, and are described in detail below.

3.2.3.1 Sources

There are two broad potential sources of uranium for this system (Skirrow *et al*., 2009; van der Wielen *et al*., 2011): (1) uranium leached from source rocks within the hinterland and (2) uranium leached from detritus within sedimentary aquifers (e.g., metamict zircon). While the latter may be important for the formation of these systems, insufficient information exists on the uranium content and leachability of the aquifers to incorporate this as a criterion within the assessment. Thus, one criterion has been used to map potential uranium sources within the basement:

- Igneous uranium sources in basement.

The criterion for igneous uranium sources was derived by buffering igneous rocks to 100 km. The buffer distance selected corresponds to the maximum distance used by van der Wielen *et al*. (2011), and is based on theoretical modelling of sandstone-hosted uranium deposits in Kazakhstan. Two classes of igneous rocks are recognised, which are weighted differently (Table 3.2.1): uranium-rich igneous rocks and other felsic igneous rocks. Uranium-rich igneous rocks were identified according to the same approach used in the assessment for magmatic-related uranium systems (see Section 3.5), although sub-categories of uranium enrichment have not been retained. Suitable uranium-rich igneous sources exist adjacent to the margins of the Amadeus, Ngalia and Georgina basins (Figure 3.2.4). The extensive occurrence of other felsic igneous rocks in the study area results in a large proportion of the study area being favourable for uranium sources.

The sources system component includes sources of metals, mineralising fluids and ligands. In sandstone-hosted uranium systems, the fluids involved are oxidised groundwaters initially derived from a meteoric source (Skirrow *et al*., 2009; Figure 3.1.1). At the low temperatures prevalent in these systems, geologically significant concentrations of uranium are only possible under highly oxidising conditions (Skirrow *et al*., 2009). At temperatures less than 100^{o}C, uranium solubility is highest at neutral to alkaline pH. Uranium-phosphate complexes dominate at relatively neutral pH (four to eight), while under more alkaline conditions (pH>8), uranium-carbonate complexes are the most important (Cuney and Kyser, 2008). Uranium is less soluble at low temperatures under acidic conditions, with fluoride and sulfate complexes being the most important (Cuney and Kyser, 2008). Thus, a highly oxidised fluid with neutral to alkaline pH and with phosphate or carbonate will have the highest potential for transporting uranium in sandstone-hosted systems. Since these are difficult to map, sources of fluids and ligands are not included as criteria in the sandstone-hosted uranium assessment, but are rather assumed. In the two-fluid mineral system model, the source of mobile reductants at depth within a basin becomes important. This will be discussed more fully under the depositional mechanisms system component.

Table 3.2.1: Theoretical and mappable criteria for sandstone-hosted uranium systems

MINERAL SYSTEM COMPONENT	CRITERIA		DATASET	IMPOR-TANCE	APPLIC-ABILITY	CONFI-DENCE	WEIGHTING	COMMENTS
	THEORETICAL	MAPPABLE						
Source	Igneous U source in basement	100 km buffer around U-enriched igneous rocks	Radiometric map of Australia (Minty *et al*., 2010); Geochemical data; Basement solid geology (see Appendix 1)	0.9	0.7	0.8	0.504	
		100 km buffer around other felsic igneous rocks		0.9	0.6	0.8	0.432	
Drivers	(Paleo)topographic-driven fluid flow	100 km buffer around interpreted areas of uplifted basement	Isotope data (see text for details)	1.0	0.5	0.5	0.250	Areas uplifted during orogeny (Alice Springs, Petermann orogenies). Intensity of uplift determined from isotopic data and geological literature
		100 km buffer around interpreted areas of weakly uplifted basement		1.0	0.3	0.5	0.150	
	Sediments generated during uplift of hinterland regions	Distribution of syn-orogenic sedimentary rocks	Basin solid geology (see Appendix 1); literature review (see text for details)	0.6	0.6	0.6	0.216	
		Distribution of syn-Mount Eclipse/Brewer movement sedimentary rocks		0.6	0.7	0.6	0.252	Mount Eclipse/Brewer Movement is the main phase of basement exhumation according to Maidment *et al*. (2007)
Fluid-flow pathways and architecture	Favourable geological setting	Distribution of sedimentary basins	Provinces dataset	1.0	1.0	1.0	1.000	
	Favourable fluid-flow aquifers	Units with proven aquifer potential	Basin solid geology (see Appendix 1); literature review (see text for details)	1.0	0.9	0.6	0.540	Aquifers were ranked using published descriptions (see text for details)
		Units with good aquifer potential		1.0	0.8	0.6	0.480	
		Units with possible aquifer potential		1.0	0.6	0.6	0.360	
		Units with some aquifer potential		1.0	0.3	0.6	0.180	
	Fluid pathways for reductants at depth in basin	Faults buffered to 2.5 km	Basin solid geology (see Appendix 1)	0.5	0.6	0.6	0.180	Relates to depositional mechanism
Depositional mechanisms	Distribution of reduced units within basin	Unit with excellent reductant potential	Basin solid geology (see Appendix 1); literature review (see text for details)	0.9	0.9	0.7	0.567	Reductant potential was ranked using published descriptions (see text for details)
		Unit with good reductant potential		0.9	0.6	0.7	0.378	
		Unit with moderate reductant potential		0.9	0.3	0.7	0.270	
		Unit with low reductant potential		0.9	0.2	0.7	0.126	
	Sources of reducing fluids	Known petroleum fields buffered to 5 km	Encom petroleum fields (proprietary); wells	0.6	0.4	0.3	0.072	
		Distribution of hydrocarbon-bearing basins	Provinces dataset	0.6	0.2	0.3	0.036	
	Direct evidence of elevated U	U^2/Th values one standard deviation above the mean for each unique geological unit	Radiometric map of Australia (Minty *et al*., 2010); Surface geology of Australia (Raymond and Retter, 2010)	0.7	0.7	0.6	0.294	See text for details
		U^2/Th values two standard deviations above the mean for each unique geological unit		0.7	0.8	0.6	0.336	

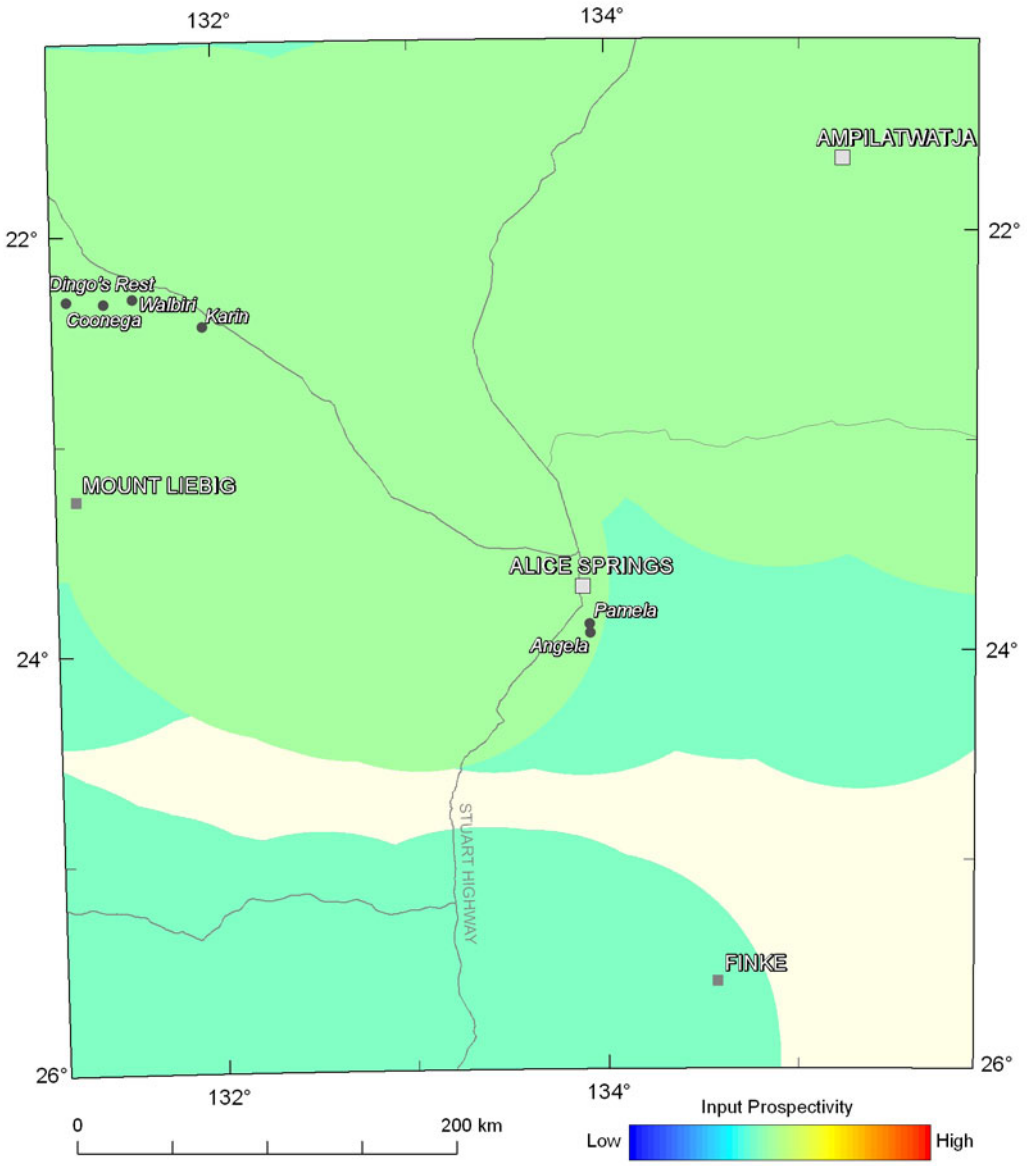

Figure 3.2.4: *Variation in the weightings for basement igneous uranium sources buffered to 100 km. The colour stretch for the mappable criteria used in the assessment for sandstone-hosted uranium systems uses a numerical range from the minimum to the maximum weighting of all criteria used (0.036 to 1.000; see Table 3.2.1), and utilises 20 equal-interval breaks. Note: for this and subsequent figures, the cream colour denotes the absence of weighted criteria, and is assigned a null value.*

3.2.3.2 Drivers

Topographic gradient is the main driver for fluid flow in sandstone-hosted uranium systems. Other drivers may include convection and deformation-driven fluid flow, but the significance of these is uncertain at present. Unlike the very young deposits of the Frome Embayment (van der Wielen *et al*., 2011), the sandstone-hosted deposits in the study area probably formed during the Devonian to Carboniferous, and hence present-day topography cannot be assumed to reflect paleotopography. Two criteria have been used to map potential paleotopographic fluid-flow drivers in the study area:

- Areas of uplifted basement; and
- Distribution of syn-orogenic sedimentary rocks.

Central Australia has been subject to a number of episodes of intraplate deformation and uplift (e.g., Korsch and Lindsay, 1989). The ~580–530 Ma Petermann Orogeny (e.g., Edgoose *et al*., 2004) and the ~450–300 Ma Alice Springs Orogeny (e.g., Shaw *et al*., 1992) generated uplift and paleorelief in the Musgrave and Arunta regions respectively. These are interpreted to be fluid-flow drivers for sandstone-hosted uranium systems in the Neoproterozoic to Paleozoic basins within the study area.

Uplift during the Petermann Orogeny was accommodated along the Woodroffe Thrust (Edgoose *et al*., 2004). According to Edgoose *et al*. (2004), the most intense exhumation occurred in the Mann Ranges-Umutju region of the Fregon Domain, whereas deformation was much less intense to the east. Following Edgoose *et al*. (2004), a wedge of interpreted 'strong' Petermann Orogeny uplift was delineated between the Woodroffe Thrust and the Mann Fault (Figure 3.2.5). The rest of the Musgrave Province in the Northern Territory south of the Woodroffe Thrust is interpreted to have only undergone 'weak' uplift (Figure 3.2.5).

Areas of interpreted Alice Springs Orogeny uplift were delineated using muscovite and biotite (K-, Ar-) Ar and Rb-Sr isotope data compiled from published sources (Allen and Stubbs, 1982; Shaw and Black, 1991; Cartwright *et al*., 1999; Mawby, 2000; Scrimgeour and Raith, 2001; Biermeier *et al*., 2003; Wygralak and Mernagh, 2005; Fraser *et al*., 2006; McLaren *et al*., 2009; Huston *et al*., 2011a; G. Fraser, unpublished data). The interpreted extent of Alice Springs Orogeny uplift extends from the Harts Ranges westward along two prongs (Figure 3.2.5). The southern prong extends west along the Desert Bore Shear Zone and Redbank Thrust to the central Amadeus Basin. The northern prong extends west along the northern margin of the Ngalia Basin. The westernmost portion of this northern prong is interpreted to have generated 'weak' uplift, while the remaining areas are interpreted to be 'strong' (Figure 3.2.5), based on the isotopic evidence.

Regions of interpreted 'weak' and 'strong' uplift during these orogenic episodes were buffered to a subjectively determined distance of 100 km (corresponding to the maximum buffer distance used in the source system component). These buffers were further modified by clipping out sedimentary units younger than the overlapping buffer for the period of uplift using data presented by Maidment *et al*. (2007; Figure 3.2.5). This final step is important, as topographic relief can only be confidently inferred to have driven fluid flow in aquifers deposited pre- or syn-orogenesis. Topography may persist long after the cessation of orogenic activity and drive fluid flow in younger sedimentary sequences. However, the role of this is difficult to assess and map.

The second criterion used to map fluid-flow drivers, the distribution of syn-orogenic sedimentary rocks, also seeks to delineate paleotopographically-driven fluid flow (Figure 3.2.6). Significantly, both the Bigrlyi and Angela uranium deposits are hosted within syn-orogenic sedimentary rocks (see above). The occurrence of syn-orogenic sediments indicates the presence of elevated topography in the hinterland. Syn-orogenic sediments were identified using information presented in Cook (1988) and Haines *et al*. (2001), and were extracted from the basin solid geology dataset (see Appendix 1).

Based on these criteria, large areas of the northern Amadeus Basin are highlighted (Figure 3.2.7). Almost the entire Ngalia Basin is highlighted due to the extensive syn-orogenic Mount Eclipse Sandstone (Figure 3.2.7). In the Georgina Basin, the driver system component highlights the Dulcie Sandstone (Figure 3.2.7).

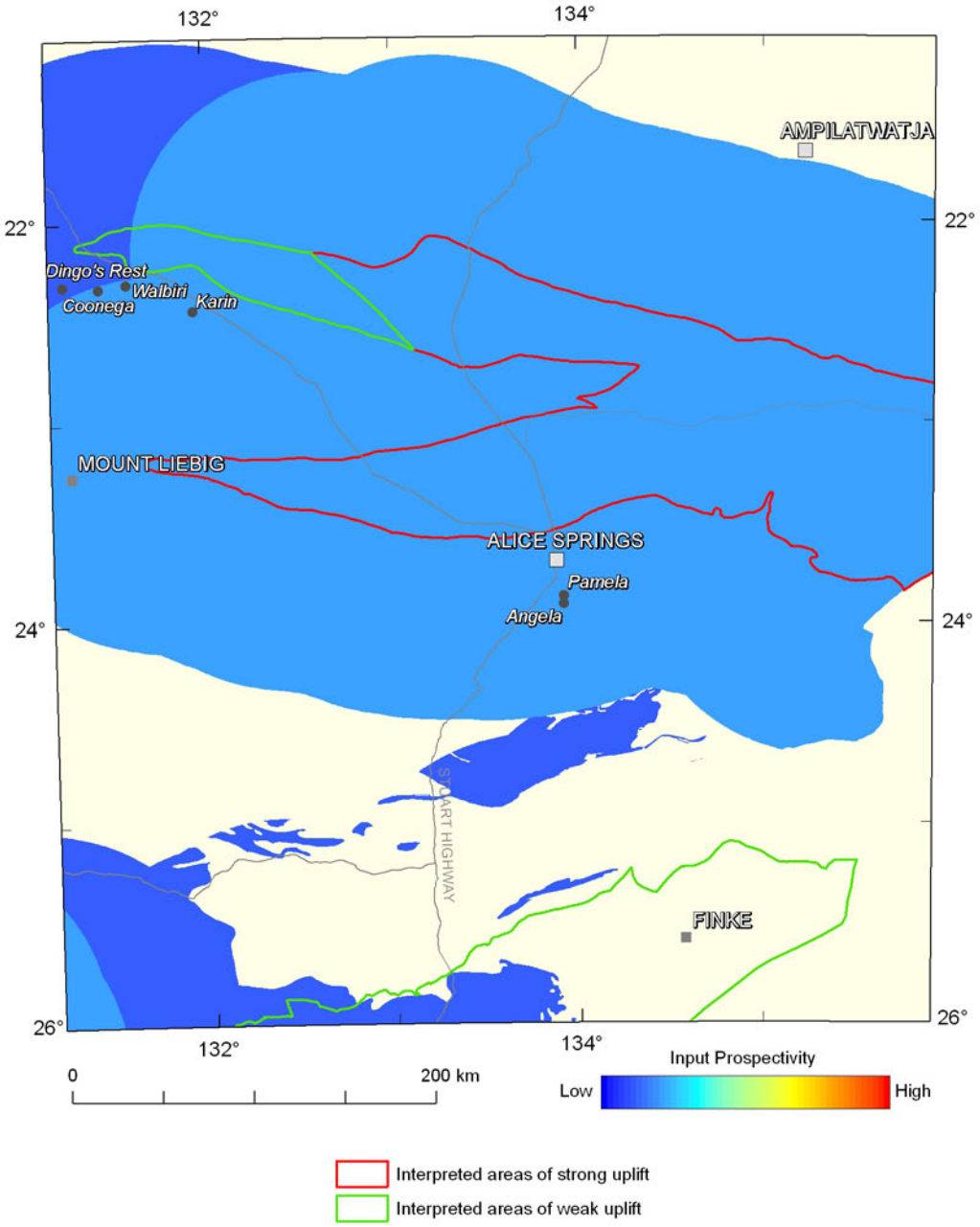

Figure 3.2.5: *Variation in the weightings for uplifted basement generating potential paleorelief, buffered to 100 km. Areas of interpreted 'weak' and' strong' uplift are shown (note that areas of 'strong' uplift during the Petermann Orogeny occurs to the southwest of the study area). The colour stretch for the mappable criteria used in the assessment for sandstone-hosted uranium systems uses a numerical range from the minimum to the maximum weighting of all criteria used (0.036 to 1.000; see Table 3.2.1), and utilises 20 equal-interval breaks.*

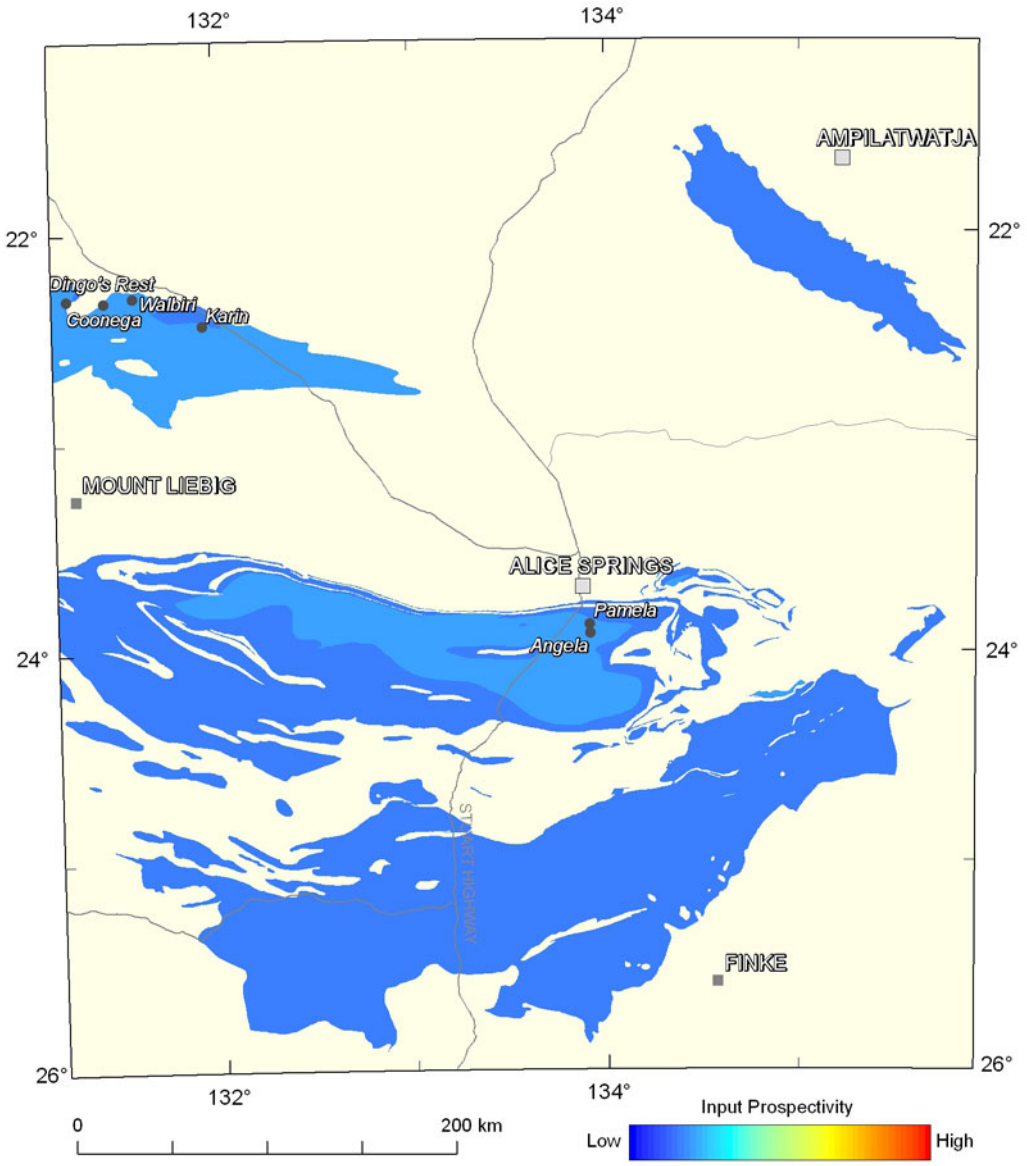

Figure 3.2.6: *Variation in the weightings for the distribution of syn-orogenic sedimentary rocks. The colour stretch for the mappable criteria used in the assessment for sandstone-hosted uranium systems uses a numerical range from the minimum to the maximum weighting of all criteria used (0.036 to 1.000; see Table 3.2.1), and utilises 20 equal-interval breaks.*

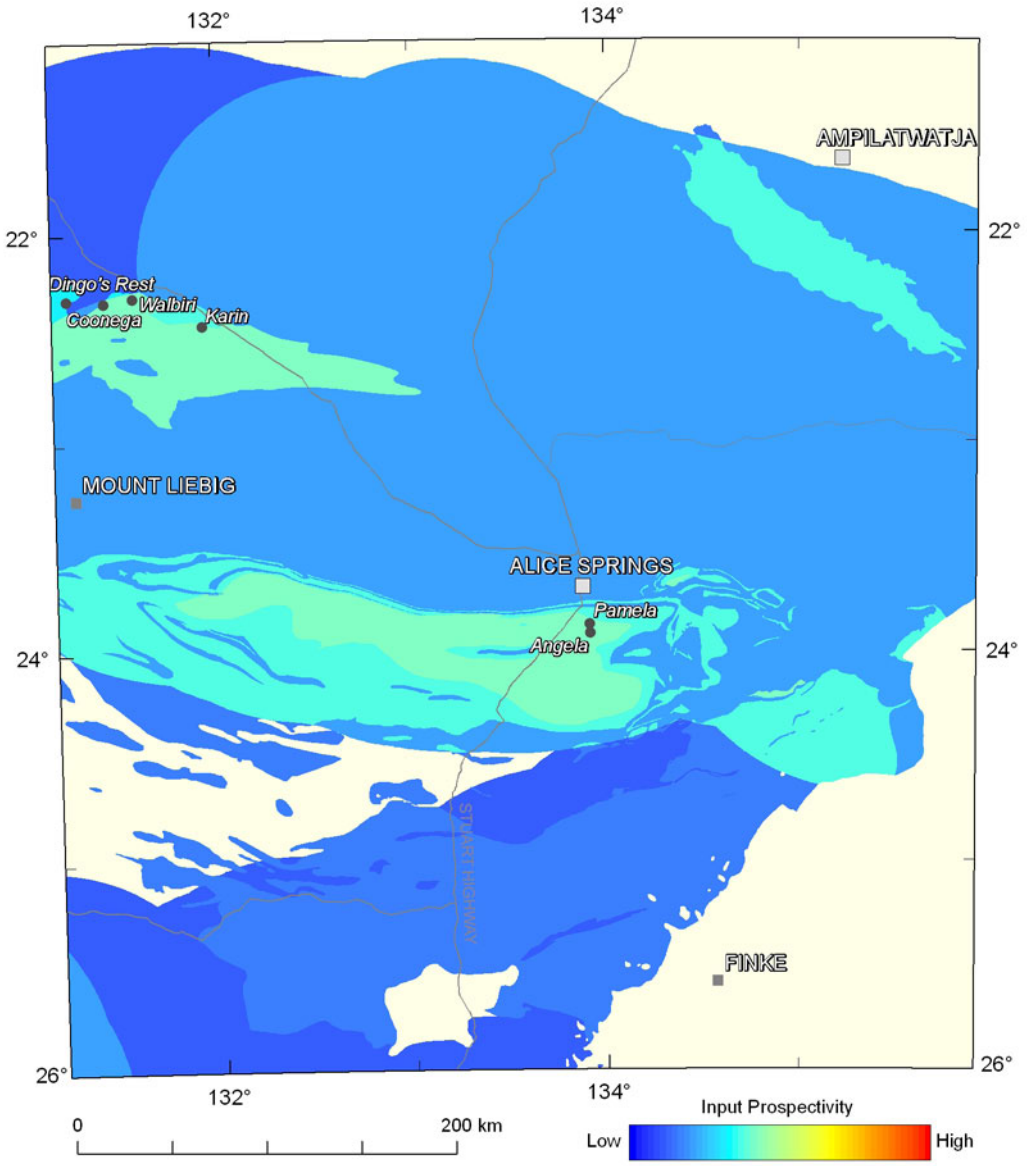

Figure 3.2.7: *Variation in the weightings of the driver system component for sandstone-hosted uranium systems. The colour stretch for each mineral system component in the assessment for sandstone-hosted uranium systems uses a numerical range from the minimum to the maximum weighting for each of the system components (0.012 to 0.573), and utilises 20 equal-interval breaks.*

3.2.3.3 Fluid-flow pathways and architecture

The geological setting for sandstone-hosted uranium is within sedimentary depocentres, such as basins and paleochannels. Within these depocentres, fluid flow is controlled by variations in permeability and porosity. Fluid-flow pathways are particularly significant for mobile reductants, and enable reductants sourced deep within the basin to interact with shallow, uranium-bearing groundwaters. The following criteria have been used in this assessment to map the fluid-flow pathways and architecture systems component:

- The distribution of sedimentary basins;
- Favourable fluid-flow aquifers; and
- Faults that may act as pathways for mobile reductants.

The first criterion, distribution of sedimentary basins, uses the distribution of the Amadeus, Eromanga, Georgina, Ngalia, Pedirka and Warburton basins to delineate favourable geological settings for sandstone-hosted uranium deposits (Figure 3.2.8). Cenozoic basins were not included, as other criteria listed here are targeted towards Paleozoic to Mesozoic uranium systems. Favourable aquifers within these basins were identified and ranked for aquifer potential based on a review of relevant literature (Table 3.2.2; Smith, 1972; Wells and Moss, 1983; Lindsay, 1993; Pegum, 1997; Radke, 2000; Ambrose, 2006a, b; Figure 3.2.9). Pathways for mobile reductants were mapped using buffered faults from the basin solid geology dataset (Figure 3.2.10; see Appendix 1).

From these criteria, large areas of the Ngalia, Georgina and northern Amadeus basins are highlighted (Figure 3.2.11). The highest potential occurs where faults have been mapped.

Table 3.2.2: Criteria used for ranking aquifer potential

AQUIFER RANKING	DESCRIPTION
No aquifer potential	No potential (e.g., shale)
Some aquifer potential	Interpreted based on unit descriptions. Sandstones are present, but unsure of grain size or abundance of coarser fraction in mixed sandstone/mudstone units
Possible aquifer potential	Interpreted based on unit descriptions (mainly medium-coarse sandstones)
Good aquifer potential	Noted aquifer or hydrocarbon reservoir in published sources, but some doubts as to aquifer potential
Proven aquifer potential	Noted aquifer or good hydrocarbon reservoir

Table 3.2.3: Criteria used for ranking in-situ reductant potential

REDUCTANT RANKING	DESCRIPTION
No reductant potential	No potential
Low reductant potential	Unit has hydrocarbon shows
Moderate reductant potential	Unit is dark coloured, pyritic or contains local coal
Good reductant potential	Unit is noted as a possible hydrocarbon source rock
Excellent reductant potential	Unit is carbonaceous or is identified as a good hydrocarbon source rock

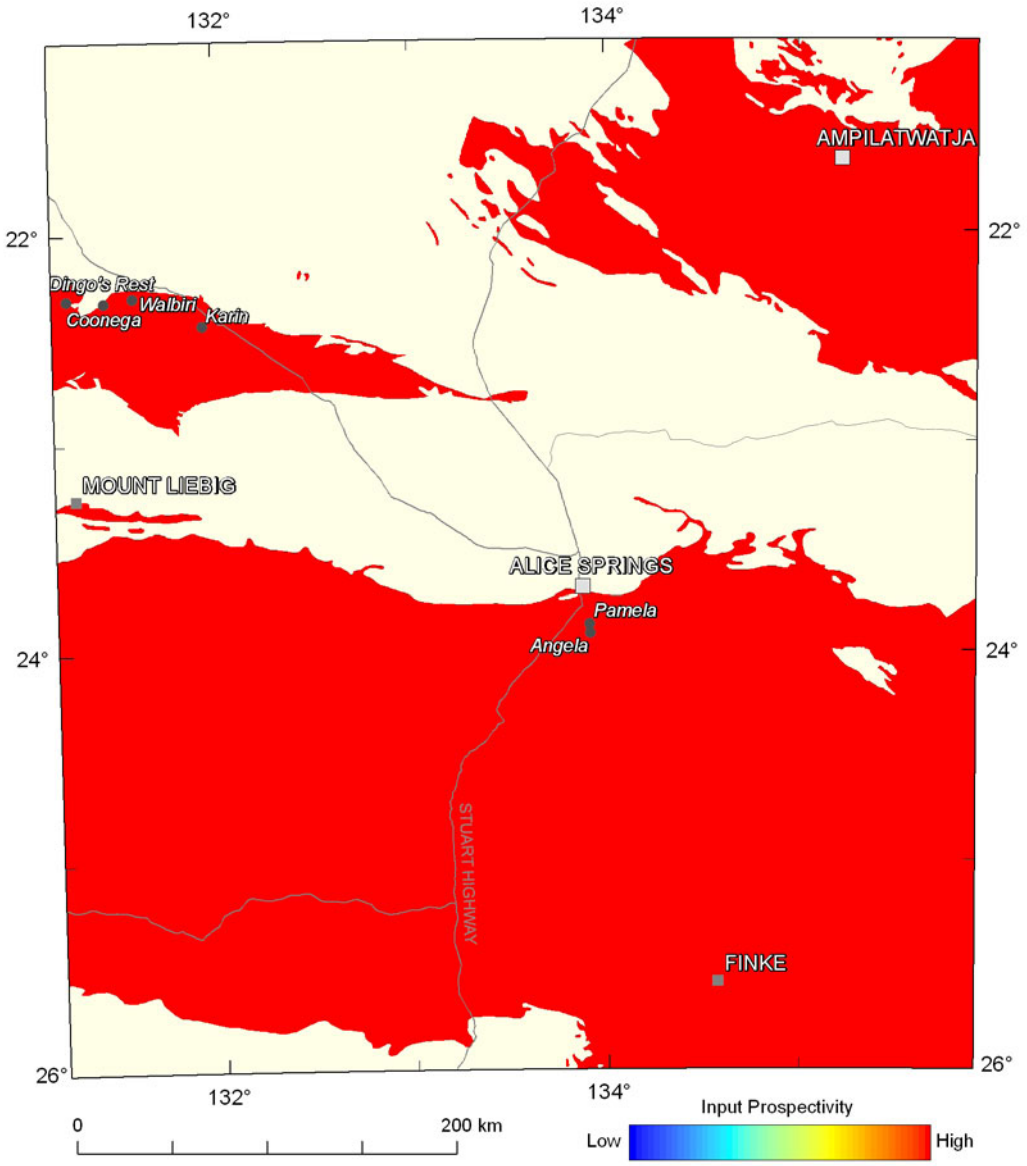

Figure 3.2.8: *Weighting for sedimentary basins, representing the favourable geological setting for sandstone-hosted uranium systems. The colour stretch for the mappable criteria used in the assessment for sandstone-hosted uranium systems uses a numerical range from the minimum to the maximum weighting of all criteria used (0.036 to 1.000; see Table 3.2.1), and utilises 20 equal-interval breaks.*

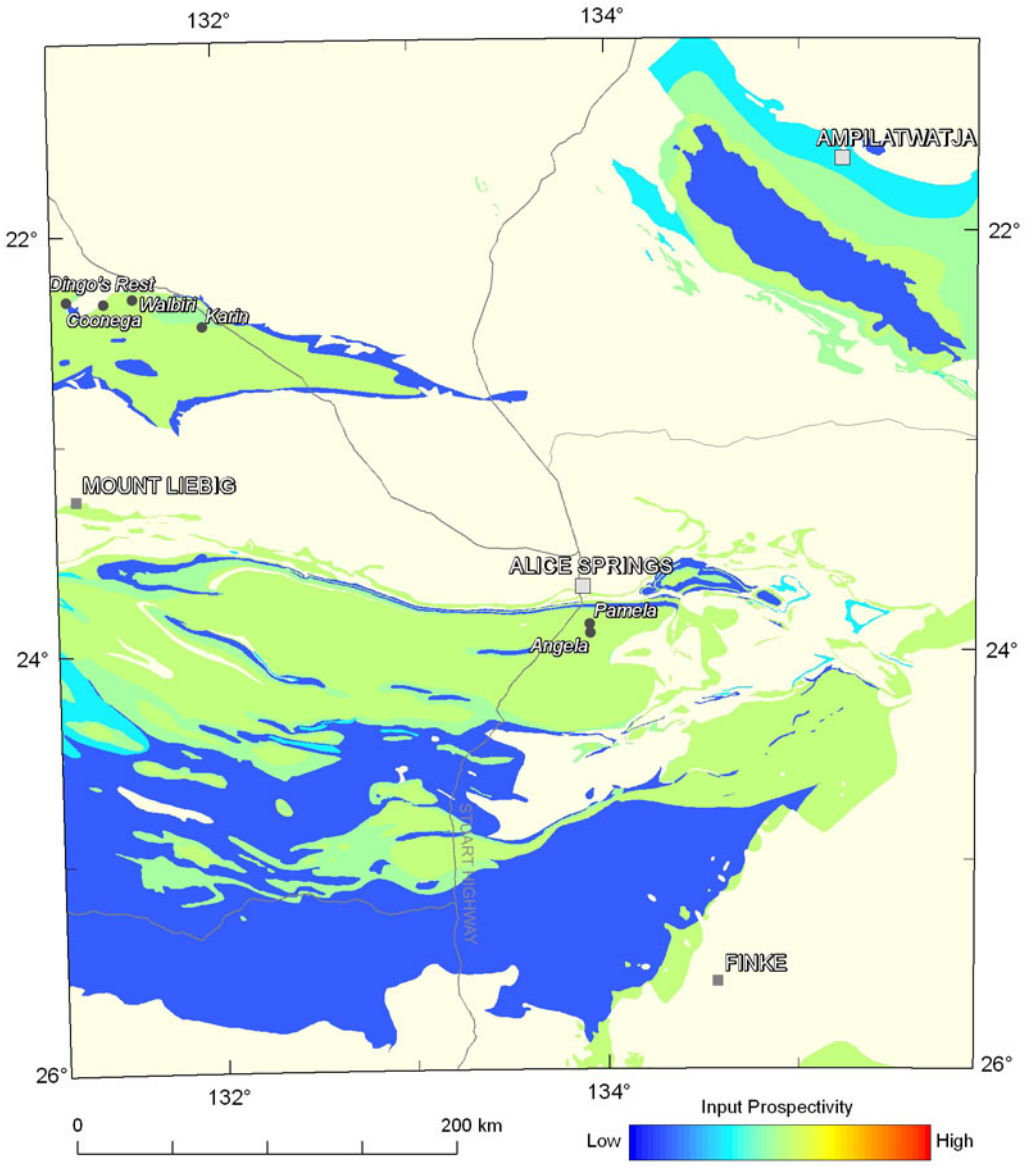

Figure 3.2.9: *Variation in the weightings for potential fluid-flow aquifers. The colour stretch for the mappable criteria used in the assessment for sandstone-hosted uranium systems uses a numerical range from the minimum to the maximum weighting of all criteria used (0.036 to 1.000; see Table 3.2.1), and utilises 20 equal-interval breaks.*

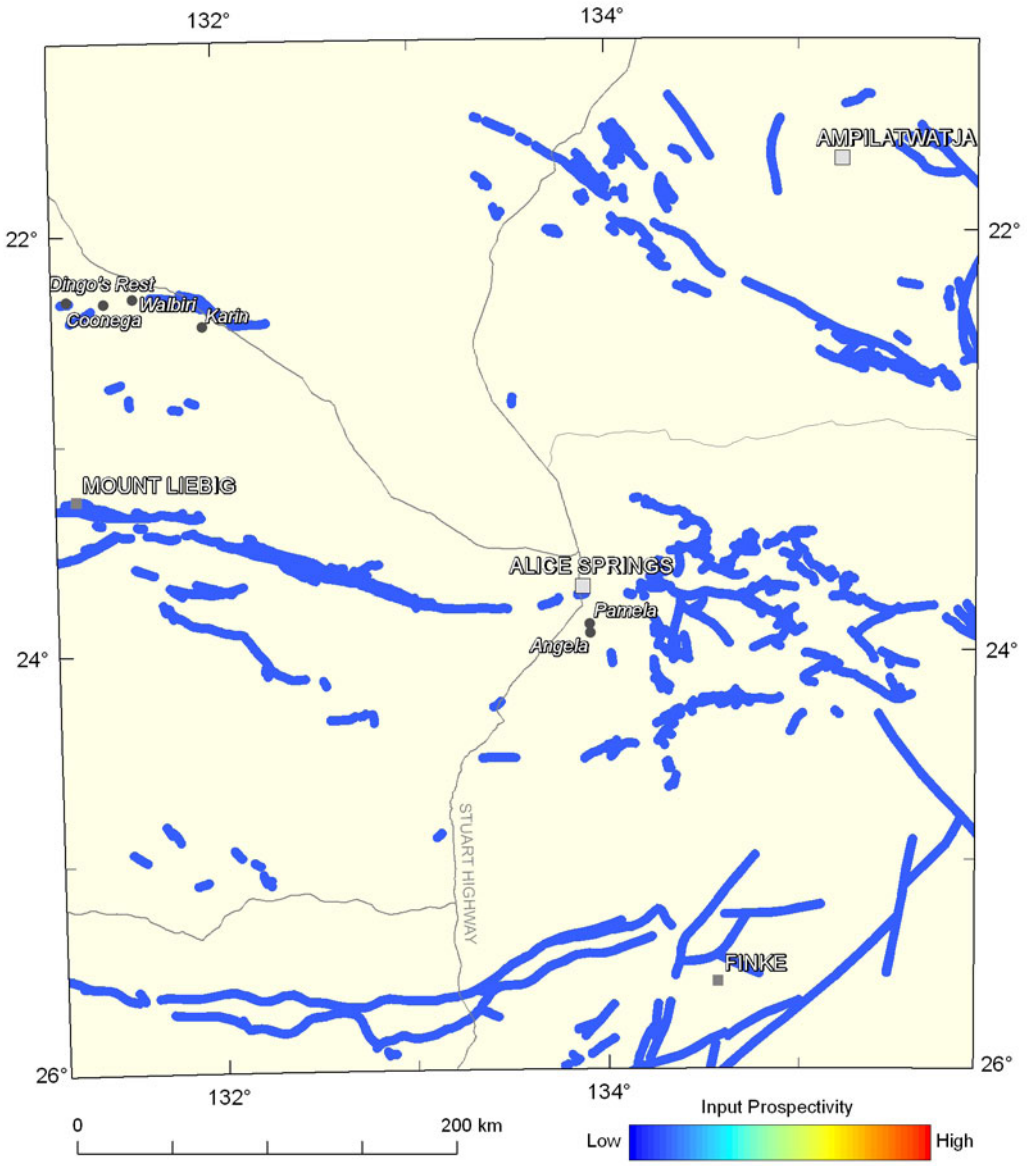

Figure 3.2.10: *Weighting for potential fluid-flow pathways for reducing fluids. The colour stretch for the mappable criteria used in the assessment for sandstone-hosted uranium systems uses a numerical range from the minimum to the maximum weighting of all criteria used (0.036 to 1.000; see Table 3.2.1), and utilises 20 equal-interval breaks.*

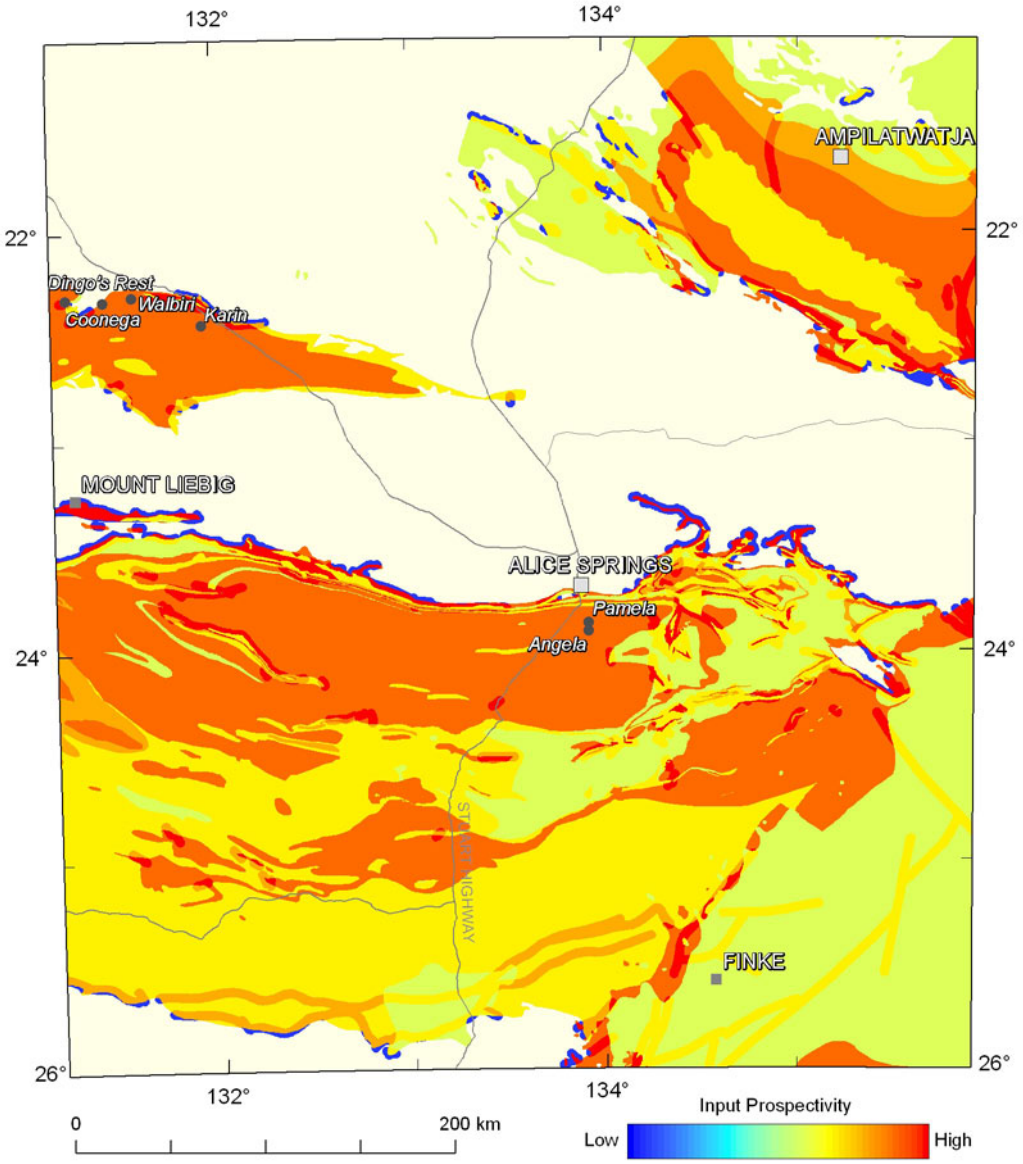

Figure 3.2.11: *Variation in the weightings of the fluid-flow pathways system component for sandstone-hosted uranium systems. The colour stretch for each mineral system component in the assessment for sandstone-hosted uranium systems uses a numerical range from the minimum to the maximum weighting for each of the system components (0.012 to 0.573), and utilises 20 equal-interval breaks.*

3.2.3.4 Depositional mechanisms

Three separate criteria were used to map the depositional mechanisms systems component:

- Distribution of units with reductant potential;
- Sources of reducing fluids (hydrocarbons); and
- Radiometric anomalies showing direct evidence of elevated uranium.

As mentioned above, deposition of uranium in sandstone-hosted systems principally occurs via the reduction of oxidised uranium-bearing groundwaters. Suitable reductants may be in-situ or may be sourced from depth in the basin. In-situ reduction may take place in the presence of certain bacteria, Fe^{2+}-rich minerals or organic matter. Units contained within the basin solid geology (see Appendix 1) were investigated to assess reductant potential and were rated based on a review of relevant literature (Table 3.2.3; Wells and Moss, 1983; Questa, 1989; Pegum, 1997; Ambrose, 2006a, b; Ambrose and Putnam, 2006; Figure 3.2.12).

Mobile reductants were mapped using the distribution of hydrocarbon occurrences within the study area (Figure 3.2.13). Three known major hydrocarbon fields occur within the study area (Dingo, Mereenie and Palm Valley), all of which are hosted within the Amadeus Basin. These were buffered to a distance of 5 km. In addition, over 30 wells and drill holes with hydrocarbon shows were identified from the literature across the study area (Lindsay, 1993; Pegum, 1997; Ambrose, 2006a, b; Ambrose and Putnam, 2006) and were likewise buffered. The Amadeus, Eromanga, Georgina and Ngalia basins are recognised as hydrocarbon-bearing basins and potential hydrocarbon accumulations may occur outside of those already known. In order to account for the location of possible, as-yet unrecognised hydrocarbon occurrences, the distribution of these basins has also been used to map sources of reducing fluids. These have been assigned a lower applicability value, since the occurrence of hydrocarbons is not guaranteed outside of those occurrences already known (Table 3.2.1).

Direct evidence of elevated uranium is the third criterion used to map the depositional mechanisms systems component and is derived from radiometric data. Radiometric data from Minty *et al*. (2010) were processed to generate the U^2/Th product, which has been shown to be useful in identifying areas of uranium anomalism (Wilford *et al*., 2009). Zonal statistics (mean and standard deviation) were calculated for non-regolith units in Geoscience Australia's 1:1 000 000 surface geology of Australia dataset (Raymond and Retter, 2010). Surface geology unit distribution was used for the calculations, as radiometric data reflects only the abundances of radioactive elements at the earth's surface, and hence solid geology unit distribution, of which a significant proportion often occurs beneath regolith cover, was not used. Using the calculated statistics, regions of uranium anomalism one and two standard deviations above the mean for each geological unit were extracted (Figure 3.2.14).

The combined criteria for the depositional mechanisms system component highlight almost the entire Ngalia Basin, an area corresponding to the distribution of the Brewer Conglomerate in the Amadeus Basin, and the Georgina Basin in the study area (Figure 3.2.15).

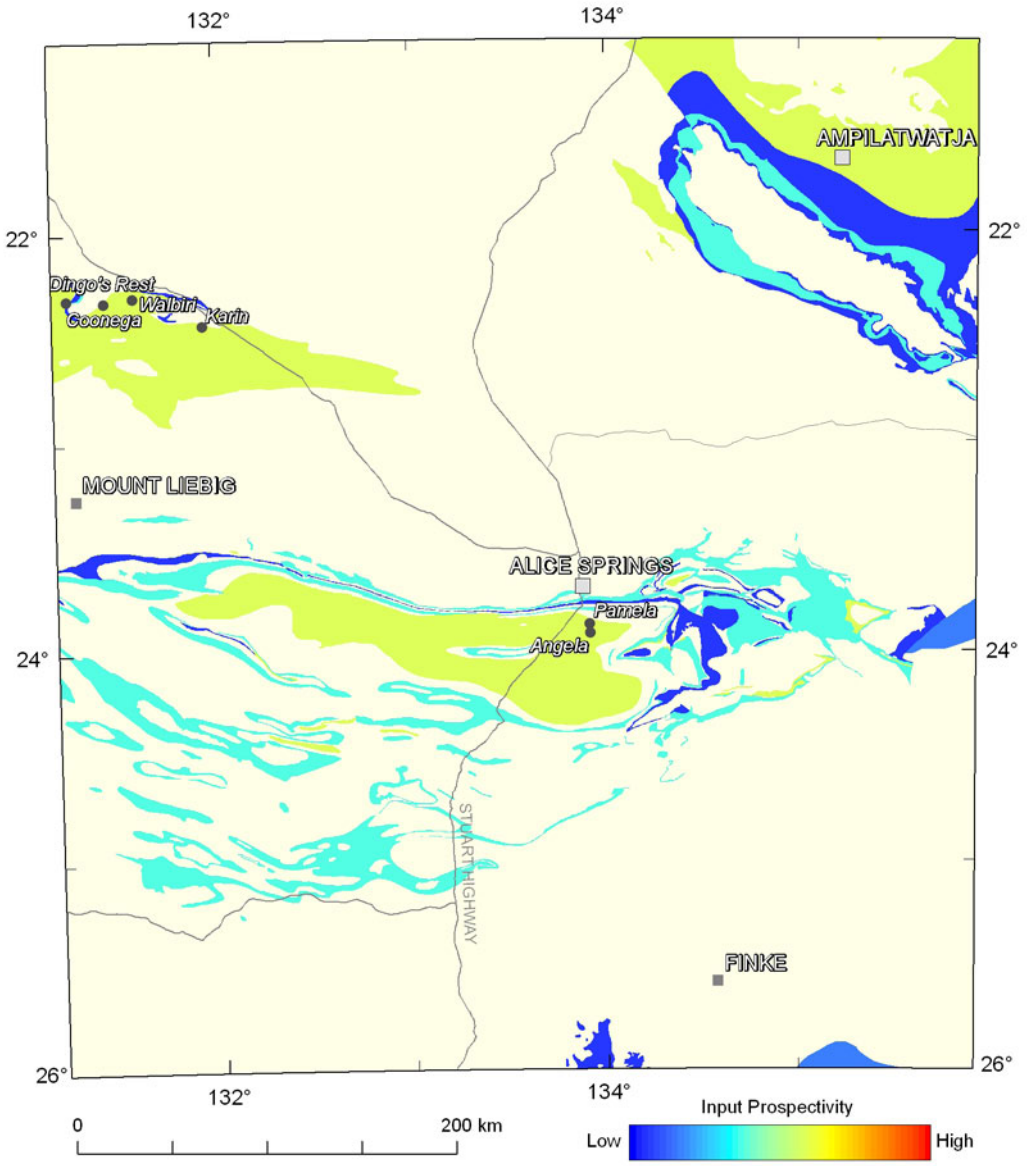

Figure 3.2.12: *Variation in the weightings for potential reducing units. The colour stretch for the mappable criteria used in the assessment for sandstone-hosted uranium systems uses a numerical range from the minimum to the maximum weighting of all criteria used (0.036 to 1.000; see Table 3.2.1), and utilises 20 equal-interval breaks.*

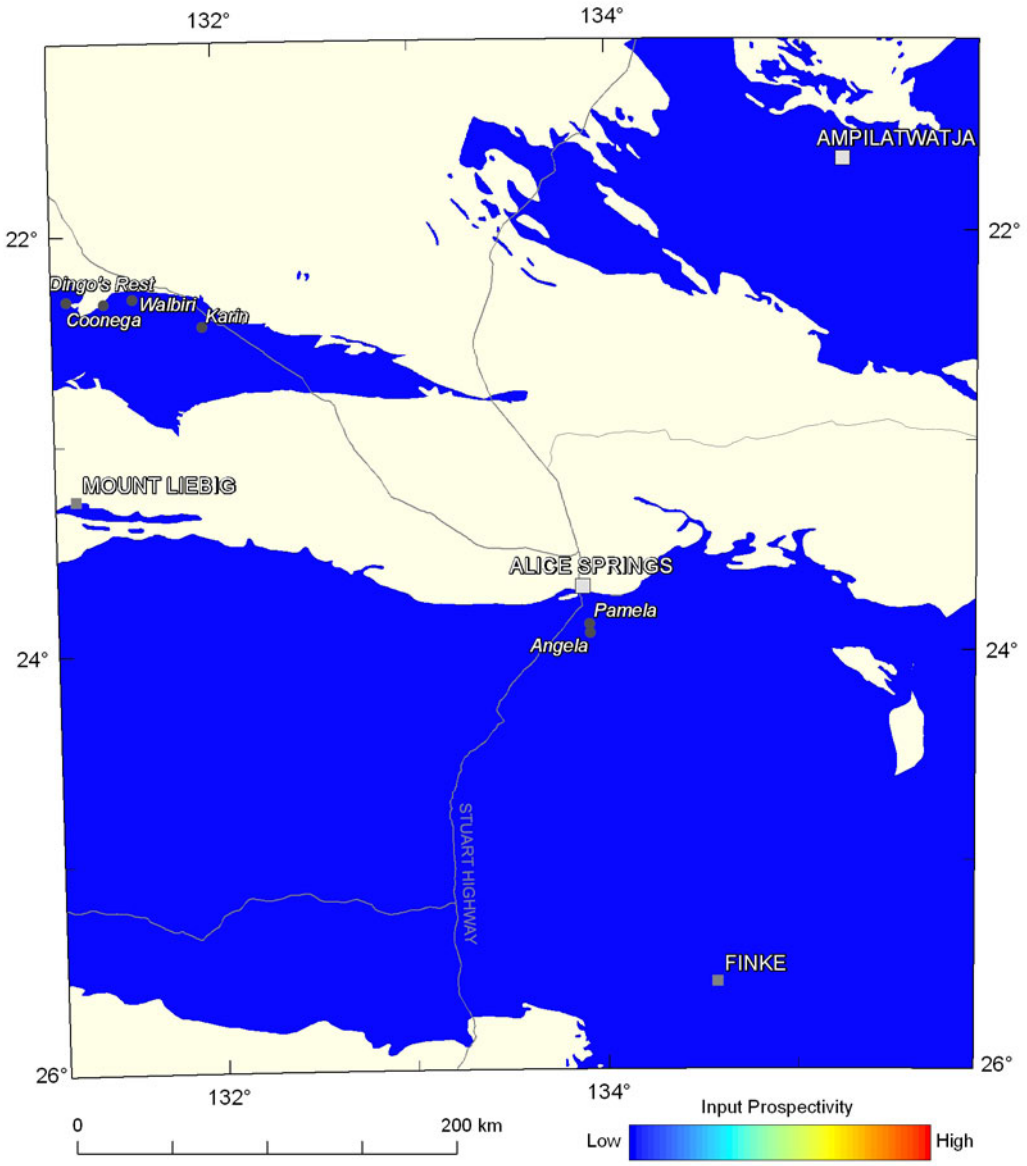

Figure 3.2.13: *Variation in the weightings for potential sources of reducing fluids. The colour stretch for the mappable criteria used in the assessment for sandstone-hosted uranium systems uses a numerical range from the minimum to the maximum weighting of all criteria used (0.036 to 1.000; see Table 3.2.1), and utilises 20 equal-interval breaks. Due to the colour stretch used, variations in weightings for this criterion are not apparent.*

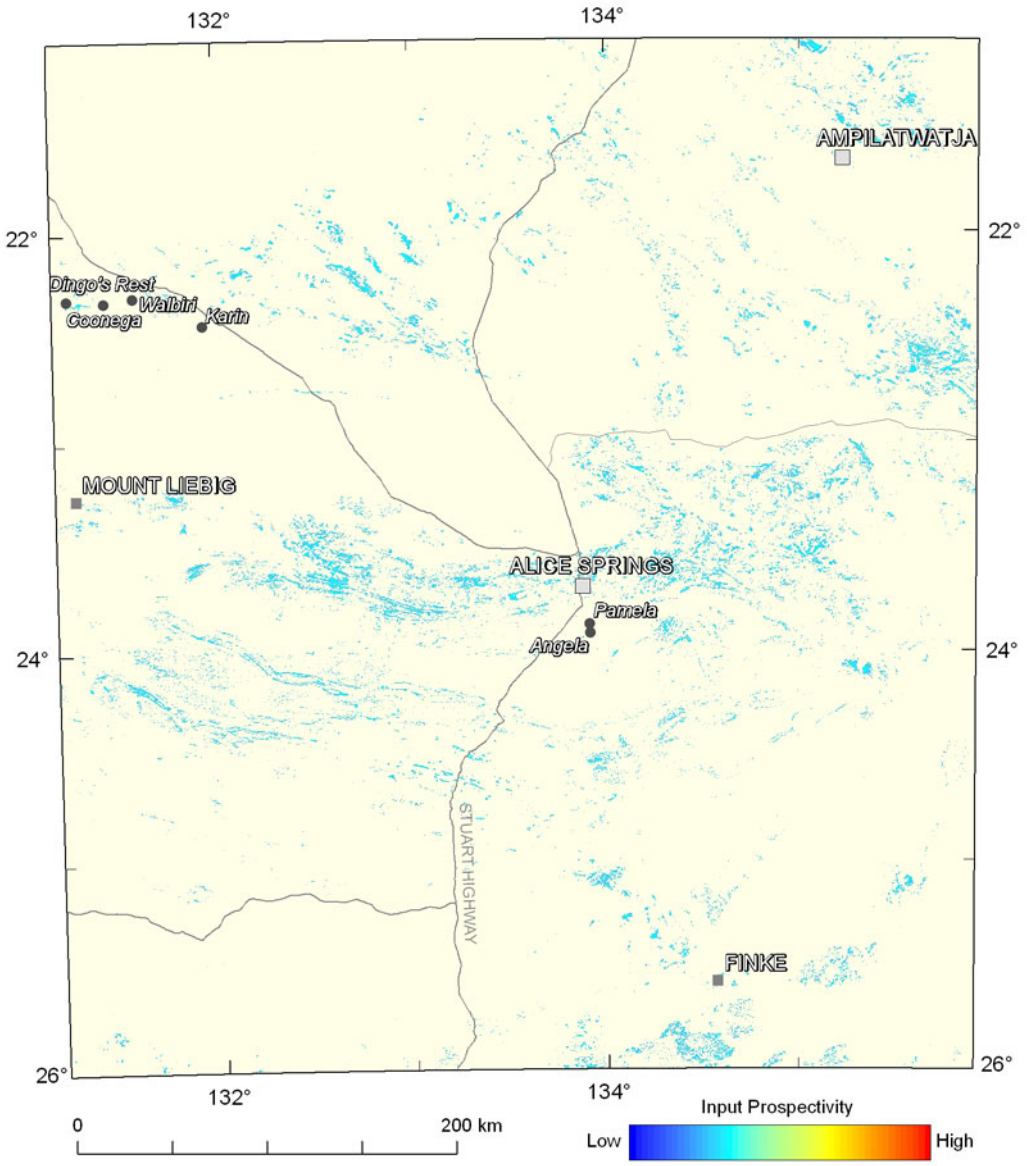

Figure 3.2.14: *Variation in the weightings for direct evidence of elevated uranium, as indicated by radiometric anomalies. The colour stretch for the mappable criteria used in the assessment for sandstone-hosted uranium systems uses a numerical range from the minimum to the maximum weighting of all criteria used (0.036 to 1.000; see Table 3.2.1), and utilises 20 equal-interval breaks.*

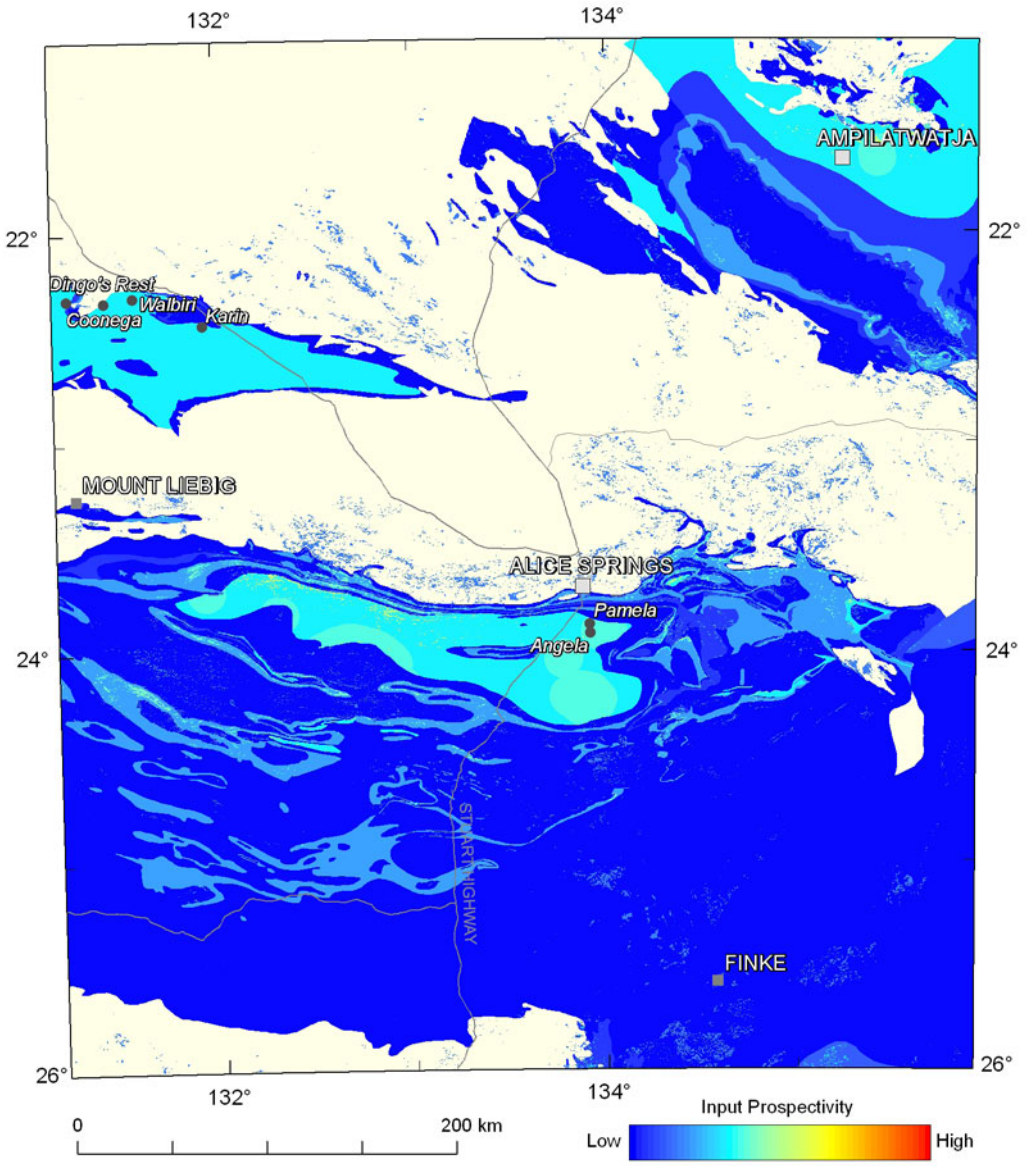

Figure 3.2.15: *Variation in the weightings of the depositional mechanisms system component for sandstone-hosted uranium systems. The colour stretch for each mineral system component in the assessment for sandstone-hosted uranium systems uses a numerical range from the minimum to the maximum weighting for each of the system components (0.012 to 0.573), and utilises 20 equal-interval breaks.*

3.2.4 Results

3.2.4.1 Neoproterozoic-Paleozoic potential

The results of the assessment for Neoproterozoic-Paleozoic sandstone-hosted uranium systems are shown in Figure 3.2.16 and Plate 3.2. Broad regions of high potential occur across the study area. The highest modelled potential is in the Ngalia Basin in the Mount Eclipse Sandstone (labelled as A on Figure 3.2.16) and in the northern Amadeus Basin in the Brewer Conglomerate (B). These units host known uranium mineralisation. The Finke Group in the southern Amadeus Basin exhibits low to moderate potential. This unit is a temporal equivalent of the Pertnjara Group, of which the Brewer Conglomerate is a component, and is syn-orogenic. Therefore, while the modelled potential is not high, this unit warrants further investigation. Other areas identified are:

- Elements of the Larapinta Group in the central-northern Amadeus Basin (C_{1-3});
- A region incorporating several units (mainly Arumbera Sandstone) in the northeastern Amadeus Basin (D);
- A small occurrence of the Areyonga Formation in the northeastern Amadeus Basin (E);
- The southern Georgina Basin in the study area, incorporating mainly Tomahawk Formation sediments (F); and
- An irregular arcuate belt consisting of several units in the western Georgina Basin (G).

Within the broadly identified regions, localised patches of higher potential occur coincident with faults. These may have acted as fluid-flow pathways for reducing fluids, as suggested by the two-fluid model (Figure 3.2.3b), and suggests the potential for different styles of sandstone-hosted uranium mineralisation within the sedimentary basins in the study area.

3.2.4.2 Qualitative assessment of potential in Cenozoic basins

A number of small fluvial-lacustrine basins developed across the study area during the Cenozoic. The potential of these basins for recent sandstone-hosted uranium mineralisation analogous to the deposits of the Frome Embayment in South Australia has previously been highlighted by van der Wielen *et al*. (2011). Descriptions of the stratigraphy within these basins given by Senior *et al*. (1995) note the presence of both potential fluid-flow aquifers and organic-rich horizons that may have potential as uranium depositional sites. Uranium for such systems may have been sourced from deeply weathered (Senior *et al*., 1995) felsic igneous rocks within the Aileron Province. Together with the recent discovery of Cenozoic uranium mineralisation at Afghan Swan (see Section 2.2), the potential of these sedimentary basins for recent paleochannel-hosted uranium is qualitatively inferred to be high and warranting additional investigation.

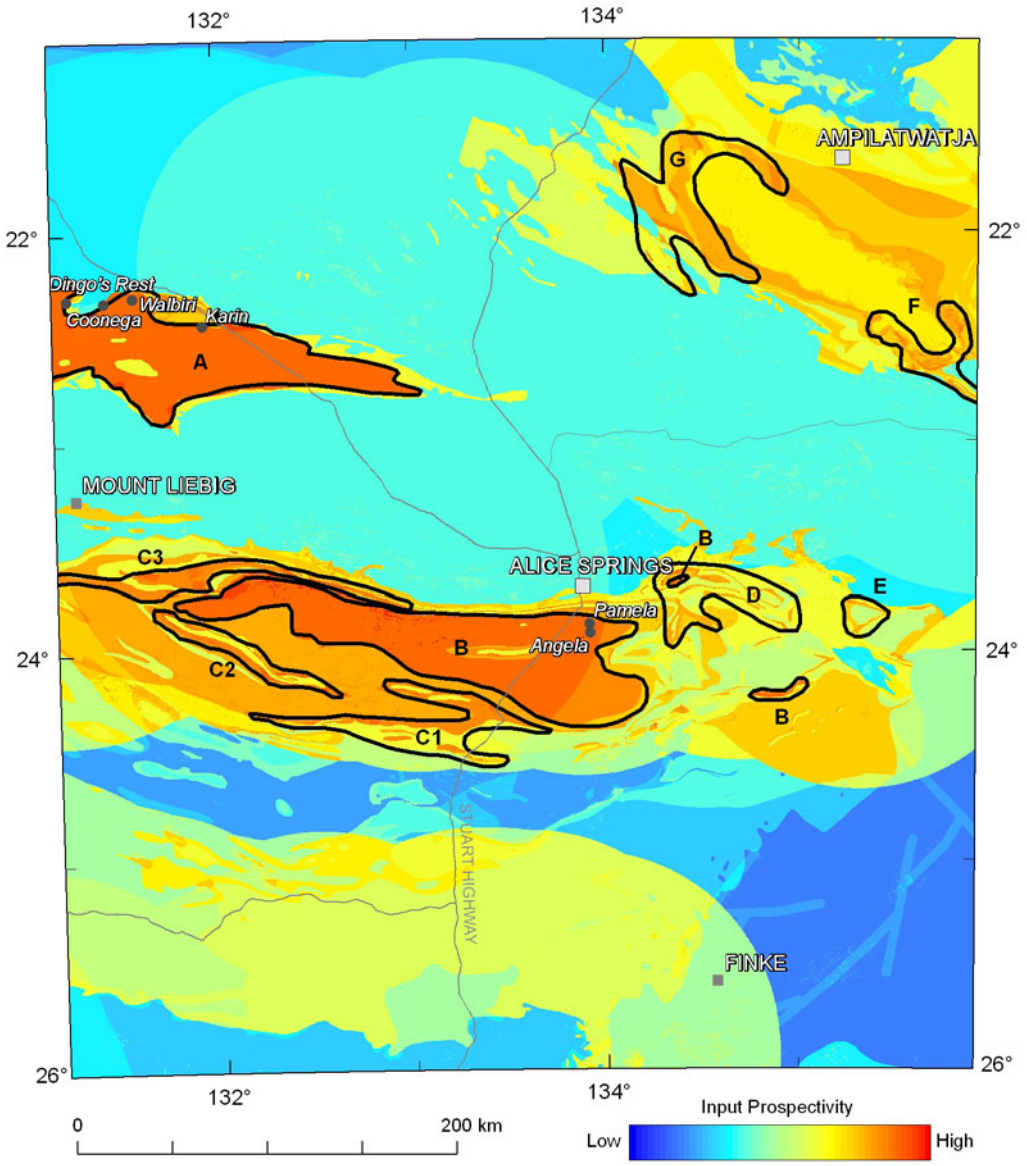

Figure 3.2.16: *Final modelled potential for sandstone-hosted uranium systems. The colour stretch used for this figure has a minimum value of 0.015 and a maximum value of 0.413, and utilises 20 equal-interval breaks. Areas outlined in black are discussed in Section 3.2.4.*

3.3 URANIUM-RICH IRON OXIDE-COPPER-GOLD SYSTEMS

D.L. Huston, J.A. Whelan, A. Schofield, R.G. Chopping and R.G. Gallagher

Iron oxide copper-gold (IOCG) deposits (Hitzman *et al*., 1992) are a diverse family of mineral deposits characterised by the following features: (1) Cu, with or without Au, as economic metals, (2) hydrothermal ore styles and strong structural controls, (3) abundant magnetite and/or hematite, (4) Fe oxides with Fe/Ti greater than those in most igneous rocks, and (5) no direct spatial associations with igneous intrusions as, for example, displayed by porphyry- and skarn-related deposits (Williams *et al*., 2005). In addition, most IOCG deposits display a broad space-time association with batholithic granitoids, occur in crustal settings with very extensive, and commonly pervasive, alkali metasomatism, and enrichment in a distinctive and geochemically diverse suite of minor elements including various combinations of F, P, Co, Ni, As, Mo, Ag, Ba, LREE and uranium (Williams *et al*., 2005).

Uranium-rich IOCG deposits in which uranium is an economic metal are an important, yet rare, subset of the IOCG family (Hitzman and Valenta, 2005). Currently the Olympic Dam deposit is the only IOCG deposit in which uranium is extracted as a major economic commodity. Nevertheless, this deposit is the world's largest single resource of uranium ore (BHP Billiton, 2010 Annual Report, www.bhpb.com). In a global context, most of the other IOCG deposits containing higher grades of uranium are found in the Proterozoic of South Australia, in the Gawler Craton and Curnamona Province (Hitzman and Valenta, 2005; Skirrow, 2011).

Some of the largest known IOCG deposits are in the Gawler Craton in South Australia (Olympic IOCG Province) and the Mt Isa Province in north Queensland (Cloncurry district). As the Aileron Province shares much of the geological history (e.g., similar timing and nature of tectonothermal events, deposition and magmatism) that characterises the Gawler Craton and Mt Isa Provinces, and as small IOCG deposits have been recognised in the study area, below we present a mineral potential assessment directed at uranium-rich IOCG deposits in the study area.

3.3.1 Iron oxide-copper-gold deposits in the southern Northern Territory

Although the Aileron Province is not known to contain major IOCG deposits, it shares many geological features and similarities with the well-endowed Gawler Craton and Mt Isa Province, including similarly-aged stratigraphy and event histories. Moreover, there are several prospects, including the Johnnies Reward prospect and prospects in the Jervois district that have been interpreted as IOCG deposits (Figure 3.3.1). To the north of the study area, in the Tennant Region, Au-Cu-Bi deposits of the Tennant Creek and Rover goldfields have many characteristics of IOCG deposits (Huston *et al*., 1993; Skirrow and Walshe, 2002). In addition to these more established deposits and districts, recent exploration has identified IOCG prospects within the east-central part of the study area and to the west of the study area. Below, these deposits are briefly described, although it must be noted that the geological detail available in the Olympic IOCG Province (Skirrow *et al*., 2011) and the Cloncurry district (Skirrow and Huston, 2010) is not available for deposits in the Aileron Province and Tennant Region.

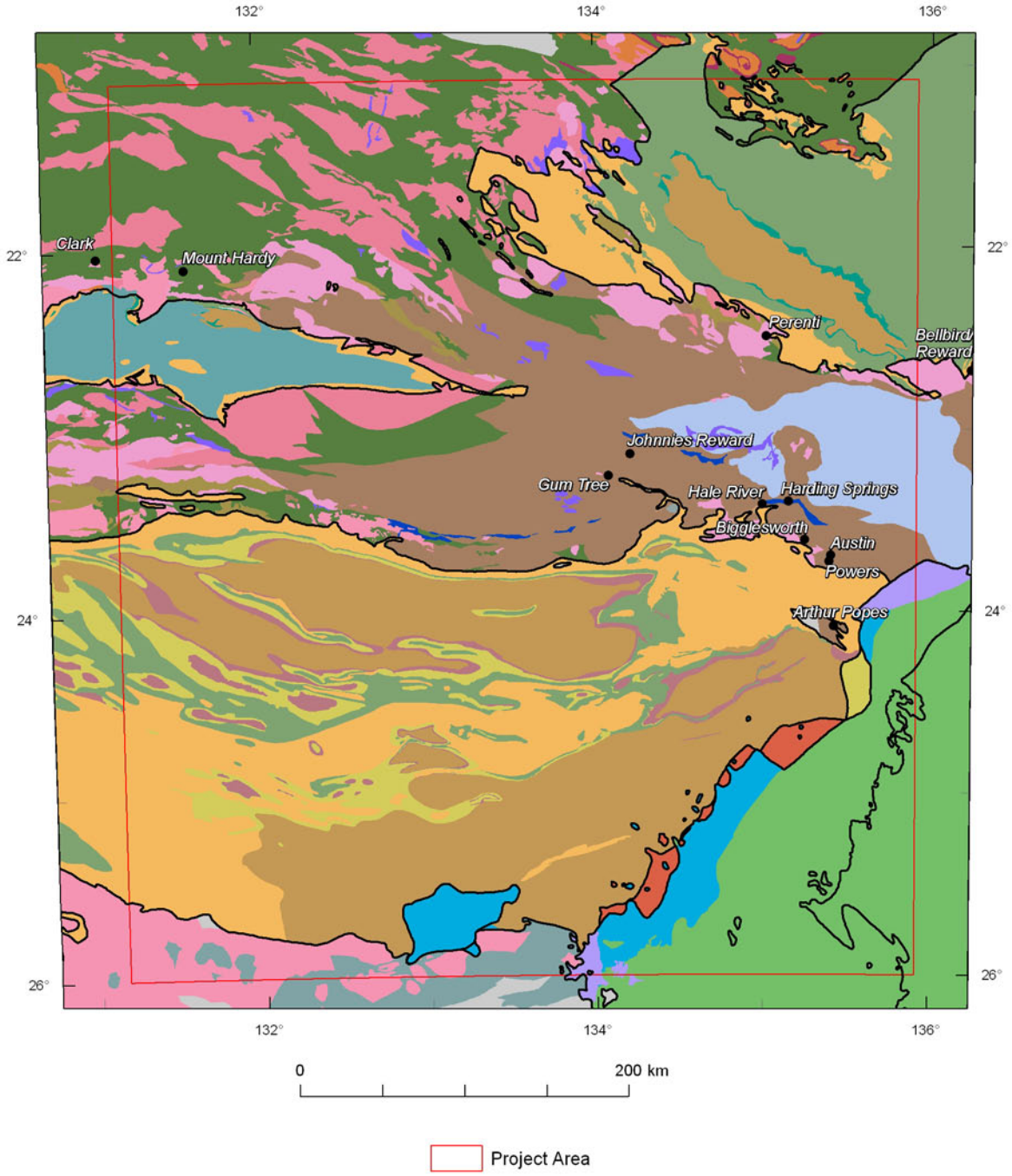

Figure 3.3.1: *Solid geology of the southern Northern Territory showing the locations of IOCG deposits and prospects in the study area. Legend for geology is given in Figures 2.1.1 and 2.1.2.*

3.3.1.1 Johnnies Reward prospect

The Johnnies Reward prospect is the best documented of the IOCG deposits in the study area. Following discovery of the Johnnies Reward prospect in 1964, the Bureau of Mineral Resources conducted an airborne magnetic survey in 1965 (Tipper, 1966), followed by a ground magnetic survey in 1967 (Haigh, 1971). These surveys, which were confirmed by later ground surveys (Mackie, 2002), indicated that the ironstone at Johnnies Reward was coincident with a dipole magnetic anomaly. In addition, it is associated with both ground and helicopter-based

electromagnetic anomalies (Mayer *et al*, 2009). A one kilometre-spaced gravity survey failed to identify the ironstone (probably because the grid was too coarse), but indicated that the prospect is associated with north-northeast-striking structure (Mayer *et al*, 2009).

The following description is based mostly on Hussey *et al*. (2005) and Mackie (2002). At surface the prospect consists of Cu-stained massive ironstone within quartz-biotite-garnet gneiss in the lower part of the Cadney Metamorphics of the 1810–1790 Ma Strangways Metamorphic Complex. The deposit is overlain by marble and calc-silicate rock, and these same units host mineralisation in the Pinnacles Cu district to the east (Warren 1980).

The mineralised ironstone can be traced at surface for 200 m and is up to 50 m wide (Figure 3.3.2: Chuck, 1984). The ironstone consists of magnetite with variable amounts of pyroxene (diopside, salite and hypersthene), amphibole (hornblende, tremolite, anthophyllite and manganocummingtonite), quartz and sulfide minerals. The presence of local lenses of forsteritic marble suggests that the ironstone replaced a carbonate lens, an interpretation supported by the geochemistry of the ironstone (Hussey *et al*., 2005).

The sulfide mineralogy is relatively simple, and is dominated by pyrite, chalcopyrite, galena and sphalerite, with minor to trace pyrrhotite, molybdenite, scheelite, native Bi and bismuthinite. Hussey *et al*. (2005) showed that the prospect has two distinct metal assemblages — (1) Cu-Pb-(Zn-Ag-Au), which is present in the ironstone, and (2) Au-(Cu), which is present at the base of the ironstone and in quartz-biotite-garnet gneiss underlying the ironstone. Moreover, there is a distinct metal zonation present through much of the mineralised interval. Metal zonation, from footwall into the ironstone, is as follows: Au-(Cu-B-S ± Mo) → Cu-Pb-S-(Zn-Ag-Au) → Pb-Mn-(Cu-S ± Ca) → REE-high field strength element (HFSE) → Ca, with Fe- and Mg-enrichment. Thorium and total REE locally exceed 200 ppm and 3200 ppm, respectively (Hussey *et al*., 2005). Uranium contents are relatively low, with a maximum value of 13 ppm associated with high Th and REE. The metal zonation at Johnnies Reward is similar to that seen in the Tennant Creek goldfield (see below).

Although the age of Johnnies Reward has not been definitively established, a maximum age is provided by the age of the host Strangways Metamorphic Complex, and an indicative age is provided by locally constrained Pb isotope model ages. Hussey *et al*. (2005) reported ages of between 1810–1800 Ma for volcaniclastic units that they interpreted to stratigraphically underlie the Cadney Metamorphics. Lead isotope data, using a local Strangways model, of galena from the Johnnies Reward prospect yielded model ages of between 1798–1769 Ma. These ages overlap with the timing of the culmination of the 1810–1790 Ma Stafford Event and the beginning of the 1780–1770 Ma Yambah Event (Hussey *et al*., 2005).

3.3.1.2 Jervois district

Other than the Nolans Bore REE-U-P deposit, the Jervois district, which occurs just east of the study area (Figure 3.3.1), is the most significant mineral district in the area (Figure 3.3.3). The district contains four deposits for which mineral resources have been defined (Table 3.3.1). One of these deposits, Green Parrot, was mined for a few months in the early 1980s by Plenty River Mining. Metallogenically, the district is complex, with significant Cu-Ag-(Zn-Pb-Au) deposits and minor W deposits. Although historically the base metal deposits have been interpreted as syngenetic (e.g., volcanic-hosted or sediment-hosted massive sulfide deposits: Ypma *et al*., 1984; Mackie, 1984), they share a number of features with IOCG deposits (e.g., Frater, 2006).

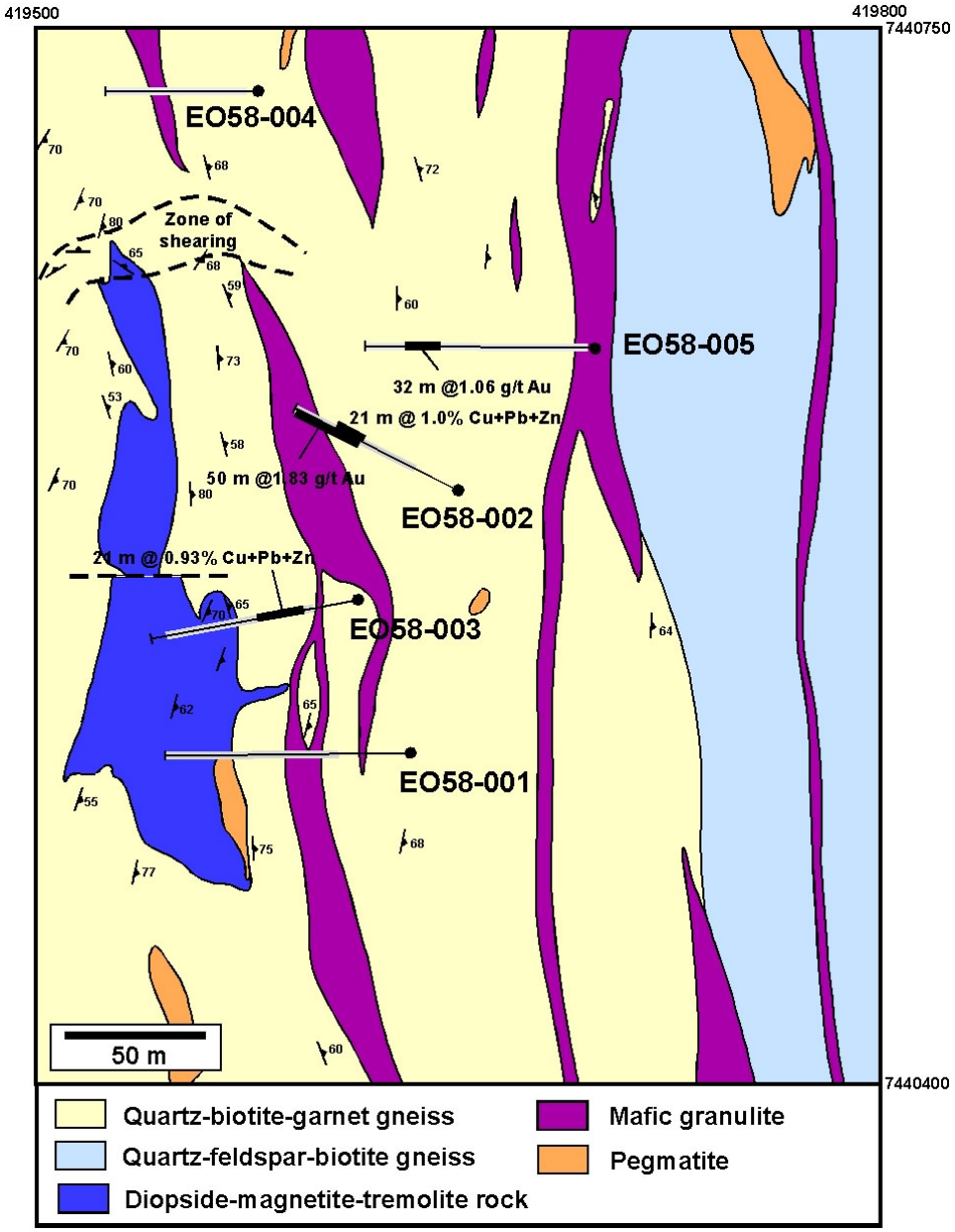

Figure 3.3.2: *Geology of the Johnnies Reward prospect, Arunta Province (modified after Chuck, 1984).*

Table 3.3.1: JORC-compliant resources for deposits in the Jervois district (from www.kentorgold.com.au)

DEPOSIT	TONNAGE (MT)	Cu (%)	Pb (%)	Zn (%)	Ag (g/t)
Reward	7.0	1.3	-	-	28.2
Bellbird	3.9	1.2	-	-	7.5
Green Parrot	0.689	0.97	2.52	1.18	93.5
Bellbird North	0.305	0.72	2.71	4.53	27.4

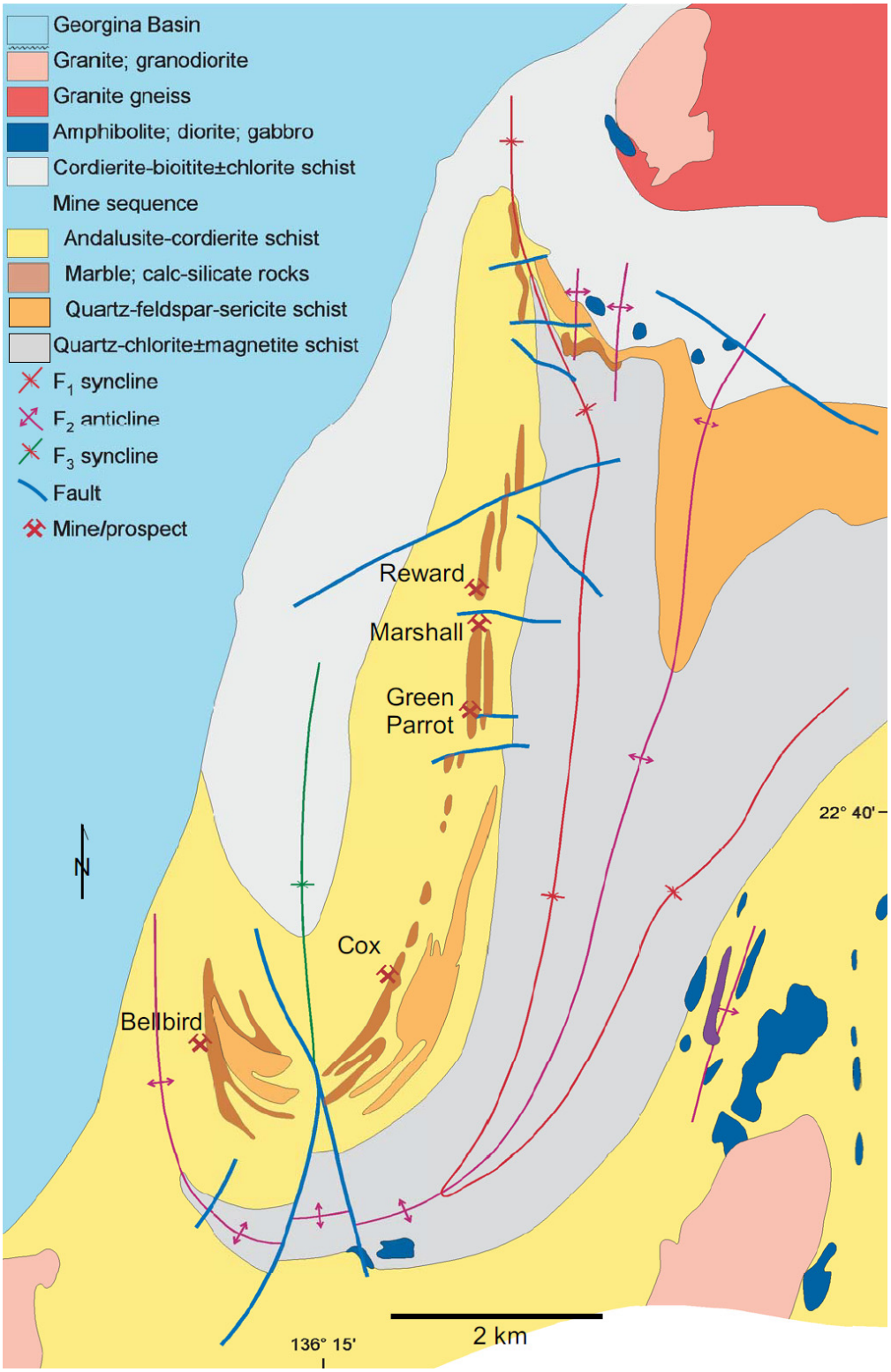

Figure 3.3.3: *Geology of the Jervois district (modified after Ypma et al., 1984).*

The Jervois district is hosted by the Bonya Schist, which has a maximum depositional age of 1807 ± 17 Ma (Claoué-Long and Hoatson, 2005). Although this is strictly a maximum depositional age, Claoué-Long and Hoatson (2005) inferred this age to be close to the actual depositional age on the basis of uniformity of ages and intrusion by the 1786 ± 4 Ma Attutra Metagabbro to the east of the Jervois district (Figure 3.3.3). The Bonya Schist in the Jervois district is dominated by metapelitic rocks, including cordierite-biotite schist, andalusite-muscovite schist and quartz-chlorite ± magnetite schist. The mineral deposits are located within a local succession that is characterised by felsic volcanics at the base (the quartz-sericite schist in Figure 3.3.3), which is overlain by a lode package comprising calc-silicate rock and quartzite (Frater, 2006), which is in turn overlain by andalusite-muscovite schist (Figure 3.3.3). Magnetite preferentially replaces calc-silicate rock in the lode package to produce massive ironstone (Frater, 2006). The andalusite-muscovite schist, together with associated quartz-sericite schist (metamorphosed volcanic rocks according to Frater, 2006), host the deposits. In detail, the local host to the deposits consists of andalusite-quartz-mica schist, slate and calc-silicate rocks that overlies the quartz-sericite schist and underlies the andalusite-muscovite schist (Frater, 2006).

Frater (2006) suggested that although the deposits are hosted at a specific stratigraphic horizon defined by the lode package, in detail they are associated with late, *en echelon* shear zones. Frater (2006) inferred that magnetite was emplaced early, during D_1, possibly associated with early granite emplacement (most granites in southeast Huckitta, as well as the Attutra Metagabbro, were emplaced between 1789 ± 3 Ma and 1773 ± 3 Ma, although a phase of the Jervois Granite was emplaced at 1746 ± 4 Ma: Kositcin *et al*., 2011), with the sulfide minerals introduced into brecciated and mylonitised rocks during D_3.

Ypma *et al*. (1984) described three types of mineralised lodes in the Jervois district: (1) chalcopyrite-pyrite lodes in magnetite-chlorite-garnet rocks, (2) galena-sphalerite lodes in both magnetite-chlorite-garnet rocks and in manganese-rich calc-silicate rocks, and (3) scheelite in marble and calc-silicate rocks. The first lode type, which characterises the Reward (Marshall) and Bellbird deposits, is the most important economically, and is enriched Ag and Au (Table 3.3.1; www.kentorgold.com.au; Frater, 2006). At Bellbird (Figure 3.3.4) and Reward (Marshall; not shown in Figure 3.3.1), the mineralised zones strike north, have a sub-vertical dip and plunge moderately to the north. Mineralogically, the ores appear to be simple, with the dominant sulfide minerals being chalcopyrite and pyrite, apparently without pyrrhotite. Frater (2006) noted Co, uranium and P enrichment. Figure 3.3.5 suggests that uranium is variably enriched (to nearly 300 ppm) with Cu, but not with Pb, suggesting that the uranium-enrichment described by Frater (2006) is associated with the chalcopyrite-pyrite lodes and not the galena-sphalerite lodes.

Galena-sphalerite lodes characterise the Green Parrot and Bellbird North deposits. In contrast with the chalcopyrite-pyrite lodes, pyrrhotite appears to be present in these lodes (MODAT), along with pyrite and minor to trace bornite, tetrahedrite and fluorite (Mackie, 1984). Scheelite lodes are physically separate from the other two lode types, leading Mackie (1984) to infer a separate genesis, consistent with a later timing for W-bearing deposits elsewhere in the study area (e.g., Molyhil at ~1720 Ma: Cross, 2009). MODAT indicates that powellite is also present in the scheelite lodes, along with variable quantities of chalcopyrite, pyrite, bornite and hematite. The gangue minerals, which include actinolite, calcite, diopside, epidote, fluorite, garnet, hornblende, and vesuvianite, are typical of hydrothermal skarn deposits.

Based upon the association of the deposits with magnetite, and the enrichment of Co, uranium and P, Frater (2006) interpreted the Jervois deposits as IOCG deposits, although he suggested the possibility that the deposits may have inherited their high base metal content from a pre-existing sediment-hosted system. Alternatively, Ferenczi (2005) interpreted the Pb-Zn-Ag mineralisation at Jervois to be similar to Broken Hill-type mineralisation. The locally-constrained Strangways Pb isotope model for galena from the Green Parrot deposit yielded indicative ages of 1791–1773 Ma (D. Huston, unpublished data), again overlapping with the age range of the Yambah Event.

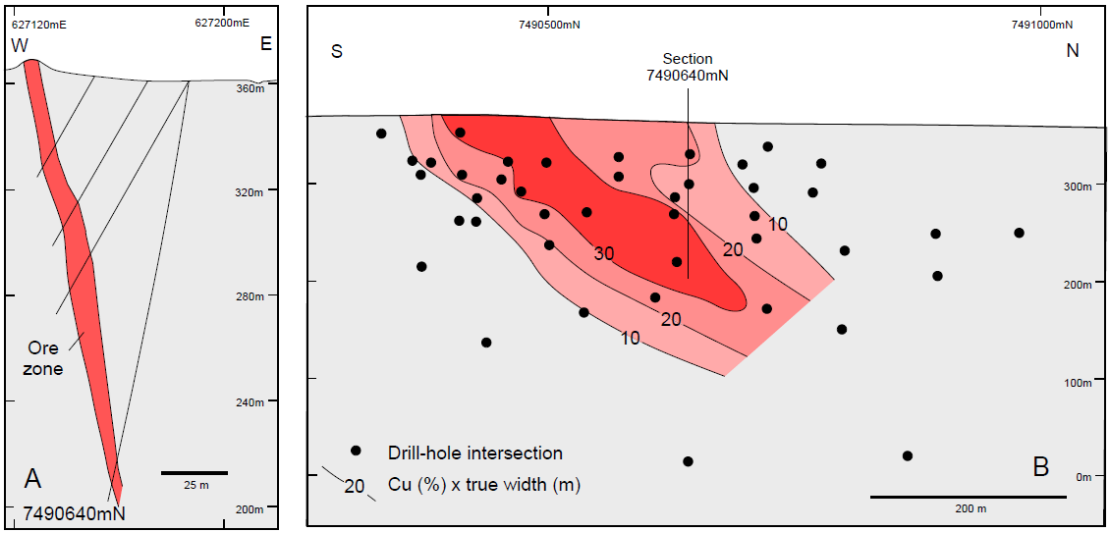

Figure 3.3.4: *Geology of the Bellbird deposit: (A) cross section (looking north) and (B) longitudinal section (looking west) showing variations in grade equivalence (after www.kentorgold.com.au).*

3.3.1.3 Tennant Creek goldfield

Although located about 200 km to the north of the study area, the Tennant Creek goldfield is described here as it is the third largest IOCG province in Australia after the Olympic IOCG Province and the Cloncurry district. Although mostly a producer of Cu and Au, the metallogeny of the field, and of the similar Rover field to the southwest, is complex. Historically, Tennant Creek was Australia's largest producer of Bi and Se, and a significant Zn-Pb-Ag prospect, Rover 108, has been defined by Westgold Resources in the Rover field. Significant uranium has been identified at the Edna Beryl and North Star deposits in the northern part of the Tennant Creek field, and at the Juno deposit in the central part of the field. Despite these occurrences, the distribution of uranium in the Tennant Creek and Rover fields is poorly defined.

The Tennant Creek goldfield is hosted by the turbiditic Warramunga Formation, which consists of interbedded sandstone, siltstone, mudstone and banded ironstone (Donnellan *et al*., 1995). SHRIMP analyses of volcanic rocks within this succession yielded indistinguishable ages of 1862 ± 9 Ma (Compston, 1995) and 1862 ± 5 Ma (Smith, 2001), consistent with ~1860 Ma ages of youngest detrital zircons from the turbidites (Compston, 1995). However, a felsic porphyritic sill with peperitic textures (McPhie, 1993) and a felsic volcaniclastic rock from the Rover field yielded ages of 1848 ± 2 Ma and 1842 ± 5 Ma, respectively (Maidment *et al*., *in prep*.), suggesting that either the Warramunga Formation was deposited over a period of 20 million years, or that there are unresolved stratigraphic complexities.

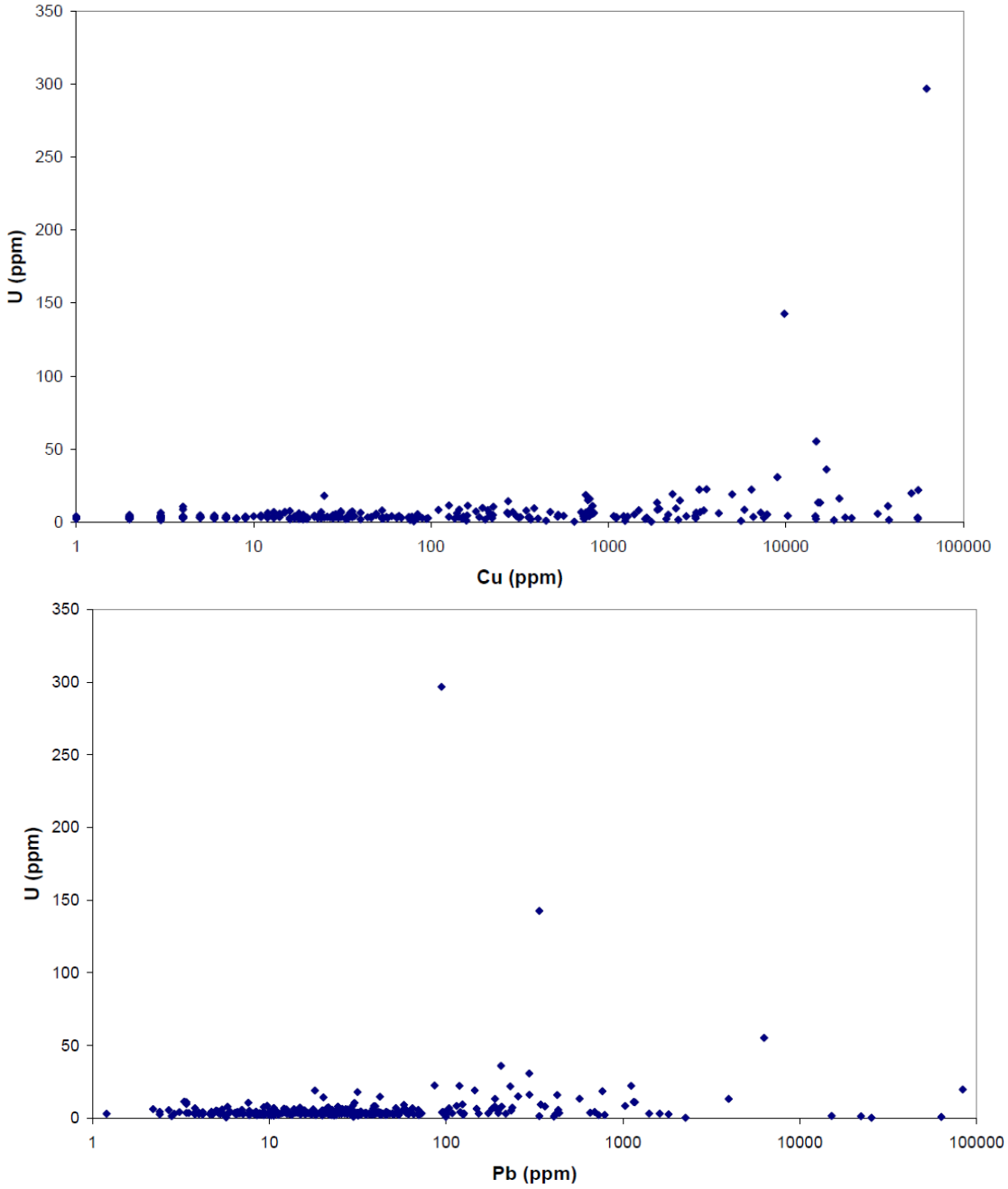

Figure 3.3.5: *Scattergrams illustrating the relationship of uranium to (top) copper and (bottom) lead in the Jervois district. The data are from the NTGS geochemical database and are of samples collected by M. Frater and analysed by Geoscience Australia.*

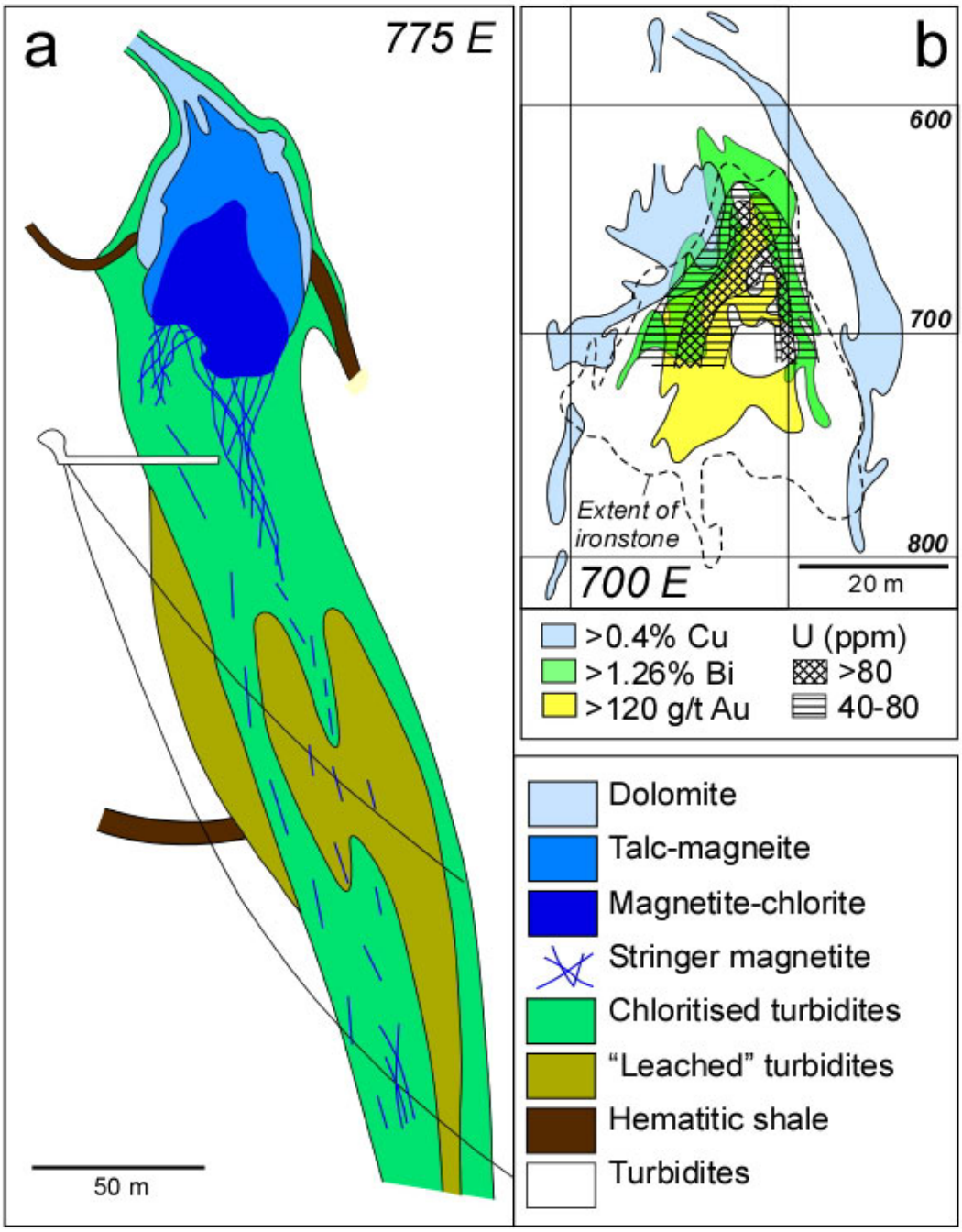

Figure 3.3.6: *Cross sections from the Juno deposit, showing: (a) geology (775E), and (b) metal zonation (700E). The mine grid is in feet (modified after Large, 1975).*

These younger ages correspond with the emplacement of the Tennant Creek Supersuite (Maidment *et al*., *in prep*.), which consists of high-K rapakivi granites and associated felsic porphyry dykes, and includes the syn-tectonic Tennant Creek Granite which intrudes the Warramunga Formation. Although early SHIRMP U-Pb zircon dating indicated a large spread in ages (1858–1840 Ma: Compston, 1995) for these rocks, large uncertainties did not allow resolution of this apparent spread. More recent analyses from these rocks indicate a much narrower spread in ages (1851–1846 Ma: Maidment *et al*., *in prep*.), suggesting a very short span for emplacement of the Tennant Creek Supersuite. This suite was overprinted by east-west trending structural elements that correspond to

open to close folding in the Warramunga Formation, with an associated axial planar slaty cleavage. This deformation (D_1) has been termed the Tennant Event (Donnellan and Johnstone, 2004). Dolerite dykes, with ages of 1842 ± 8 Ma, 1840 ± 8 Ma and 1821 ± 8 Ma (Compston, 1994), appear to be the last expression of this event or the initiation of extension after this event.

Despite recent discoveries of shear-zone hosted mineralisation (see below), the vast majority of ore in the Tennant Creek and Rover fields is spatially associated with ironstone and semi-massive to massive accumulations of Fe-oxide minerals with chlorite, quartz, talc and carbonate gangue (Wedekind *et al*., 1989; Huston *et al*., 1993; Skirrow and Walshe, 2002). As first recognised by Wedekind *et al*. (1989), Au and sulfide minerals texturally overprint the ironstone bodies, typically infilling fractures and breccia zones. However, less than a third of the over 650 known ironstones in the Tennant Creek field contain economic mineralisation and only 30 have produced more than 30 kg of Au (Wedekind *et al*., 1989; Le Messurier *et al*., 1990). The ironstones concentrate in a series of four, broadly west-northwest trending lines (Wedekind *et al*., 1989) and are locally controlled by anticlinal hinges and/or reverse faulting (Ivanac, 1954; Rattenbury, 1992).

Three broad styles of ironstone-related mineralisation are known in the Tennant Creek field (Huston *et al*., 1993; Skirrow and Walshe, 2002): (1) well-zoned, Au-rich deposits (Juno-type), (2) poorly-zoned, chalcopyrite-pyrite-hematite-rich deposits (Gecko-type), and (3) poorly-zoned, chalcopyrite-pyrrhotite-rich deposits (Peko-type). In addition, hematitic and chloritic shear zones also contain non-ironstone-hosted Au-rich deposits (Orlando-type; Skirrow and Walshe, 2002). Although these deposits to date have been minor, recent discoveries by Emmerson Resources (www.emmersonresources.com.au) highlight the potential of shear-hosted deposits (see below).

The Au-rich Juno-type deposits are characterised not only by the highest grades of major Australian Au deposits (e.g., Juno produced 450 000 tonnes of ore grading 56.1 g/t Au), but by a well-developed and consistent metal zonation, which is best illustrated by the Juno deposit (Figure 3.3.6; Large, 1975). From the base upwards through the ironstone, the zonation is Au → Bi-Pb-Se → Cu → pyrite. In the other two types of ironstone-hosted deposits, Au grades are much lower and there is no consistent metal zonation.

The Tennant Creek deposits are closely associated with chlorite-dominant alteration assemblages, but unlike most other IOCG provinces, regional Na-Ca alteration assemblages are not recognised. Typically, these chloritic assemblages form transgressive zones that envelop ironstones and form cross-cutting pipes that can be traced hundreds of metres below or extend above the ironstones (Large, 1975; Figure 3.3.6). In addition to chlorite, these pipes also contain veins of magnetite, along with variable amounts of pyrite and hematite (Le Messurier *et al*., 1990; Large, 1975). Generally, the chloritic alteration zones do not extend more than a few metres laterally from the ironstones. In addition to magnetite and hematite, the ironstones commonly contain as gangue one or more of chlorite, quartz, talc, and dolomite. In some deposits these gangue minerals are zoned within the ironstone (e.g., Juno, Large, 1975; Figure 3.3.6), but in others they are less well ordered (Le Messurier *et al*., 1990). In recently discovered shear-hosted deposits such as Goanna, mineralisation is present in quartz-chalcopyrite-chlorite veins within chloritised and sheared sediments (see below; www.emmersonresources.com.au). These shear zones also contain small ironstone and dolomite-quartz bodies.

Reinterpretation of the $^{40}Ar/^{39}Ar$ data of Compston and McDougall (1994) by Fraser *et al*. (2008) from ironstone- and ore-related white mica has tightly constrained the timing of mineralisation to between 1851–1847 Ma, both for the ironstone stage and the Au-Cu stage. This new age range suggests that mineralisation overlapped with the emplacement of the Tennant Creek Supersuite, and may suggest that magmatism, mineralisation and deformation may have occurred concurrently, after cessation of sedimentation in the Warramunga Basin.

As mentioned above, uranium is known, but poorly described in Tennant Creek deposits. Uraninite and pitchblende are present as trace primary minerals in some deposits (Le Messurier *et al*., 1990; MODAT), and torbernite has been reported at the Edna Beryl prospect (MODAT). MODAT indicates uranium as a minor commodity at Edna Beryl and at Northern Star, both in the northern part of the Tennant Creek field. The best description of uranium in the Tennant Creek field, however, is at the Juno deposit, where Large (1975) established that uranium values in excess of 80 ppm define a zone that overlaps the boundary between the Au and Bi zones (Figure 3.3.6).

Following a period of low activity in the 1990s and early 2000s, exploration has increased in the Tennant Creek area in recent years, with new discoveries in both the Tennant Creek and Rover fields. Importantly, the majority of these new discoveries are quite different to most of the previous discoveries. In the Tennant Creek field, Emmerson Resources discovered Cu-Au-Bi mineralisation using helicopter-borne transient electromagnetics (HeliTEM) within 'mineralised' shear zones at the Monitor and Goanna prospects along strike from the historic Gecko mine. Although small ironstones are present within the shears, the mineralisation is not directly associated with them.

In the Rover field, Westgold Resources (www.westgoldresources.com.au) discovered a significant Zn-Pb-Ag deposit at Explorer 108, with a JORC-compliant resource of 8.733 Mt grading 3.7% Pb, 2.0% Zn, 20 g/t Ag, 0.1% Cu and 0.3 g/t Au. This deposit, hosted mostly by brecciated dolomite and overlying sheared volcanics, is the first major Zn-Pb deposit known in the Tennant Creek region, although locally dolomitic zones in the Tennant Creek field contain elevated Zn (e.g., up to 2.5% Zn over one metre at Navigator 7 West: unpublished Geopeko drill hole assay). Westgold Resources has also identified more typical Tennant Creek-style mineralisation at the Rover 1 prospect, where they have identified a total resource of 6.81 Mt grading 1.21% Cu, 1.73 g/t Au, 0.14% Bi, 0.06% Co and 2.07 g/t Ag. This deposit crosses a lease boundary into ground held by Adelaide Resources (www.adelaideresources.com.au), who have reported significant intersections, but to date have not estimated a mineral resource. Adelaide Resources has also intersected ironstone-hosted Cu-Au mineralisation at the Rover 4 and Rover 12 prospects.

3.3.1.4 Other occurrences

The Gumtree prospect (Warren, 1980; Warren and Shaw, 1985), which is interpreted to be a Johnnies Reward-type deposit (Hussey *et al*., 2005), is located in the west-central part of the study area (Figure 3.3.1). Here, secondary Cu minerals stain a narrow lens of layered hematite-magnetite-quartz rock that can be traced for over a kilometre along strike. Warren (1980) interpreted cummingtonite-orthopyroxene rocks located to the north (and in the presumed stratigraphic footwall of the deposits) of the hematite-magnetite-quartz rock as a metamorphosed chloritic alteration zone and the deposit as a metamorphosed volcanogenic massive sulfide deposit. Alternatively, Hussey *et al*. (2005) interpreted the prospect as an IOCG deposit. Lead isotope data yielded ages of 1770–1769 Ma for Pb-rich samples from the Gumtree prospect, based on the Strangways model (D. Huston, unpublished data).

Copper and Au mineralisation also occurs in the eastern part of the study area, southwest of the Jervois district. Here mineralisation occurs within discrete shear zones (e.g., Harding Springs) and quartz veins (e.g. Hale River) which cross-cut the north-dipping and east- to southeast-trending Illogwa Shear Zone. The source of metals is interpreted to be the I-type, ca 1760 Ma Aremra Granodiorite. Remobilisation and deposition of metals in these northwest-trending cross-cutting structures likely occurred during Paleozoic fluid flow along the Illogwa Shear Zone (Whelan *et al*., 2009b). Both mineralisation styles are characterised by chalcopyrite, malachite and azurite. Paragenetic studies indicate that chalcopyrite formed pre- to syn-deformation. Rock chip assays yielded assay results of 13.0% Cu, 2.9 ppm Au and 37 ppm Ag for Hale River and 35.4% Cu, 0.2 ppm Au and 92 ppm Ag for Harding Springs (Whelan *et al*., 2009a).

South of the Harding Springs and Hale River occurrences in the Limbla 1:100 000 map sheet, the recent identification of a regional-scale alteration system characterised by fluorite-hematite-silica alteration, hydrothermal brecciation and veining and lesser potassic alteration (Whelan *et al*., 2011; 2012) is consistent with alteration systems that are known to be associated with IOCG-style mineralisation. Recent work by Mithril Resources Ltd. (www.mithril.com.au) in the area has identified Cu ± Au-Ag mineralisation at surface at the Powers, Austin and Bigglesworth prospects (Figure 3.3.1). Mineralisation is hosted in the strongly oxidised, weakly peraluminous 1750–1740 Ma Atneequa Granitic Complex and appears to be spatially associated with west to northwest trending quartz-breccia and structures (Whelan *et al*., 2012). Petrographic work on samples of altered granite from the Powers prospect shows evidence for intense hydrothermal brecciation, with minor hematised K-feldspar observed in a fine-grained matrix comprising fluorite-hematite-quartz-K-feldspar. Paragenetic studies indicate that both vein and disseminated fluorite are present as least some of the fluorite veins pre-date brecciation, as angular clasts of fluorite and altered host granite are clearly visible in the matrix. Disseminated fluorite is interpreted to have been deposited syn- to post-brecciation along with fine-grained decussate and micaceous hematite (Whelan *et al*., 2011; 2012).

At the Powers prospect, anomalous Cu is associated with intensely altered micro-brecciated granite with hematite-fluorite veining. At the Austin and Powers prospects, malachite is associated with silica-hematite-carbonate-altered granite. At Austin, the exposed Cu-mineralised zone extends 200 m along strike within a west-northwest-trending zone of intense alteration that extends for over two kilometres. This altered zone lies on the northern side of a gravity high and coincides with an IP anomaly. At the Bigglesworth prospect, Cu mineralisation, with grades in surface samples to 4.5% Cu and 0.2 g/t Au, has been identified within a kilometre-long zone (Mithril Resources Ltd ASX Release, 31st January 2012). This zone is located along the northwestern margin of a large gravity high. These prospects are interpreted by Mithril as IOCG-type deposits bearing similarities to those in the Cloncurry district (www.mithril.com.au).

To the west of the study area, Tanami Gold discovered Cu-Au mineralisation associated with ironstone at the Tekapo, Te Anau and Manapouri prospects during the 2000s. The Tekapo prospect, which is associated with a hematitic gossanous breccia, is hosted by schists of the Lander Rock Formation and dolerite. Drilling at Tekapo in 2006 returned an intersection of 16 m at 3.4 g/t Au. Follow-up drilling intersected significant Cu and Au mineralisation, including four metres at 2.7% Cu and four metres at 3.27 g/t Au. Pink-red hematite alteration has been observed in fresh rock, suggesting that this may be an IOCG system (Tanami Gold NL ASX Announcement, 27 September 2006). These prospects are currently being explored by ABM Resources, who released in late 2011 initial drilling results including 18 m grading 2.2 g/t Au and 17 m grading 0.25% Cu (separate holes) from the Tekapo prospect.

3.3.2 Mineral system model for uranium-rich iron oxide-copper-gold systems

As mineral system models have been developed for both the Olympic IOCG Province (Hayward and Skirrow, 2010; Skirrow *et al*., 2011; and references therein), the Cloncurry district (Skirrow and Huston, 2010; and references therein) and for IOCG deposits in general (Hitzman *et al*., 1992; Hitzman and Valenta, 2005; Williams *et al*., 2005), this section only briefly describes the general mineral system model and highlights differences between these previous models and the model used in this investigation.

Following Skirrow and Huston (2010) and Skirrow *et al*. (2011), Figure 3.3.7 illustrates the general IOCG mineral system model, highlighting features that are favourable for uranium-rich systems. An apparently fundamental control on the distribution of these deposits is the association with major crustal boundaries, with the deposits generally occurring in the hanging wall to these structures. These boundaries are possible sutures (e.g., Korsch *et al*., 2011), formed along convergent margins by the accretion of an exotic block. The association of IOCG deposits with these sutures may be the consequence of one or both of two processes: (1) fertilisation of the upper mantle during subduction, pre-conditioning it and the adjacent lower crust for decompression melting to form high-temperature A- and I-type melts during later extension (Oliver *et al*., 2008), and/or (2) provision of fluid pathways during reactivation of collisional and related structures during later extension. Suturing can predate the timing of mineralisation by tens to many hundreds of millions of years.

In the Olympic IOCG Province, Hayward and Skirrow (2010) have assembled strong evidence that the IOCG event there coincided with a shift from contraction to extension. In both the Olympic IOCG Province and the Cloncurry district, IOCG mineralisation is temporally and broadly spatially associated with A-type and high-temperature I-type granites of the Hiltaba and Williams-Naraku Suites, respectively (Wyborn *et al*., 2001). Geochemically, these suites are most consistent with melting of the lower crust with a component of fertilised upper mantle during decompression and heating associated with extension.

The granite geochemistry and tectonic setting of the Olympic IOCG Province and the Cloncurry district differ from those of Tennant Creek and the Aileron Province. According to Wyborn (2001), the 1850–1840 Ma Tennant Creek Supersuite is an I (granodiorite)-type, restite-dominated suite with some fractionation apparent later in its history. Geochemically, the Tennant Creek and Red Bluff granites, which were emplaced at the same time as mineralisation, along with associated porphyry sills and dykes, have a granitic to trondhjemitic composition. These rocks are moderately to strongly oxidised, although this may in part reflect alteration (Wyborn, 2001).

Following earlier work by Foden *et al*. (1988) and Warren (1989), Zhao and McCulloch (1995) classified granites in the Aileron Province into three geochemical groups: (1) the calc-alkaline-trondhjemitic (CAT) group, interpreted to be analogous to modern-day cordilleran suites for which they inferred a subduction-related setting; (2) a volumetrically-dominant main group, which has geochemical similarities to the Barramundi Igneous Association (e.g., ASI < 1.1, enriched K_2O, Rb, Th, uranium, LREE, Zr and Y and depleted MgO, CaO, Sr, Ni and Cr compared to Phanerozoic I-type granites; Zhao and McCulloch, 1995) seen elsewhere in northern Australia, and (3) the high-heat producing (HHP) group, which is enriched in K, uranium and Th. The first two groups were emplaced prior to or syn- to post-Yambah Event between 1795–1745 Ma, whereas the last group was emplaced mostly during the Strangways Event (1735–1690 Ma). Recent data (Smith, 2001; Beyer *et al*., 2012), however, indicate that some granites of the HHP group were emplaced earlier (e.g., the 1790–1780 Ma Wangala Granite) and later (e.g., the ~1621 Ma Ennungan Mountains Granite) than the Strangways Event. Zhao and McCulloch (1995) showed that the CAT group of granites is mostly restricted to the southern margin of the Aileron Province, possibly marking a subduction-related magmatic arc. The main group of granites, which occur throughout the Aileron Province, may be related to extension in the associated back-arc.

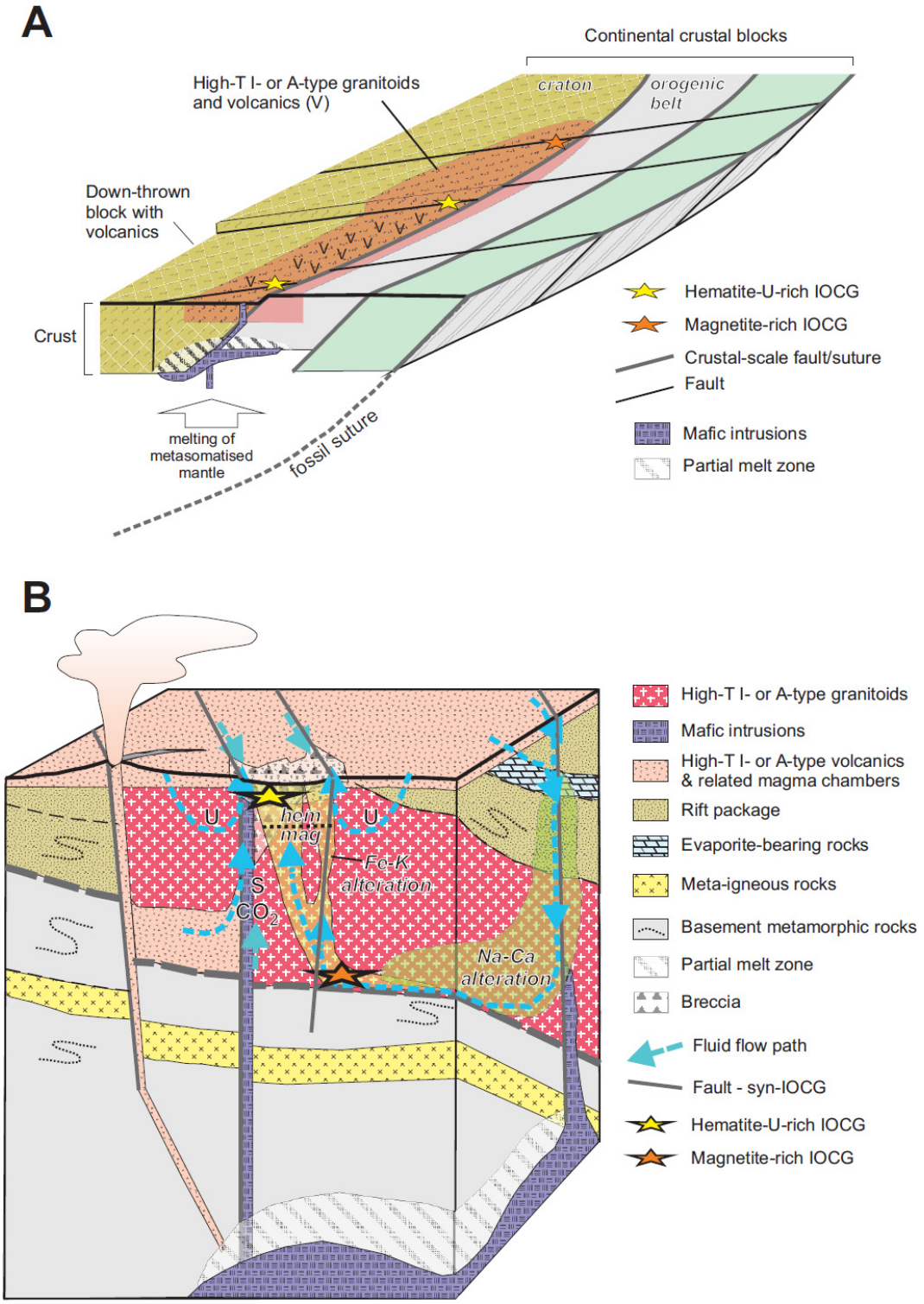

Figure 3.3.7: *Mineral system model for uranium-rich IOCG mineral systems (after Skirrow and Huston, 2010).*

From the discussion above, granites coeval with IOCG mineralisation in both the Tennant Region and the Aileron Province do not have an affinity with A-type granites, but rather have a closer affinity with I-type granites, some of which may have arc affinities. Hitzman (2000) identified three tectonic settings for IOCG deposits: (1) orogenic basin collapse (e.g., Cloncurry district), (2) anorogenic magmatism (e.g. Olympic IOCG Province); and (3) subduction-related continental margin (e.g., Mesozoic deposits in northern Chile). Although it is likely that the first two environment may be variants of the same overall geodynamic setting (i.e., intracratonic extension following collision), the third reflects a different setting, that of a convergent margin. It is possible that the different magmatic association noted for the Tennant Creek and, particularly, the syn- to post-Yambah Event-related deposits in the Aileron Province may relate to development along a convergent continental margin, as is the case in northern Chile. Even if a convergent continental margin setting is not correct for the Aileron Province deposits, the spatial association of IOCG deposits with major crustal boundaries and the temporal association with high-temperature I-type (in this case) granites in an extensional environment still are useful as mappable criteria in the mineral potential analysis.

Most global IOCG deposits are associated closely with Fe- and K-enrichment (Williams *et al*., 2005). In the case of Fe, the dominant minerals are magnetite and hematite, with Fe-bearing silicates (e.g., biotite, chlorite and amphibole) present in some deposits. In the case of K, many deposits are closely associated with biotite- and/or K-feldspar-dominant assemblages, although these minerals are not present at the Olympic Dam deposit, where the proximal alteration assemblage is dominated by sericite-hematite with variable amounts of chlorite and siderite. Barite, fluorite and REE-carbonate minerals are also common (Oreskes and Einaudi, 1992). Regionally and at deeper crustal levels, the sodic-calcic alteration assemblages dominate, and some Chilean deposits are associated with proximal sodic-calcic assemblages (Williams *et al*., 2005).

These assemblages differ from those observed with many of the IOCG deposits in the study area. At Jervois, the proximal assemblage is chlorite-magnetite-garnet, and chlorite and magnetite are the dominant proximal alteration minerals at Tennant Creek. Both of these systems mostly lack the potassic assemblage that characterises many IOCG deposits, although white mica is present the Tennant Creek deposits. The proximal assemblages at Johnnies Reward and the Mithril prospects, however, have closer affinities to typical IOCG assemblages. The quartz-garnet-biotite gneiss underlying Johnnies Reward has affinities with biotite-rich assemblages seen in other IOCG deposits, and the hematite-fluorite-silica proximal assemblage at Bigglesworth, Austin and Powers has similarities to the assemblage that characterises Olympic Dam. Regional sodic-calcic assemblages are not noted in the vicinity of IOCG deposits in the study area, although this may be due to a lack of regional-scale data on alteration assemblages. The Pb-Zn lodes in the Jervois district, however, are associated with proximal skarn assemblages.

According to Hitzman and Valenta (2005), most IOCG deposits, with the important exception of the Chilean deposits, are anomalous with respect to uranium, with values ranging from 30 to nearly 700 ppm, although uranium is only economically extracted as a by-product of Cu and Au. Hitzman and Valenta (2005) argue that elevated uranium content is related to the original concentration of uranium in the host rock. Skirrow (2010; 2011) suggested that, in addition to host-rock uranium levels, uranium-rich IOCG are also favoured by highly oxidised (i.e., hematite-rich) alteration assemblages, particularly where there is evidence of brecciation and involvement of low-temperature fluids at high crustal levels. In contrast, more reduced, magnetite-dominated IOCG deposits, which are interpreted to form at deeper crustal levels, are less likely to concentrate uranium to ore grades.

Table 3.3.2: Theoretical and mappable criteria for uranium-rich iron oxide-copper-gold systems

MINERAL SYSTEM COMPONENT	CRITERIA		DATASET	IMPOR-TANCE	APPLIC-ABILITY	CONFI-DENCE	WEIGHTING	COMMENTS
	THEORETICAL	MAPPABLE						
Source	Sources of brines, Fe, Cl and S	Fe-rich back-arc and other basins; 20 km buffer	Basement solid geology (see Appendix 1)	0.8	0.5	0.8	0.320	
	Sources of U: distribution of U-enriched igneous rocks	Igneous rocks with high U contents; 20 km buffer	Basement solid geology (see Appendix 1); geochemical data	0.8	0.5	0.5	0.200	High U defined as greater than the 75th percentile for each rock class
	Sources of U: high-T breakdown of U-bearing minerals in the magma source region	Igneous rocks with high zircon saturation temperatures; 20 km buffer	Basement solid geology (see Appendix 1); geochemical data	0.6	0.6	0.6	0.216	Temperatures are based on zircon saturation temperature calculated according to Watson and Harrison (1983). High temperatures are defined as greater than the 75th percentile
		Igneous rocks with transitional zircon saturation temperatures; 20 km buffer		0.6	0.4	0.6	0.144	
	Sources of Cu	Mafic-ultramafic igneous rocks (abundant); 20 km buffer	Basement solid geology (see Appendix 1)	0.8	0.8	0.8	0.512	
		Mafic-ultramafic igneous rocks (minor); 20 km buffer		0.8	0.5	0.8	0.320	
	Igneous sources of volatiles	F-rich and/or fluorite- and tourmaline-bearing igneous rocks; 20 km buffer	Basement solid geology (see Appendix 1); geochemical data	0.5	0.5	0.5	0.125	High-F defined as greater than the 75th percentile for each rock class
Drivers	High paleo-geothermal gradient	Units with good evidence for high-level intrusion; 20 km buffer	Basement solid geology (see Appendix 1)	0.8	0.8	0.8	0.512	
		Units with moderate evidence for high-level intrusion; 20 km buffer		0.8	0.5	0.8	0.320	
		Units with poor evidence for high-level intrusion; 20 km buffer		0.8	0.2	0.8	0.128	
	Volatile-fluid release	Breccias in igneous units; 20 km buffer	Basement solid geology (see Appendix 1); literature review	0.5	0.8	0.8	0.320	
	Large volume, high-T crustal melts	A- and high-T I-type felsic intrusive and volcanic rocks; 20 km buffer	Basement solid geology (see Appendix 1); literature review	0.8	0.8	0.8	0.512	
	(Metasomatised) mantle melts	Mafic-ultramafic igneous rocks (abundant); 20 km buffer	Basement solid geology (see Appendix 1)	1.0	0.8	0.8	0.640	
		Mafic-ultramafic igneous rocks (minor); 20 km buffer		1.0	0.8	0.5	0.400	
Fluid-flow pathways and architecture	Fluid flow along permeable structures	Faults with 2.5 km buffer	Basement solid geology (see Appendix 1)	0.8	0.5	0.5	0.200	
	Crustal-scale weak zones allowing mantle to crust magmatism and fluid flow	Crustal domain boundaries; 100 km buffer	Basement solid geology (see Appendix 1)	1.0	0.8	0.7	0.560	Buffer into over-riding plate
		Crustal domain boundaries; 30 km buffer		1.0	0.3	0.7	0.210	Buffer into under-riding plate
Depositional mechanisms	Direct evidence of elevated U	U^2/Th values one standard deviation above the mean for each unique geological unit	Radiometric map of Australia (Minty *et al*., 2010); Surface geology of Australia (Raymond and Retter, 2010)	0.3	0.5	0.8	0.12	
		U^2/Th values two standard deviations above the mean for each unique geological unit		0.3	0.8	0.8	0.192	
	Chemical gradients	Inversion model volumes of magnetite alteration buffered to 2.5 km	Inversion model (see text for details)	1.0	0.4	0.4	0.200	
		Inversion model volumes of hematite alteration buffered to 2.5 km		1.0	0.7	0.4	0.280	
		Ironstones and iron formations (abundant)	Basement solid geology (see Appendix 1)	0.5	0.8	0.8	0.320	
		Ironstones and iron formations (minor)		0.5	0.5	0.8	0.200	

Although IOCG deposits in the study area differ in many respects to deposits in the Olympic IOCG Province and the Cloncurry district, many of the criteria established using the mineral system model from these two regions still apply. The association with major crustal sutures is still valid as is the association with high-temperature I-type granites.

3.3.3 System components and mappable criteria

Using the mineral system model described above, mappable criteria were developed for uranium-rich IOCG deposits in the study area (Table 3.3.2). These criteria are very similar to those used by Skirrow *et al*. (2011), excluding only the criteria for which insufficient data are available in the study area.

3.3.3.1 Sources

The most fundamental component of a mineral system is a source for the commodities ultimately concentrated into a mineral deposit, in this case, Cu, Au, Fe and uranium. These metals are thought to be mobilised by either magmatic-hydrothermal or basinal fluids, or a combination of both. Five criteria have been used to map the source system component:

- Sources of brines, Fe, Cl and S in Fe-rich back-arc and other basins;
- Uranium-rich igneous rocks;
- High-temperature granites;
- Mafic-ultramafic igneous rocks; and
- Volatile-rich igneous rocks.

Figure 3.3.8 shows the distribution of basins containing Fe-rich lithologies (based upon the basement solid geology assembled for this analysis; see Appendix 1 for details), that are possible sources of basinal brines and Fe. The rocks are extensively developed in the east-central part of the study area and mostly include rocks of the Harts Range Metamorphic Complex. Such rocks are not extensively developed in the Paleoproterozoic succession.

The distribution of uranium-enriched and high-temperature granites is shown in Figures 3.3.9 and 3.3.10 respectively. These have been determined using geochemical data, and their derivation is described in Section 3.5. The latter criterion was mapped based on the assumption that high temperatures allow breakdown of uranium-rich phases (e.g., zircon) during melting of the magma source and permit concentration of uranium during ongoing fractional crystallisation (see Section 3.5). In both cases, favourable granites are located in the northern part of the study area, especially to the east in the case of high-temperature granites. Twenty kilometre buffers were placed around the favourable granites to allow for fluid migration into country rocks. Experience from previous studies (Huston, 2010; Huston and van der Wielen, 2011) indicated this to be an appropriate buffer for many components of uranium mineral systems.

Figure 3.3.11 shows the abundance of mafic to ultramafic intrusive and volcanic rocks buffered to a distance of 20 km. Mafic to intermediate igneous rocks are generally enriched in Cu relative to felsic igneous rocks and most sedimentary rocks (Wedepohl, 1974a, b). Mafic intrusions and volcanic rocks are most common in the central and northern parts of the study area, particularly in the central-east.

Figure 3.3.12 shows the distribution of volatile-rich igneous rocks buffered to a distance of 20 km, as indicated by high F analyses and/or the presence of fluorite and/or tourmaline. Fluorine is a common component of IOCG ores and may be a complexing agent for uranium and HFSE (including REE) that are present in IOCG ores (Haas *et al*., 2000; Bastrakov *et al*., 2010). Volatile-rich igneous rocks are known in the northern to central parts of the study area, particularly in the east.

Overall, the analysis of potential sources of metals and fluids highlights the east-central part of the study area, with some potential through much of the northern to central part of the study area (Figure 3.3.13). However, the apparent lack of sources in the southern part of the study area may be due to a lack of exposure, as most of the criteria used in this analysis of sources are based upon geochemical analyses and petrographic observations from surface or near-surface samples.

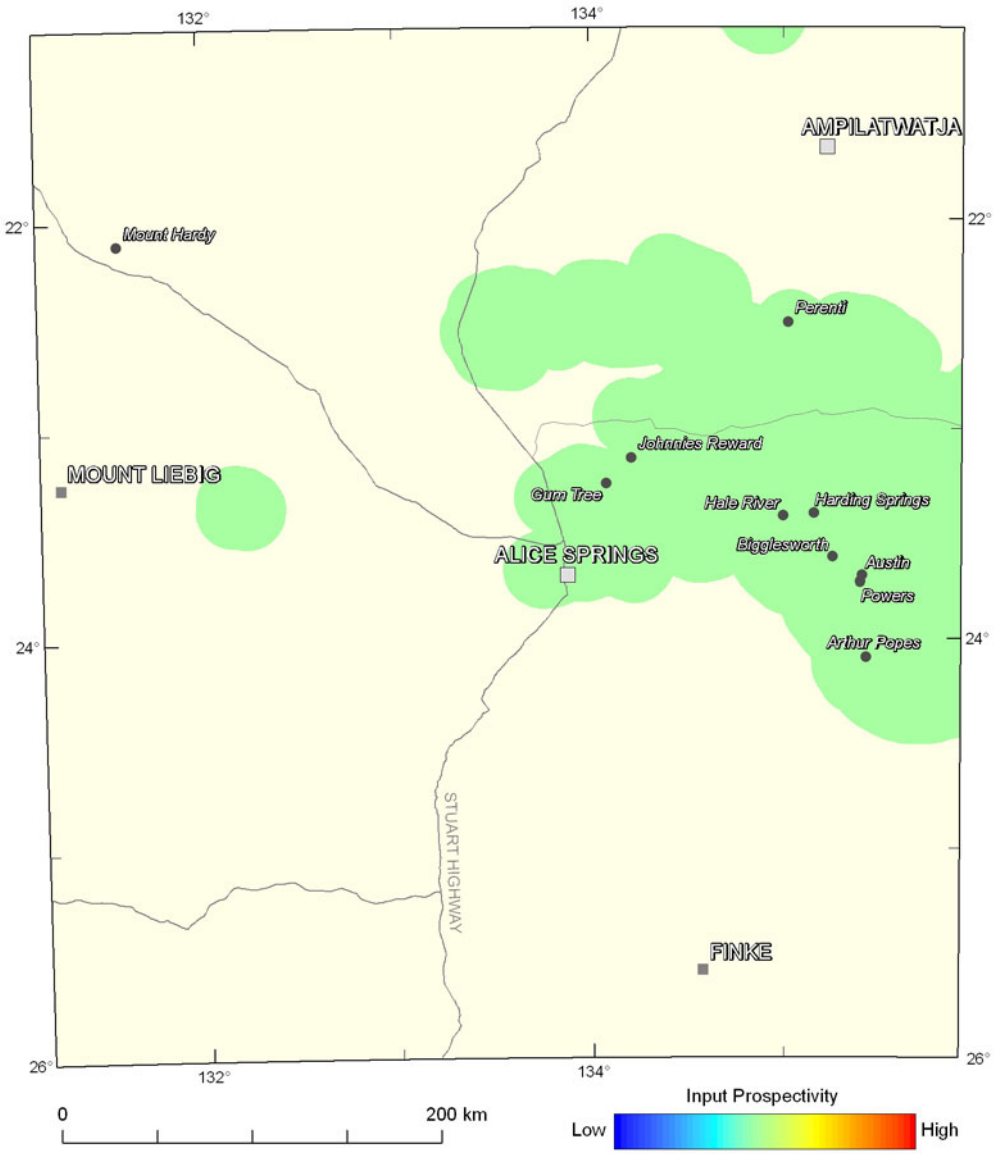

Figure 3.3.8: *Variations in the weighting for the sources of brines, iron, chlorine and sulfur based on the distribution of iron-rich basins. The colour stretch for the mappable criteria used in the assessment for uranium-rich iron oxide-copper-gold systems uses a numerical range from the minimum to the maximum weighting of all criteria used (0.004 to 0.560; see Table 3.3.2), and utilises 20 equal-interval breaks.*

***Figure 3.3.9**: Variations in the weighting for the source of uranium as determined from the uranium contents of igneous units. The colour stretch for the mappable criteria used in the assessment for uranium-rich iron oxide-copper-gold systems uses a numerical range from the minimum to the maximum weighting of all criteria used (0.004 to 0.560; see Table 3.3.2), and utilises 20 equal-interval breaks.*

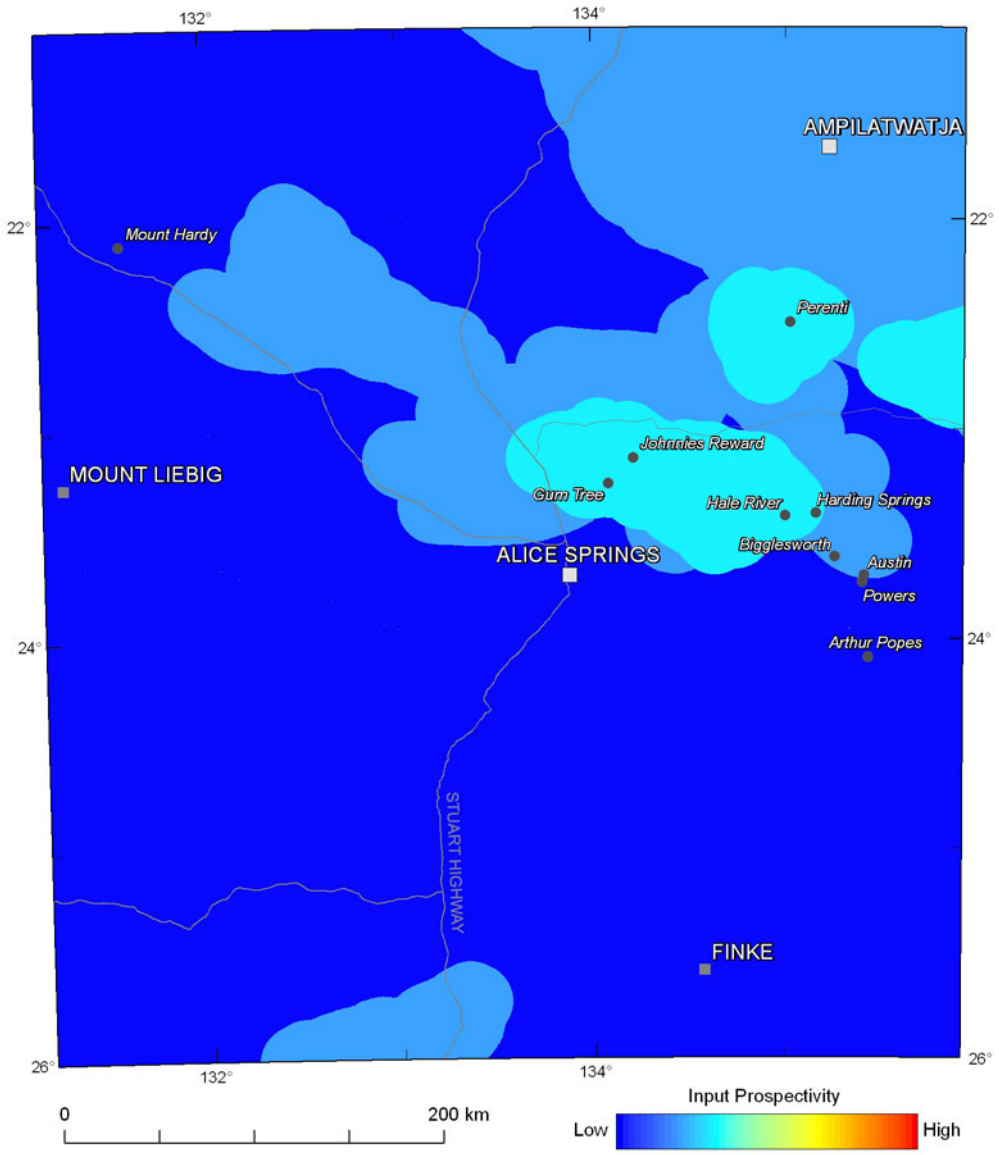

Figure 3.3.10: *Variations in the weighting for the availability of uranium for leaching as determined using zircon saturation temperatures of igneous units (see text for details). The colour stretch for the mappable criteria used in the assessment for uranium-rich iron oxide-copper-gold systems uses a numerical range from the minimum to the maximum weighting of all criteria used (0.004 to 0.560; see Table 3.3.2), and utilises 20 equal-interval breaks.*

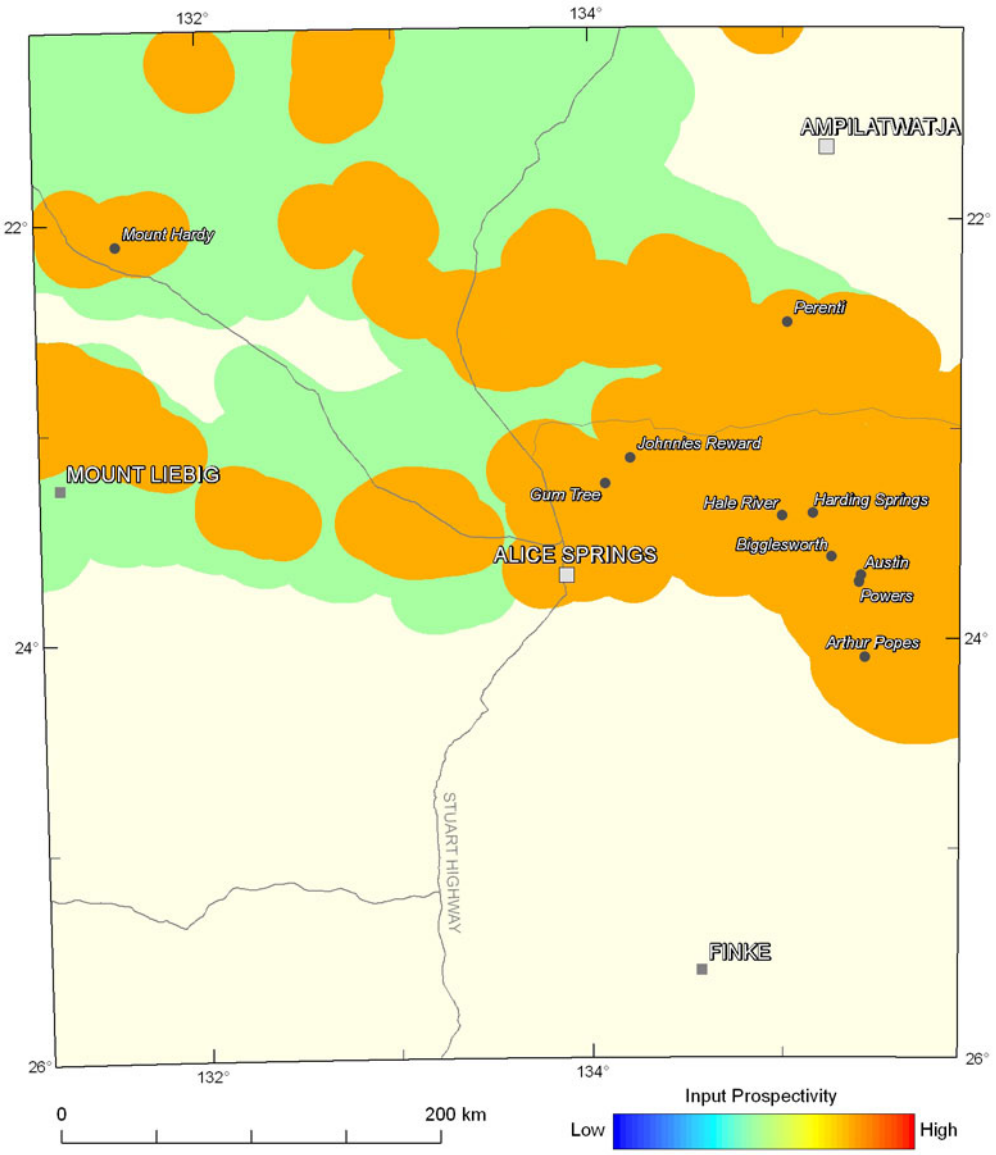

Figure 3.3.11: *Variations in the weighting for copper source as determined from the distribution of mafic and ultramafic igneous rocks. The colour stretch for the mappable criteria used in the assessment for uranium-rich iron oxide-copper-gold systems uses a numerical range from the minimum to the maximum weighting of all criteria used (0.004 to 0.560; see Table 3.3.2), and utilises 20 equal-interval breaks.*

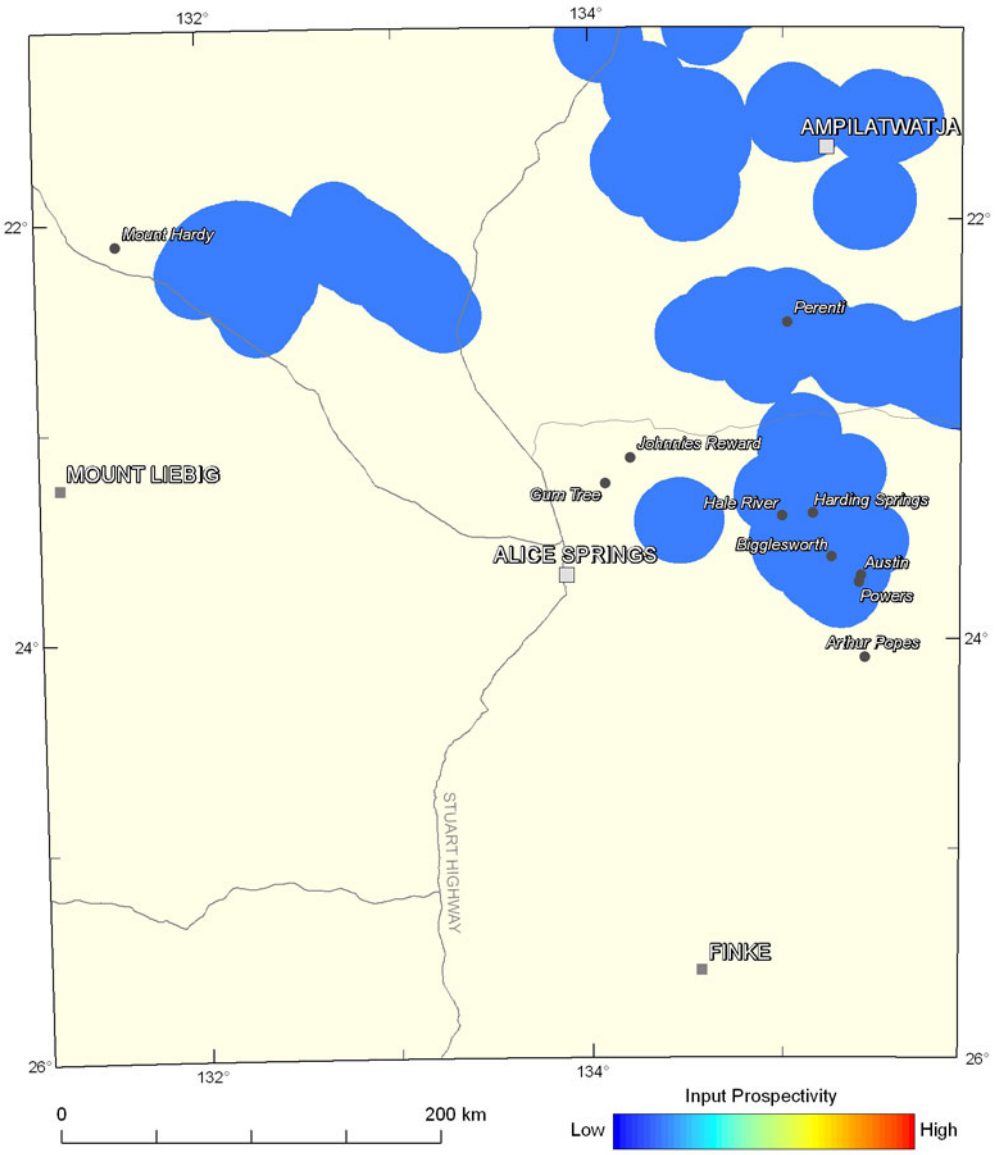

Figure 3.3.12: *Variations in the weighting for volatile-rich granitic melts as determined from the distribution of fluorine-rich granitic rocks and granitic rocks containing fluorite and/or tourmaline. The colour stretch for the mappable criteria used in the assessment for uranium-rich iron oxide-copper-gold systems uses a numerical range from the minimum to the maximum weighting of all criteria used (0.004 to 0.560; see Table 3.3.2), and utilises 20 equal-interval breaks.*

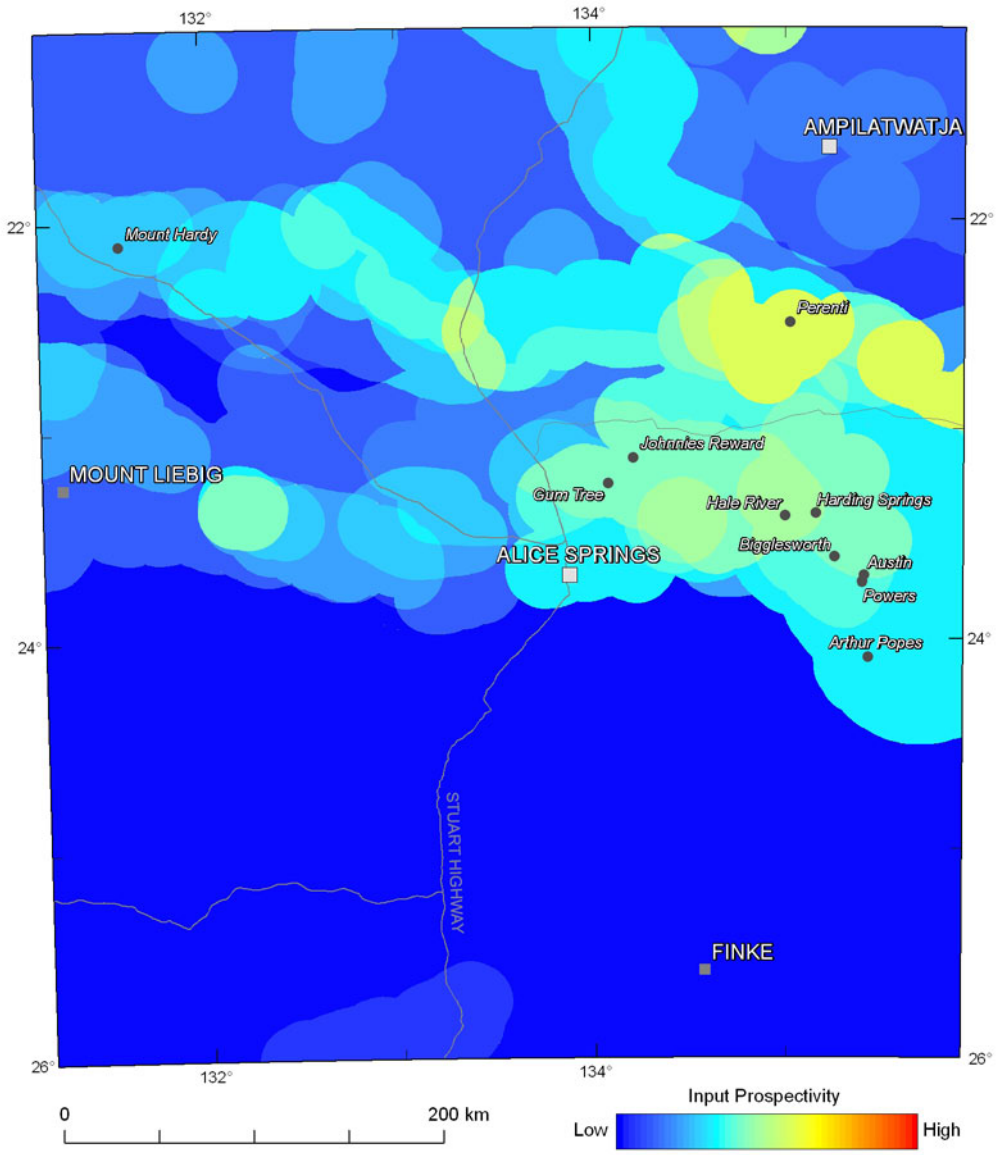

Figure 3.3.13: *Variation in the weightings for the source system component for uranium-rich iron oxide-copper-gold systems. The colour stretch for each mineral system component in the assessment for uranium-rich iron oxide-copper-gold systems uses a numerical range from the minimum to the maximum weighting for each of the system components (0.001 to 0.496), and utilises 20 equal-interval breaks.*

3.3.3.2 Drivers

The drivers of fluid flow in IOCG mineral systems are controversial and varied. As discussed above and by Skirrow *et al*. (2011), the relative roles of basinal and magmatic fluids are a major topic of contention. In our analysis we have considered possible drivers for both basinal and magmatic-hydrothermal fluid flow. Four criteria have been used to map the fluid-flow drivers system component:

- High-level intrusive igneous rocks;
- Brecciated igneous rocks, potentially reflecting volatile-release;
- Large volume, high-temperature crustal melts; and
- Metasomatised mantle melts.

Figure 3.3.14 shows likely zones of high paleo-geothermal gradients based upon the distribution of igneous rocks with evidence of high-level emplacement, and buffered to a distance of 20 km. Evidence for high-level intrusion includes miarolitic cavities and porphyritic textures (see Section 3.5). A high or extreme paleo-geothermal gradient at the time of mineralisation would have driven convective fluid flow in both basinal-brine- and magmatic-hydrothermal-dominated systems. Figure 3.3.14 suggests that high-level intrusives were relatively widespread, with the best evidence preserved for granites in the northwestern and southeastern Aileron Province.

Figure 3.3.15 shows the distribution of zones with magmatic fluid release, as suggested by brecciated zones within granites, buffered to a distance of 20 km. Fluid release would have driven magmatic-hydrothermal fluid flow. Known exposures of brecciated granites are restricted to the eastern Aileron Province.

Figure 3.3.16 shows the distribution of A- and high-temperature I-type granites (with a 20 km buffer). These granites may have driven fluid flow and are mostly known in the Aileron Province. The distribution of mafic to ultramafic igneous rocks (Figure 3.3.17; see also Section 3.3.3.1) also indicates the distribution of thermal anomalies that could have driven fluid flow. This criterion is the same as that shown in Figure 3.3.11, but is weighted differently. In both cases the distribution of a buffer of 20 km was placed around these intrusive rocks.

Overall, analysis of drivers highlights areas in the eastern Arunta Region, in the Reynolds Ranges, and in the southern Davenport Province (Figure 3.3.18).

3.3.3.3 Fluid-flow pathways and architecture

In most mineral systems, fluid pathways and architecture govern the flow of hydrothermal fluids from their source to their depositional site. However, in the case of the IOCG mineral system, architecture established well before the mineralising event may, to large extent, govern regions where a mineral system may operate. Two criteria have been used to map the fluid pathways and architecture system component:

- Fluid flow along permeable structures; and
- Crustal domain boundaries.

Fluid flow along permeable structures has been mapped using the distribution of buffered (2.5 km) faults contained within the basement solid geology dataset (Figure 3.3.19; see Appendix 1 for details). This map highlights structures in near-surface basement, but not in regions overlain by basins, particularly by the Amadeus Basin. This result is the consequence of the inability to interpret through thick basin successions to identify basement structure.

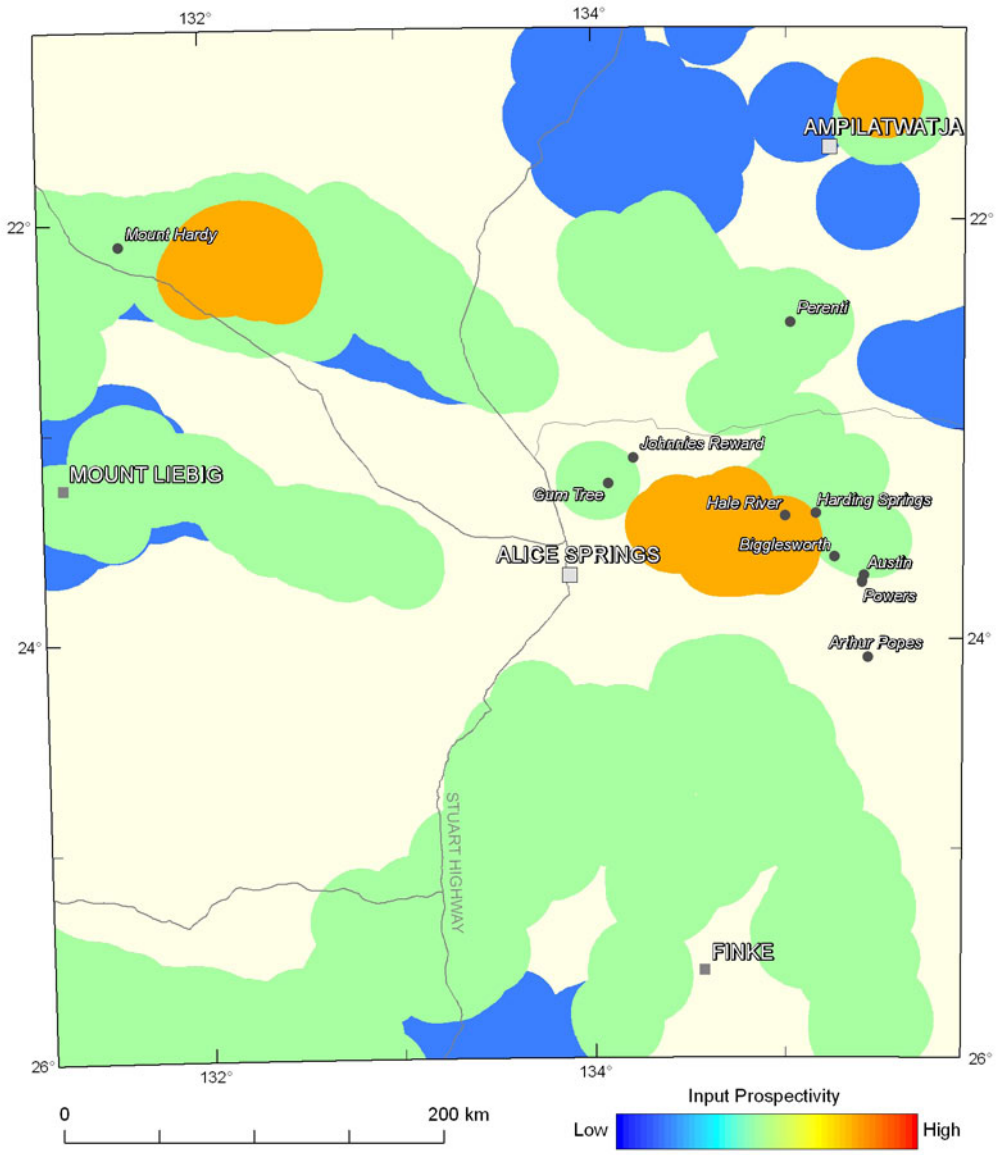

Figure 3.3.14: *Variations in the weighting for paleo-geothermal gradient as determined from evidence of high-level emplacement for igneous suites. The colour stretch for the mappable criteria used in the assessment for uranium-rich iron oxide-copper-gold systems uses a numerical range from the minimum to the maximum weighting of all criteria used (0.004 to 0.560; see Table 3.3.2), and utilises 20 equal-interval breaks.*

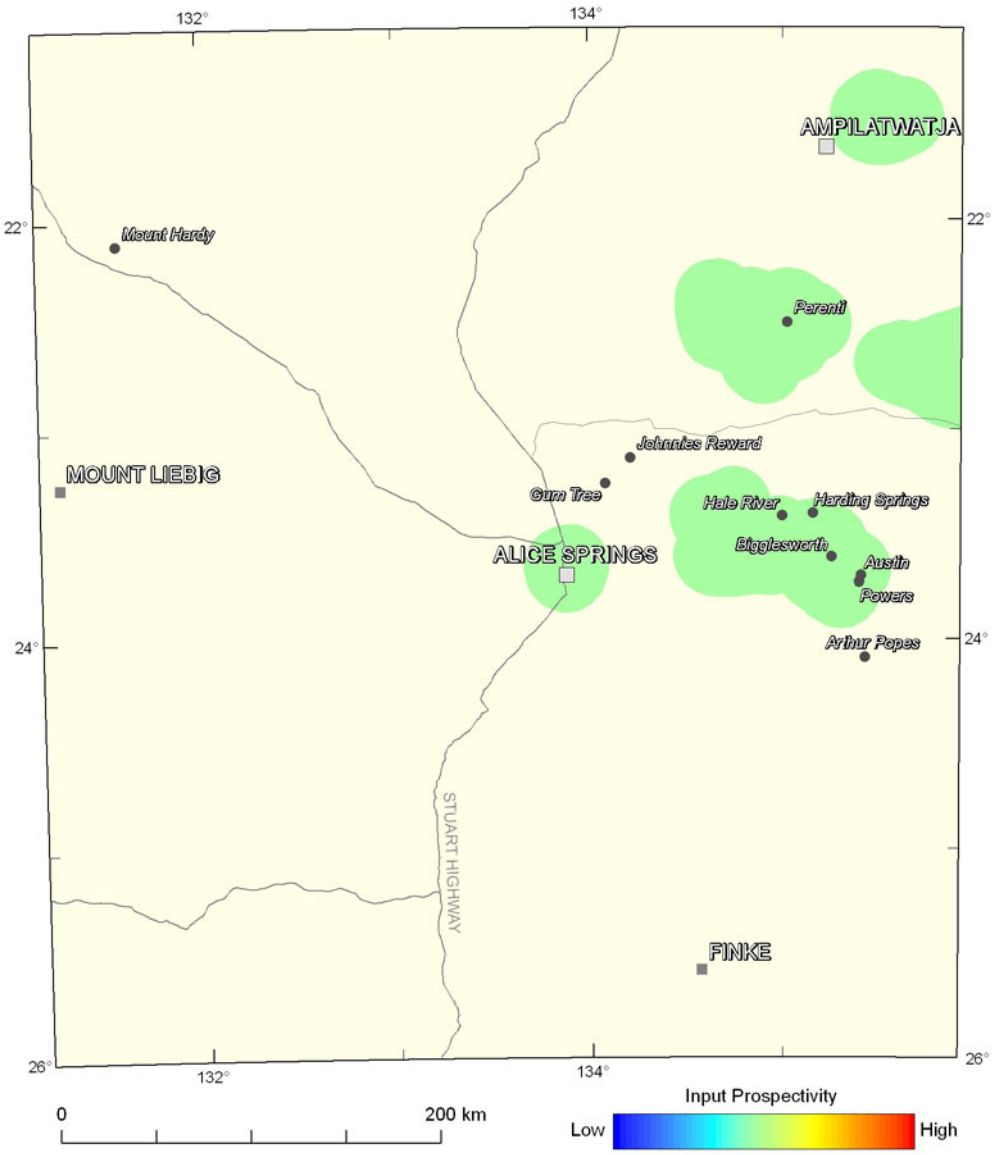

Figure 3.3.15: *Variations in the weighting for volatile fluid release as indicated by the presence of breccias within igneous suites. The colour stretch for the mappable criteria used in the assessment for uranium-rich iron oxide-copper-gold systems uses a numerical range from the minimum to the maximum weighting of all criteria used (0.004 to 0.560; see Table 3.3.2), and utilises 20 equal-interval breaks.*

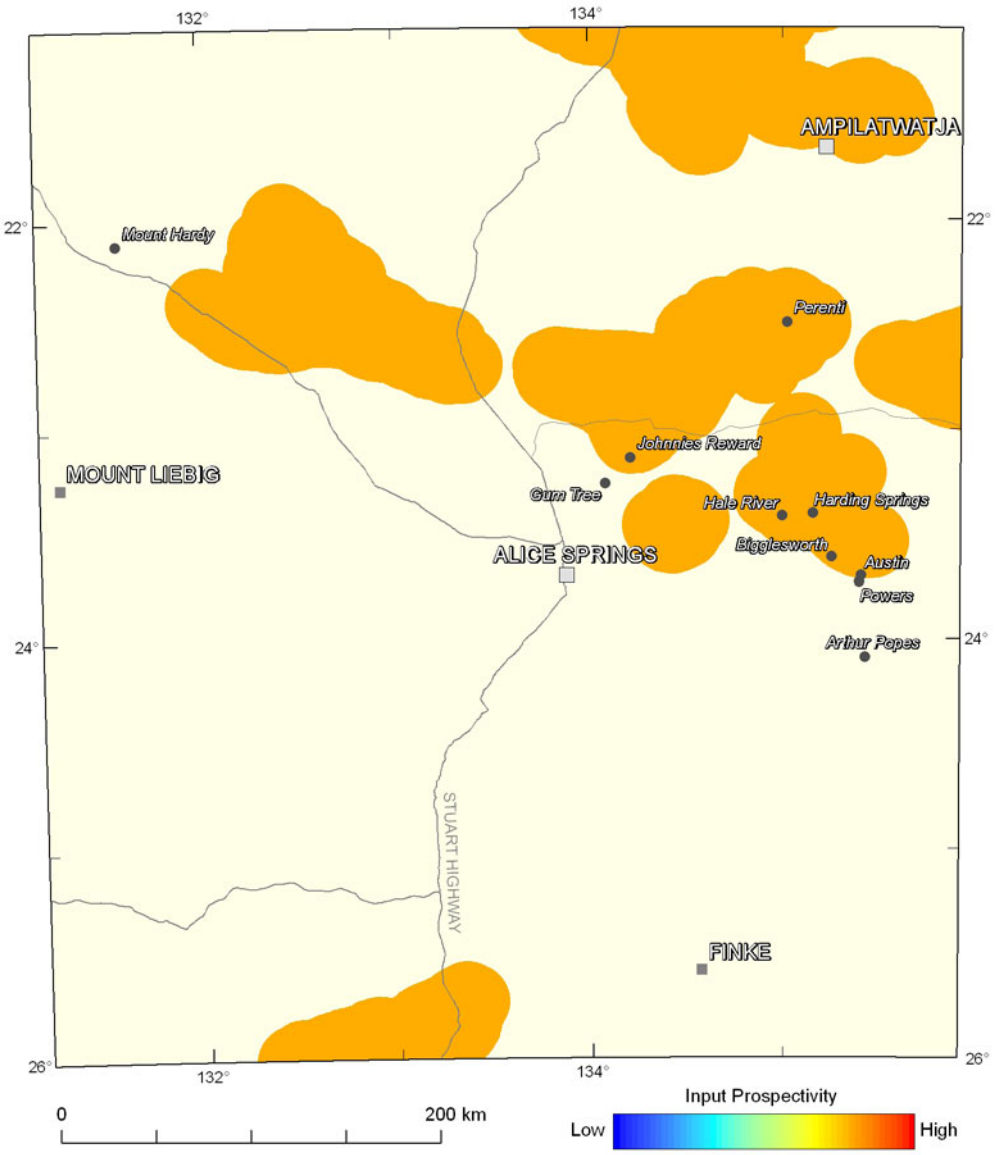

Figure 3.3.16: *Variations in the weighting of high-temperature, crustally derived granites as determined from the distributions of high temperature A- and I-type igneous rocks. The colour stretch for the mappable criteria used in the assessment for uranium-rich iron oxide-copper-gold systems uses a numerical range from the minimum to the maximum weighting of all criteria used (0.004 to 0.560; see Table 3.3.2), and utilises 20 equal-interval breaks.*

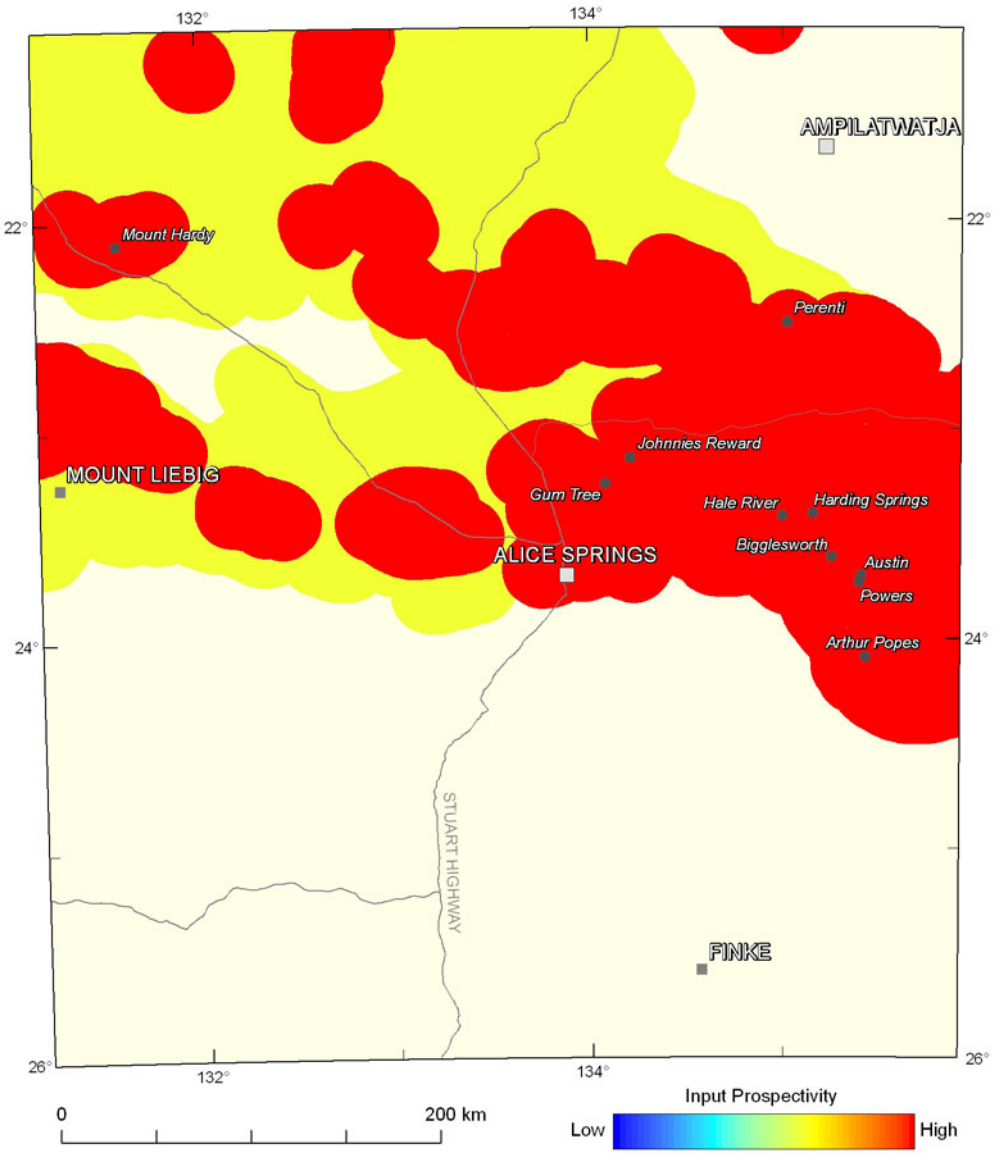

Figure 3.3.17: *Variations in the weighting for metasomatised mantle melts, as indicated by the presence of mafic to ultramafic igneous rocks. The colour stretch for the mappable criteria used in the assessment for uranium-rich iron oxide-copper-gold systems uses a numerical range from the minimum to the maximum weighting of all criteria used (0.004 to 0.560; see Table 3.3.2), and utilises 20 equal-interval breaks.*

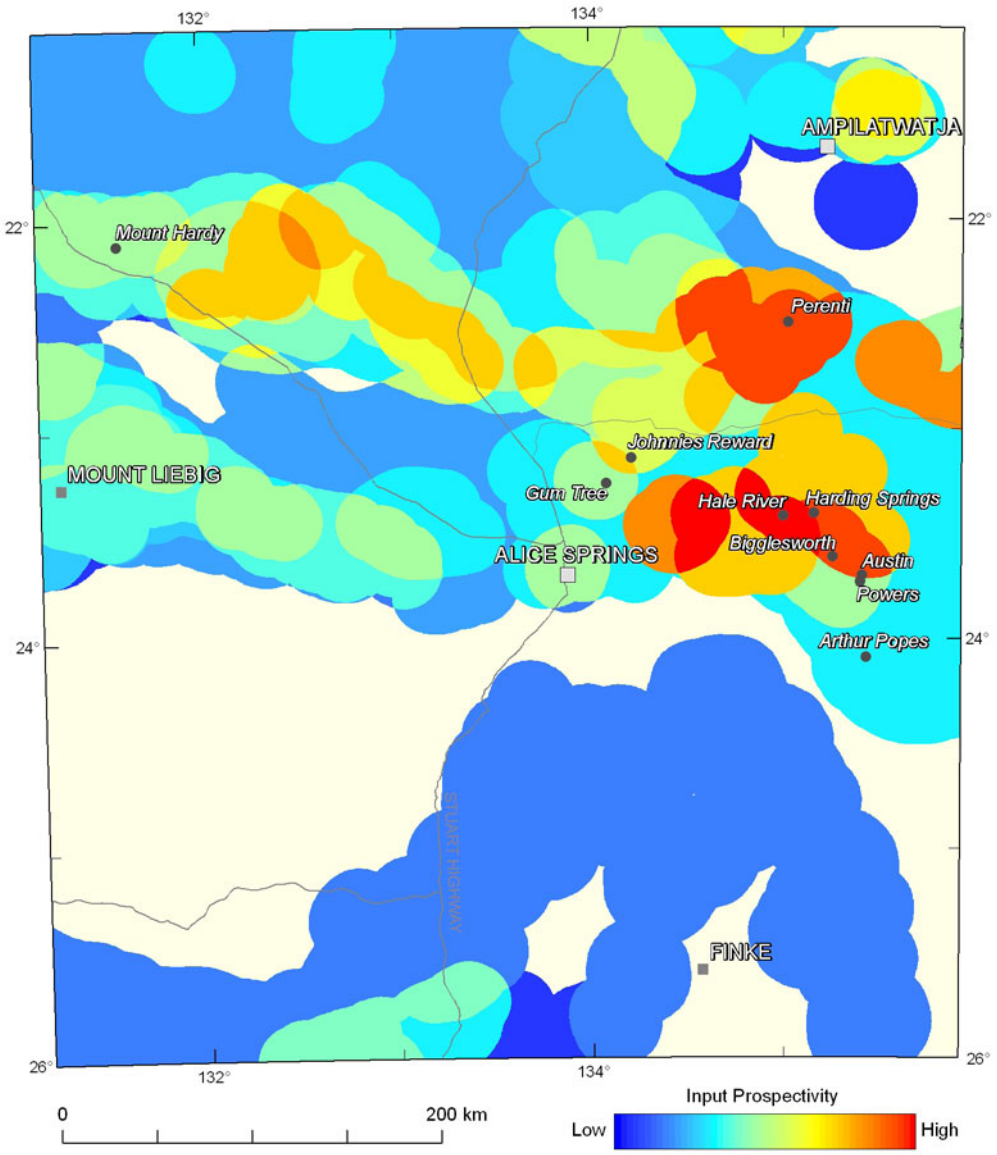

Figure 3.3.18: *Variation in the weightings for the driver system component for uranium-rich iron oxide-copper-gold systems. The colour stretch for each mineral system component in the assessment for uranium-rich iron oxide-copper-gold systems uses a numerical range from the minimum to the maximum weighting for each of the system components (0.001 to 0.496), and utilises 20 equal-interval breaks.*

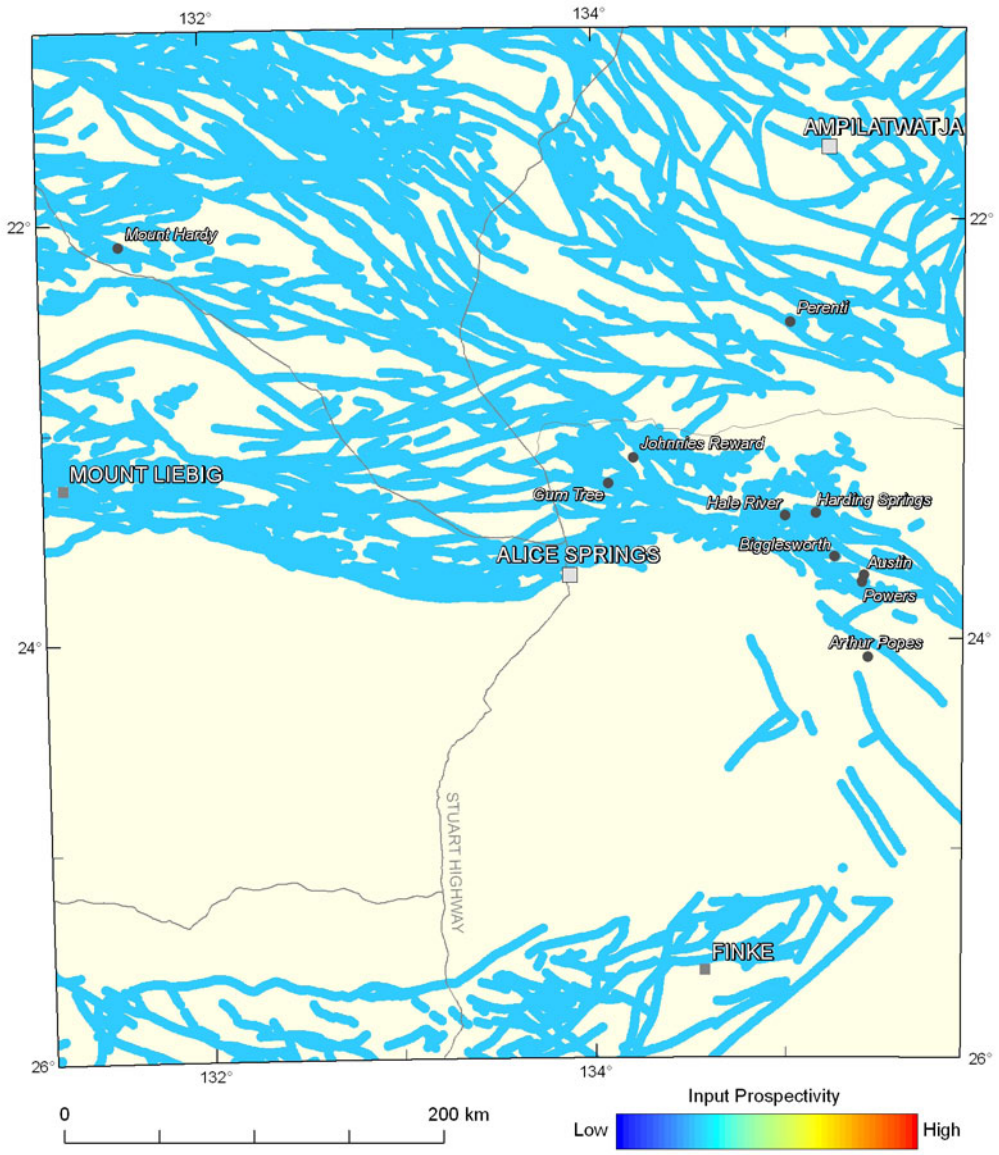

Figure 3.3.19: *Variations in the weighting for fluid flow pathways as determined by the distribution of major faults. The colour stretch for the mappable criteria used in the assessment for uranium-rich iron oxide-copper-gold systems uses a numerical range from the minimum to the maximum weighting of all criteria used (0.004 to 0.560; see Table 3.3.2), and utilises 20 equal-interval breaks.*

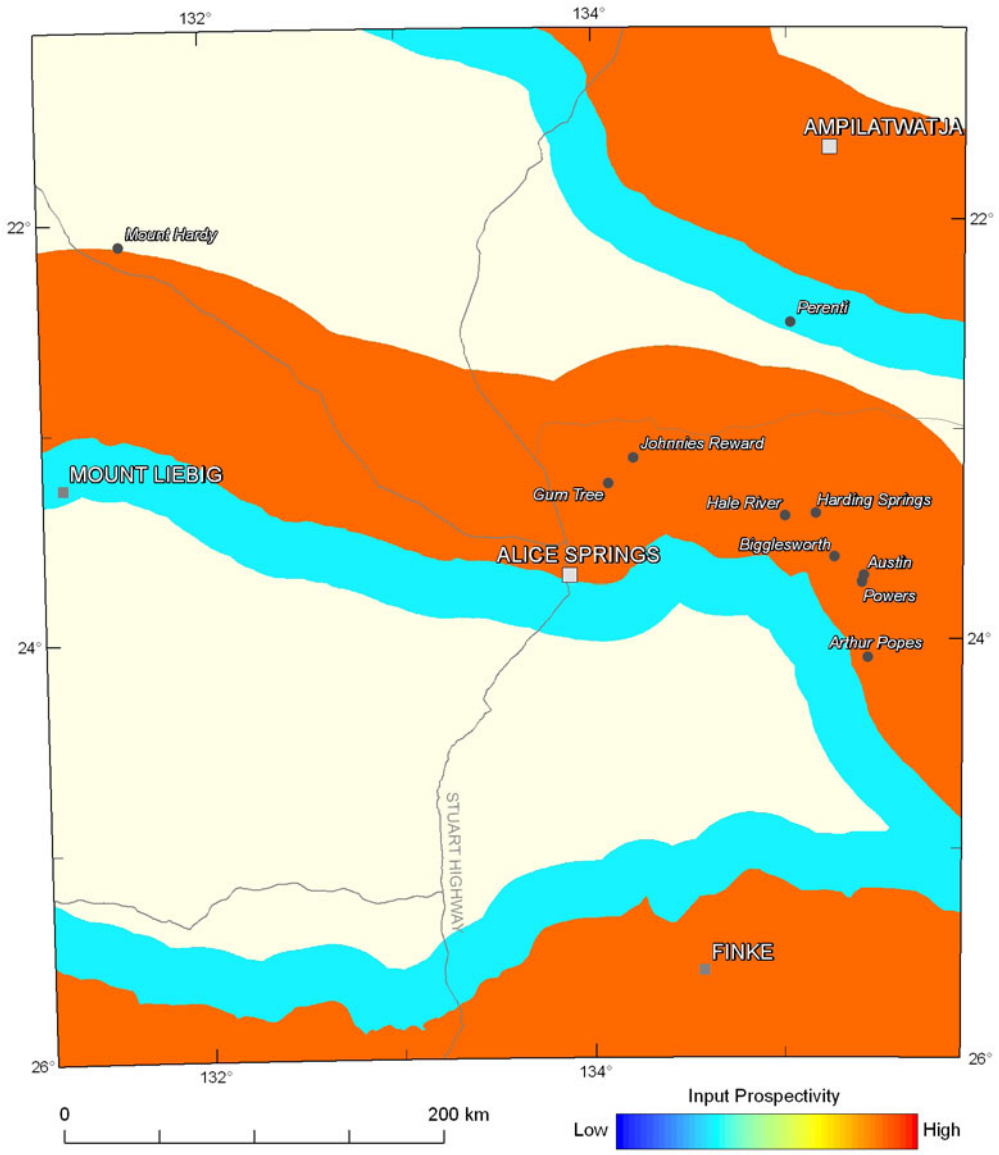

Figure 3.3.20: *Variations in the weighting for proximity to crustal domain boundaries (see text for details). The colour stretch for the mappable criteria used in the assessment for uranium-rich iron oxide-copper-gold systems uses a numerical range from the minimum to the maximum weighting of all criteria used (0.004 to 0.560; see Table 3.3.2), and utilises 20 equal-interval breaks.*

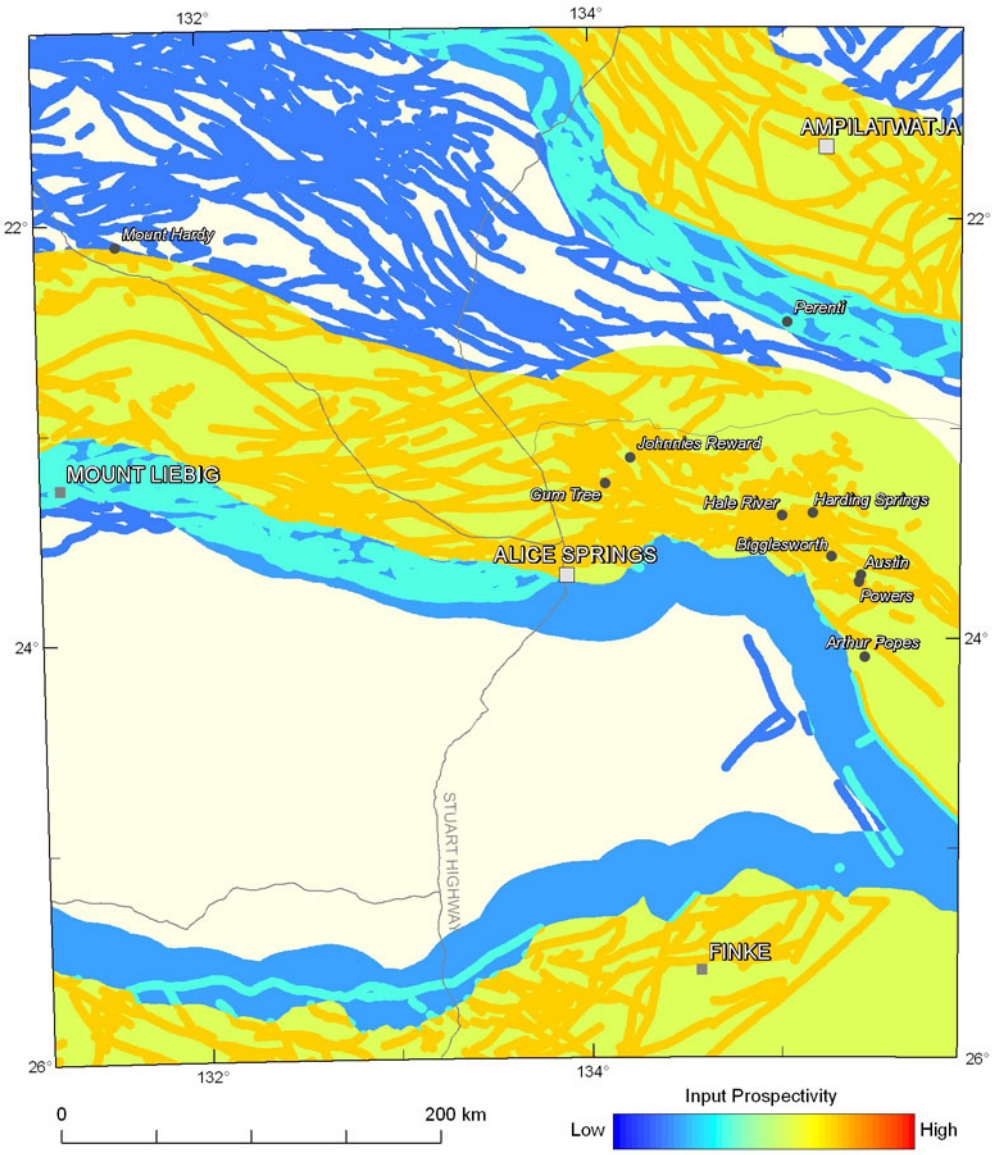

Figure 3.3.21: *Variation in the weightings for the fluid-flow pathways and architecture system component for uranium-rich iron oxide-copper-gold systems. The colour stretch for each mineral system component in the assessment for uranium-rich iron oxide-copper-gold systems uses a numerical range from the minimum to the maximum weighting for each of the system components (0.001 to 0.496), and utilises 20 equal-interval breaks.*

As discussed by Skirrow and Huston (2010) and Skirrow *et al*. (2011), IOCG deposits in the Olympic IOCG Province and in the Cloncurry IOCG district are located in the hanging wall of major crustal boundaries interpreted as sutures that terminated subduction. Groves *et al*. (2010) extended this relationship more broadly, noting that globally IOCG deposits are located within 100 km of margins of Archean or Proterozoic cratons. Oliver *et al*. (2008) suggested that IOCG deposits in the Cloncurry district were the final product of protracted hydrothermal evolution that initiated with the development of a west-dipping subduction below the Mt Isa Province before about 1840 Ma. A key consequence of this subduction was metasomatism and fertilisation of the mantle wedge that enabled subsequent melting to form the A-type and high-temperature I-type Williams-Naraku igneous suite that is spatially and temporally associated with mineralisation (Oliver *et al*., 2008). Hence, the link of IOCG deposits with major crustal boundaries may be a consequence of pre-fertilisation of the province and underlying mantle for later mineralisation.

The criterion that IOCG deposits are localised within 100 km, and generally within the hanging wall, of major crustal boundaries has been used to construct Figure 3.3.20. Three crustal boundaries are interpreted in the study area: (1) the boundary between the Davenport and Aileron provinces, which was active prior to 1840 Ma (Goleby *et al*., 2009; Korsch *et al*., 2011) and may have involved north-dipping subduction, (2) the southeastern margin of the Aileron Province, which was active between 1810–1740 Ma and involved north-dipping subduction (Betts and Giles, 2006; Huston *et al*., 2012), and (3) the boundary between the Warumpi and Musgrave provinces, which was active between 1600–1555 Ma and involved south-dipping subduction (Wade *et al*., 2006; Cawood and Korsch 2008; Korsch *et al*., 2011). Based on these relationships, the crustal boundaries were buffered 100 km into the over-riding province (with an applicability value of 0.8) and 30 km into under-riding province (with an applicability value of 0.3). The boundary between the Aileron and Irindina provinces was not considered, as the Irindina Basin formed in an extensional (rift or pull-apart) environment and did not involve subduction.

Figure 3.3.21 shows the combined fluid pathway/architecture system component, which highlights the southern margins of the Tennant Region and the Aileron Province and the northern margin of the Musgrave Province. Zones within these areas with a high density of interpreted faults are particularly highlighted.

3.3.3.4 Depositional mechanisms

The last component of the mineral system, depositional mechanisms and sites, was mapped using both direct evidence of uranium deposition and evidence for chemical gradients that could cause uranium deposition. The following criteria have been used:

- Direct evidence of uranium enrichment mapped from U^2/Th radiometric data. The process for developing this criterion is described in Section 3.2; and
- Chemical gradient sites.

Variations in U^2/Th radiometric data, which were used for direct evidence for uranium enrichment, are shown in Figure 3.3.22. In the basement, this parameter highlights areas along the southern margin of the Aileron Province, along the northern margin of the Musgrave Province, in the southeastern part of the Huckitta 1:250 000 sheet, in the southern Davenport Province and in the Reynolds Range area of the Aileron Province. In the overlying basins, the U^2/Th ratio highlights stratigraphically controlled zones within the northern Amadeus Basin. In the Ngalia Basin, the anomalies are less extensive and appear to be controlled by stratigraphy. However, the dataset used for this criterion only images surface variations, and does not indicate variations at depth.

Potential depositional sites at depth can be imaged by inverting aeromagnetic and gravity data to indicate the subsurface distribution of inferred magnetite (Figure 3.3.23) and inferred hematite (Figure 3.3.24). The inversions were undertaken in a 3D environment, and the centroid of cells indicating the presence of magnetite and hematite were buffered to a distance of 2.5 km. These

minerals are essential features of the alteration associated with IOCG deposits, and are indicators of potential for redox reactions involving Fe-oxides, which can deposit Cu, Au and uranium from oxidised fluids (e.g., Huston *et al*., 1993).

The estimates of a possible alteration assemblage in this study are conducted using the alteration cone concept (Chopping and van der Wielen, 2009; 2011). Alteration cones are trends away from the properties of host (unaltered) rocks to alteration mineral(s). Trends in magnetic susceptibility and density, derived from 3D regular-mesh geophysical inversions of magnetic and gravity data in the study region (using the codes of Li and Oldenburg, 1996;1998) were used for the analysis. Alteration to different end-member mineral assemblages produces different trends, when viewed on crossplots of magnetic susceptibility versus density (Figure 3.3.25). The alteration systems associated with IOCG deposits are best characterised by examining trends to magnetite and to hematite or sulfides. Generally, magnetite alteration produces cells in the 3D inversions which are both significantly denser and more magnetically susceptible than expected for unaltered host rocks; likewise, hematite and sulfides (predominantly pyrite) will produce denser results when compared to the properties of unaltered host rocks.

It is apparent from Figure 3.3.25 that the alteration cones for both magnetite, and for hematite and sulfides overlap. Where very limited property contrasts between unaltered and altered rocks are observed, such as in this study, Euclidean distances have been calculated in magnetic susceptibility-density space to magnetite and hematite for each cell in the inversion results. Cells which are altered, but plot within both alteration cones with properties closer to magnetite are thus attributed to be altered to magnetite, whereas cells with properties closer to hematite are attributed to be altered to hematite or sulfides.

Both the inversions for magnetite and hematite (Figures 3.3.23 and 3.3.24 respectively) highlight similar areas, although there is more variability in the magnetite map. Areas highlighted include two areas along the southern margin of the Aileron Province (the far east and the centre-west), the northern margin of the Musgrave Province, and area in the southeastern part of the Tennant Region that extends to the Aileron Province.

Other chemical gradients have been mapped using the distribution of Fe-bearing formations (Figure 3.3.26). These units are restricted to the northwestern part of the study area and correspond to the distribution of Tanami Group equivalents (minor iron formation) and the very restricted distribution of the Peculiar Complex (abundant iron formation).

In composite, the depositional mechanisms system component highlights three main areas, two along the southern margin of the Aileron Province, and a third in the far east along the boundary between the Tennant Region and the Aileron Province (Figure 3.3.27). The highlighted areas along the southern margin of the Aileron provinces correspond to the far eastern and central-west areas identified in the magnetite (Figure 3.3.23) and hematite (Figure 3.3.24) inversion maps.

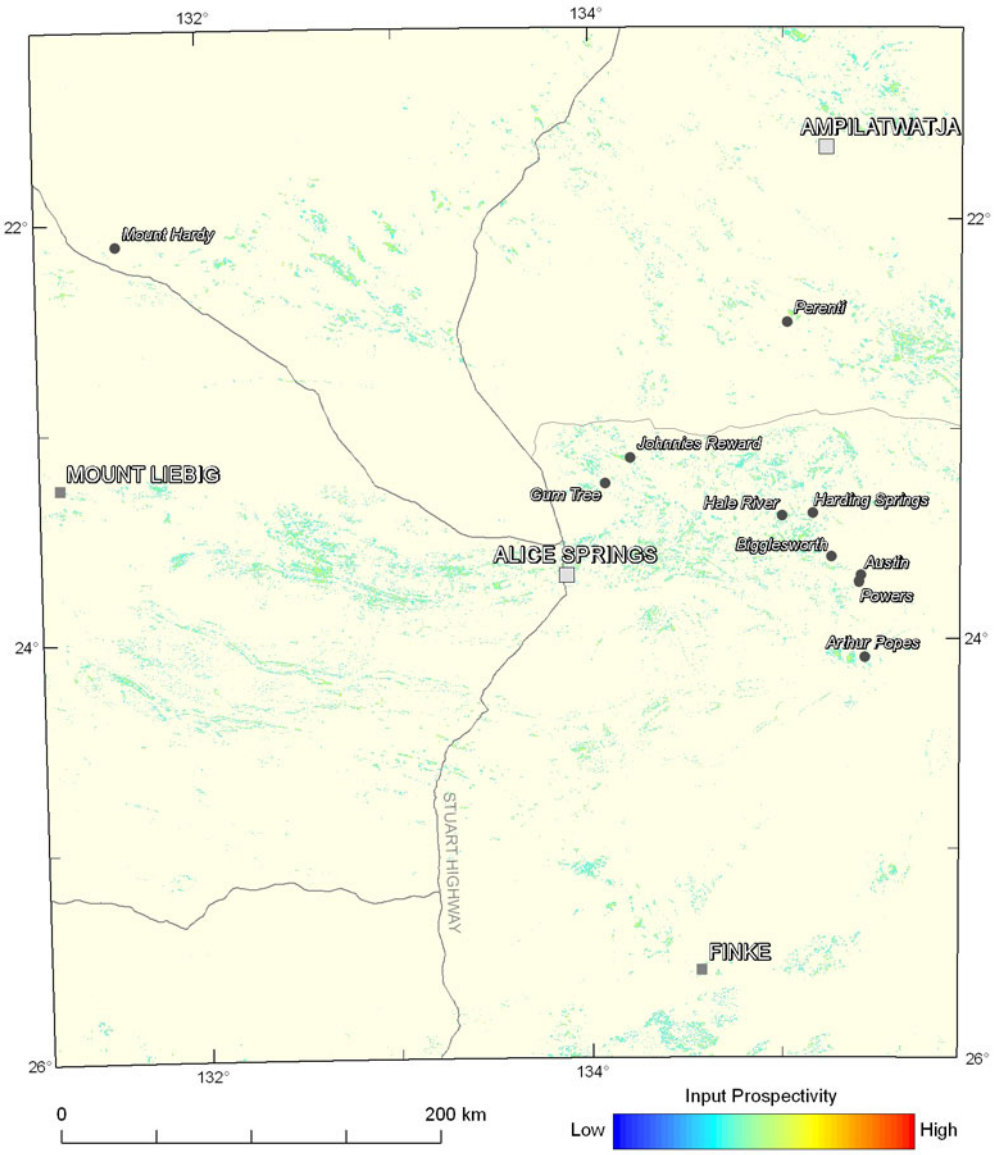

Figure 3.3.22: *Variations in the weighting for evidence of elevated uranium as determined from U^2/Th values from radiometric data. The colour stretch for the mappable criteria used in the assessment for uranium-rich iron oxide-copper-gold systems uses a numerical range from the minimum to the maximum weighting of all criteria used (0.004 to 0.560; see Table 3.3.2), and utilises 20 equal-interval breaks.*

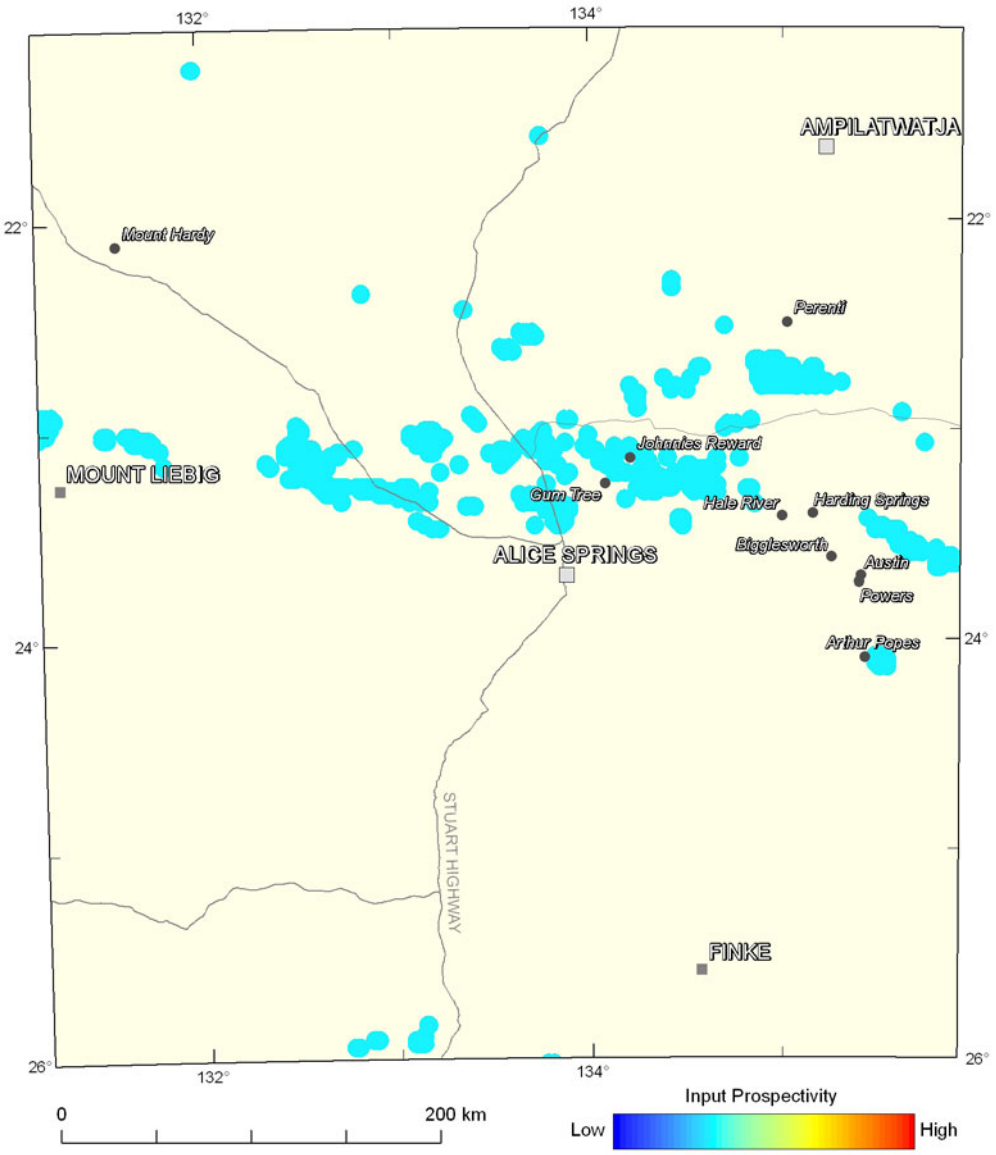

Figure 3.3.23: *Variations in the weighting for the distribution of magnetite-bearing alteration assemblages as determined from inversion model volumes from aeromagnetic and gravity data. The colour stretch for the mappable criteria used in the assessment for uranium-rich iron oxide-copper-gold systems uses a numerical range from the minimum to the maximum weighting of all criteria used (0.004 to 0.560; see Table 3.3.2), and utilises 20 equal-interval breaks.*

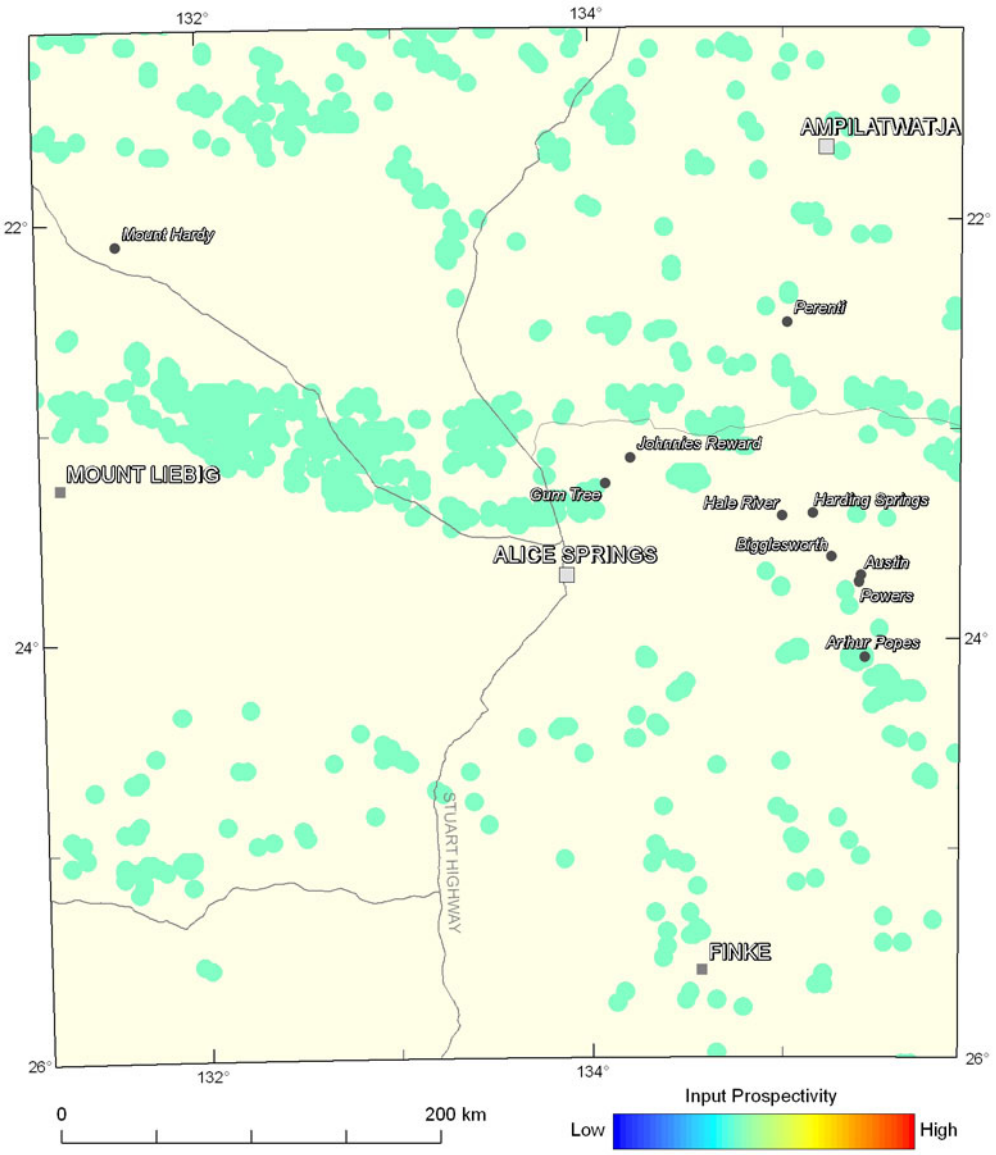

Figure 3.3.24: *Variations in the weighting for the distribution of hematite-bearing alteration assemblages as determined from inversion model volumes from aeromagnetic and gravity data. The colour stretch for the mappable criteria used in the assessment for uranium-rich iron oxide-copper-gold systems uses a numerical range from the minimum to the maximum weighting of all criteria used (0.004 to 0.560; see Table 3.3.2), and utilises 20 equal-interval breaks.*

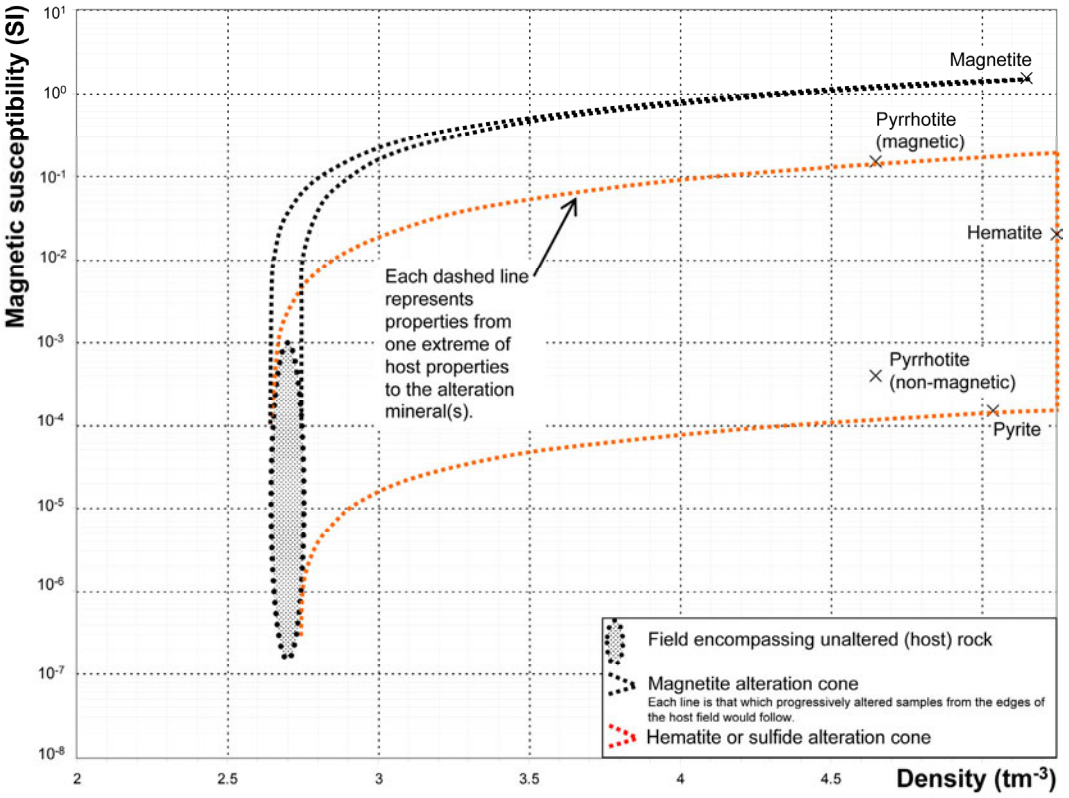

Figure 3.3.25: *Alteration trends to different end-member alteration minerals. In this example, alteration to magnetite versus alteration to either hematite or sulfides (such as pyrite or pyrrhotite) are shown.*

Figure 3.3.26: *Variations in the weighting from the distribution of ironstone-bearing units. The colour stretch for the mappable criteria used in the assessment for uranium-rich iron oxide-copper-gold systems uses a numerical range from the minimum to the maximum weighting of all criteria used (0.004 to 0.560; see Table 3.3.2), and utilises 20 equal-interval breaks.*

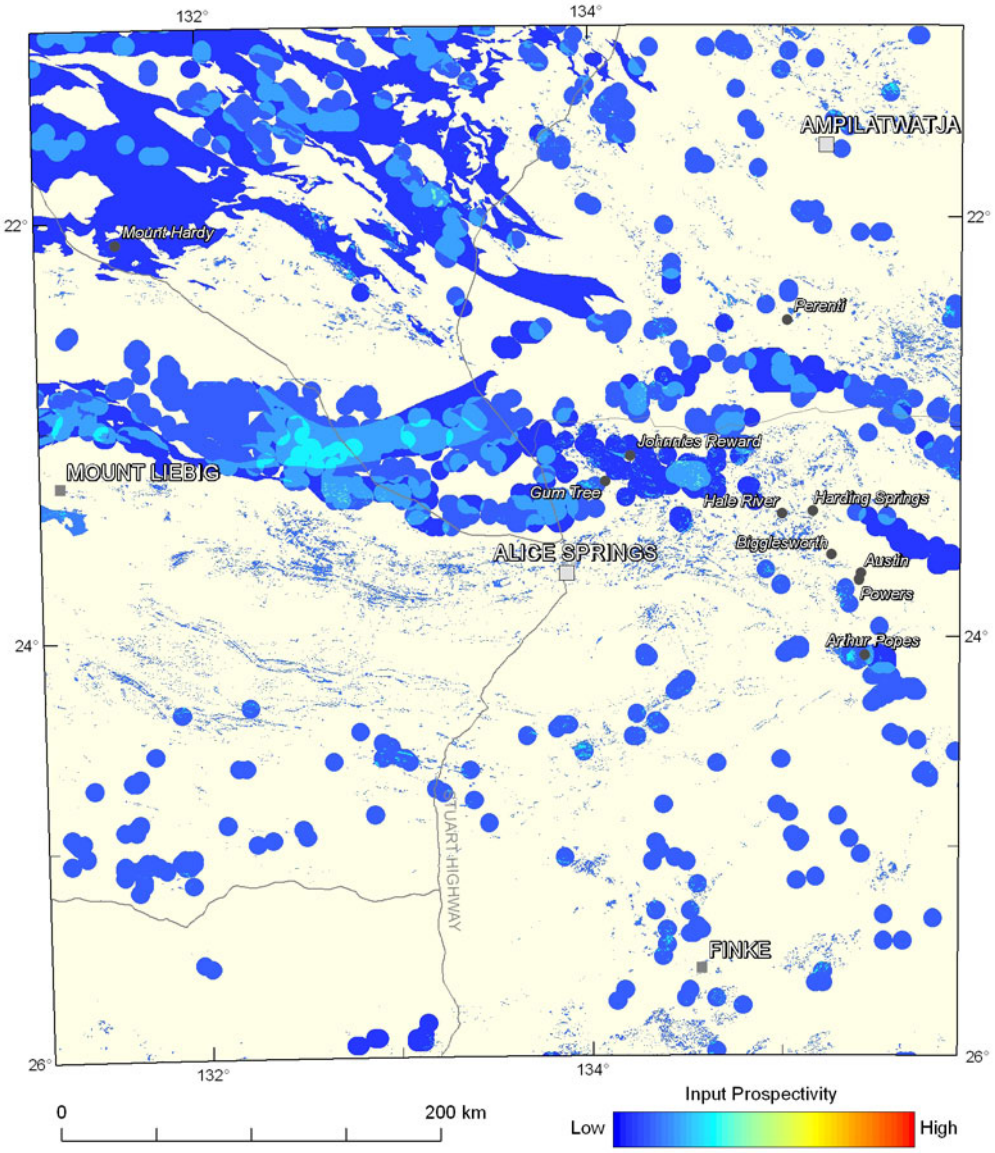

Figure 3.3.27: *Variation in the weightings for the depositional mechanisms system component for uranium-rich iron oxide-copper-gold systems. The colour stretch for each mineral system component in the assessment for uranium-rich iron oxide-copper-gold systems uses a numerical range from the minimum to the maximum weighting for each of the system components (0.001 to 0.496), and utilises 20 equal-interval breaks.*

3.3.4 Results

The modelled mineral potential for IOCG deposits in the study area is shown in Figure 3.3.28 and Plate 3.3. Six areas have been highlighted, as follows:

- An extensive area along the southern margin of the Aileron Province (A). This area appears to widen in the southeast where two zones of highest potential (A_1 and A_2) have been identified. The recently-discovered Powers, Austin and Bigglesworth prospects (described above) are located along the southern margin of zone A_1. The Johnnies Reward deposit is located to the northwest of zone A_1. Iron oxide-copper-gold prospects in the western Aileron Province, including Te Anau and Manapouri, are located to the west of the study area (not shown), along strike of area A. It is likely that area A extends along the entire length of the southern margin of the Aileron Province. Recent exploration in Western Australia in the western Aileron Province has identified Cu mineralisation north of the Aileron-Warumpi boundary at the Pokali and nearby prospects (http://www.ashmin.com.au);
- A small area along the southern margin of the Huckitta 1:250 000 map sheet (B). This area of potential extends known IOCG deposits in the Jervois district such as Bellbird outside of the study area (e.g., Figure 3.3.1);
- A moderate-sized area in the southern Davenport Province (C). This area contains the Silver Valley Pb-Ag veins;
- A small area in the very far southeast Davenport Province (D);
- A small area in the north-central Barrow Creek 1:250 000 map sheet (E). This area of potential includes a number of small vein Cu-Ni prospects that are hosted in dolerite (e.g., Camel Bore and Mt Strzeleckie); and
- A moderate-sized area that includes the Reynolds Ranges (F). This area contains a number of small vein-related Cu-Au occurrences (e.g., White Yard Hill, Copper Show and Reward), and several unnamed uranium-, Th-, REE- and fluorite-bearing occurrences are present just to the northeast of this area.

These areas should be considered to have potential for both uranium and Cu. Other areas not highlighted in Figure 3.3.28 may have potential for one or both of these commodities based upon other mineral system models. It must be noted that in some IOCG systems Cu and uranium are not coincident.

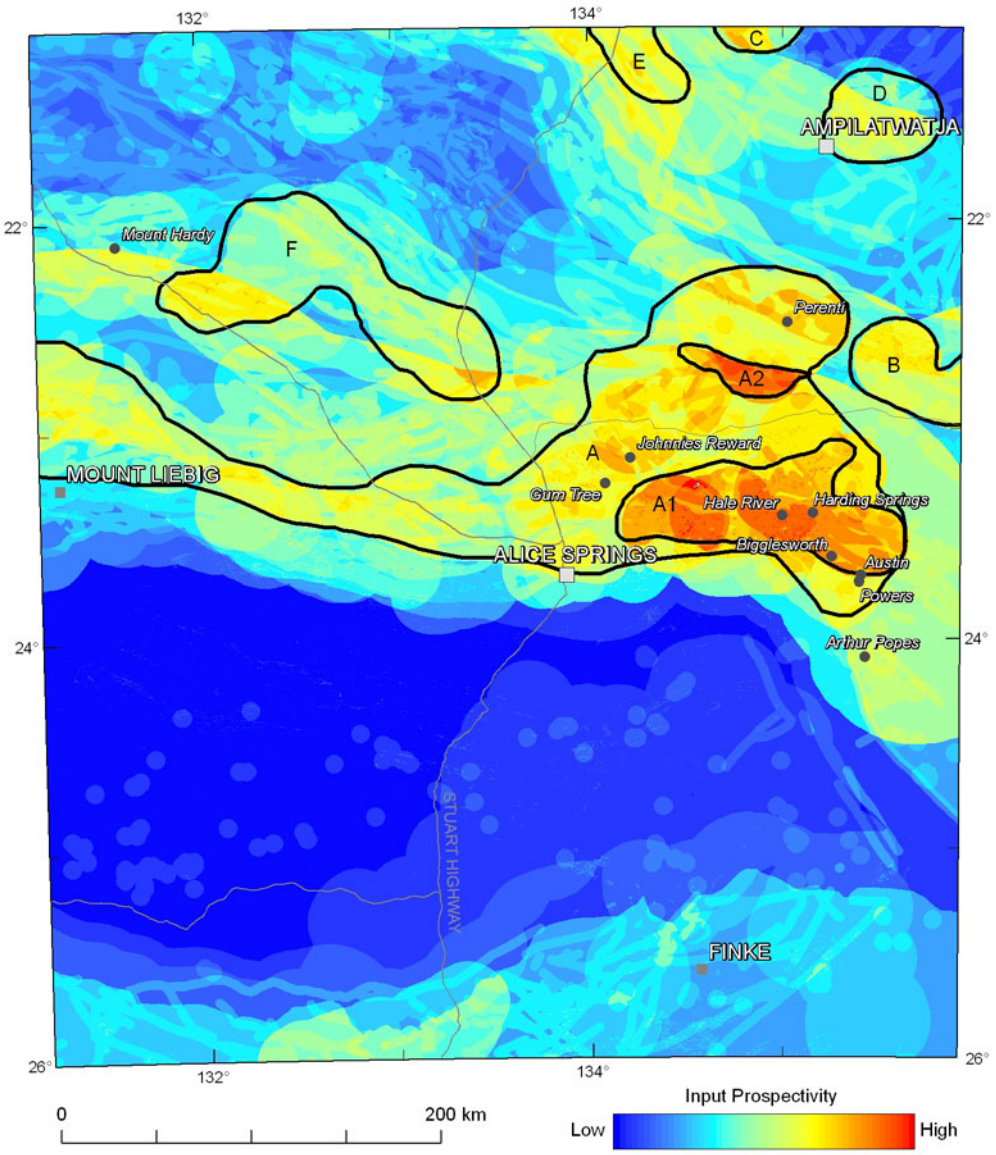

Figure 3.3.28: *Map showing interpreted prospectivity for uranium-rich iron oxide-copper-gold deposits in the southern Northern Territory and the location of known IOCG deposits and prospects. The colour stretch used for this figure has a minimum value of 0.0001 and a maximum value of 0.326, and utilises 20 equal-interval breaks. Areas outlined in black are discusses in Section 3.3.4.*

3.4 UNCONFORMITY-RELATED URANIUM SYSTEMS

T.P. Mernagh and R.G. Gallagher

Unconformity-related uranium systems are the largest known high-grade uranium deposits, and currently constitute approximately 33% of the western world's uranium resources (World Nuclear Association, 2010). All unconformity-related uranium deposits currently being exploited occur in the Athabasca Basin in Canada or the Kombolgie sub-basin, which is a constituent of the McArthur Basin in northern Australia.

Cuney (2010) has defined four major periods of uranium deposition throughout Earth's history. Unconformity-related uranium deposits occur in the third period which began with the strong increase in oxygen content of the atmosphere at around 2200 Ma, making possible the oxidation of U^{4+} to U^{6+}. These deposits formed mainly after 1750 Ma during a long period of relative tectonic quiescence recorded by numerous highly oxidised (red bed) intracontinental siliciclastic basins of broad geographic extent. The unconformity-related deposits are hosted either within the basement to these basins or just above the unconformity in the overlying sediments. Most of the basins that still exist are approximately one to three kilometres thick, flat lying, unmetamorphosed and pervasively altered. When preserved, the sedimentary units of these basins are mainly fluvial sandstone sequences which overly basement rocks that have been paleoweathered, with variable preservation of a clay-altered, hematitic regolith grading down through a chloritic zone into fresh rocks. However, the basin fill can be absent and completely removed by erosional processes (Cuney, 2010).

Although the formation of the major unconformity-related uranium deposits may be related to the initial oxygenation of the Earth's atmosphere, a second oxygenation event occurred at about 600 Ma, as indicated by the colonisation of the oceans by animal life (Farquhar *et al*., 2010). This resulted in the development of new sedimentary successions comprising alternating oxidised and reduced layers which became the major setting for some sandstone-hosted uranium deposits (Cuney, 2010). However, these basins still retain all the parameters needed for the formation of unconformity-related deposits. Therefore, we have assessed the prospectivity of the study area for the existence of unconformity-related uranium deposits over two time periods: the Precambrian and the Phanerozoic. The former accounts for the main period of unconformity-related mineralisation while the latter eon, which commenced at 542 Ma, covers most of the period after the second oxygenation event and explores the potential for this style of mineralisation in younger host rocks.

3.4.1 Deposit overviews

The unconformity-related uranium deposits in the Northern Territory constitute a major proportion (19%) of Australia's total uranium resources (Lambert *et al*., 2005), and since 1980, most of this uranium has been mined from two deposits — Nabarlek (now mined out) and Ranger 1 and 3. Unconformity-related uranium deposits are known to occur in the Alligator Rivers Uranium Field (e.g. Nabarlek and Ranger), and the South Alligator Valley (e.g. Coronation Hill) in the northern part of the McArthur Basin, while a similar style of mineralisation associated with intrusive units occurs in the Westmoreland region in the southern McArthur Basin.

3.4.1.1 Prospects within the study area

While there are no known unconformity-related uranium deposits in the study area, the Albarta and Tourmaline Gorge prospects have some characteristics of other unconformity-related uranium deposits. They occur in metamorphosed rocks of the Aileron Province near the interface between the Aileron Province basement rocks and the unconformably overlying Heavitree Quartzite of the Amadeus Basin.

During the late 1970s Esso Australia Limited's exploration program in the southern Harts Range area identified minor uranium mineralisation at Albarta and Tourmaline Gorge. The Albarta prospect (Figure 3.4.1) occurs below an unconformity with overlying Heavitree Quartzite. At surface, the mineralised shear zone is approximately three to four metres wide and consists of an inner strongly silicified zone and an outer chlorite-rich zone with minor pyrite. Quartz veins within the shear zone are 1–20 mm thick and are highly irregular. The veins cut the fabric and are folded by the fabric suggesting a syn-kinematic timing (D. Huston, *pers. comm.*). A 400 m by 100 m uranium anomaly has been delineated at Albarta, with surface samples containing up to 0.9% uranium hosted within the shear zone in adjacent quartzo-feldspathic gneiss. (Western Desert Resources Ltd. Annual Report, 2011).

The Tourmaline Gorge prospect (Figure 3.4.1) is located in sheared, sericitised and chloritised, 1730–1720 Ma, tourmaline-rich granite of the Atneequa Granitic Complex (Lally and Bajwah, 2006, Whelan *et al*., 2011). Although the prospect is in close proximity to the Albarta prospect, its host rocks suggest that it may have affinities with magmatic-related uranium systems rather than unconformity-related systems. Detailed radiometric surveys have outlined a 600 m by 100 m uranium anomaly, which has currently not been drilled. Other exploration work targeting unconformity-related uranium was undertaken by PNC Exploration between 1992 and 1996, which identified a number of other prospects, most of which are located on the margin of the Entia Dome.

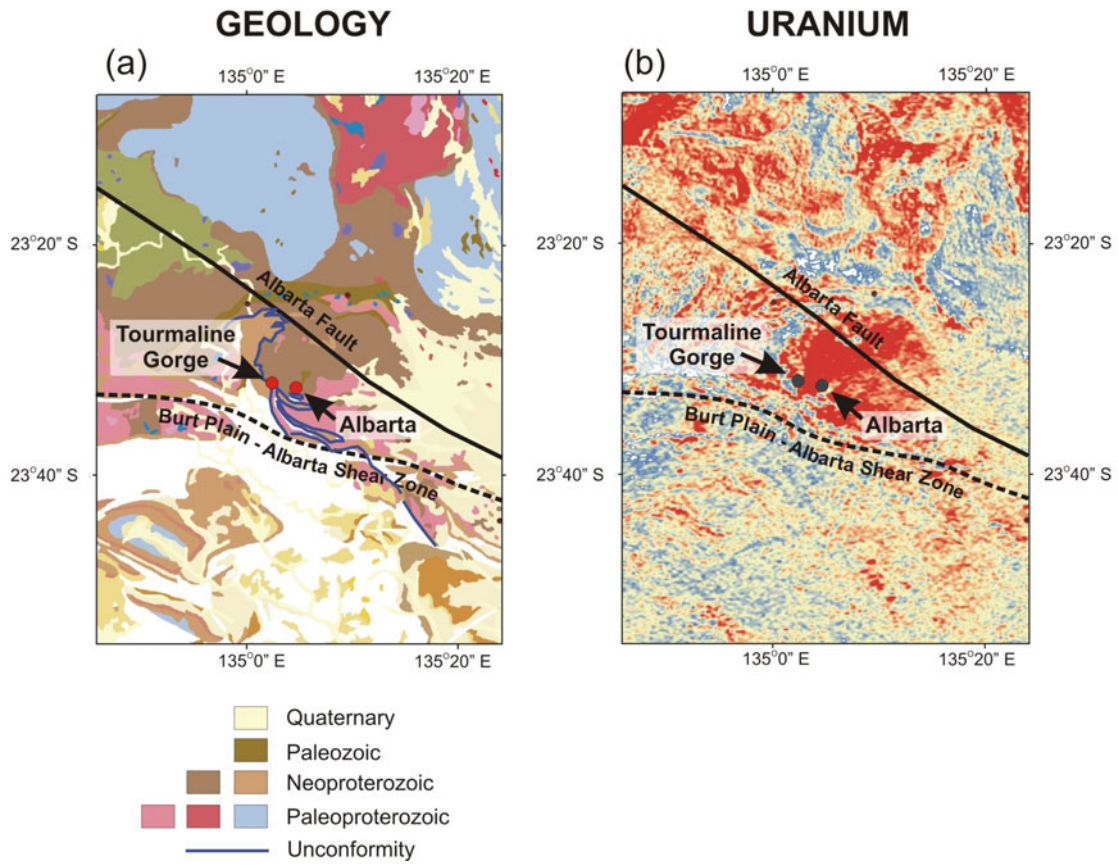

Figure 3.4.1: *(a) Geological setting of the Albarta and Tourmaline Gorge uranium prospects showing their proximity to regional unconformities, and (b) uranium concentration map from the airborne radiometric survey over this area (modified from Western Desert Resources Ltd Annual Report, 2007).*

3.4.1.2 Unconformity-related uranium deposits in Australia

The northern McArthur Basin includes the Kombolgie sub-basin which overlies steeply-dipping Paleoproterozoic metasedimentary basement. The Kombolgie Subgroup consists of sandstone and conglomerate, and interlayered volcanic units of the Nungbalgarri Formation and Gilruth Member. The sediments of the Kombolgie Subgroup were deposited in fluvial and eolian environments with occasional marine incursions that deposited marine sandstone and evaporites. Marine conditions dominated in the McKay Formation, as suggested by the presence of glauconite, halite crystal casts, and wave ripple marks in sandstone. Sandstone of the McKay Formation shows minimal diagenesis relative to the rest of the units in the Kombolgie Subgroup (Lally and Bajwah, 2006). Economic deposits of uranium have primary mineralisation ages of 1675–1650 Ma (Maas, 1989; Polito *et al*., 2005a, b), and are hosted in Paleoproterozoic basement rocks, but near the unconformity with the overlying Kombolgie Subgroup.

3.4.1.2.1 Ranger

The Ranger 1 and 3 orebodies are located 10 km east-southeast of the township of Jabiru. Although the Kombolgie Subgroup is not present in the region of the Ranger orebodies, the deposits lie within a few hundred metres below the unconformity at the base of the Kombolgie Subgroup (Lally and Bajwah, 2006). The deposits occur in the lower member of the Cahill Formation, close to the contact with the underlying Nanambu Complex. Quartz-feldspar-tourmaline pegmatite bodies intrude mine sequence rocks which also include dolerite dykes, veins or blocks interpreted to be the same age as the ~1720–1690 Ma Oenpelli Dolerite (Lally and Bajwah, 2006). The primary uranium mineralogy in both orebodies consists of uraninite or pitchblende, with some coffinite and minor brannerite and curite. Mineralisation generally occurs as subhedral to euhedral uraninite grains, often pitted, with chlorite or quartz inclusions, and as granular masses, and as veins and veinlets of variable thickness (Lally and Bajwah, 2006).

Lithologies within the mine lease area have been informally subdivided into the footwall (FWS), lower mine (LMS), upper mine (UMS) and hangingwall sequences (HWS) by mine geologists. The dominant feature is a synformal structure, or basin, formed by the thinning of LMS carbonate, relative to UMS rocks. Upper mine sequence rocks within the synform are extensively brecciated, particularly near the UMS–LMS contact, and the contact itself is folded (Lally and Bajwah, 2006).

3.4.1.2.2 Jabiluka

The Jabiluka 1 and Jabiluka 2 orebodies are located 20 km north of Jabiru, on the edge of an outlier of Mamadawerre Sandstone. Mineralisation is hosted by shallow- to steeply-dipping Paleoproterozoic basement rocks comprising graphitic units of chlorite-biotite-muscovite schists belonging to the Cahill Formation (Lally and Bajwah, 2006). These rocks are overlain by the Mamadawerre Sandstone, which is the lowest unit of the Kombolgie Subgroup. The uranium mineralisation is structurally controlled within brittle shears that are subconformable to the basement stratigraphy, and breccia that is developed within the hinge zone of fault-related folds adjacent to the shears (Polito *et al*., 2006).

Alteration associated with mineralisation can be loosely divided into an outer and inner halo, with the main difference being an increase in chlorite and sericite associated with brecciation in the inner halo (Lally and Bajwah, 2006). The alteration halo extends at least 200 m beyond known uranium mineralisation (Lally and Bajwah, 2006). Mineralisation is dominated by uraninite, which is intimately associated with chlorite, sericite and hematite (Polito *et al*., 2006). The mineralised breccia is cross-cut by an unmineralised breccia cemented by chlorite, quartz and sericite which is in turn cut by straight-sided, high-angle veins of drusy quartz, sulfide and dolomite. Drusy quartz ± dolomite ± pyrite ± chalcopyrite veins also occur in the basement units and overlying sandstone (Polito *et al*., 2006).

3.4.1.2.3 Nabarlek

Mineralisation at Nabarlek is hosted within altered amphibolite and metapelitic rocks that were previously included within the Myra Falls Metamorphics, but which are now considered part of the Nourlangie Schist (Hollis and Glass, 2012). The mine succession comprises about 200 m of muscovite-quartz-biotite schist ('Pelitic Schist') which is overlain by 100 m of interlayered hornblende amphibolite and muscovite-biotite-quartz schist ('Footwall Amphibolite'), which is in turn overlain by biotite-muscovite-quartz and feldspar schist ('Hanging Wall Schist'). Rare quartz-feldspar-muscovite-tourmaline pegmatite veins intrude the schist and amphibolite units. Although now eroded from above the deposit, sandstone of the Kombolgie Subgroup forms escarpments 1.5 km to the north and south, and from extrapolation, the unconformity was about 50 m above the current ground surface.

High-grade ore is confined to the Nabarlek fault, a reverse fault/shear zone that cross-cuts a series of interbedded muscovite-quartz-biotite schists and amphibolites. Primary ore is restricted to deeper parts of the orebody, and is composed of uraninite and rare brannerite in a gangue of magnesian chlorite, anatase with rare hematite, apatite and illite-sericite (Lally and Bajwah, 2006). Uraninite occurs as fine disseminations or veins and veinlets, which are anastomosing or reticulate in character but some massive or colloform uraninite also occurs in the upper part of the orebody due to remobilisation of uranium (Polito *et al*., 2004). In the upper parts of the orebody, uraninite is replaced by coffinite as the predominant uranium-bearing mineral. Gangue minerals include mostly fine grained illite and hematite (Polito *et al*., 2004). Weathered ore near the surface contains sklodowskite, rutherfordine, kasolite and curite in a matrix of illite, kaolinite, anatase and hematite. Torbernite and autunite occupy open fractures that cross-cut all other features and represent the most recent remobilisation of uranium (Wilde and Wall, 1987).

3.4.1.2.4 Westmoreland mineral field

The Westmoreland mineral field is located near the south-eastern margin of the Paleoproterozoic to Mesoproterozoic McArthur Basin. The northern and southern ends of the McArthur Basin share numerous geological attributes, including similar stratigraphic rock types and metal inventories. The three largest deposits in the Westmoreland mineral field are Redtree, Hurabagoo and Junnagunna (Figure 3.4.2) which together have a collective Inferred and Indicated resource of 23.6 kt U_3O_8 (Laramide Resources Press Release 23/04/2009).

The Redtree deposit flanks the Redtree dyke zone immediately north of the northwest-trending Namalangi Fault (Figure 3.4.2). It comprises stratiform and discordant uranium mineralisation with grades ranging from 0.15 to over 2% U_3O_8 in four lenses (Rheinberger *et al*., 1998). Stratiform mineralisation up to 15 m thick is hosted entirely within the Westmoreland Conglomerate just below the Seigal Volcanics. Vertically discordant mineralisation occurs in the Westmoreland Conglomerate and dolerite of the Redtree dyke zone and may be up to 40 m thick.

The Junnagunna deposit occurs at a fault intersection west of the Redtree dyke zone and south of the north-west trending Cliffdale Fault (Figure 3.4.2). Uranium mineralised zones in the Junnagunna deposit are predominantly flat-lying and concentrated within the upper unit of the Westmoreland Conglomerate, just below the Seigal Volcanics. Minor discordant mineralisation occurs within the Westmoreland Conglomerate adjacent to the Redtree dyke zone. The stratiform mineralisation is 0.5 m to 10 m thick and grades from ~0.3 to 1% U_3O_8. Limited mineralised zones also occur on the northern side of the Cliffdale Fault and the eastern side of the Redtree dyke zone.

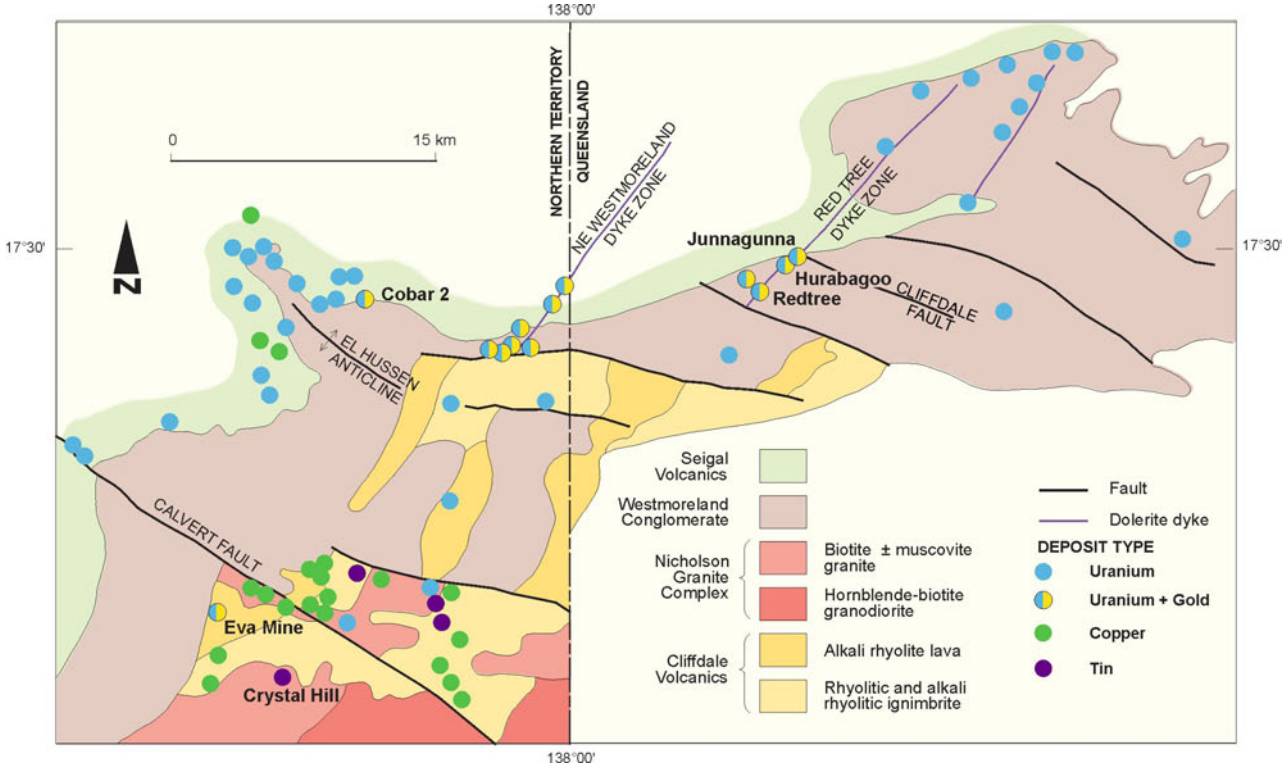

Figure 3.4.2: *Geological setting of mineral deposits and mineral occurrences in the Westmoreland uranium field (modified from Lally and Bajwah. 2006).*

The Hurabagoo deposit is located approximately three kilometres north-east of the Redtree deposit (Figure 3.4.2) and is a zone of vertical mineralisation in a structurally complex area of the Redtree dyke zone. In this zone there were multiple injections of smaller dykes (steeply dipping and horizontal) associated with the two main vertical dykes. Most of the mineralisation is within the Westmoreland Conglomerate adjacent to the dykes and the remainder is in the dykes. No grades are available for Hurabagoo but it is thought to be geologically similar to the Redtree deposit (Laramide Press Release 23/04/2009).

3.4.1.2.5 Kintyre

The Kintyre deposit is another unconformity-related uranium deposit in northern Australia. Kintyre is located about 500 km south-east of Port Hedland, Western Australia. The deposit is hosted by metasediments of the Yandagooge Formation of the Rudall Complex, and is adjacent to the unconformity with the Neoproterozoic Coolbro Sandstone (Jackson and Andrew, 1990; Hickman and Clarke, 1994). The host metasedimentary rocks originally consisted of limestone, black shale, sandy shale, sandstone and iron formation. The unconformable contact with the Coolbro Sandstone and Rudall Complex is tightly folded and sheared at the deposit, which is hosted by sheared and altered chlorite-garnet-quartz schists in contact with metadolomite and graphitic schist of the Yandagooge Formation (Figure 3.4.3). Permian glacial tillite beds overlie the eastern portion of the Kintyre deposit.

Uranium occurs mostly as pitchblende in a series of narrow, closely-spaced carbonate-chlorite veins (McKay and Miezitis, 2001). The veins are hosted by chlorite-quartz schist, chlorite-carbonate quartz schist and chloritic and garnetiferous quartzite (Jackson and Andrew, 1990), which form a stratigraphic unit that is structurally overlain by dolomite and underlain by biotite-graphite schist (McKay and Miezitis, 2001; Figure 3.4.3). Although the host unit contains a wide variety of rock types, the more competent siliceous chloritic and garnetiferous quartzite preferentially host the

uraniferous veins (Root and Robertson, 1994). The host rocks are extensively chloritised, with primary garnet totally altered to chlorite near mineralised zones. Other alteration minerals include carbonate and martite (hematite), which replaces magnetite. The veins are dominated by a chlorite-carbonate assemblage. Colloform pitchblende is the dominant ore mineral, with minor bismuthinite, chalcopyrite, bornite and galena, and trace native Bi and Au. Platinum group elements have also been noted with Au, which has a geochemical association with Cu and Bi (Jackson and Andrew, 1990). Small quantities of pitchblende are also present as microscopic disseminated grains in the wall rock, although this style of mineralisation is much lower grade than the vein-hosted style, and forms only a minor part of the total resource (Jackson and Andrew, 1990).

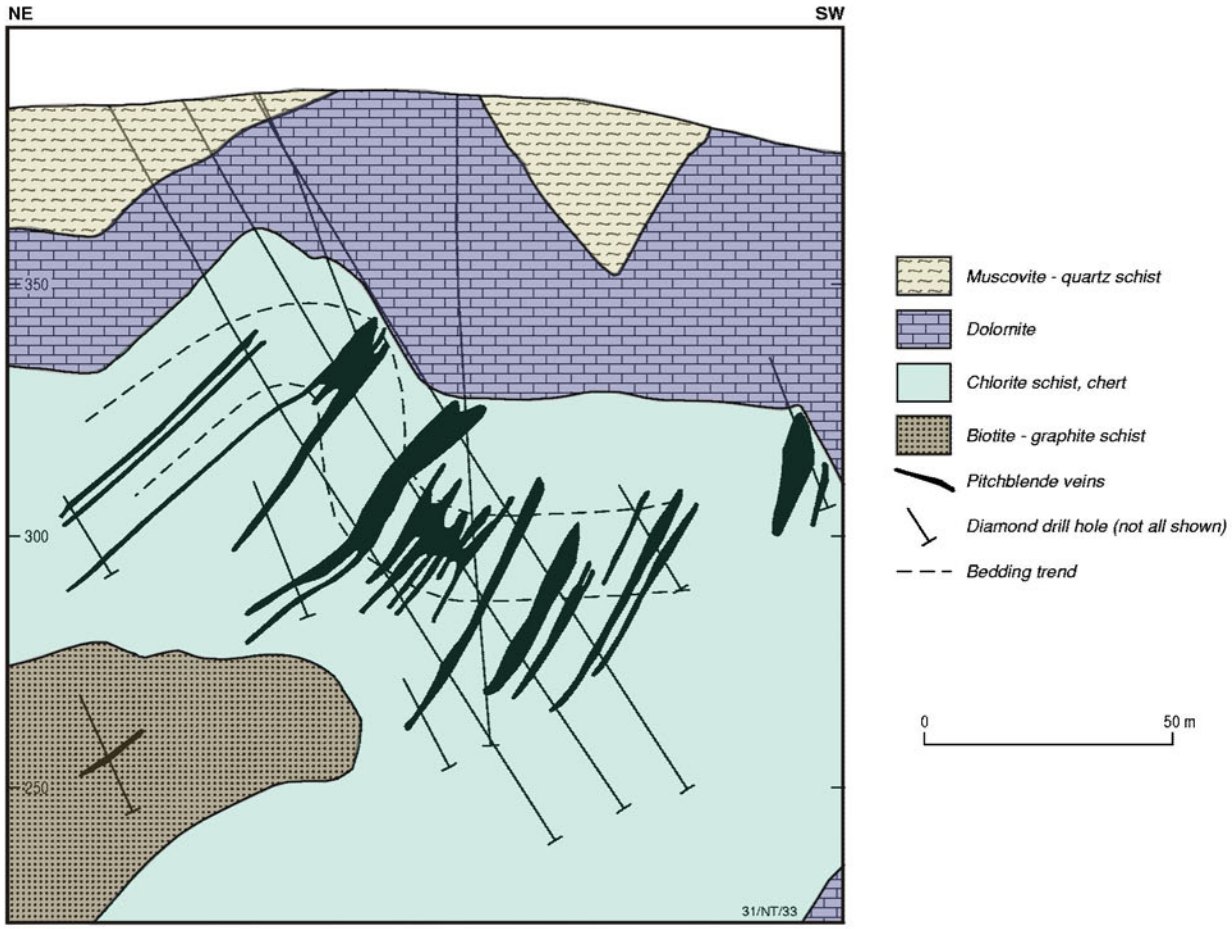

Figure 3.4.3: *Geological cross section of the Kintyre uranium deposit (modified from McKay and Miezitis, 2001, after Gauci, 1997).*

3.4.2 Mineral system model for unconformity-related uranium systems

In the classification scheme of Skirrow *et al*. (2009; Figure 3.1.1) unconformity-related uranium deposits belong to the basin-related family of uranium systems, as they involve mixing of fluids derived from dehydration reactions during metamorphism and/or diagenesis and surface-derived fluids. Mernagh *et al*. (1998) previously defined the essential components associated with some of the unconformity-related uranium deposits in the McArthur Basin in the Northern Territory. The following discussion describes the key features of the unconformity-related mineral system model used in this study.

Current models for the formation of unconformity-related uranium deposits can be divided into two general types. The first involves the basement as the source of uranium and the basins as the source of

the fluids (e.g., Johnston, 1984; Mernagh *et al*., 1994; Cuney *et al*., 2003; Derome *et al*., 2005). The second involves the overlying basin as a source for both the uranium and fluids (e.g. Hoeve *et al*., 1980; Ruzicka, 1993; Kyser, 2007). In the first model, uranium is sourced from the breakdown of monazite along fault zones as basinal brines interact with the basement. Uranium is precipitated when the oxidised fluid carrying uranium interacts with a reduced basement lithology (Hoeve *et al*., 1980), encounters reductants in the basin such as volcanic units (Ahmad and Wygralak, 1990), or mixes with reduced fluids derived from the basement (Johnston, 1984; Mernagh *et al*., 1994). In some cases, fluid interaction with feldspathic or calcareous rocks may cause only a moderate increase in pH and a decrease in the oxidation state (fO_2), leading to precipitation of other metals (e.g., Au and PGEs), but little or no uranium (e.g., the Coronation Hill deposit; Mernagh *et al*., 1994).

In the second model, uranium is sourced from the breakdown of uranium-bearing detrital minerals such as monazite, zircon, phosphates, tourmaline and uraninite by basinal fluids in deep basin paleoaquifers (e.g., Hoeve *et al*., 1980; Ruzicka, 1993; Kyser, 2007). These fluids flow laterally along paleoaquifers, but may also flow downward due to the higher density of the highly saline fluid. Some models allow part of the fluid to enter faults and fracture zones in the basement rocks and thus become reduced before ascending again along faults and fractures, where it mixes with laterally moving oxidised fluids. Precipitation of the uranium (and other metals) takes place at the interface between the oxidising and reducing fluids. High-grade uranium or polymetallic mineralisation forms directly at the unconformity. Medium-grade uranium mineralisation may form below the unconformity and low-grade uranium mineralisation may form within the overlying sediments at some distance above the unconformity.

Migration of oxidised, uranium-bearing fluids in deep basinal settings may be driven by gravity (topography or salinity-related density controls), diagenesis/compaction, convection/temperature variations or tectonic processes such as basin inversion. During basin inversion, fluid flow patterns will be significantly different, and in some cases reversed, relative to directions during extension. Switches in fluid-flow direction may be partly responsible for the variations in local settings and characteristics of basement-hosted versus basin-hosted styles of unconformity-related uranium deposits. Additionally, the role of basement fluid in unconformity-related systems may vary in importance with switches in fluid flow direction (Cuney *et al*., 2003). Paleomagnetic studies in the McArthur Basin also support a link between tectonic processes and uranium mineralisation in that setting. Changes in the apparent polar wander path at 1640–1680 Ma (Idnurm, 2000) correspond with uranium mineralisation ages, suggesting that these tectonic processes may have stimulated fluid flow in the McArthur Basin.

Diagenesis and concurrent compaction of basinal sediments was also an important driver of fluid flow in these basins. The ages of diagenetic phases extracted from aquifer lithologies reveals that fluid migration in the diagenetic aquifers effectively covers the period of formation of unconformity-related uranium deposits (Polito *et al*., 2006). Sequence stratigraphic analysis and models of fluid flow also indicate that basinal reservoirs were likely sources for mineralising fluids (Kyser, 2007). Thus, diagenetic aquifer lithologies were being drained of fluids at the same time as the deposits were forming from fluids that were chemically and isotopically similar, thus linking diagenesis and fluid flow events within the basins to the formation of the unconformity-related uranium deposits.

Unconformity-related uranium systems are generally located in intracratonic, epicontinental or foreland basins which unconformably overly uranium-rich basement rocks. A critical element in these systems is a major disconformity (generally an unconformity) between the basement containing relatively reduced rocks and the overlying basin which contains oxidised, highly permeable sedimentary rocks. There is often an onlapping relationship between the basin and basement. Periodic reactivation of basement faults during and after basin development creates the faults and architecture for later fluid-flow pathways. The faults generally exhibit relatively small displacement (less than a few hundred metres) and form conjugate networks but may include fault strands with strike lengths of tens to hundreds of kilometres. The deposits sometimes also show a

close association with gravity highs and/or ridges which may reflect major structures in the basement that control later fluid flow in the system.

The migration of fluids into deep basinal settings requires particular geological architectures to maintain the high oxidation state necessary for the transport of uranium. The fluids may be buffered and/or maintained at high oxidation states by the presence of Fe^{3+}-bearing minerals such as hematite and goethite, or by sulfate minerals, provided that reductants are in low abundance. Thus, red bed and/or evaporate-bearing sequences may be favourable reservoirs for the storage of oxidised fluids deep within basins. Fluid-flow pathways are influenced by the formation of aquifers and aquitards during diagenesis, and other lateral and vertical variations in permeability caused by faulting and shearing during episodes of basin extension and basin inversion. The aquifers are typically defined by illite-kaolinite alteration or hematite-bearing oxidised assemblages whereas aquitards are typically associated with intense silicification. Basement penetrating faults are often defined by illite-kaolinite and/or chloritic alteration.

Uranium has the ability to complex with a large number of ligands depending on the pH and oxidation state of the fluid. Uranium is deposited from oxidised fluids when they come in contact with reductants in the basin or in the basement rocks. Examples of possible reductants include carbonaceous shales, Fe^{2+}-rich rocks, hydrocarbons and H_2S in reduced fluids (Bastrakov *et al*., 2010). Zones of faulting and brecciation, particularly in the basement, are important for focusing the fluids and enhancing their interaction with reduced rock assemblages. There is also a general association of calcareous rocks with reduced rocks in the basement which may indicate that changes in pH are also important during the depositional process.

As most unconformity-related uranium deposits occur close to the basal unconformity between the sedimentary basin and the basement rocks there is a good chance of preservation for this style of mineralisation. Most of the basins that still exist are one to three kilometres thick, flat-lying and essentially unmetamorphosed. However, in some cases, the basin fill can be absent, having been removed by erosion, leaving the basement rocks outcropping at the surface and exposing the ore to possible leaching by surface waters.

3.4.3 System components and mappable criteria

As mentioned above, the potential of the study area for unconformity-related uranium deposits has been carried out for two time periods: the Precambrian and the Phanerozoic. The former accounts for the main period of known unconformity-related mineralisation and the latter explores the potential for this style of mineralisation in younger host rocks. The criteria used in each of these time slices overlap, and hence they will be discussed together. In many cases, the criteria used are identical, while in others they vary only in detail. The criteria used are listed in Tables 3.4.1 and 3.4.2.

3.4.3.1 Sources

There are two main models for potential metal and fluid sources in unconformity-related uranium systems. The first involves the basement as the source of uranium and the basins as the source of the fluids and in the second model the source of uranium is from the breakdown of uranium-bearing detrital minerals from within the basin. In both cases the uranium is thought to be transported in highly saline basinal fluids. Three criteria have been used to map the sources system component:

- Uranium-rich igneous rocks in the basement;
- Uranium-rich sedimentary rocks belonging to each time slice; and
- Evaporitic units, which may represent production of basinal brines.

Table 3.4.1: Theoretical and mappable criteria for unconformity-related uranium in the Precambrian Eon

MINERAL SYSTEM COMPONENT	CRITERIA		DATASET	IMPOR-TANCE	APPLIC-ABILITY	CONFI-DENCE	WEIGHTING	COMMENTS
	THEORETICAL	MAPPABLE						
Source	Presence of U-enriched igneous rocks	10 km buffer around U-enriched basement rocks	Radiometric map of Australia (Minty *et al*., 2010); geochemical data; basement solid geology (see Appendix 1)	0.8	0.7	0.7	0.392	Presence of U-rich igneous rocks defined as greater than the 75th percentile for each rock class (intrusive and volcanic)
		30 km buffer around U-enriched basement rocks		0.8	0.5	0.7	0.280	
		100 km buffer around U-enriched basement rocks		0.8	0.3	0.7	0.168	
	Presence of U-enriched sediments of Precambrian age	Presence of U-enriched sediments of Precambrian age	Radiometric map of Australia (Minty *et al*., 2010); Surface geology of Australia (Raymond and Retter, 2010)	0.6	0.6	0.5	0.180	Presence of U-rich sediments of Precambrian age (see text for details)
	Presence of evaporite minerals of Precambrian age within lithological unit indicating production of basinal brines	Lithological units selected from the literature	Basin solid geology (see Appendix 1); literature review (see text for details)	0.5	0.4	0.6	0.120	Distribution of evaporite-bearing units or shallow water units of Precambrian age as cited in the literature
Drivers	Presence of thick, intracratonic, epicontinental or foreland basin of Precambrian age	Amadeus Basin	Provinces dataset	0.9	0.7	1.0	0.630	
		Amadeus Basin; 40 km buffer		0.6	0.5	1.0	0.300	
		Ngalia Basin		0.9	0.7	1.0	0.630	
		Ngalia Basin; 40 km buffer		0.6	0.5	1.0	0.300	
		Georgina Basin		0.9	0.7	1.0	0.630	
		Georgina Basin; 40 km buffer		0.6	0.5	1.0	0.300	
Fluid-flow pathways and architecture	Presence of unconformity in solid geology	Distribution of unconformities in solid geology; 10 km buffer	Basement solid geology (see Appendix 1)	1.0	1.0	0.7	0.700	Unconformities were interpreted from solid geology
		Distribution of unconformities in solid geology; 20 km buffer		1.0	0.6	0.7	0.420	
	Presence of unconformity in basins of Precambrian age	Amadeus Basin;10km buffer	Provinces dataset	1.0	0.8	1.0	0.800	
		Amadeus Basin; 20km buffer		1.0	0.6	1.0	0.600	
		Amadeus Basin; 40 km buffer		1.0	0.4	1.0	0.400	
		Ngalia Basin;10km buffer		1.0	0.8	1.0	0.800	
		Ngalia Basin; 20 km buffer		1.0	0.6	1.0	0.600	
		Ngalia Basin; 40 km buffer		1.0	0.4	1.0	0.400	
		Georgina Basin;10km buffer		1.0	0.8	1.0	0.800	
		Georgina Basin; 20 km buffer		1.0	0.6	1.0	0.600	
		Georgina Basin; 40 km buffer		1.0	0.4	1.0	0.400	
	Distribution of extensional faults	Barramundi Extension; 2.5 km buffer	OZ SEEBASE™ Study, 2005	0.7	0.5	0.5	0.175	
		Post-Barramundi Extension; 2.5 km buffer		0.7	0.5	0.5	0.175	
		Leichardt Extension; 2.5 km buffer		0.7	0.5	0.5	0.175	
		Calvert Extension; 2.5 km buffer		0.7	0.5	0.5	0.175	
		Musgrave Event; 2.5 km buffer		0.7	0.5	0.5	0.175	
		Warakurna; 2.5 km buffer		0.7	0.5	0.5	0.175	
		Centralian; 2.5 km buffer		0.7	0.5	0.5	0.175	
	Evidence of oxidised fluids leading to demagnetisation of rock units	Demagnetised zones - magnetic data one standard deviation below mean for the study area	Magnetic anomaly map of Australia (Milligan *et al*., 2010)	0.5	0.3	0.8	0.120	
		Demagnetised zones - magnetic data two standard deviations below mean for the study area		0.5	0.5	0.8	0.200	

Table 3.4.1 (cont'd): Theoretical and mappable criteria for unconformity-related uranium in the Precambrian Eon

MINERAL SYSTEM COMPONENT	CRITERIA		DATASET	IMPOR-TANCE	APPLIC-ABILITY	CONFI-DENCE	WEIGHTING	COMMENTS
	THEORETICAL	MAPPABLE						
Depositional mechanisms	Direct evidence of elevated U	U^2/Th values one standard deviation above the mean for each unique geological unit	Radiometric map of Australia (Minty *et al*., 2010); Surface geology of Australia (Raymond and Retter, 2010)	0.7	0.6	0.6	0.252	
		U^2/Th values two standard deviations above the mean for each unique geological unit		0.7	0.8	0.6	0.336	
	Thorium enrichment that may indicate uranium deposition at depth	Thorium radiometric data one standard deviation above mean for the study area	Radiometric map of Australia (Minty *et al*., 2010); Surface geology of Australia (Raymond and Retter, 2010)	0.4	0.5	0.5	0.100	
		Thorium radiometric data two standard deviations above mean for the study area		0.4	0.7	0.5	0.140	
	Redox gradients along and below basal unconformity	Carbonaceous rocks of Precambrian age	Basin solid geology (see Appendix 1); literature review	0.8	0.7	0.5	0.280	Units with potential redox gradients were selected from the solid geology based on a review of relevant literature (see text for details)
		Presence of Fe^{2+}-rich rocks of Precambrian age		0.5	0.5	0.5	0.125	

Table 3.4.2: Theoretical and mappable criteria for unconformity-related uranium in the Phanerozoic Eon

MINERAL SYSTEM COMPONENT	CRITERIA		DATASET	IMPOR-TANCE	APPLIC-ABILITY	CONFI-DENCE	WEIGHTING	COMMENTS
	THEORETICAL	MAPPABLE						
Source	Presence of U-enriched igneous rocks	10 km buffer around U-enriched basement rocks	Radiometric map of Australia (Minty *et al*., 2010); geochemical data; basement solid geology (see Appendix 1)	0.8	0.7	0.7	0.392	Presence of U-rich igneous rocks defined as greater than the 75th percentile for each rock class (intrusive and volcanic)
		30 km buffer around U-enriched basement rocks		0.8	0.5	0.7	0.280	
		100 km buffer around U-enriched basement rocks		0.8	0.3	0.7	0.168	
	Presence of U-enriched sediments of Phanerozoic age	Pertaoorta Group	Radiometric map of Australia (Minty *et al*., 2010); Surface geology of Australia (Raymond and Retter, 2010)	0.6	0.6	0.5	0.180	Presence of U-rich sediments of Precambrian age (see text for details)
		Larapinta Group		0.6	0.1	0.5	0.030	Presence of U-rich sediments of Phanerozoic age (see text for details). Where a group is used instead of a unit the applicability has been reduced to reflect the number of U-rich units in the group
		Finke Group		0.6	0.5	0.5	0.150	
		Kelly Creek Formation		0.6	0.6	0.5	0.180	
		Tomahawk Formation		0.6	0.6	0.5	0.180	
		Eurowie Sandstone Member		0.6	0.6	0.5	0.180	
		Arthur Creek Formation		0.6	0.6	0.5	0.180	
		Red Heart Dolostone		0.6	0.6	0.5	0.180	
	Presence of evaporite minerals of Phanerozoic age within lithological unit indicating production of basinal brines	Chandler Formation	Basin solid geology (see Appendix 1); literature review (see text for details)	0.5	0.4	0.6	0.120	Distribution of evaporite-bearing units or shallow water units of Phanerozoic age as cited in the literature. Where a group is used instead of a unit the applicability has been reduced to reflect the number of evaporite-bearing units in the group
		Shannon Formation		0.5	0.4	0.6	0.120	
		Larapinta Group		0.5	0.1	0.6	0.030	
		Chabalowe Formation		0.5	0.4	0.6	0.120	
		Thorntonia Limestone		0.5	0.4	0.6	0.120	
Drivers	Presence of thick, intracratonic, epicontinental or foreland basins	Amadeus Basin	Provinces dataset	0.9	0.5	1.0	0.450	
		Amadeus Basin; 40 km buffer		0.6	0.3	1.0	0.180	
		Ngalia Basin		0.9	0.4	1.0	0.360	
		Ngalia Basin; 40 km buffer		0.6	0.2	1.0	0.120	
		Georgina Basin		0.9	0.5	1.0	0.450	
		Georgina Basin; 40 km buffer		0.6	0.3	1.0	0.180	
		Eromanga Basin		0.9	0.5	1.0	0.450	
		Eromanga; 40 km buffer		0.9	0.3	1.0	0.270	
		Lake Eyre Basin		0.7	0.7	1.0	0.490	
		Lake Eyre; 40 km buffer		0.7	0.5	1.0	0.350	
		Warburton Basin		0.5	0.7	1.0	0.350	
		Warburton Basin; 40 km buffer		0.5	0.5	1.0	0.250	
Fluid-flow pathways and architecture	Presence of unconformity in solid geology	Distribution of unconformities in solid geology; 10 km buffer	Basement solid geology (see Appendix 1)	1.0	1.0	0.7	0.700	Unconformities were interpreted from solid geology
		Distribution of unconformities in solid geology; 20 km buffer		1.0	0.6	0.7	0.420	
	Presence of basal unconformity in basins of Phanerozoic age	Amadeus Basin;10km buffer	Provinces dataset	1.0	0.6	1.0	0.600	
		Amadeus Basin; 20km buffer		1.0	0.4	1.0	0.400	
		Amadeus Basin; 40 km buffer		1.0	0.2	1.0	0.200	
		Ngalia Basin;10km buffer		1.0	0.6	1.0	0.600	
		Ngalia Basin; 20 km buffer		1.0	0.4	1.0	0.400	
		Ngalia Basin; 40 km buffer		1.0	0.2	1.0	0.200	
		Georgina Basin;10km buffer		1.0	0.6	1.0	0.600	
		Georgina Basin; 20 km buffer		1.0	0.4	1.0	0.400	
		Georgina Basin; 40 km buffer		1.0	0.2	1.0	0.200	

Table 3.4.2 (cont'd): Theoretical and mappable criteria for unconformity-related uranium in the Phanerozoic Eon

MINERAL SYSTEM COMPONENT	CRITERIA		DATASET	IMPORTANCE	APPLICABILITY	CONFIDENCE	WEIGHTING	COMMENTS
	THEORETICAL	MAPPABLE						
Fluid-flow pathways and architecture	Presence of basal unconformity in basins of Phanerozoic age (cont'd)	Pedirka Basin;10km buffer	Provinces dataset	1.0	0.8	1.0	0.800	
		Pedirka Basin; 20km buffer		1.0	0.6	1.0	0.600	
		Pedirka Basin; 40 km buffer		1.0	0.4	1.0	0.400	
		Eromanga Basin;10km buffer		1.0	0.8	1.0	0.800	
		Eromanga Basin; 20 km buffer		1.0	0.6	1.0	0.600	
		Eromanga Basin; 40 km buffer		1.0	0.3	1.0	0.300	
		Lake Eyre Basin;10km buffer		1.0	0.6	1.0	0.600	
		Lake Eyre Basin; 20 km buffer		1.0	0.5	1.0	0.500	
		Lake Eyre Basin; 40 km buffer		1.0	0.4	1.0	0.400	
		Warburton Basin;10km buffer		1.0	0.8	1.0	0.800	
		Warburton Basin; 20 km buffer		1.0	0.6	1.0	0.600	
		Warburton Basin; 40 km buffer		1.0	0.4	1.0	0.400	
	Distribution of extensional faults	Antrim; 2.5 km buffer	OZ SEEBASE™ Proterozoic Basins Study (De Vries *et al.*, 2006)	0.7	0.5	0.5	0.175	
		Larapintine; 2.5 km buffer		0.7	0.5	0.5	0.175	
		Pillara; 2.5 km buffer		0.7	0.5	0.5	0.175	
	Evidence of oxidised fluids leading to demagnetisation of rock units	Demagnetised zones - magnetic data one standard deviation below mean for the study area	Magnetic anomaly map of Australia (Milligan *et al.*, 2010)	0.5	0.3	0.8	0.120	
		Demagnetised zones - magnetic data two standard deviations below mean for the study area		0.5	0.5	0.8	0.200	
Depositional mechanisms	Direct evidence of elevated U	U^2/Th values one standard deviation above the mean for each unique geological unit	Radiometric map of Australia (Minty *et al.*, 2010); Surface geology of Australia (Raymond and Retter, 2010)	0.7	0.6	0.6	0.252	
		U^2/Th values two standard deviations above the mean for each unique geological unit		0.7	0.8	0.6	0.336	
	Thorium enrichment that may indicate uranium deposition at depth	Thorium radiometric data one standard deviation above mean for the study area	Radiometric map of Australia (Minty *et al.*, 2010); Surface geology of Australia (Raymond and Retter, 2010)	0.4	0.5	0.5	0.100	
		Thorium radiometric data two standard deviations above mean for the study area		0.4	0.7	0.5	0.140	
	Redox gradients along and below basal unconformity (carbonaceous or Fe^{2+}-rich)	Chandler Formation (carbonaceous)	Basin solid geology (see Appendix 1); literature review (see text for details)	0.8	0.7	0.5	0.280	Based on description in literature. Where a group is used instead of a unit the applicability has been reduced to reflect the number of favourable units in the group
		Larapinta Group (carbonaceous and Fe^{2+}-rich)		0.8	0.4	0.5	0.160	
		Brewer Conglomerate (carbonaceous)		0.8	0.7	0.5	0.280	
		Winton Formation (carbonaceous)		0.8	0.7	0.5	0.280	
		Bulldog Shale (carbonaceous and Fe^{2+}-rich)		0.8	0.7	0.5	0.280	
		Tomahawk Formation (carbonaceous)		0.8	0.7	0.5	0.280	
		Chabalowe Formation (carbonaceous)		0.8	0.7	0.5	0.280	
		Arthur Creek Formation (carbonaceous and Fe^{2+}-rich)		0.8	0.7	0.5	0.280	
		Thorntonia Limestone (carbonaceous and Fe^{2+}-rich)		0.8	0.7	0.5	0.280	
		Winton Formation (Fe^{2+}-rich)		0.5	0.5	0.5	0.125	

The process for identifying uranium-rich igneous rocks is described in Section 3.5. Identified uranium-rich igneous rocks were buffered to distances of 10, 30 and 100 km (Figure 3.4.4). The buffer distances selected correspond to those used by van der Wielen *et al*. (2011).

The distribution of uranium-enriched sediments was determined as those units from the surface geology of Australia map (Raymond and Retter, 2010) with an elevated uranium response in uranium channel radiometrics (Minty *et al*., 2010). These were identified subjectively based on visual inspection of the data. Units identified in the Precambrian time slice consist mainly of parts of the Heavitree Quartzite, Bitter Springs Formation and the Pertatataka Formation (Figure 3.4.5). Phanerozoic uranium-enriched sediments are most extensive in the Georgina and southern Amadeus basins (Figure 3.4.6).

The presence of evaporite minerals was used as an indicator of potential sources of Cl^- ligands for the high salinity fluids believed to transport uranium. The distribution of evaporite-bearing units or shallow water units of Precambrian age is shown in Figure 3.4.7. The presence of evaporite minerals within lithological units of Phanerozoic age is shown in Figure 3.4.8. This includes units within the Pertaoorta Group and the Larapinta Group in the Amadeus Basin and the Chabalowe Formation in the Georgina Basin (Ambrose, 2006a; Ambrose and Putnam, 2006).

The Precambrian and Phanerozoic sources system component maps are shown in Figures 3.4.9 and 3.4.10 respectively. The areas of highest source potential in the Precambrian are where the Heavitree Quartzite and Bitter Springs Formations overlap with the buffer around the Teapot Granite Complex on the northern margin of the Amadeus Basin. A small area of higher potential also occurs near the Albarta and Tourmaline Gorge prospects where the Heavitree Quartzite and Bitter Springs Formation overlap with the 100 km buffer around the igneous source rocks. Another region of moderate source potential occurs in the Mopunga Formation in the east of the study area. In the Phanerozoic, the areas of highest source potential occur in the Georgina Basin particularly where it overlaps with the Davenport Province and also along the northern margin of the Amadeus Basin within the vicinity of the Teapot Granite Complex.

3.4.3.2 Drivers

The movement of oxidised, uranium-bearing fluids in deep-basinal settings may be driven by gravity (topography or salinity-related density controls), diagenesis/compaction, convection/temperature variations or tectonic processes (e.g., basin inversion). Based on these considerations, one criterion has been used to map the drivers system component:

- Presence of thick, intracratonic, epicontinental or foreland basins.

For the Precambrian assessment, suitable basins include the Neoproterozoic parts of the Amadeus, Georgina and Ngalia basins, which have been assigned the highest weightings in Figure 3.4.11 (see also Table 3.4.1). The Amadeus Basin overlies the Warumpi and Aileron provinces to the north and the Musgrave Province to the south and is up to 14 km thick (http://www.nt.gov.au/d/Minerals_Energy/Geoscience/). The Georgina Basin overlies the Aileron and Davenport provinces in the north. The basin deepens towards the south along the margin of the Arunta Region with thicknesses up to 3.7 km. The Ngalia Basin unconformably overlies the Aileron Province and is up to 6 km thick (http://www.nt.gov.au/d/Minerals_Energy/Geoscience/). Basins used for this criterion for the Phanerozoic assessment are shown in Figure 3.4.12. The region in the southeast part of the study area (in the vicinity of the Lake Eyre Basin) has the highest potential due to the overlap of several basins, resulting in a thicker sedimentary sequence. Other areas of moderately high potential include the Eromanga, Amadeus, and Georgina basins with the Ngalia Basin also having moderate potential. The Pedirka Basin was not included as it is only up to 1.5 km thick (http://www.nt.gov.au/d/Minerals_Energy/Geoscience/).

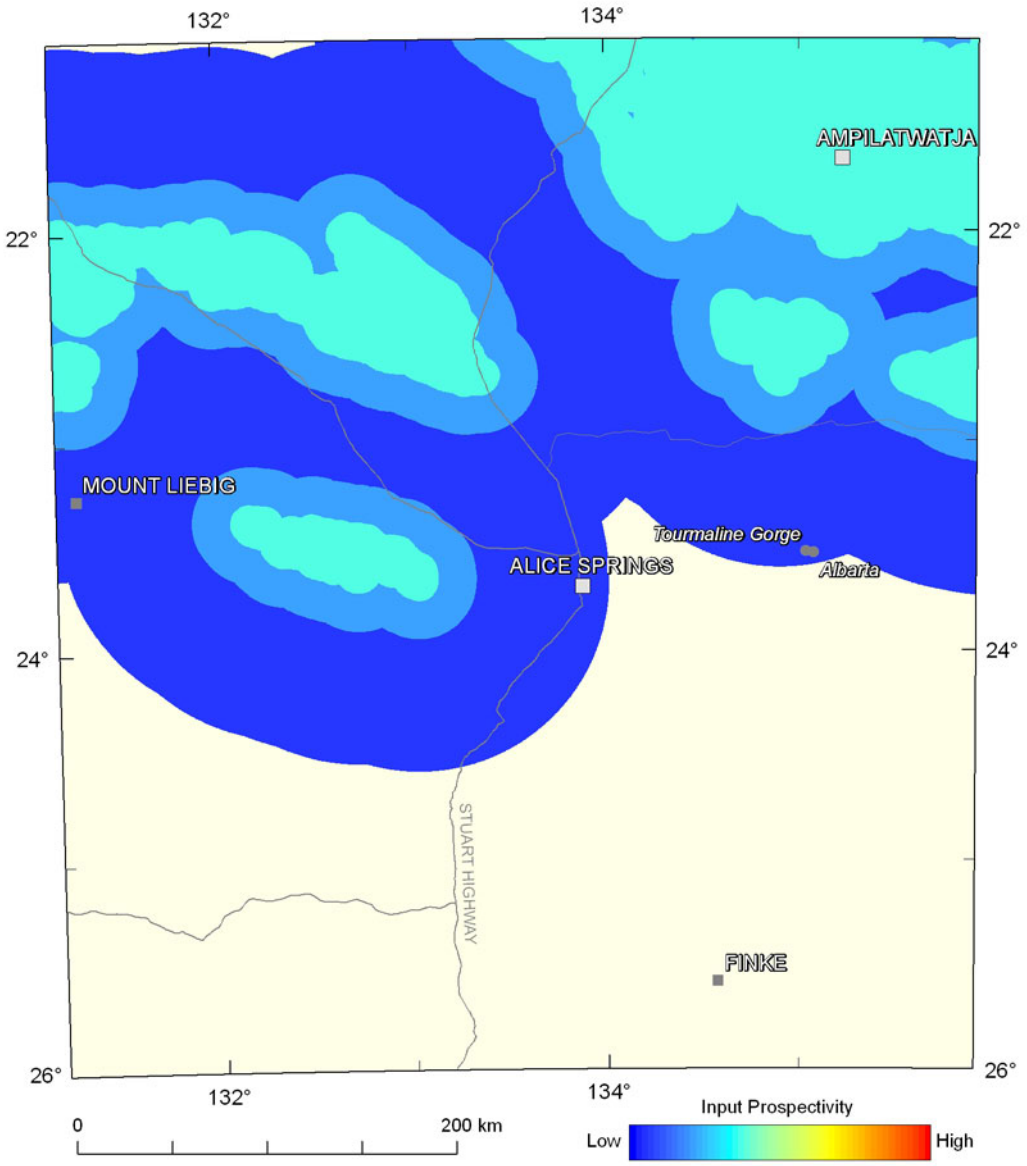

Figure 3.4.4: *Variations in the weighting for the presence of uranium-rich igneous rocks (intrusive or volcanic) with 10, 30 and 100 km buffers. This criterion is identical for both the Precambrian and Phanerozoic assessments. The colour stretch for the mappable criteria used in the assessment for unconformity-related uranium systems uses a numerical range from the minimum to the maximum weighting of all criteria used (0.100 to 0.800; see Table 3.4.1; note: range is that for Precambrian unconformity systems), and utilises 20 equal-interval breaks.*

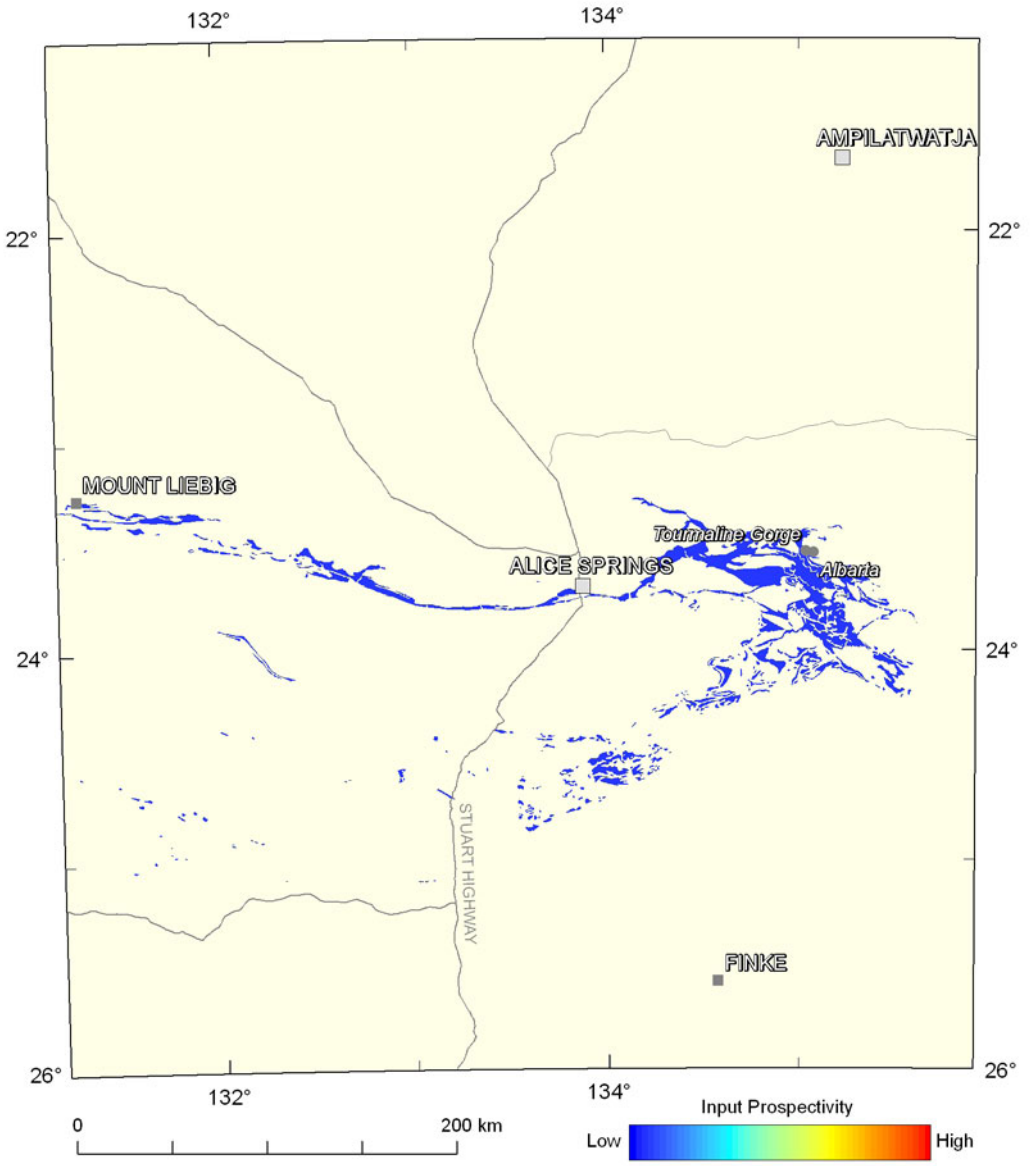

Figure 3.4.5: *Variations in the weighting for the presence of uranium-enriched sediments of Precambrian age. The colour stretch for the mappable criteria used in the assessment for Precambrian unconformity-related uranium systems uses a numerical range from the minimum to the maximum weighting of all criteria used (0.100 to 0.800; see Table 3.4.1), and utilises 20 equal-interval breaks.*

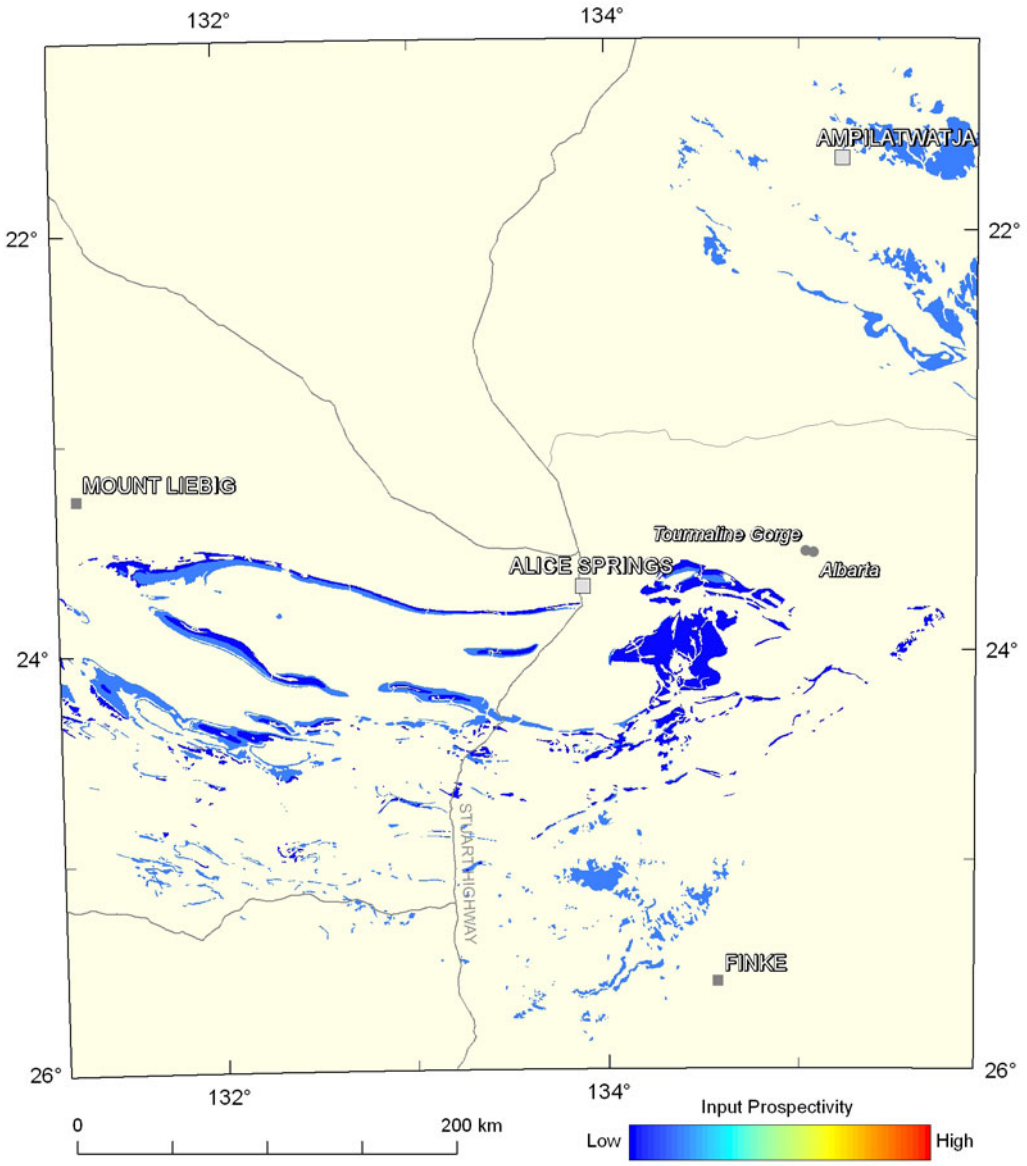

Figure 3.4.6: *Variations in the weighting for the presence of uranium-enriched sediments of Phanerozoic age. The colour stretch for the mappable criteria used in the assessment for Phanerozoic unconformity-related uranium systems uses a numerical range from the minimum to the maximum weighting of all criteria used (0.030 to 0.800; see Table 3.4.2), and utilises 20 equal-interval breaks.*

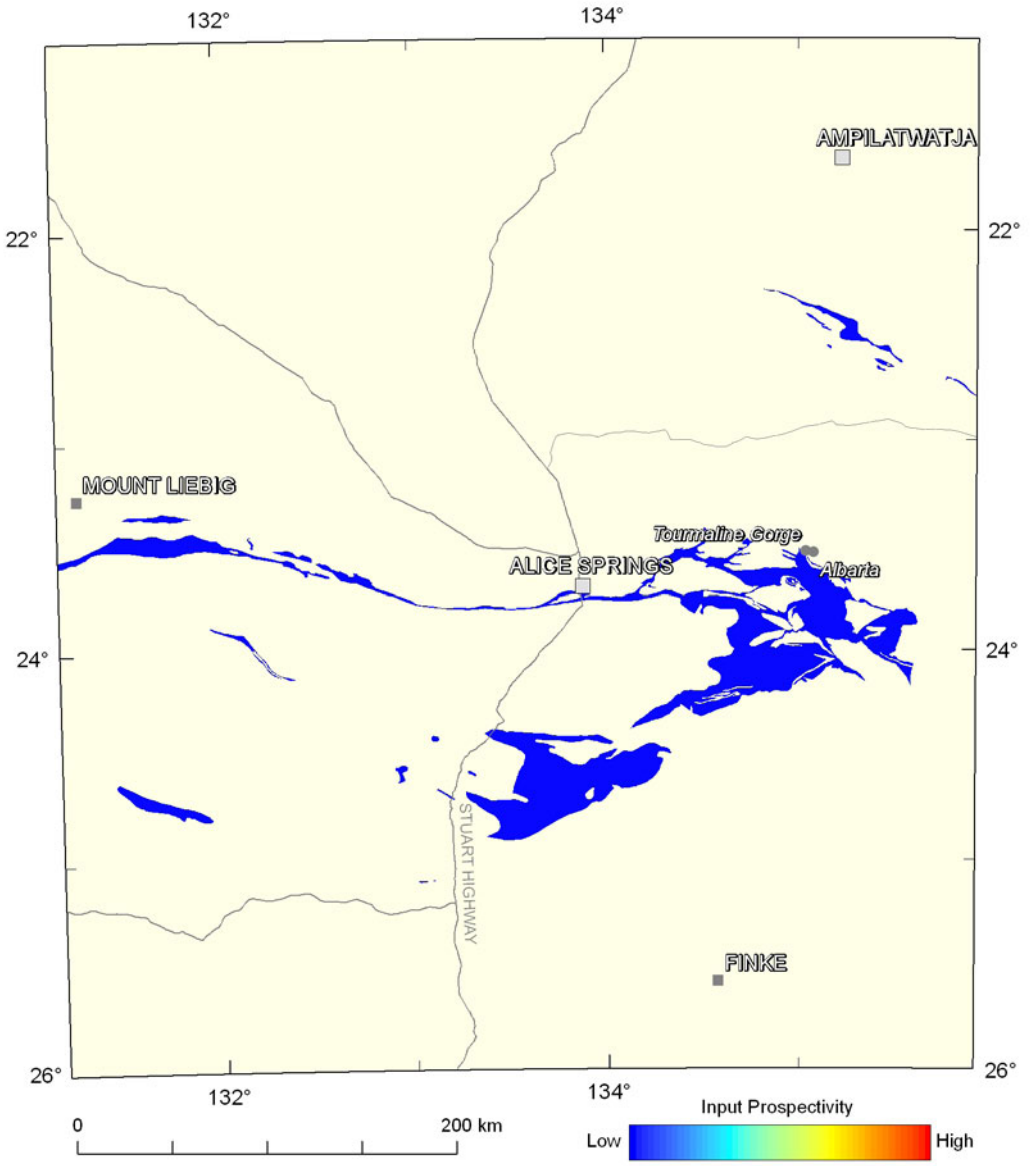

Figure 3.4.7: *Variations in the weighting for the presence of sediments of Precambrian age indicating the presence of evaporite minerals. The colour stretch for the mappable criteria used in the assessment for Precambrian unconformity-related uranium systems uses a numerical range from the minimum to the maximum weighting of all criteria used (0.100 to 0.800; see Table 3.4.1), and utilises 20 equal-interval breaks.*

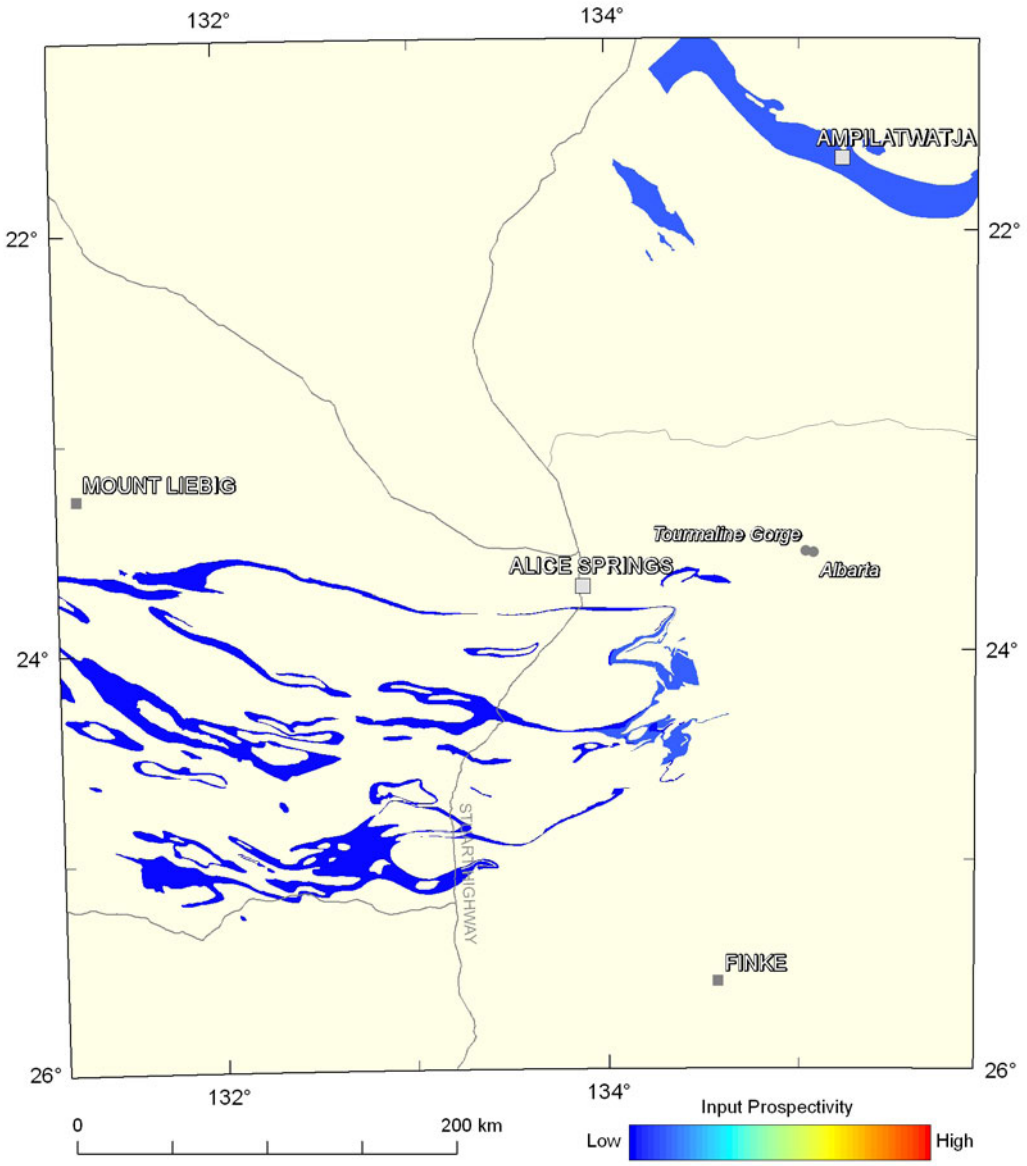

Figure 3.4.8: *Variations in the weighting for the presence of sediments of Phanerozoic age indicating the presence of evaporite minerals. The colour stretch for the mappable criteria used in the assessment for Phanerozoic unconformity-related uranium systems uses a numerical range from the minimum to the maximum weighting of all criteria used (0.030 to 0.800; see Table 3.4.2), and utilises 20 equal-interval breaks.*

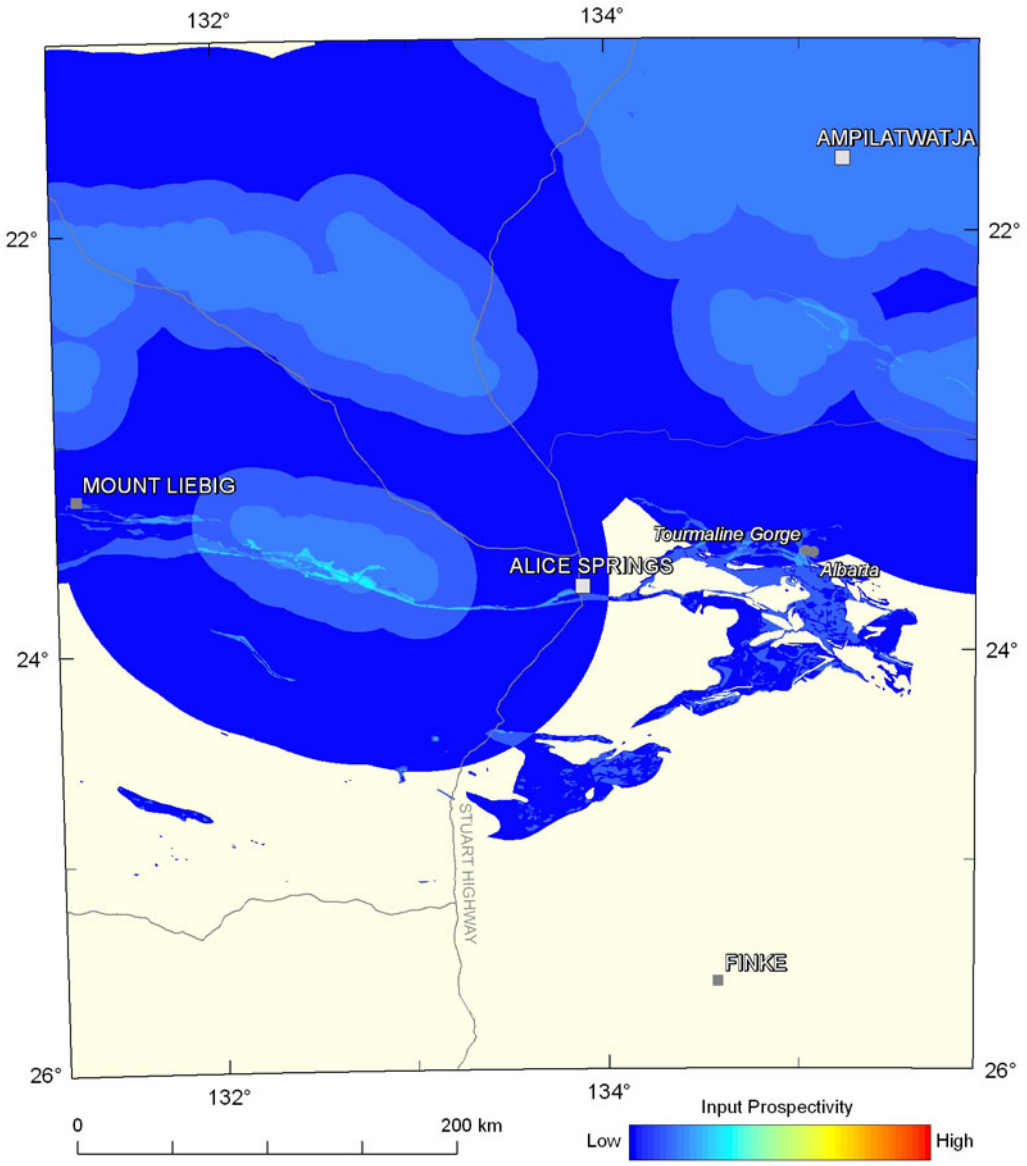

Figure 3.4.9: *Variation in the weightings for the source system component for Precambrian unconformity-related uranium systems. The colour stretch for each mineral system component in the assessment for Precambrian unconformity-related uranium systems uses a numerical range from the minimum to the maximum weighting for each of the system components (0.030 to 0.630), and utilises 20 equal-interval breaks.*

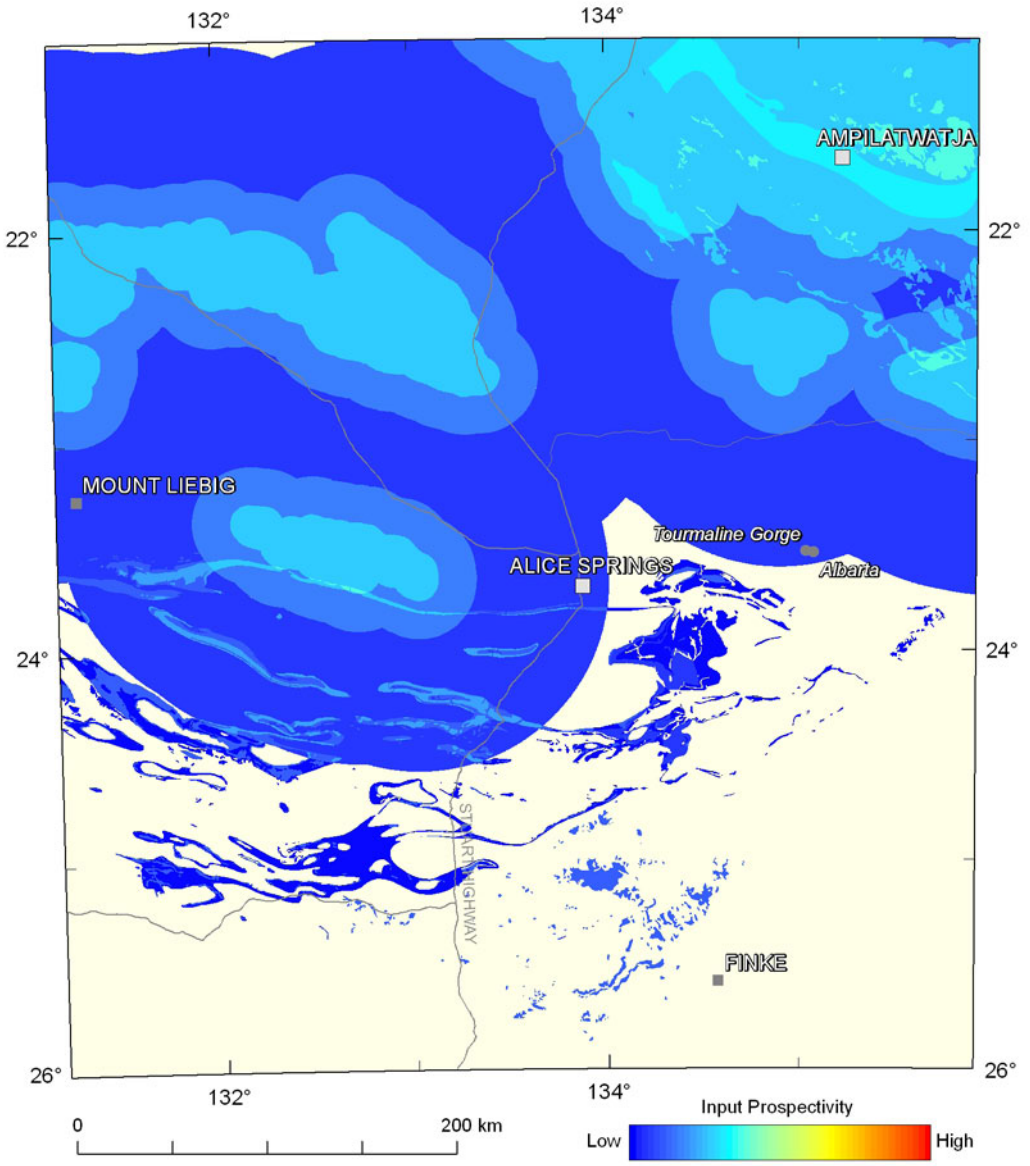

Figure 3.4.10: *Variation in the weightings for the source system component for Phanerozoic unconformity-related uranium systems. The colour stretch for each mineral system component in the assessment for Phanerozoic unconformity-related uranium systems uses a numerical range from the minimum to the maximum weighting for each of the system components (0.010 to 0.490), and utilises 20 equal-interval breaks.*

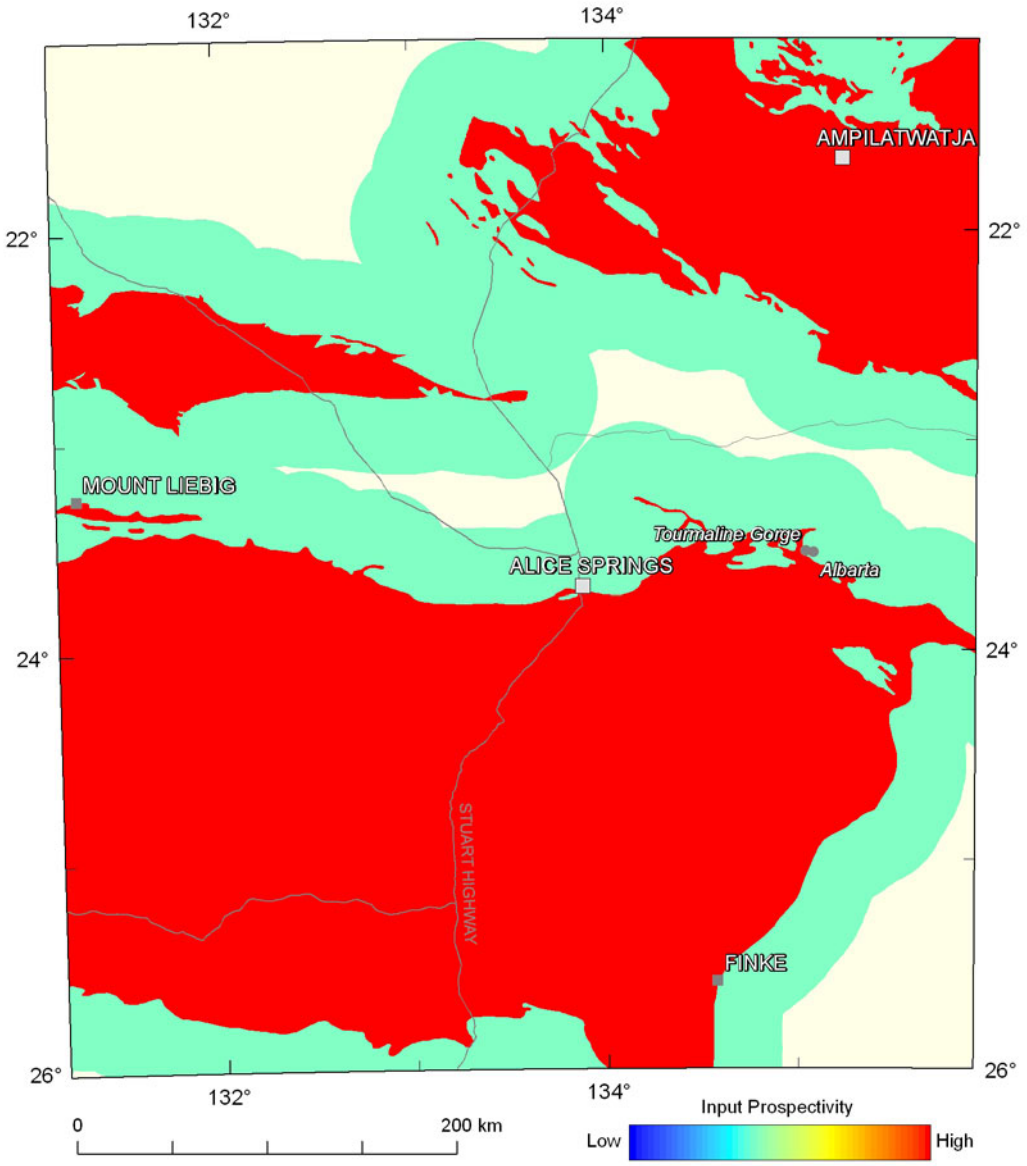

Figure 3.4.11: *Variations in the weighting for the presence of thick intracratonic, epicontinental or foreland basins of Precambrian age with 40 km buffer. This also represents the weightings for the Precambrian drivers system component, as it is the sole criterion used. The colour stretch for each mineral system component in the assessment for Precambrian unconformity-related uranium systems uses a numerical range from the minimum to the maximum weighting for each of the system components (0.030 to 0.630), and utilises 20 equal-interval breaks.*

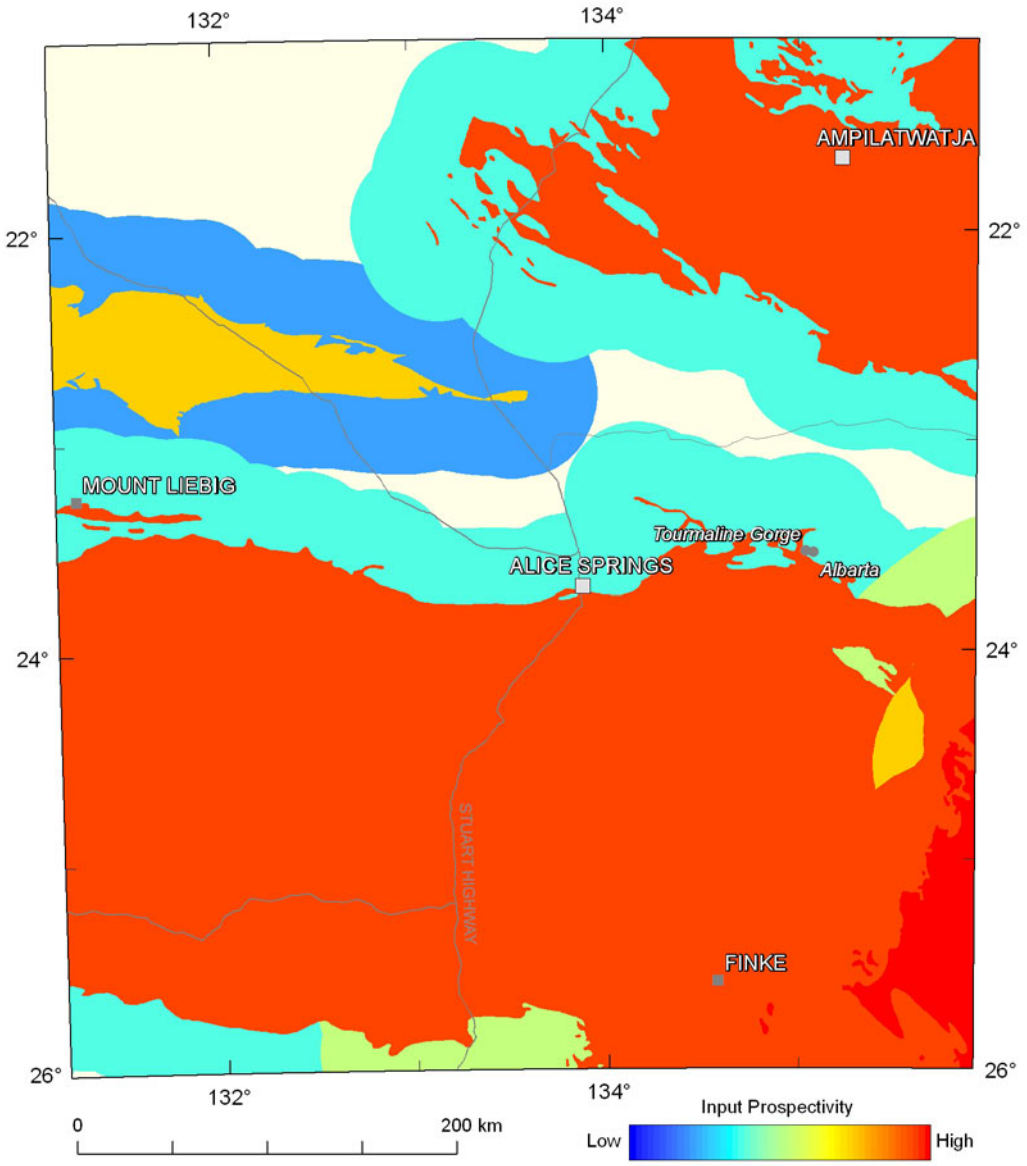

Figure 3.4.12: *Variations in the weighting for the presence of thick intracratonic, epicontinental or foreland basins of Phanerozoic age with 40 km buffer. This also represents the weightings for the Precambrian drivers system component, as it is the sole criterion used. The colour stretch for each mineral system component in the assessment for Phanerozoic unconformity-related uranium systems uses a numerical range from the minimum to the maximum weighting for each of the system components (0.010 to 0.490), and utilises 20 equal-interval breaks.*

3.4.3.3 Fluid-flow pathways and architecture

Favourable fluid-flow pathways and architecture include favourable lithologies and structures that enable movement of fluids to the site of ore deposition. Of particular importance to unconformity-related uranium deposits are unconformities that separate oxidised and reduced lithologies. Three criteria have been used to map this system component:

- Presence of unconformities;
- Distribution of extensional faults; and
- Demagnetised zones, potentially indicating flow of oxidised fluids.

Unconformities were identified from the basement solid geology dataset (see Appendix 1) and were buffered to 10 km and 20 km to allow for uncertainties in their location and dip. The results are shown in Figure 3.4.13. This criterion is identical for both the Precambrian and Phanerozoic assessments.

The presence of basal unconformities associated with basins was mapped using the distribution of sedimentary basins. As exploration is mainly interested in the near-surface parts of these unconformities, the basal unconformity at the edge of each basin was used to represent this part of the unconformity. They were also given a 10, 20 and 40 km buffer to account for the fact that the margins of these basins may have been eroded away through time. The results are shown in Figures 3.4.14 and 3.4.15 for the Precambrian and Phanerozoic assessments respectively.

Major extensional faults may also act as important fluid-flow pathways channeling fluids into the vicinity of basal unconformities. Limited information is available on the age of faults in this region for the Precambrian assessment, so faults associated with the Leichardt, Calvert, Musgrave, Warakurna and Centralian extensional events have been used, as described in the OZ SEEBASE Report (2005). The results are shown in Figure 3.4.16. For the Phanerozoic assessment, faults associated with the Antrim, Larapintine and Pillara extensional events, as described in De Vries *et al*. (2006), have been used. These are shown in Figure 3.4.17.

Highly oxidised fluids are required to transport uranium in solution (Bastrakov *et al*., 2010), and such fluids would be expected to oxidise any Fe-rich rocks to hematite along their pathways. Therefore, strongly demagnetised zones (two standard deviations or more below the mean for all magnetic data (Milligan *et al*., 2010) occurring in the study area) were used to indicate possible oxidation due to fluid flow and are shown in Figure 3.4.18. The most demagnetised zones occur in the Aileron Province and where the Eromanga Basin onlaps the Aileron Province.

The Precambrian fluid pathways and architecture system component map is shown in Figure 3.4.19. As expected, this map highlights the unconformities around the edge of the major Neoproterozoic basins, particularly for buffers around the margins of the Georgina, Amadeus and Ngalia basins. The Phanerozoic fluid pathways and architecture system component map is shown in Figure 3.4.20. This map shows areas of high potential around the margins of the Georgina, Amadeus and Ngalia basins, and a zone of moderate to high potential in the southeastern part of the Amadeus Basin which corresponds with a major unconformity shown in Figure 3.4.13.

3.4.3.4 Depositional mechanisms

Depositional environments in unconformity-related uranium systems include favourable lithologies and structures that can focus fluids and deposit uranium and other metals via physical and/or chemical processes. Three criteria have been used to map this system component:

- Direct evidence of elevated uranium at the surface, mapped from U^2/Th radiometric data (Figure 3.4.21). The process for developing this criterion is described in Section 3.2;
- Indicators of uranium enrichment at depth, as mapped by Th-channel radiometrics; and
- Redox gradients along and below the basal unconformity.

Identifying mineralisation at depth is more difficult than detecting surface anomalies. Thorium enrichment related to uranium can occur at the surface when uranium is leached by meteoric fluids, and therefore regions of elevated Th concentration may indicate uranium mineralisation at depth. Thorium data, from the radiometric map of Australia (Minty *et al*., 2010), one and two standard deviations above the regional mean for the study area are shown in Figure 3.4.22. Most of the high Th values occur in the Aileron Province, with another region of high Th on the edge of the Eromanga Basin.

Deposition of uranium typically occurs by reduction of U^{6+} to U^{4+} (Bastrakov *et al*., 2010) in the vicinity of a basal unconformity, and hence, the presence of reducing lithologies such as carbonaceous rocks and Fe^{2+}-rich rocks are necessary for these chemical reactions to occur. Only limited information is available about the composition of the basement units below the major sedimentary basins and this indicates that the stratigraphy is similar to basement lithologies in the Pine Creek region with granite, gneiss, quartzite and schist commonly present. However, due to the need for more geochemical information on the basement lithologies our assessment is mainly based on reducing lithologies within the basins. For the Precambrian time slice, the Bitter Springs, Areyonga, Aralka and Naburula formations were identified from literature sources (e.g., Ambrose, 2006a) as containing either carbonaceous or Fe^{2+}-rich lithologies, and these are plotted in Figure 3.4.23. The presence of reducing lithologies of Phanerozoic age are plotted in Figure 3.4.24. It can be seen that major reducing lithologies comprise the Arthur Creek, Chabalowe and Tomahawk formations in the Georgina Basin, the Pertnjara Group in the Amadeus Basin and the Bulldog Shale and Rolling Downs Group in the Eromanga Basin.

The depositional mechanisms system component map for Precambrian unconformity-related uranium systems, presented in Figure 3.4.25, shows two main regions of favourable potential. The first is the northern margin of the Amadeus Basin in the region of the Cockroach Dam prospect. The second is within the Heavitree Quartzite and Bitter Springs Formation in the vicinity of the Tourmaline Gorge and Albarta prospects. Cropping out Bitter Springs Formation in the central Amadeus Basin also shows higher potential. The Phanerozoic depositional mechanisms system component map, presented in Figure 3.4.26, shows regions of elevated potential in the Georgina Basin, particularly in areas associated with the Tomahawk, Chabalowe and Arthur Creek formations. Another region of elevated potential occurs on the northern margin of the Amadeus Basin and extends into the Warumpi Province. Higher values are also observed in the Bulldog Shale and Rolling Downs Group in the southeast of the study area.

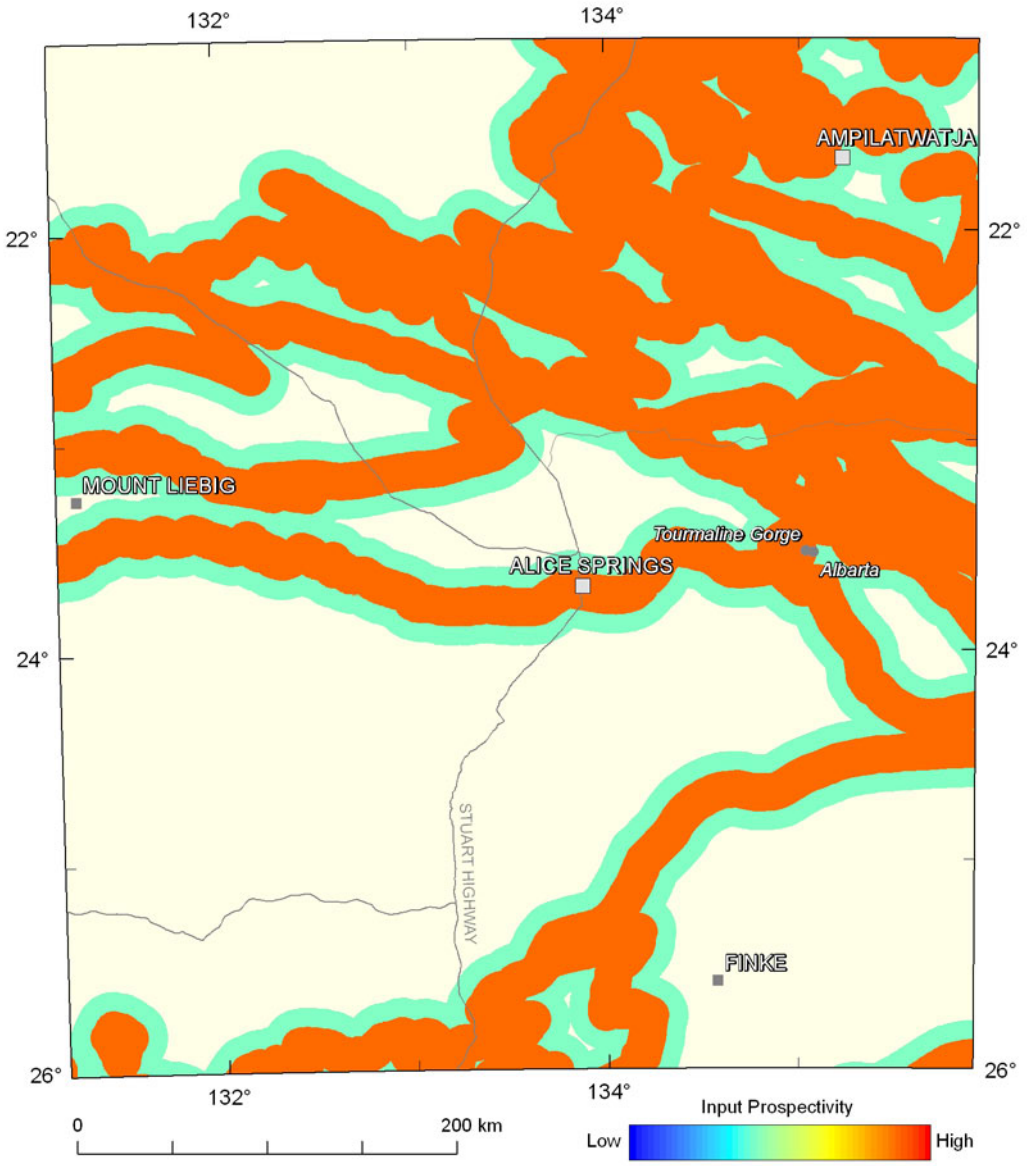

Figure 3.4.13: *Variations in the weighting for the presence of basal unconformities with 10 and 20 km buffers. This criterion is identical for both the Precambrian and Phanerozoic assessments. The colour stretch for the mappable criteria used in the assessment for unconformity-related uranium systems uses a numerical range from the minimum to the maximum weighting of all criteria used (0.100 to 0.800; see Table 3.4.1; note: range is that for Precambrian unconformity systems), and utilises 20 equal-interval breaks.*

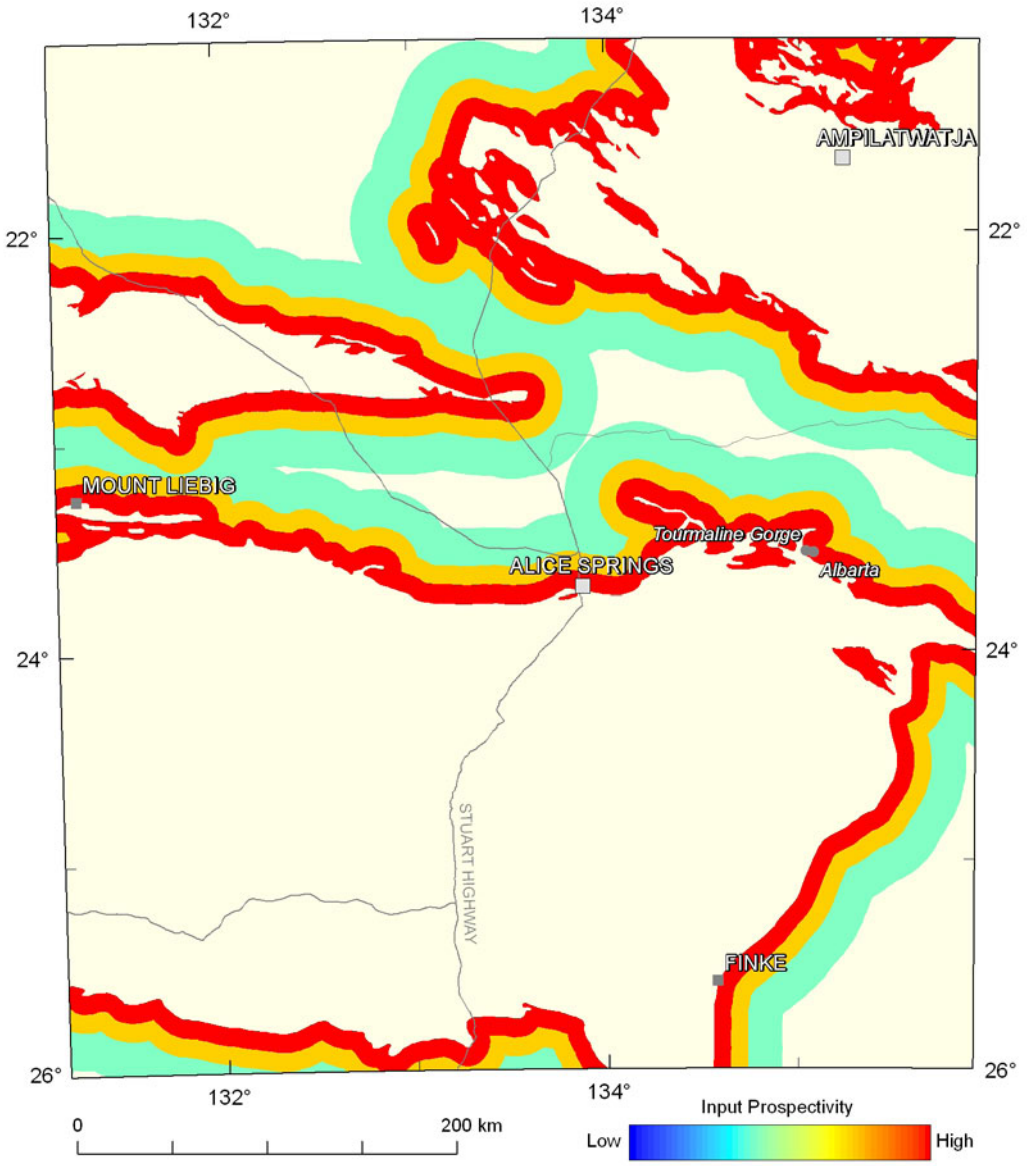

Figure 3.4.14: *Variations in the weighting for the presence of a basal unconformity in basins of Precambrian age with 10, 20 and 40 km buffers. The colour stretch for the mappable criteria used in the assessment for Precambrian unconformity-related uranium systems uses a numerical range from the minimum to the maximum weighting of all criteria used (0.100 to 0.800; see Table 3.4.1), and utilises 20 equal-interval breaks.*

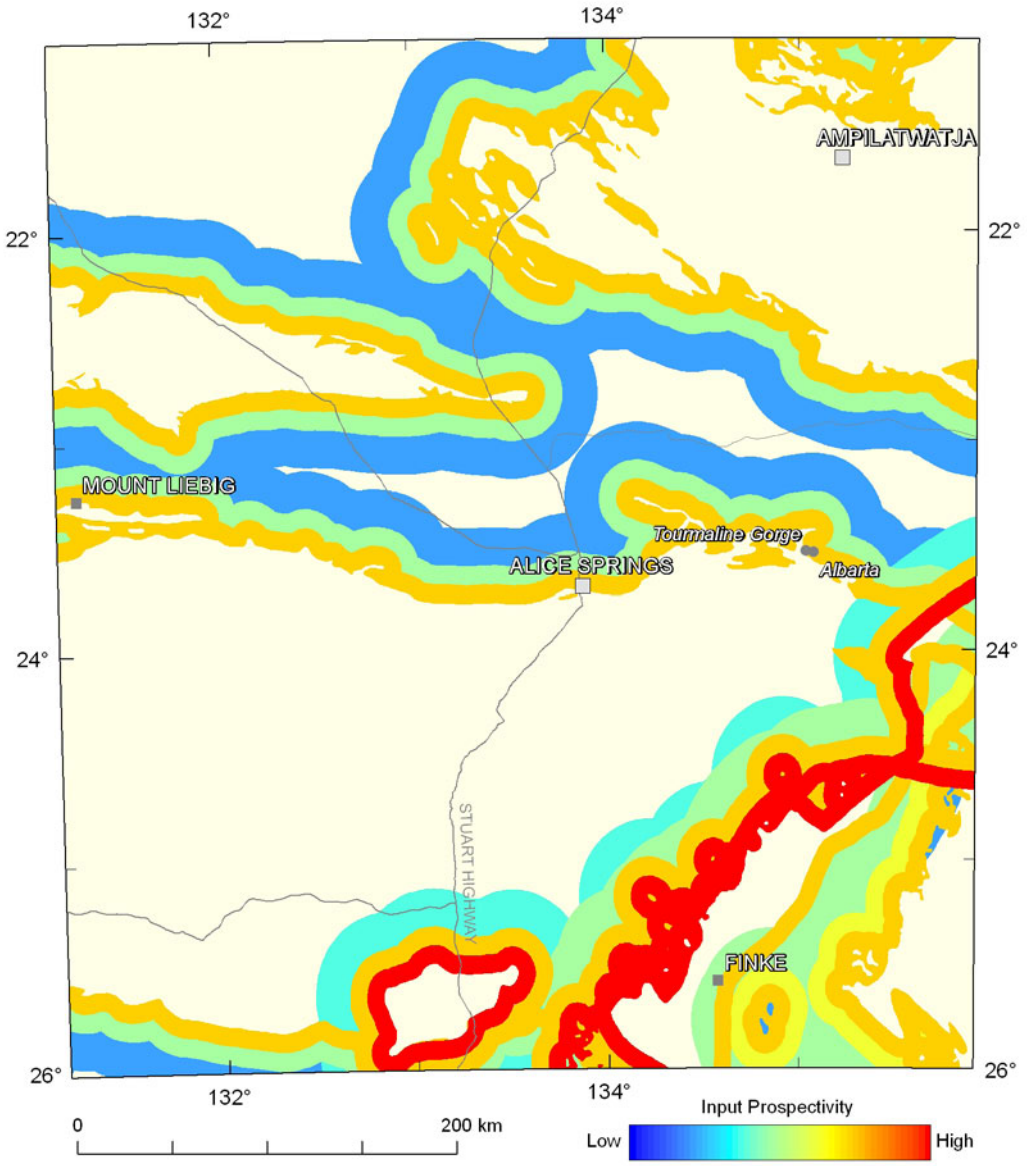

Figure 3.4.15: *Variations in the weighting for the presence of basal unconformities of Phanerozoic age with 10 and 20 km buffers. The colour stretch for the mappable criteria used in the assessment for Phanerozoic unconformity-related uranium systems uses a numerical range from the minimum to the maximum weighting of all criteria used (0.030 to 0.800; see Table 3.4.2), and utilises 20 equal-interval breaks.*

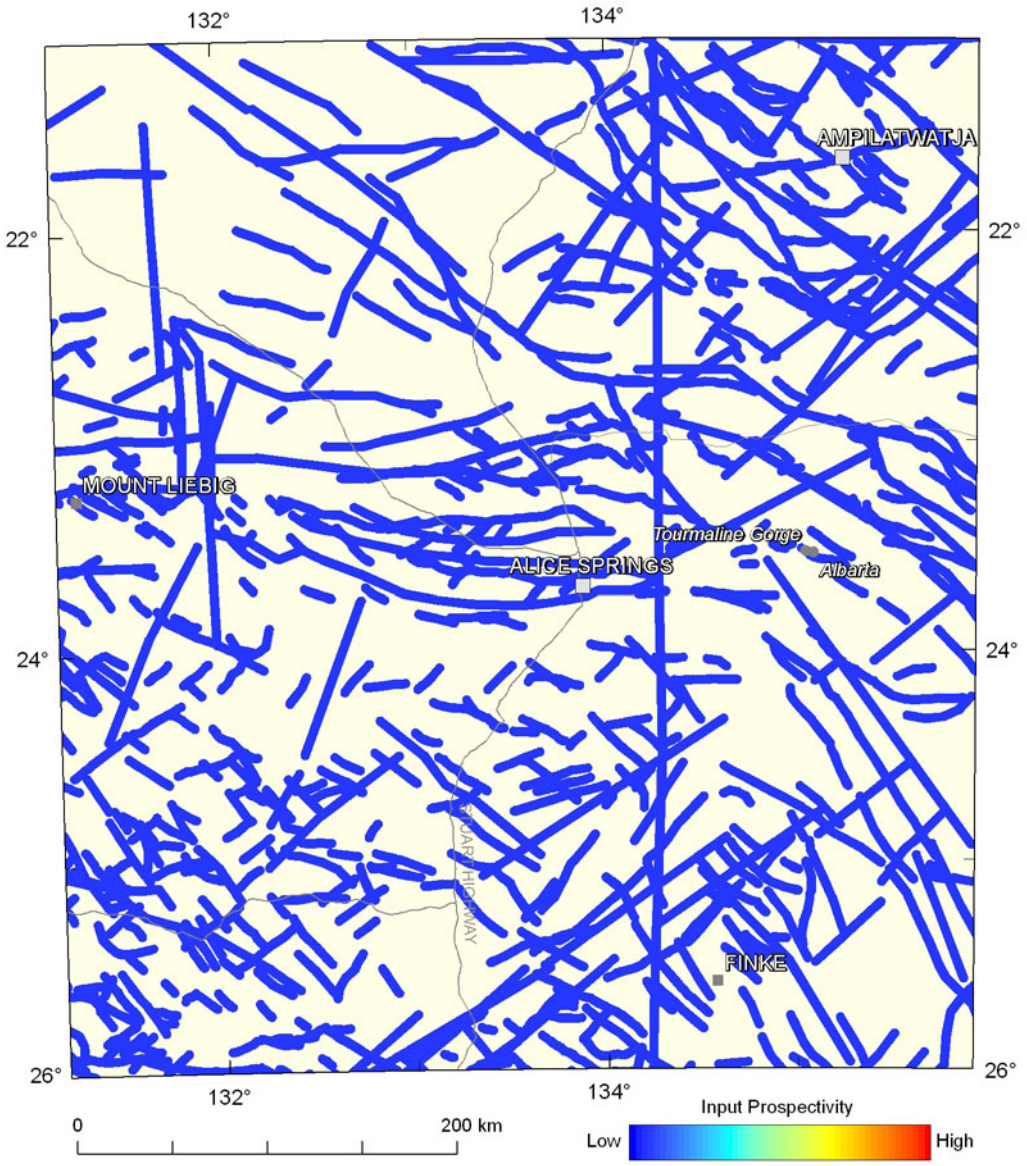

Figure 3.4.16: *Variations in the weighting for the presence of extensional faults of Precambrian age with 2.5 km buffer. The colour stretch for the mappable criteria used in the assessment for Precambrian unconformity-related uranium systems uses a numerical range from the minimum to the maximum weighting of all criteria used (0.100 to 0.800; see Table 3.4.1), and utilises 20 equal-interval breaks.*

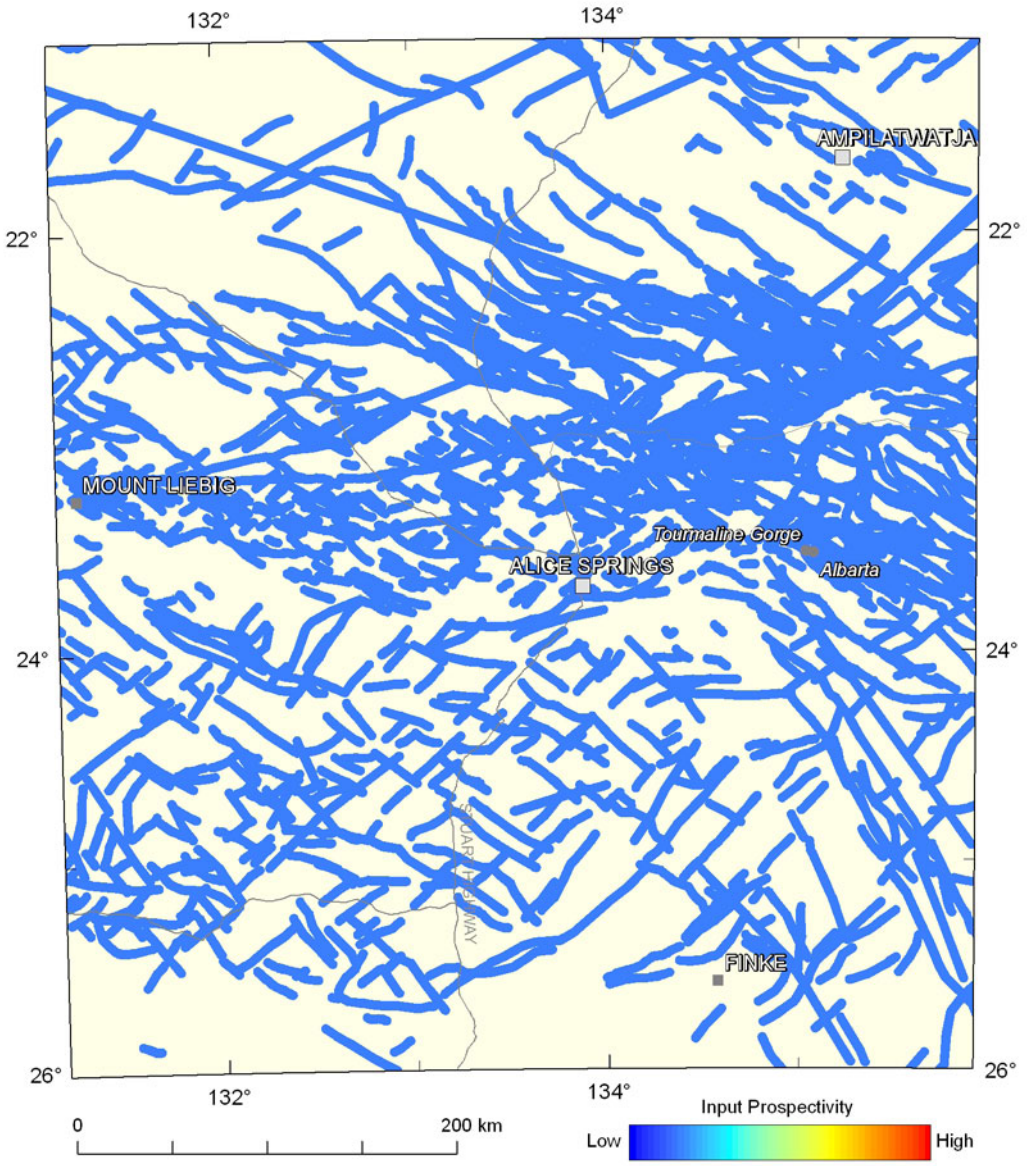

Figure 3.4.17: *Variations in the weighting for the presence of extensional faults of Phanerozoic age with 2.5 km buffer. The colour stretch for the mappable criteria used in the assessment for Phanerozoic unconformity-related uranium systems uses a numerical range from the minimum to the maximum weighting of all criteria used (0.030 to 0.800; see Table 3.4.2), and utilises 20 equal-interval breaks.*

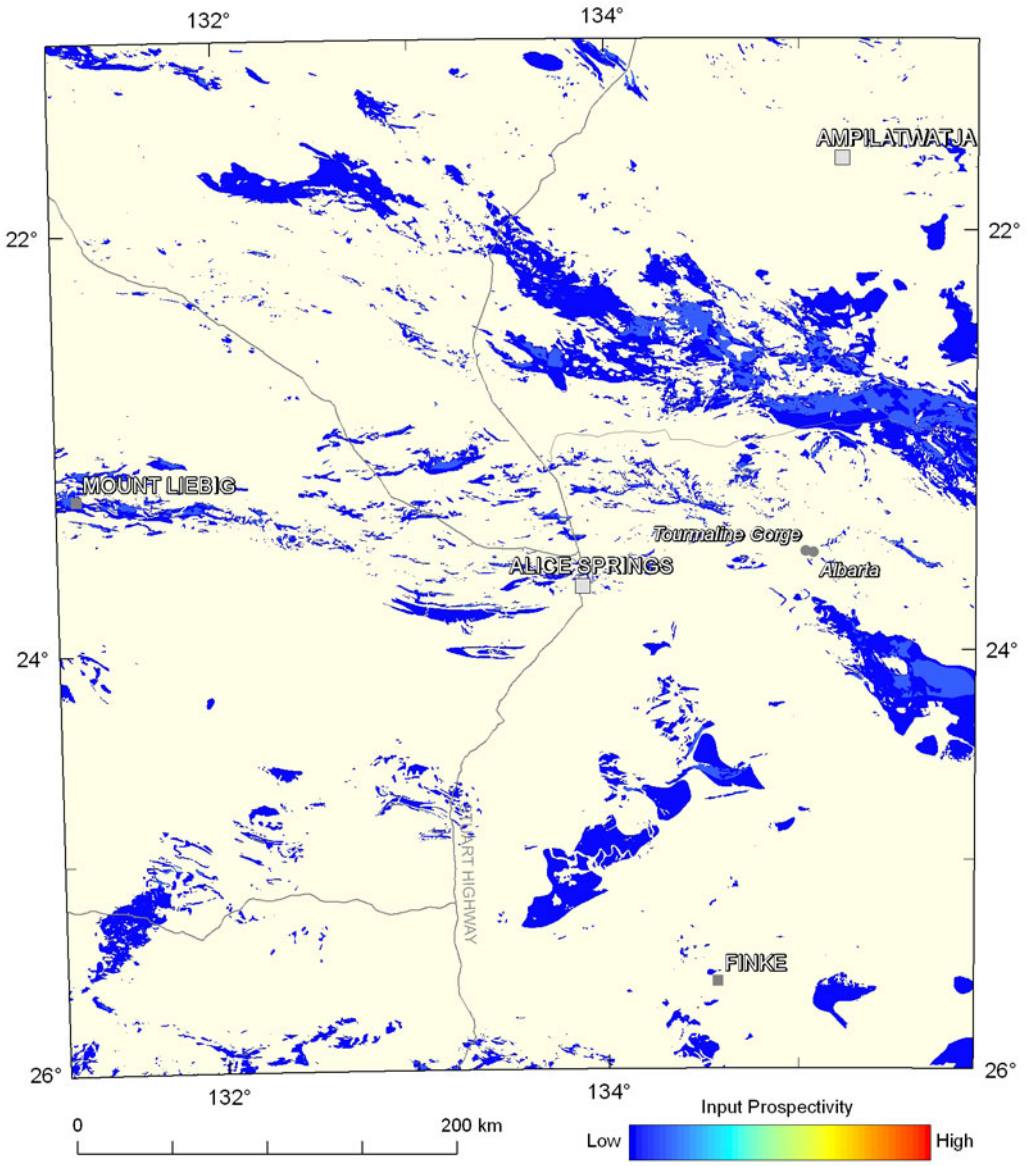

Figure 3.4.18: *Variations in the weighting for evidence of oxidised fluids leading to demagnetisation of rock units. This criterion is identical for both the Precambrian and Phanerozoic assessments. The colour stretch for the mappable criteria used in the assessment for unconformity-related uranium systems uses a numerical range from the minimum to the maximum weighting of all criteria used (0.100 to 0.800; see Table 3.4.1; note: range is that for Precambrian unconformity systems), and utilises 20 equal-interval breaks.*

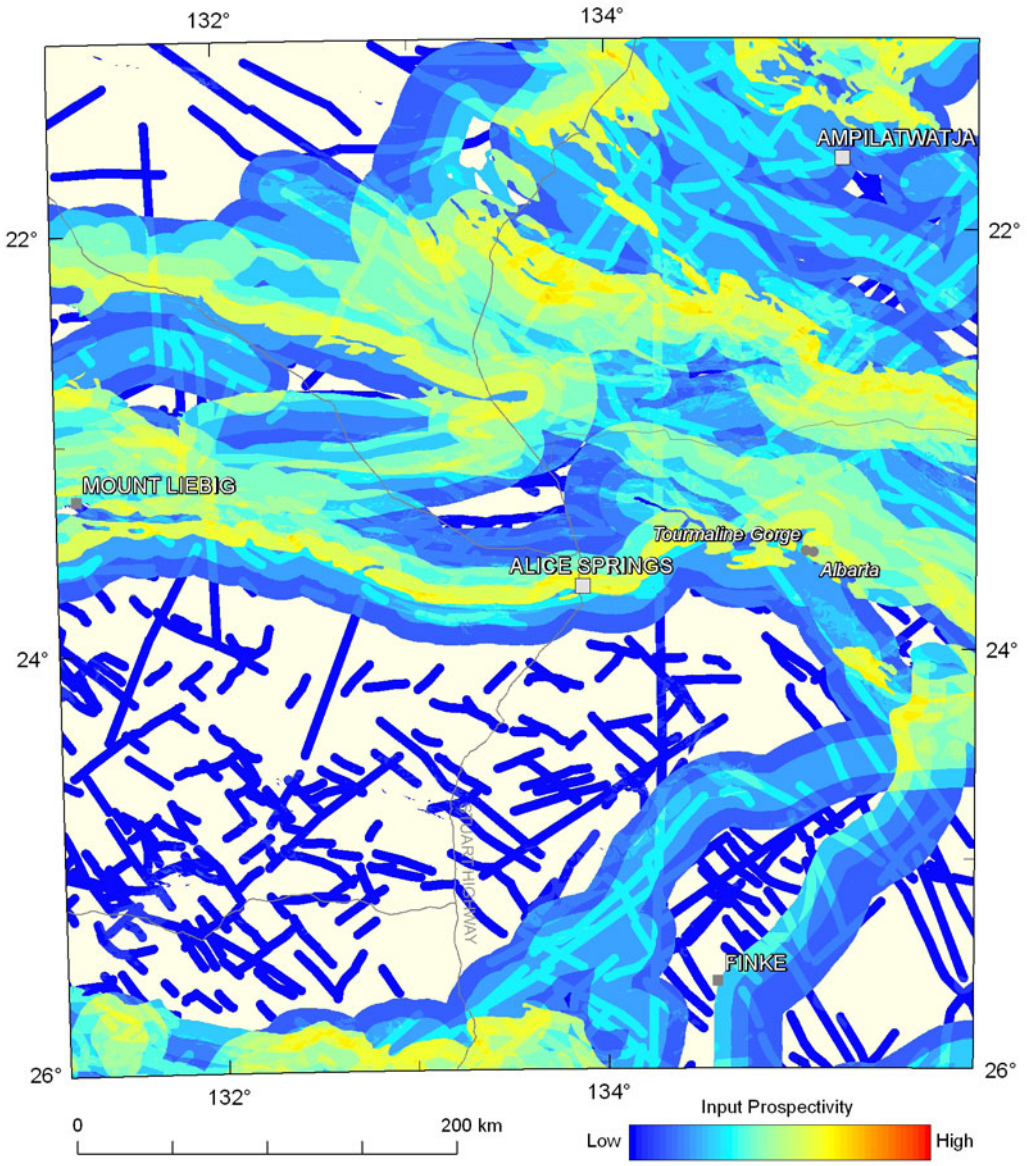

Figure 3.4.19: *Variation in the weightings for the fluid pathways and architecture system component for Precambrian unconformity-related uranium systems. The colour stretch for each mineral system component in the assessment for Precambrian unconformity-related uranium systems uses a numerical range from the minimum to the maximum weighting for each of the system components (0.030 to 0.630), and utilises 20 equal-interval breaks.*

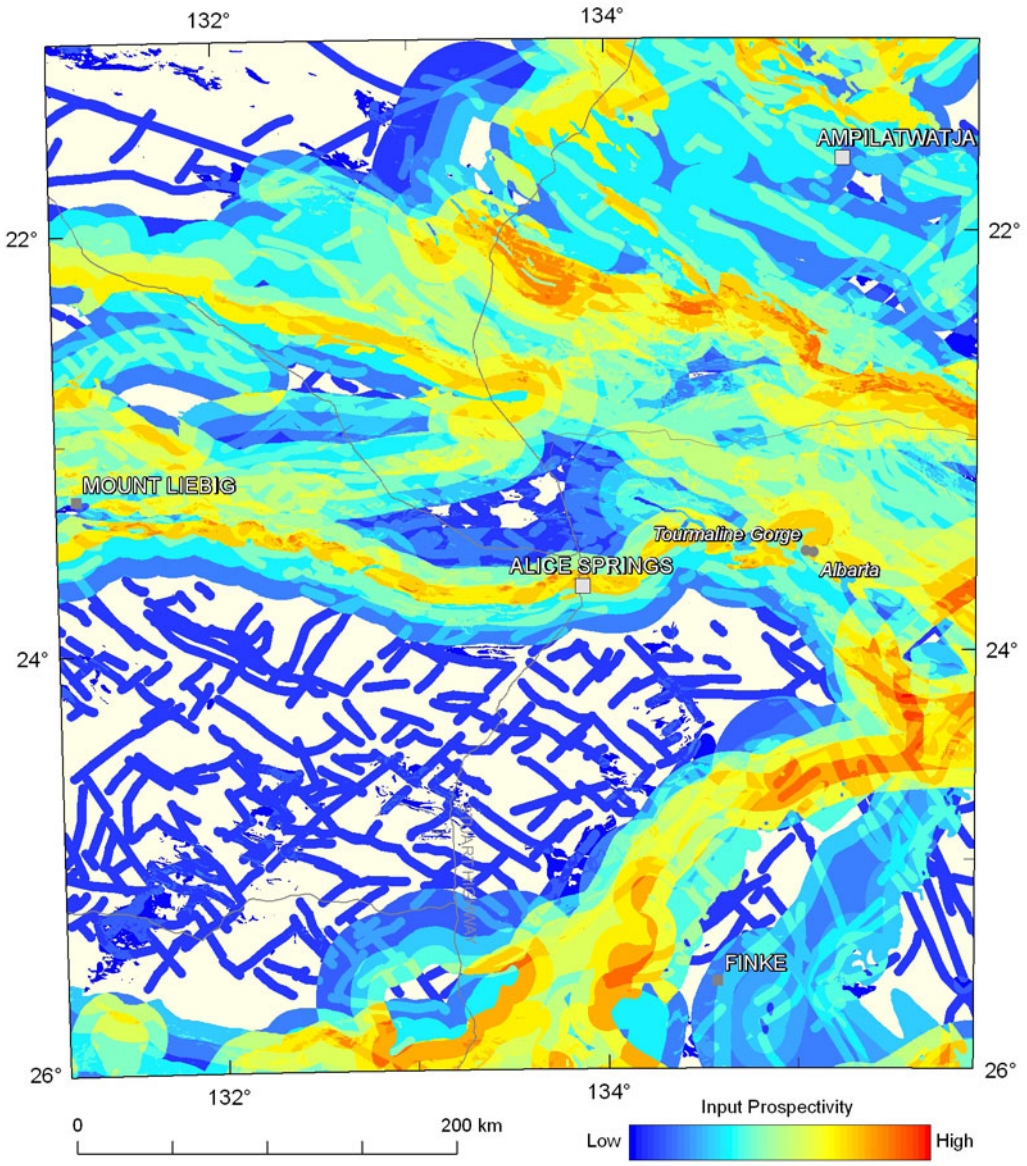

Figure 3.4.20: *Variation in the weightings for the fluid pathways and architecture system component for Phanerozoic unconformity-related uranium systems. The colour stretch for each mineral system component in the assessment for Phanerozoic unconformity-related uranium systems uses a numerical range from the minimum to the maximum weighting for each of the system components (0.010 to 0.490), and utilises 20 equal-interval breaks.*

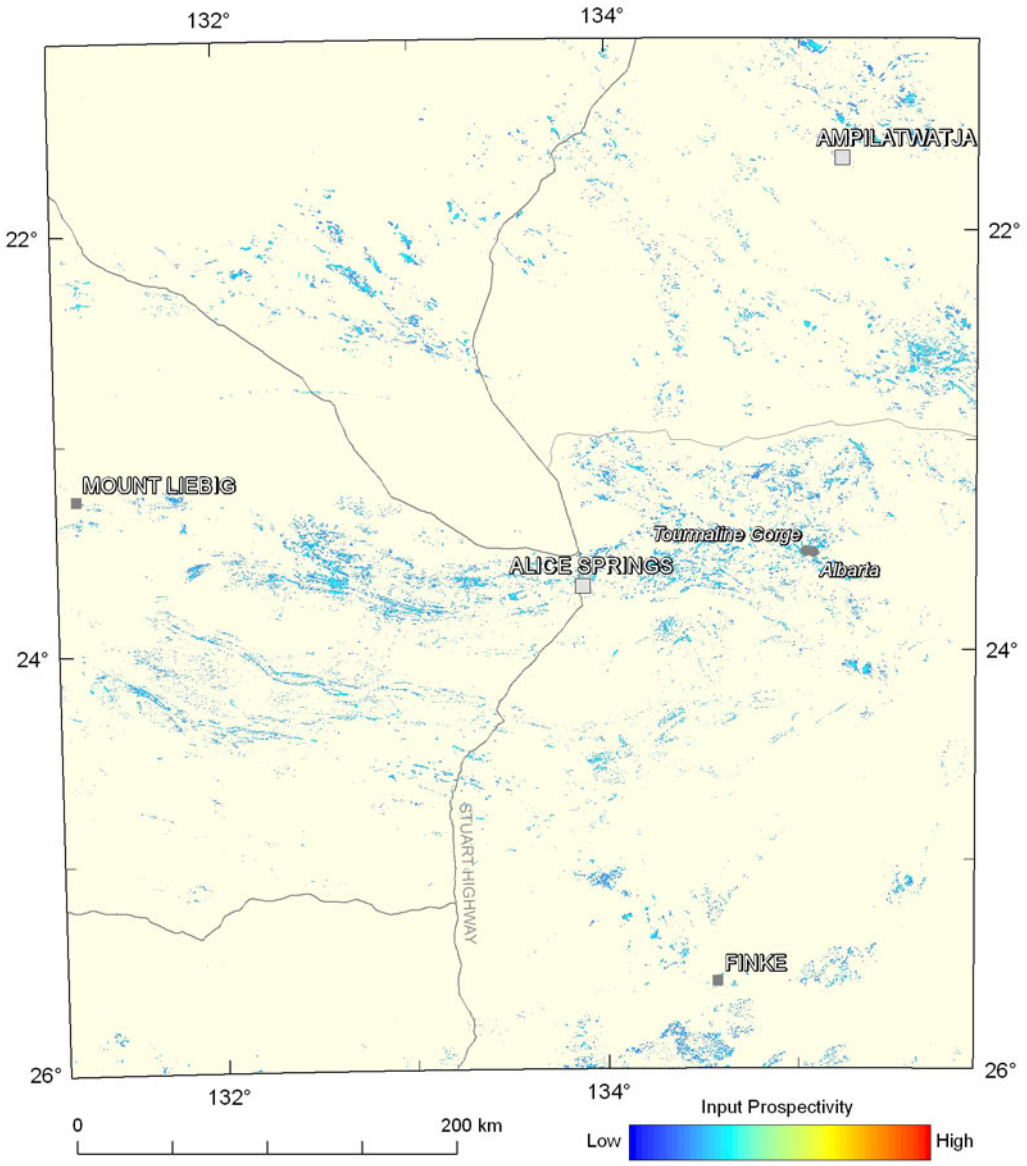

Figure 3.4.21: *Variations in the weighting for evidence of uranium deposition from the U^2/Th ratio. This criterion is identical for both the Precambrian and Phanerozoic assessments. The colour stretch for the mappable criteria used in the assessment for unconformity-related uranium systems uses a numerical range from the minimum to the maximum weighting of all criteria used (0.100 to 0.800; see Table 3.4.1; note: range is that for Precambrian unconformity systems), and utilises 20 equal-interval breaks.*

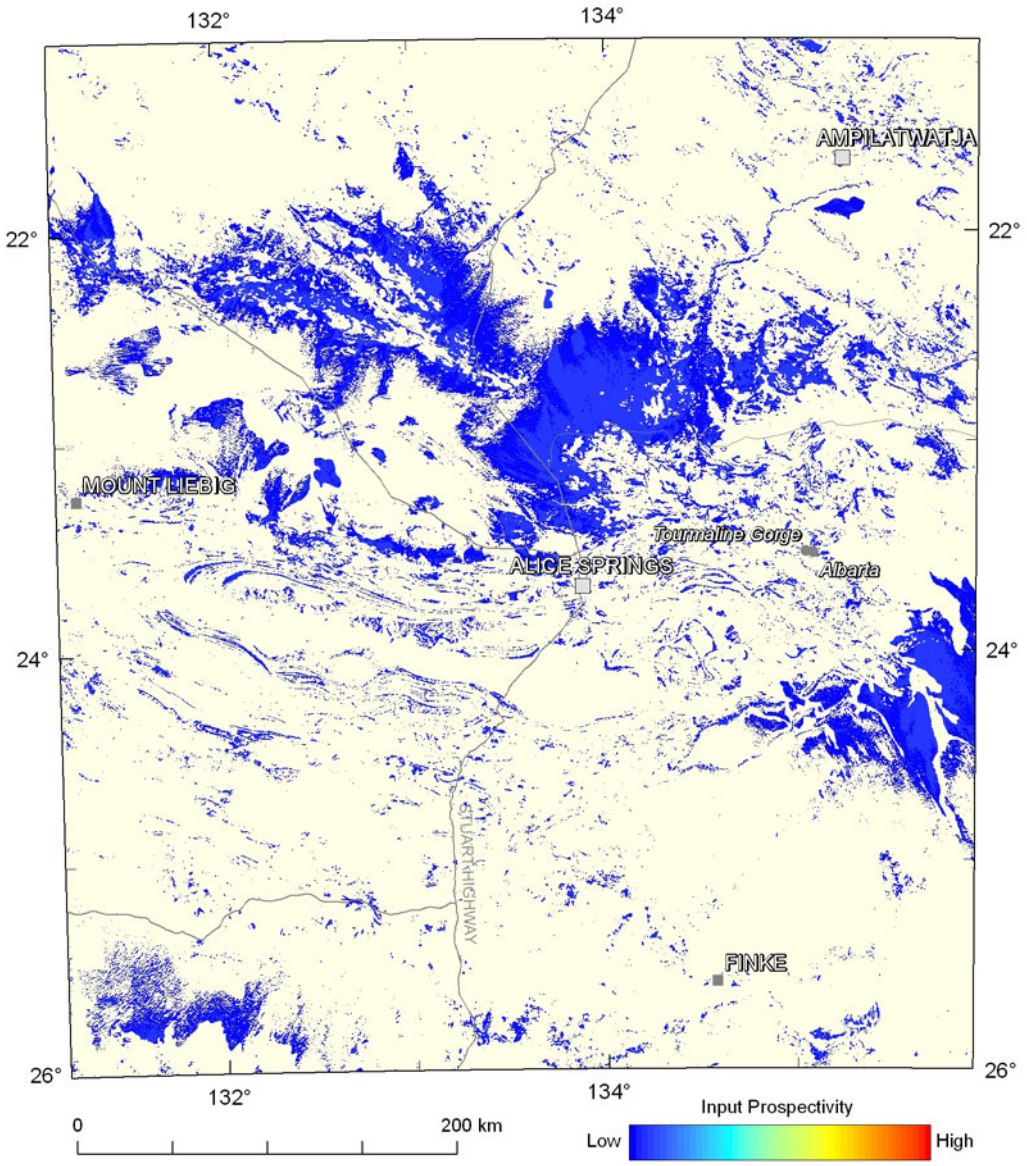

Figure 3.4.22: *Variations in the weighting for evidence of uranium deposition at depth from thorium enrichment at the surface. This criterion is identical for both the Precambrian and Phanerozoic assessments. The colour stretch for the mappable criteria used in the assessment for unconformity-related uranium systems uses a numerical range from the minimum to the maximum weighting of all criteria used (0.100 to 0.800; see Table 3.4.1; note: range is that for Precambrian unconformity systems), and utilises 20 equal-interval breaks.*

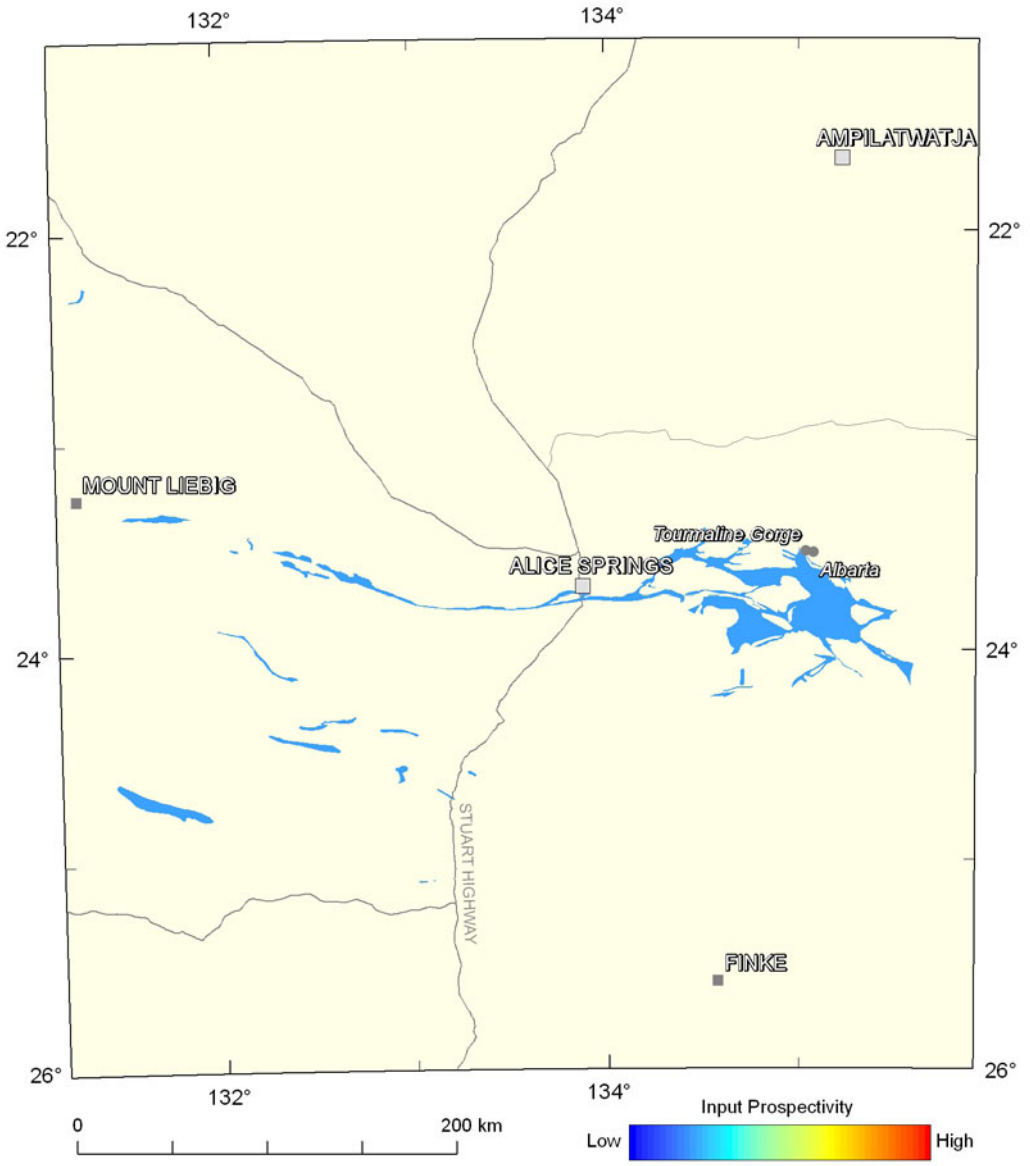

Figure 3.4.23: *Variations in the weighting for evidence of redox gradients in sediments of Precambrian age. The colour stretch for the mappable criteria used in the assessment for Precambrian unconformity-related uranium systems uses a numerical range from the minimum to the maximum weighting of all criteria used (0.100 to 0.800; see Table 3.4.1), and utilises 20 equal-interval breaks.*

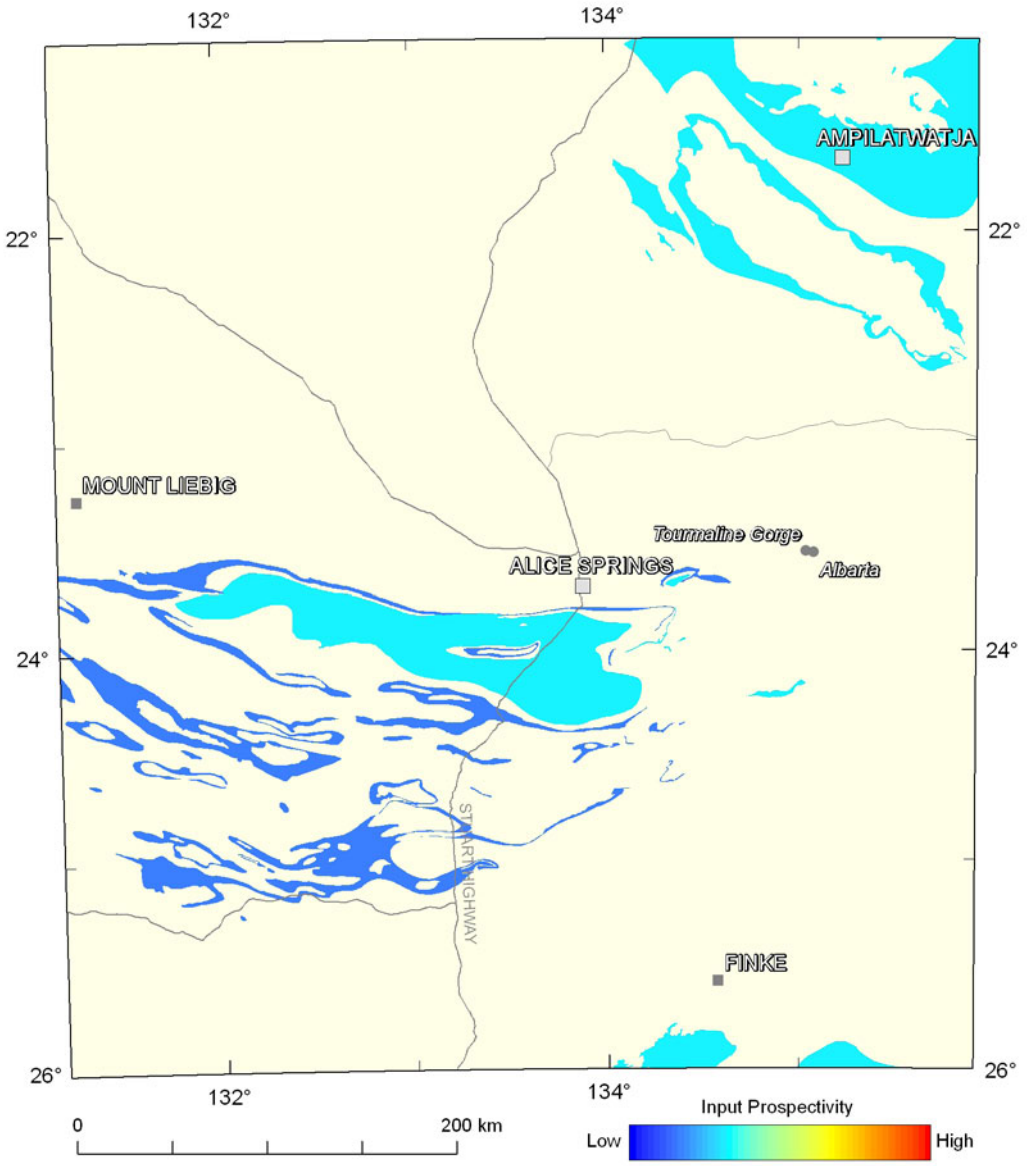

Figure 3.4.24: *Variations in the weighting for evidence of redox gradients in sediments of Phanerozoic age. The colour stretch for the mappable criteria used in the assessment for Phanerozoic unconformity-related uranium systems uses a numerical range from the minimum to the maximum weighting of all criteria used (0.030 to 0.800; see Table 3.4.2), and utilises 20 equal-interval breaks.*

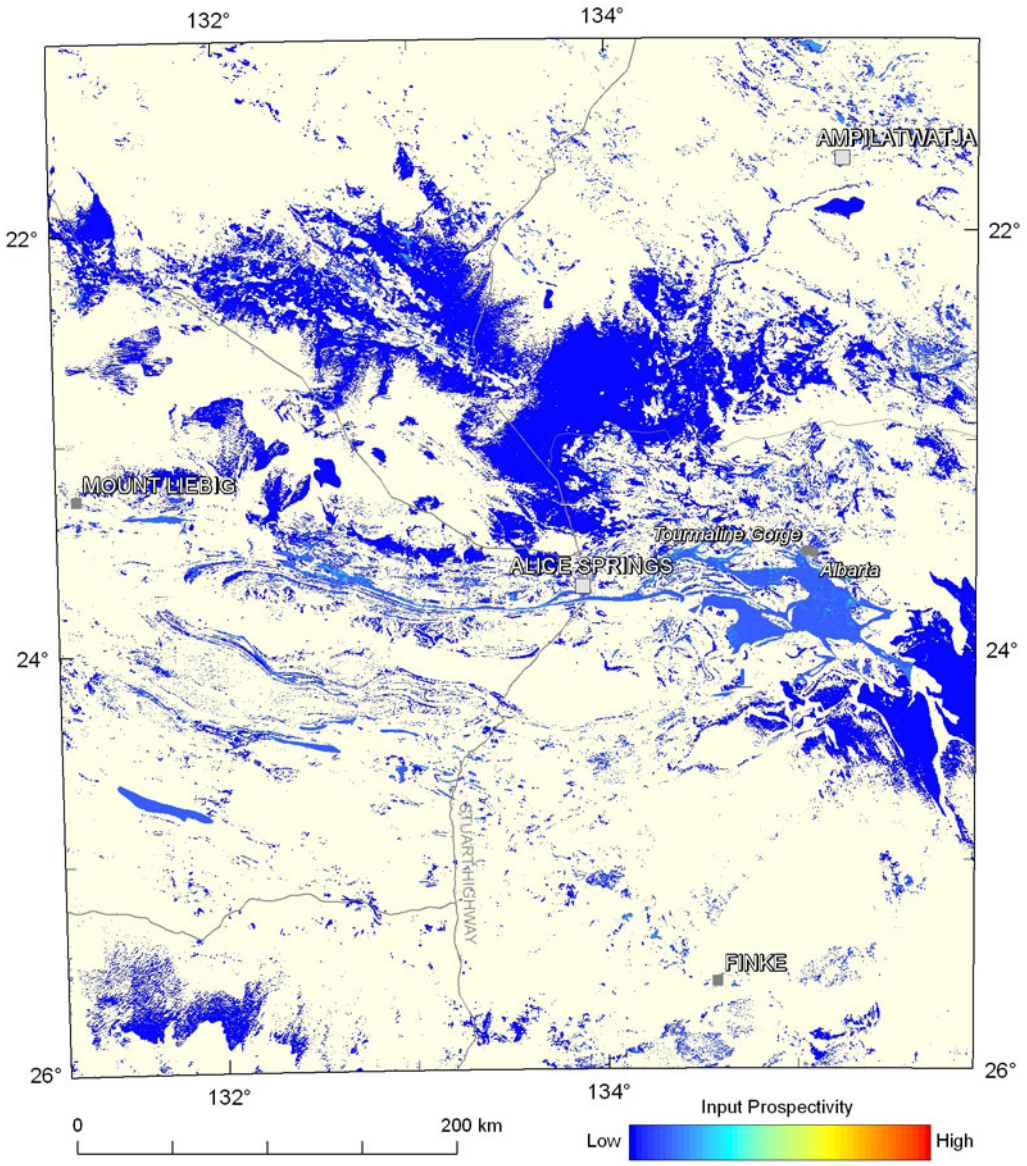

Figure 3.4.25: *Variation in the weightings for the depositional mechanisms system component for Precambrian unconformity-related uranium systems. The colour stretch for each mineral system component in the assessment for Precambrian unconformity-related uranium systems uses a numerical range from the minimum to the maximum weighting for each of the system components (0.030 to 0.630), and utilises 20 equal-interval breaks.*

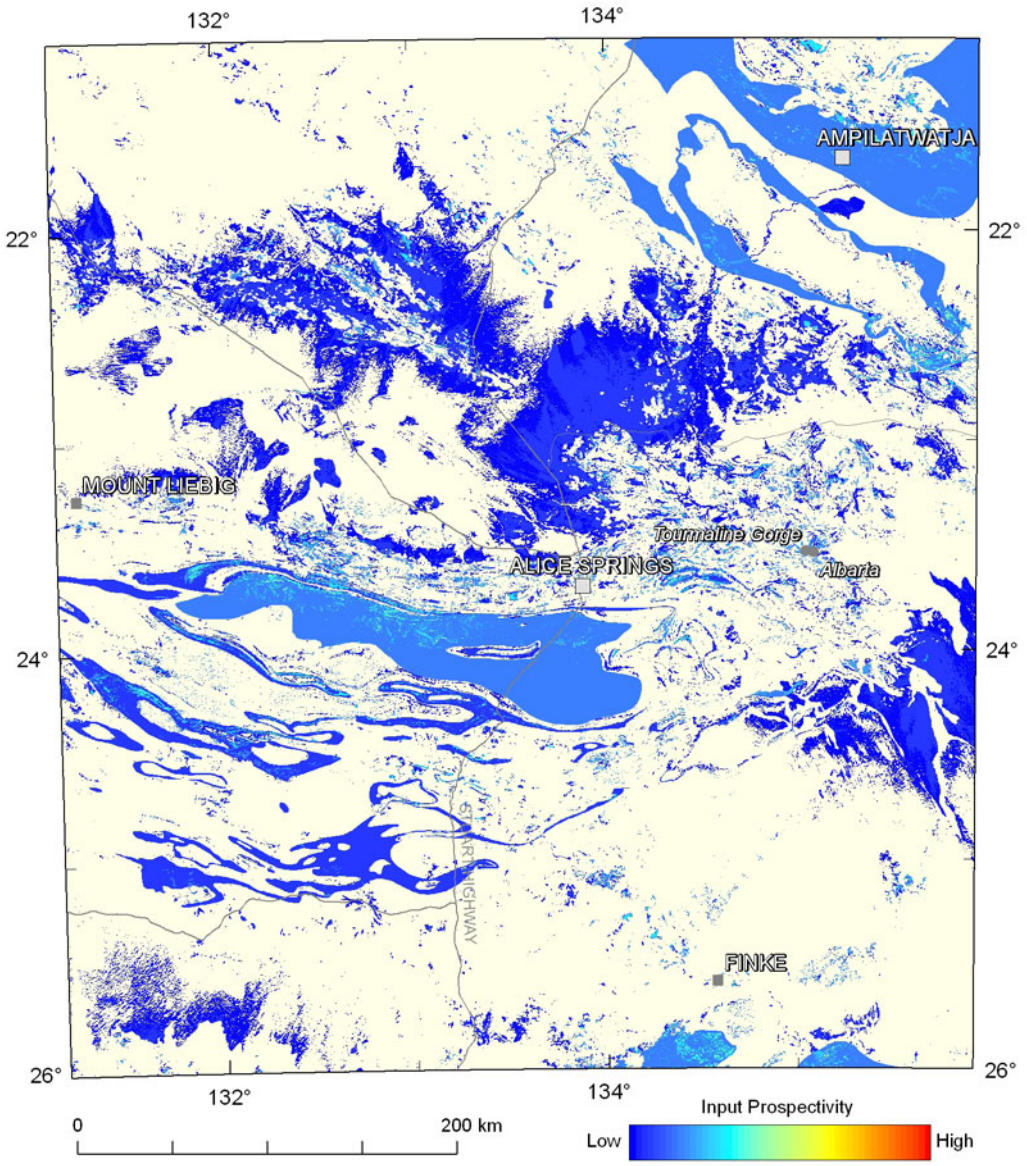

Figure 3.4.26: *Variation in the weightings for the depositional mechanisms system component for Phanerozoic unconformity-related uranium systems. The colour stretch for each mineral system component in the assessment for Phanerozoic unconformity-related uranium systems uses a numerical range from the minimum to the maximum weighting for each of the system components (0.010 to 0.490), and utilises 20 equal-interval breaks.*

3.4.4 Results

3.4.4.1 Precambrian unconformity-related uranium potential

Four areas have been highlighted in the assessment for Precambrian unconformity-related uranium systems (Figure 3.4.27), as follows:

- The area on the northern margin of the Amadeus Basin has moderate to high potential (A). This area corresponds with the basal unconformity of the Amadeus Basin and the uranium-enriched lithologies of the Heavitree Quartzite and the Bitter Springs Formation;
- Another area along the northeastern margin of the Amadeus Basin and south of the Harts Range (B). A number of prospects, including the possibly unconformity-related Albarta and Tourmaline Gorge prospects, occur in the region;
- A broad region of moderate to high potential occurs in the Georgina Basin (C) due to the potential source rocks and abundance of unconformities and fluid-flow pathways in this region; and
- The northern part of the Ngalia Basin (D) also has moderate potential due to the presence of suitable source rocks and a thick basin cover. A number of sandstone-hosted uranium prospects also occur within this region.

3.4.4.2 Phanerozoic unconformity-related uranium potential

Three areas have been highlighted in the assessment for Phanerozoic unconformity-related uranium systems (Figure 3.4.28), as follows:

- The region of highest potential occurs in the southern Davenport Province and extends south into the Georgina Basin (A). This region contains most of the essential elements of the unconformity-related uranium systems, including potential source rocks, unconformities, fluid-flow pathways, evaporitic sequences and carbonaceous units. Localised patches of higher potential occur within this broad region, particularly where there are carbonaceous units of the Arthur Creek, Chabalowe and Tomahawk formations;
- The area on the northern margin of the Amadeus Basin is again highlighted as having moderate to high potential for unconformity-related uranium mineralisation in the Phanerozoic Eon (B). This could occur if uranium was leached from the pre-existing source rocks or uranium-enriched units of the Amadeus Basin and trapped at an unconformity; and
- A region of mostly moderate potential occurs along the margin of the Eromanga Basin (C). It broadens in the northeastern part due to the overlap with the basal unconformity of the Amadeus Basin and also in the southern part due to the presence of the Bulldog Shale. The Bulldog Shale is both a reductant and an aquitard, and is associated with the uranium deposits in the Frome Embayment and other uranium occurrences within the Eromanga Basin (Skirrow, 2009).

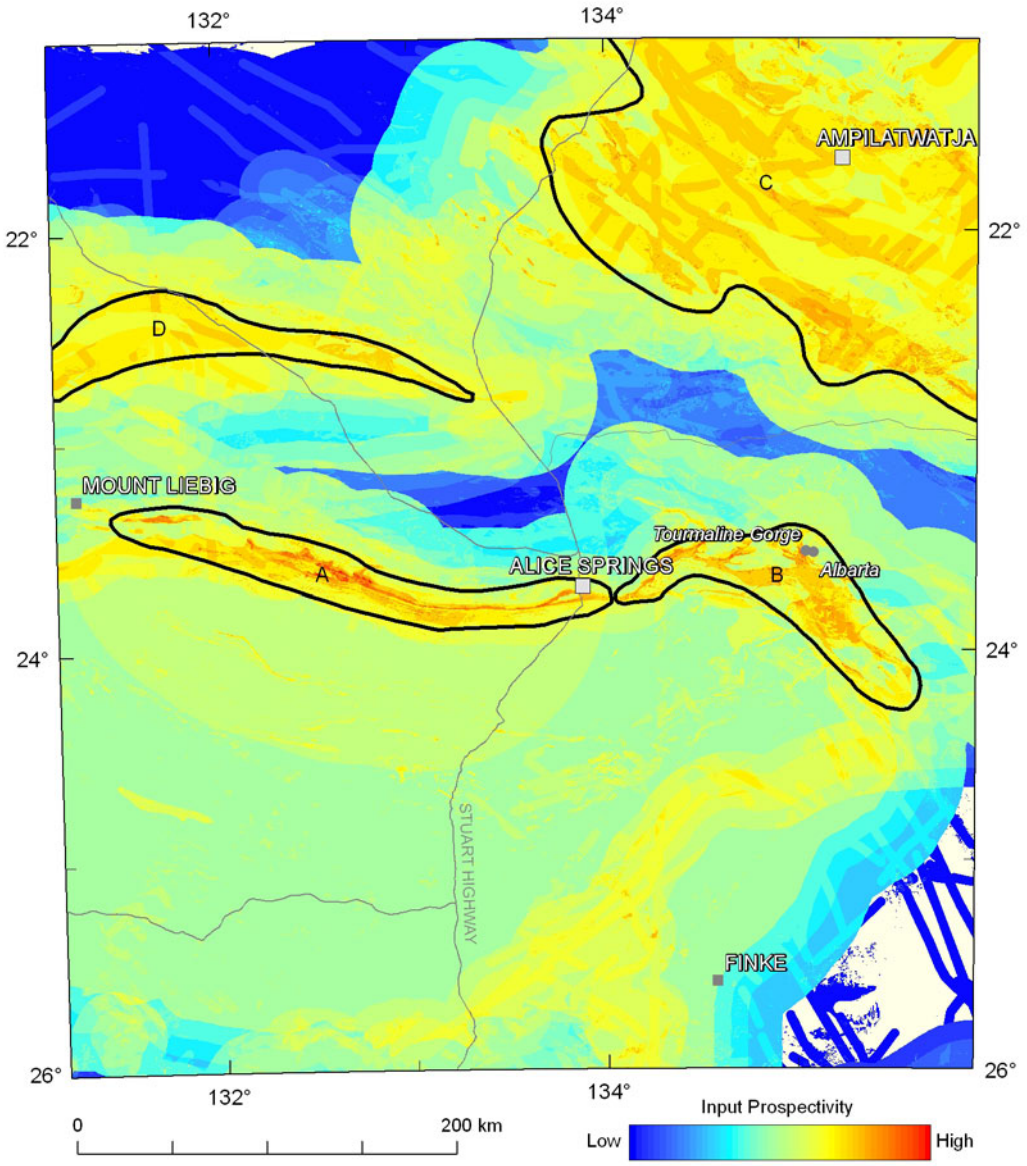

Figure 3.4.27: *Final modelled potential for Precambrian unconformity-related uranium systems. The colour stretch used for this figure has a minimum value of 0.008 and a maximum value of 0.333, and utilises 20 equal-interval breaks. Areas outlined in black are discusses in Section 3.4.4.1.*

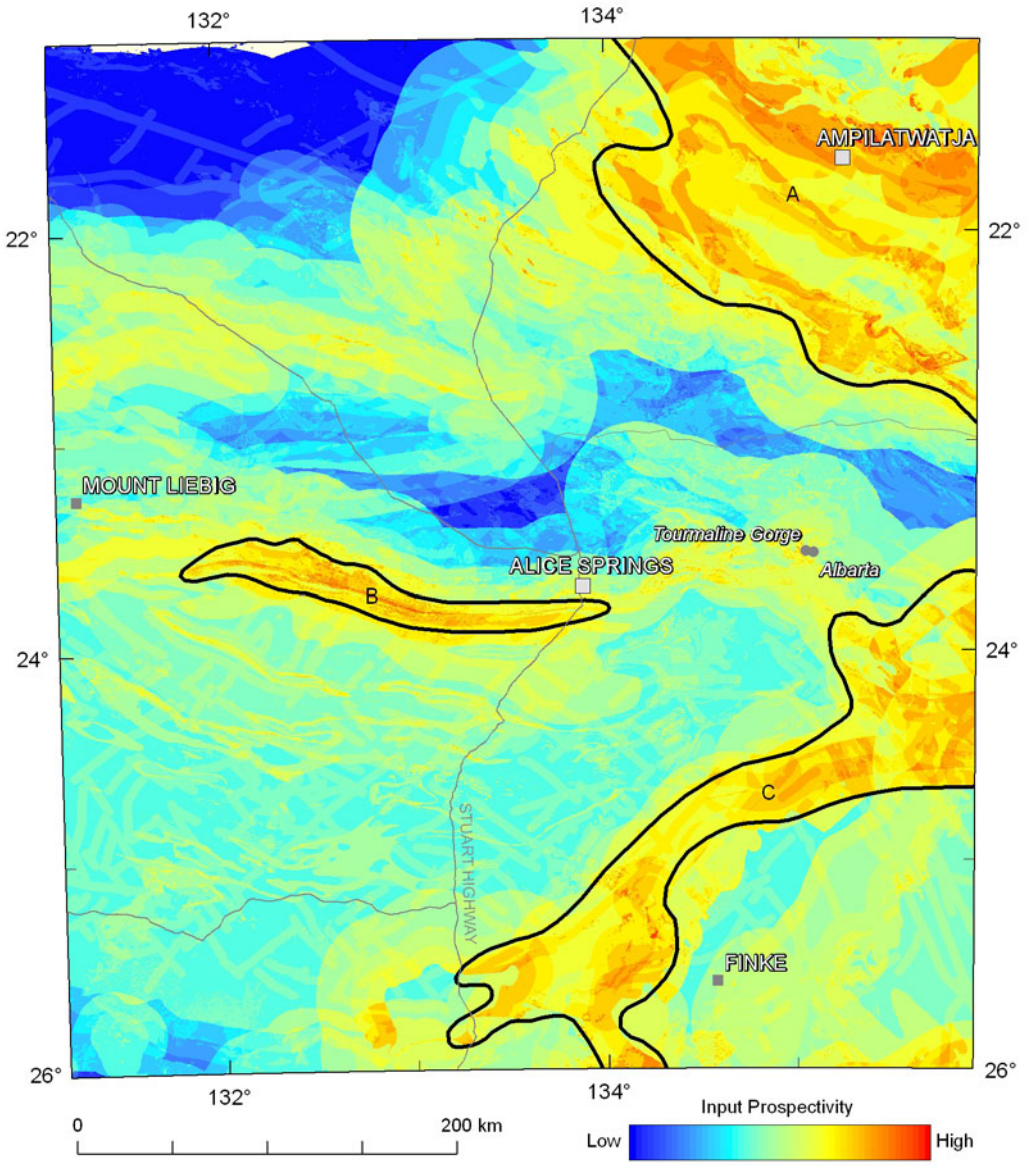

Figure 3.4.28: *Final modelled potential for Phanerozoic unconformity-related uranium systems. The colour stretch used for this figure has a minimum value of 0.003 and a maximum value of 0.281, and utilises 20 equal-interval breaks. Areas outlined in black are discusses in Section 3.4.4.2.*

3.5 MAGMATIC-RELATED URANIUM SYSTEMS

A. Schofield and R.G. Gallagher

According to the classification scheme of Skirrow *et al*. (2009), magmatic-related uranium systems comprise one end-member of a family of uranium systems (Figure 3.1.1). While other uranium systems, such as IOCG-U (Section 3.3), may involve igneous rocks in their genesis (e.g., as a uranium source or fluid-flow driver), true magmatic-related systems form as a result of fundamental igneous processes, including partial melting, magmatic evolution processes, and the exsolution of magmatic fluids. The magmatic-related family of uranium systems may be subdivided into two main subcategories: orthomagmatic and magmatic-hydrothermal. The latter of these has the greatest potential to form deposits of economic significance.

Relative to better-known styles of uranium mineralisation, magmatic-related uranium systems are poorly understood, and many of the key processes involved in generating a uranium deposit from a favourable granite remain inadequately resolved. Understanding of these processes is complicated by the fact that a syn-magmatic genetic link cannot always be easily established between mineralisation and the host igneous rocks, and many instances of igneous-hosted uranium mineralisation are probably associated with later remobilisation. As such, the assessment described below should be considered as preliminary and should be revisited as additional studies on known mineralisation become available.

Unlike the similar assessment undertaken for South Australia (Schofield and Connolly, 2011), the assessment performed during this study has focused on the potential for magmatic-related uranium systems solely in intrusive igneous rocks.

3.5.1 Deposit overviews

While a number of notable examples of magmatic-related uranium mineralisation occur globally, known mineralisation is rare in Australia despite the widespread occurrence of uranium-rich igneous rocks (Lambert *et al*., 2005; Schofield, 2009). Several deposits thought to be associated with volcanic rocks occur in northern Queensland and intrusive-related mineralisation is known most prominently from South Australia (McKay and Miezitis, 2001). Summaries of the Crocker Well (Australia), Rössing (Namibia), Ross Adams (Alaska, USA) and Kvanefjeld (Greenland) deposits are given in Schofield and Connolly (2011), and as such only a brief description will be provided here.

3.5.1.1 Magmatic-related uranium deposits in Australia

Intrusive-related uranium mineralisation in Australia is best known from the Olary Domain of the Curnamona Province in South Australia and, to a lesser extent, the Gascoyne Complex of Western Australia (McKay and Miezitis, 2001). In the Gascoyne Complex minor uranium mineralisation is associated with pegmatites and is analogous to the Rössing deposit (Carter, 1982).

At Crocker Well in the Olary Domain, uranium is hosted within Mesoproterozoic sodic trondhjemite and monzogranite with abundant pegmatites (Fricke, 2008). Mineralisation is considered to be genetically related to the host monzogranites (King, 1954; Campana and King, 1958; Ashley, 1984). Uranium-lead geochronology undertaken on brannerite is consistent with such an interpretation (Ludwig and Cooper, 1984). The most significant uranium mineralisation is contained within locally developed phlogopitic breccia bodies, although mineralisation also occurs in veins, fractures and pegmatites (King, 1954; Campana and King, 1958; Ashley, 1984). Faulting also appears to have a control on the location of mineralised zones (Campana and King, 1958; Wilson and Fairclough, 2009). Uranium mineralisation is thought to have resulted from volatile (probably F) saturation and release, with uranium partitioning into the exsolved magmatic fluid and deposited in zones of

fracturing and brecciation as a result of ligand destabilisation, due to temperature and pressure decrease, or an increase in Ca activity (Ashley, 1984; Schofield, 2011).

3.5.1.2 Prospects within the study area

A number of small intrusive-related uranium prospects occur within the study area, the main characteristics of which are summarised in Table 3.5.1. The Adnera, Cockroach Dam, Crystal Creek and Mt Denison prospects are hosted within granitic rocks. The Adnera prospect, hosted within alaskites, may have affinities with Rössing-style mineralisation (Beyer *et al*., 2010). Details of these prospects are only able to be gathered from ASX releases and, as such, a genetic link with magmatism cannot be established beyond the general evidence provided by the close spatial association. As well as the granite-hosted occurrences, a number of uranium-rich REE deposits and prospects occur within the eastern Aileron Province, including pegmatites in the Reynolds Range area (Hussey, 2003) and the Nolans Bore REE-P-U-Th deposit, which is possibly associated with carbonatitic or alkaline magmatism, as suggested by Sr and Nd isotopic constraints (Maas *et al*., 2009; Huston *et al*., 2011b). Uranium-REE pegmatites in the Entia pegmatite field lie at the eastern extent of a northwest-trending corridor of uranium and REE anomalism extending to Nolans Bore (Whelan *et al*., 2008). This corridor includes known alkaline magmatism (e.g., Mordor Igneous Complex, Mud Tank Carbonatite), and is spatially associated with the Woolanga Lineament (Close and Scrimgeour, 2009; Beyer *et al*., 2010). Ages for the alkaline rocks and pegmatites are different.

3.5.1.3 Major international deposits

The Rössing deposit in Namibia represents the best known magmatic-related uranium deposit in the world. Uranium mineralisation is hosted in alaskitic pegmatites interpreted to have been derived from low temperature, low-degree partial melting of uranium-rich metasedimentary basement (McDermott *et al*., 1996; Cuney and Kyser, 2008). Based on a lack of element correlations, it has been suggested that uranium was not concentrated as a result of fractional crystallisation (Nex *et al*., 2001; Kinnaird and Nex, 2007). However, such a lack of correlation would be expected with the post-magmatic mobilisation of uranium that has been observed at Rössing (Nex *et al*., 2002).

The Kvanefjeld and Ross Adams deposits share many similarities to each other. Both deposits are hosted in peralkaline, highly fractionated igneous rocks which were intruded to shallow crustal depths (Thompson *et al*., 1982; Bailey, 2001; Sørensen, 2001). Mineralisation at Ross Adams occurs in pipe-like bodies occurring along intrusive phase contacts within the granite, associated with syn-magmatic faults (Thompson, 1988), and in fluorite-rich veins (Staatz, 1978). At Kvanefjeld, mineralisation consists predominately of disseminated uranium-rich magmatic minerals, but late-stage veins also host uranium (Cuney and Kyser, 2008). Mineralisation at Ross Adams is interpreted to have occurred in response to devolatilisation of the magma chamber as it ascended to high crustal levels (Thompson, 1982). Exsolution of a late magmatic fluid is also evidenced at Kvanefjeld by the presence of mineralised veins.

Table 3.5.1: Summary of magmatic-related uranium prospects within the study area

NAME	LOCATION (LAT/LONG)	DESCRIPTION	HOST UNIT GEOCHEMISTRY	REFERENCES
Adnera	-21.9822, 134.2328	The Adnera U prospect occurs in cropping out, weathered, leucocratic alkali feldspar granite (alaskite). On the Barrow Creek 250k map sheet, this granite is described as biotite-muscovite, medium-grained, even-grained to porphyritic, and tourmaline-bearing. Uranium is hosted in a range of secondary U phosphate minerals which appear to replace biotite (and perhaps apatite), and vein apatite, K-feldspar and quartz. Uranium minerals also occur on fracture surfaces as yellowish coatings, and are intergrown with fine kaolinite. The best rock chip sampled gave 540 ppm U.	Only two samples correspond to the host rocks for Adnera. K_2O is moderately high. The highest U value is 8.5 ppm. HFSE contents are low. The granites appear to be unfractionated. ASI is >1.1, which together with other geochemical criteria suggests that this granite is a probable S-type.	Uramet Minerals Ltd. ASX releases
Cockroach Dam	-23.4992, 132.4905	The Cockroach Dam prospect is hosted in U-rich igneous rocks of the Teapot Granite Complex. Higher U grades at Cockroach Dam are the result of secondary processes, with elevated U occurring in fractures, proximal to basic dykes and shearing, around other veins and alteration zones within the host granite, and at granite contacts with the surrounding sediments. Primary U mineralisation has not been encountered. The highest grades are found where the granite is strongly fractured, but drill intersections with 20–50 ppm U are common in the host granite. The best drill intersection was 2 m at 876 ppm U_3O_8, but exploration during the 1970s yielded results of up to 0.22% U_3O_8.	The Teapot Granite Complex is potassic with K_2O mostly >5.5%. It is weakly peraluminous. HFSE are low, while LILE are relatively high. Th/U ratios show disturbance, with high values dominating, suggesting U loss (e.g., due to leaching). Despite this, U is mostly >5 ppm, with values up to 31 ppm. The granite is strongly fractionated and is oxidised. Zircon saturation temperatures are relatively low (~760-840^{o}C).	Crossland Uranium Mines Ltd. ASX releases and website
Crystal Creek	-22.2192, 131.3408	Two radiometric anomalies occur at the Crystal Creek prospect, referred to as Anomalies A and B. Elevated U values are associated with clay, Fe and pink-red (possibly potassic) altered granite, as well as greisenised granite. Drilling into altered granite at Anomaly A gave results up to 208 ppm U_3O_8 across 1 m. Anomaly B appears to be more highly mineralised, with surface U values of up to 4000 ppm. Thorium values are low, and Th/U is universally less than one for the analyses given. Mineralisation is poddy, and associated with ironstones in a NE-striking fault zone ranging in width from 0.3–12 m. Uranium is associated with altered Ti- and Fe-oxides, and brannerite and coffinite have been tentatively identified. The best drill intersection at Anomaly B was 3 m at 346 ppm U_3O_8. High U at Anomaly B is sometimes associated with elevated Cu (up to 1.1%, but commonly ≥0.1%).	The Yarunganyi Granite is weakly to moderately peraluminous, with elevated K_2O. Th/U is mostly high, indicating U loss or preferential transport of Th. The highest U content in the samples examined was 12 ppm. The unit is moderately fractionated, and is overall reduced. More broadly, the Southwark Suite, to which the Yarunganyi Granite belongs, has elevated U (up to 22.5 ppm), high Th, elevated HFSE, moderately high K_2O, and is strongly fractionated, reduced, and shows low zircon saturation temperatures (<853^{o}C).	Uranium Exploration Australia Ltd. ASX releases
Mt Denison project	-22.1309, 132.1887 (approx.)	A surface U anomaly of 4 km has been identified over the Wangala Granite based on the results of a Mobile Metal Ion geochemical survey. Rock chip samples taken from veined and altered Wangala Granite returned U values of 268–979 ppm U_3O_8. High U values have been attributed to secondary U minerals, although primary mineralisation may be present at depth.	The Wangala Granite has an S-type composition and is peraluminous. It is fractionated. Fluorine contents are high (generally >1000 ppm), reaching very high levels in altered samples. Incompatible elements are enriched relative to compatible elements. Uranium contents are elevated (>10 ppm in unaltered samples), particularly in altered samples. Calculated zircon saturation temperatures are low (<840^{o} C).	Beyer *et al*. (2012); Callabonna Uranium Ltd. ASX releases

Table 3.5.2: Theoretical and mappable criteria for magmatic-related uranium systems

MINERAL SYSTEM COMPONENT	CRITERIA		DATASET	IMPOR-TANCE	APPLIC-ABILITY	CONFI-DENCE	WEIGHTING	COMMENTS
	THEORETICAL	MAPPABLE						
Source	Distribution of broadly felsic intrusive igneous rocks	Felsic intrusive igneous rocks	Basement solid geology (see Appendix 1)	0.9	0.9	0.9	0.729	Compositional classification is taken from geological unit descriptions
		Intrusive igneous rocks with a felsic composition		0.9	0.5	0.9	0.405	
	High U melts	Igneous rocks showing magmatic U enrichment	Basement solid geology (see Appendix 1); geochemical data	0.6	0.7	0.7	0.294	Defined as values between the 75th and 90th percentiles
		Igneous rocks showing a high degree of magmatic U enrichment		0.6	0.8	0.7	0.336	Defined as values trending towards, or greater than, the 90th percentile
	Magmatic-stage U concentration via fractional crystallisation	Uncertain degree of fractionation	Basement solid geology (see Appendix 1); geochemical data	0.8	0.3	0.6	0.144	Fractionated granites were determined using the Rb-Ba-Sr plot of El Bouseilly and El Sokkary (1975) and Rb/Sr values
		Moderately fractionated igneous rocks		0.8	0.4	0.6	0.192	
		Fractionated igneous rocks		0.8	0.7	0.6	0.336	
		Highly fractionated igneous rocks		0.8	0.8	0.6	0.384	
	Breakdown of U-bearing minerals in magma source region	Intrusive igneous rocks with high zircon saturation temperatures	Basement solid geology (see Appendix 1); geochemical data	0.3	0.6	0.6	0.108	Temperatures are based on zircon saturation temperature calculated according to Watson and Harrison (1983). High temperatures are defined as greater than the 75th percentile of all values
		Intrusive units with transitional zircon saturation temperatures		0.3	0.4	0.6	0.072	Transitional from low to high
	Sources of ligands	Igneous rocks with high F	Basement solid geology (see Appendix 1); geochemical data; literature review	0.5	0.7	0.6	0.210	Defined as values greater than the 75th percentile. May also be applicable to enhancing U solubility in the melt
		Fluorite-bearing igneous rocks		0.5	0.5	0.5	0.125	Rocks containing fluorite are interpreted to be high in F. It is recognised in the confidence value that fluorite may not be entirely magmatic
Drivers	Fluid exsolution and volatile release	Presence of textural features indicating fluid exsolution (e.g., miarolitic cavities)	Basement solid geology (see Appendix 1); literature review	0.6	0.9	0.7	0.378	See text for details
		Units with good evidence for high-level intrusion		0.6	0.7	0.7	0.294	
		Units with moderate evidence for high-level intrusion		0.6	0.4	0.7	0.168	
		Units with poor evidence for high-level intrusion		0.6	0.2	0.7	0.084	
		Volatile-rich units or units exhibiting evidence of volatile release (breccias, greisens, veins, tourmaline-bearing rocks)		0.6	0.7	0.7	0.294	
Fluid-flow pathways and architecture	Fluid flow along permeable structures	Faults buffered to 2.5 km	Basement solid geology (see Appendix 1)	0.7	0.5	0.5	0.175	Faults could not be separated by ages. This is reflected in the confidence value
	Fluid flow along rheological contrasts	Intrusive contacts (non-faulted) buffered to 2.5 km	Basement solid geology (see Appendix 1)	0.4	0.7	0.8	0.224	

Table 3.5.2 (cont'd): Theoretical and mappable criteria for magmatic-related uranium systems

MINERAL SYSTEM COMPONENT	CRITERIA		DATASET	IMPOR-TANCE	APPLIC-ABILITY	CONFI-DENCE	WEIGHTING	COMMENTS
	THEORETICAL	MAPPABLE						
Depositional mechanisms	Chemical depositional sites	Units containing a major component of Fe-rich rocks	Basement solid geology (see Appendix 1)	0.4	0.5	0.8	0.160	Buffer contact between potentially reactive rocks and intrusives to 2.5 km (excludes faulted contacts)
		Units containing a minor component of Fe-rich rocks		0.4	0.3	0.8	0.096	
		Units containing a major component of carbonate-rich rocks		0.4	0.6	0.8	0.192	
		Units containing a minor component of carbonate-rich rocks		0.4	0.4	0.8	0.128	
		Units containing a major component of other Ca-rich rocks		0.4	0.2	0.8	0.064	
		Units containing a minor component of other Ca-rich rocks		0.4	0.1	0.8	0.032	
	Potential sites of ligand destabilisation	Units with breccias and/or veins	Basement solid geology (see Appendix 1)	0.7	0.6	0.6	0.252	Reduction in temperature and pressure are important mechanisms for fluorite crystallisation and therefore ligand destabilisation
		Units with veins only		0.7	0.8	0.6	0.336	
	Direct evidence of elevated U	U^2/Th values one standard deviation above the mean for each unique geological unit	Radiometric map of Australia (Minty et al., 2010); Surface geology of Australia (Raymond and Retter, 2010)	0.7	0.7	0.6	0.294	See text for details
		U^2/Th values two standard deviations above the mean for each unique geological unit		0.7	0.8	0.6	0.336	

3.5.2 Mineral system model for magmatic-related uranium systems

Magmatic-related uranium systems involve processes of melt generation, magmatic concentration of uranium in the melt, fluid-mediated concentration of uranium, and uranium deposition. Details of this will only be briefly described below, as the mineral systems model has been described in previous investigations (Schofield, 2010; Schofield and Connolly, 2011).

The most favourable magmas for magmatic-related uranium deposits are peralkaline melts interpreted to have been derived from the upper mantle, such as those present at Kvanefjeld and Ross Adams (Thompson *et al*., 1982; Thompson, 1988; Bailey *et al*., 2001). Crustally-derived magmas may also be favourable, as is the case at Crocker Well (Fricke, 2008; Fricke and Conor, 2010). Initial uranium content of the magma is commonly largely a function of the source region, and thus melting of uraniferous basement or metasomatised mantle is advantageous. Magmas with the highest potential are likely to be those that are restite-poor, as this allows uranium to be available to progressive magmatic concentration. Following this, high temperature melts are most favourable (Sawka and Chappell, 1986; Chappell *et al*., 2000), although examples of possible magmatic-related prospects within the study area do not have high zircon saturation temperatures (Table 3.5.1).

Magmatic concentration of uranium is best facilitated by fractional crystallisation, owing to the incompatible behaviour of uranium in early crystallising mineral phases. High uranium solubility within the melt allows uranium to concentrate into the final melt phases, and is best achieved with peralkaline bulk rock compositions or high halogen concentrations (Peiffert *et al*., 1996).

Fluid-mediated concentration of uranium is probably extremely important, and known examples of magmatic-related uranium mineralisation involve a magmatic fluid phase. Models for the genesis of the Crocker Well and Ross Adams deposits invoke volatile saturation and exsolution (Thompson, 1982; Schofield, 2011), and the presence of mineralised hydrothermal veins at Ross Adams and Kvanefjeld (Staatz, 1978; Cuney and Kyser, 2008) argue in favour of the importance of a magmatic fluid phase. Known prospects within the study area also exhibit evidence of fluid interaction and volatile enrichment (Table 3.5.1). Magmas intruded to high levels are most likely to exsolve a late-stage magmatic fluid (‘first boiling’; Candela, 1997), and the host rocks from Kvanefjeld and Ross Adams show evidence of being intruded to depths of two to four kilometres (Thompson *et al*., 1982; Sørensen, 2001). Fluid-flow pathways for the magmatic fluids may include syn-magmatic faults, fractures related to rheological contrasts (Thompson *et al*., 1982; Wilson and Fairclough, 2009) and brecciated zones or other zones of fracturing (e.g., Ashley. 1984).

Processes for the deposition of uranium are enigmatic. Low-grade uranium mineralisation may occur as a magmatic mineral phase within the host unit. However, the best uranium grades are most likely to result from deposition from a fluid phase (see below for discussion).

3.5.3 System components and mappable criteria

Using the general mineral systems model described above, mappable geological criteria have been developed for each of the four key system components (see Section 3.1): sources, drivers, fluid-flow pathways and architecture, and depositional mechanisms. These criteria are listed in Table 3.5.2 and are described below. The source system component dominates in the assessment for magmatic-related uranium systems. This is due to the importance of the host igneous rocks in these systems together with difficulties identifying mappable proxies for processes for the remaining three system components.

3.5.3.1 Data distribution issues

The knowledge-driven approach used in this assessment minimises bias towards areas of known mineralisation. However, data distribution is non-uniform across the study area and requires

accounting for so as to avoid skewing results towards data-rich regions. This is particularly the case with geochemical data, which have been used to develop many of the criteria used in the assessment for magmatic-related uranium systems. A number of units contained within the solid geology dataset lack suitable geochemical data. In order to prevent unnecessary downgrading of the potential of these units, average applicability and confidence values (calculated from all units containing geochemical information) were assigned. Values for importance were not attributed, as this is set for each mappable criterion. For other criteria based on geological observations (e.g., evidence of high-level intrusion), attribution of average values has not been applied to units containing no indication of the targeted favourable feature, since the data coverage is generally complete. However, it is possible that in some instances the absence of favourable geological features may be due to incomplete observations or recording, although this is difficult to account for. Values of zero were substituted for a nominal value of 0.01 during this assessment.

3.5.3.2 Sources

The sources system component for the magmatic-related uranium assessment consists of sources of favourable magmas (representing uranium sources) and uranium-bearing magmatic-hydrothermal fluids. Four criteria have been used to map favourable magmas, while a single criterion is used to map favourable fluids. The four criteria used for identifying favourable magmas are:

- Distribution of broadly felsic intrusive igneous rocks;
- Intrusive igneous rocks with elevated uranium content;
- Fractionated intrusive igneous rocks; and
- Intrusive igneous rocks with high magmatic temperatures.

More primitive igneous rocks, with the exception of silica-undersaturated alkaline rocks, have overall low uranium contents and are therefore unsuitable for forming magmatic-related uranium deposits. In comparison, felsic igneous rocks have typically undergone at least one episode of uranium concentration and are accordingly more favourable. The distribution of felsic intrusive igneous rocks was determined using the basement solid geology dataset (see Appendix 1) and related compositional data from GA's stratigraphic units database (http://dbforms.ga.gov.au/www/geodx.strat_units.int). Two categories have been used based on the relative abundance of felsic igneous components within the unit, with units having only a felsic component weighted lower than units dominated by felsic rocks (Figure 3.5.1; Table 3.5.2). Although peralkaline rocks are highly favourable, these are, with the exception of the Mud Tank Carbonatite, not observed within the study area.

Geochemical data were used to determine the remaining three sources system component criteria. Geochemical data were compiled from Geoscience Australia's OZCHEM dataset which was supplemented with a small number of samples from the NTGS whole rock geochemical dataset (accessed at http://geoscience.nt.gov.au/GeosambaU/strike_gs_webclient/default.aspx).The data were filtered to remove non-igneous, altered and/or weathered samples.

Units with elevated uranium (Figure 3.5.2) may indicate derivation from uranium-rich source regions (if they are relatively unevolved) and represent good sources for subsequent hydrothermal upgrading of uranium. In order to determine units with elevated uranium, samples with Th/U values significantly above or below the mean value for granitic rocks were also filtered out. Values for the 75th (7.5 ppm) and 90th (13.5 ppm) percentiles were calculated for the filtered geochemical data and were set as 'high' and 'very high' uranium respectively. Each unit was then assessed to determine the degree of enrichment and classed either as 'high', 'very high' or 'low' (less than the 75th percentile). Geochemical data were supplemented by uranium channel radiometric data. Mean uranium values were calculated for each unit and classified using the same percentile breaks used for the geochemical data. The rating for the degree of uranium enrichment was then modified using these data. The weighting assigned for the importance value for this criterion is relatively low in

recognition that elevated uranium content, while favourable, is not diagnostic of the potential for generating significant uranium grades.

The incompatible behaviour of uranium in major rock-forming minerals allows it to concentrate in the melt during fractional crystallisation. While it appears that the host rocks for Crocker Well are only moderately fractionated (Schofield, 2011), both the Kvanefjeld and Ross Adams deposits are hosted by highly differentiated rocks (Thompson *et al*., 1982; Bailey, 2001). Fractionated granites were identified using the Rb-Ba-Sr ternary plot of El Bouseilly and El Sokkary (1975), Rb/Sr values, and unit descriptions in Budd *et al*. (2001). Five categories were used to describe the degree of fractionation: unfractionated, uncertain degree of fractionation, moderately fractionated, fractionated and highly fractionated. These categories were assigned subjectively based on their location on the Rb-Ba-Sr diagram, and were weighted accordingly (Figure 3.5.3; Table 3.5.2).

If a unit contains a high percentage of uranium-rich restite mineral phases (e.g., zircon), uranium will be unable to concentrate in the melt during fractionation. High-temperature melts are likely to be restite-poor (Chappell *et al*., 2000). These have been identified using the zircon saturation temperature (Figure 3.5.4), which has been calculated according to Watson and Harrison (1983). The 75th percentile has been selected as the cutoff for 'high' temperatures, corresponding to a zircon saturation temperature of 837^{o}C. Units with zircon saturation temperatures straddling this threshold have been designated as having 'transitional' temperatures (Table 3.5.2). Whilst theoretically important, a low importance value has been assigned for this criterion since known occurrences of magmatic-related uranium in the study area typically have low zircon saturation temperatures (Table 3.5.2).

As mentioned above, only one criterion has been used to map favourable fluids. The following criterion is used to identify potential sources of ligands:

- Igneous rocks with high fluorine.

Fluorine-bearing fluids represent the most likely candidate for a favourable magmatic fluid for generating magmatic-related uranium mineralisation. At Crocker Well, fluorite and other F-rich minerals (e.g., fluorapatite) occur in close association with uranium-bearing minerals (King, 1954; Whittle, 1954; Ashley, 1984; Schofield, 2011). Breccias hosting the most significant mineralisation have elevated F content relative to the host granite, suggesting an influx of volatiles contemporary with the introduction of uranium (Ashley, 1984). At Ross Adams, evidence of the importance of F is seen in the presence of fluorite-bearing mineralised veins (Staatz, 1978). These empirical results are consistent with results from experimental studies, which suggest that F (as well as other ligands such as Cl and CO_2) is able to form stable uranium complexes over a range of temperatures (e.g., Keppler and Wyllie, 1990). Enhanced fluid/melt partitioning for uranium is facilitated by higher ligand concentration and oxygen fugacity (Keppler and Wyllie, 1991; Peiffert *et al*., 1994; 1996).

Igneous rocks with high F were determined from geochemical data (Figure 3.5.5). The 75th percentile was used as the threshold for high F (1300 ppm). Fluorine data was absent for a large number of units contained within the base solid geology dataset (see Appendix 1). In order to supplement the geochemical data, the presence of fluorite was used as a proxy for high F content in the melt. In come cases, fluorite may not be a magmatic-stage mineral phase. This uncertainty is reflected in the confidence factor. While this criterion has been used to map potential sources of favourable ligands, F also performs an important role in enhancing uranium solubility in the melt (Peiffert *et al*., 1996). This has been used as a criterion in previous uranium assessments (Schofield and Huston, 2010; Schofield and Connolly, 2011), but is not used here in order to prevent duplication of criteria.

Based on these criteria, igneous rocks in the Aileron, Warumpi and Davenport provinces are highlighted (Figure 3.5.6). These are concentrated around the margins of the major sedimentary basins within the study area (Figure 3.5.6).

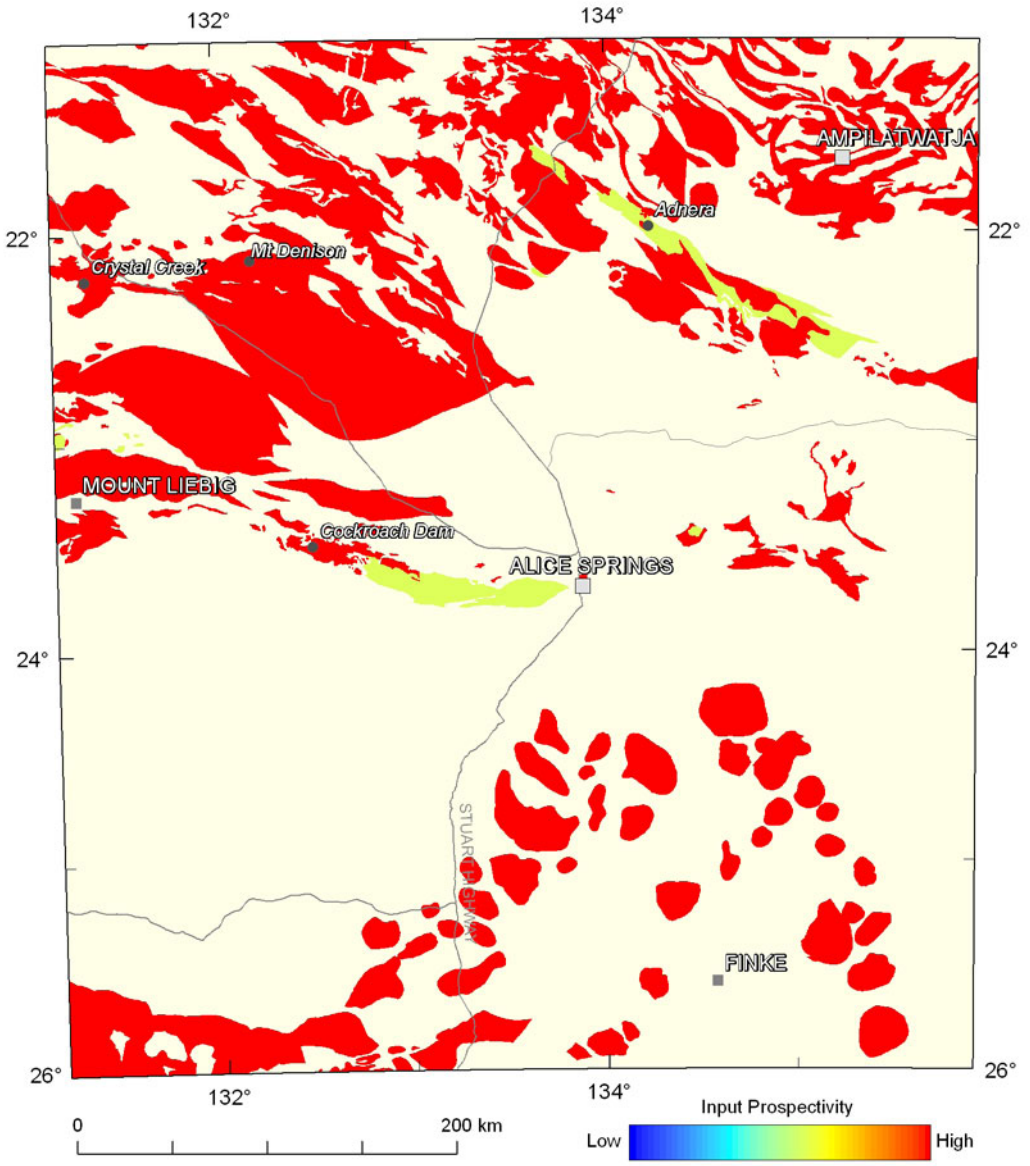

Figure 3.5.1: *Variation in the weightings for the distribution of broadly felsic igneous rocks. The colour stretch for the mappable criteria used in the assessment for magmatic-related uranium systems uses a numerical range from the minimum to the maximum weighting of all criteria used (0.002 to 0.729; see Table 3.5.2), and utilises 20 equal-interval breaks.*

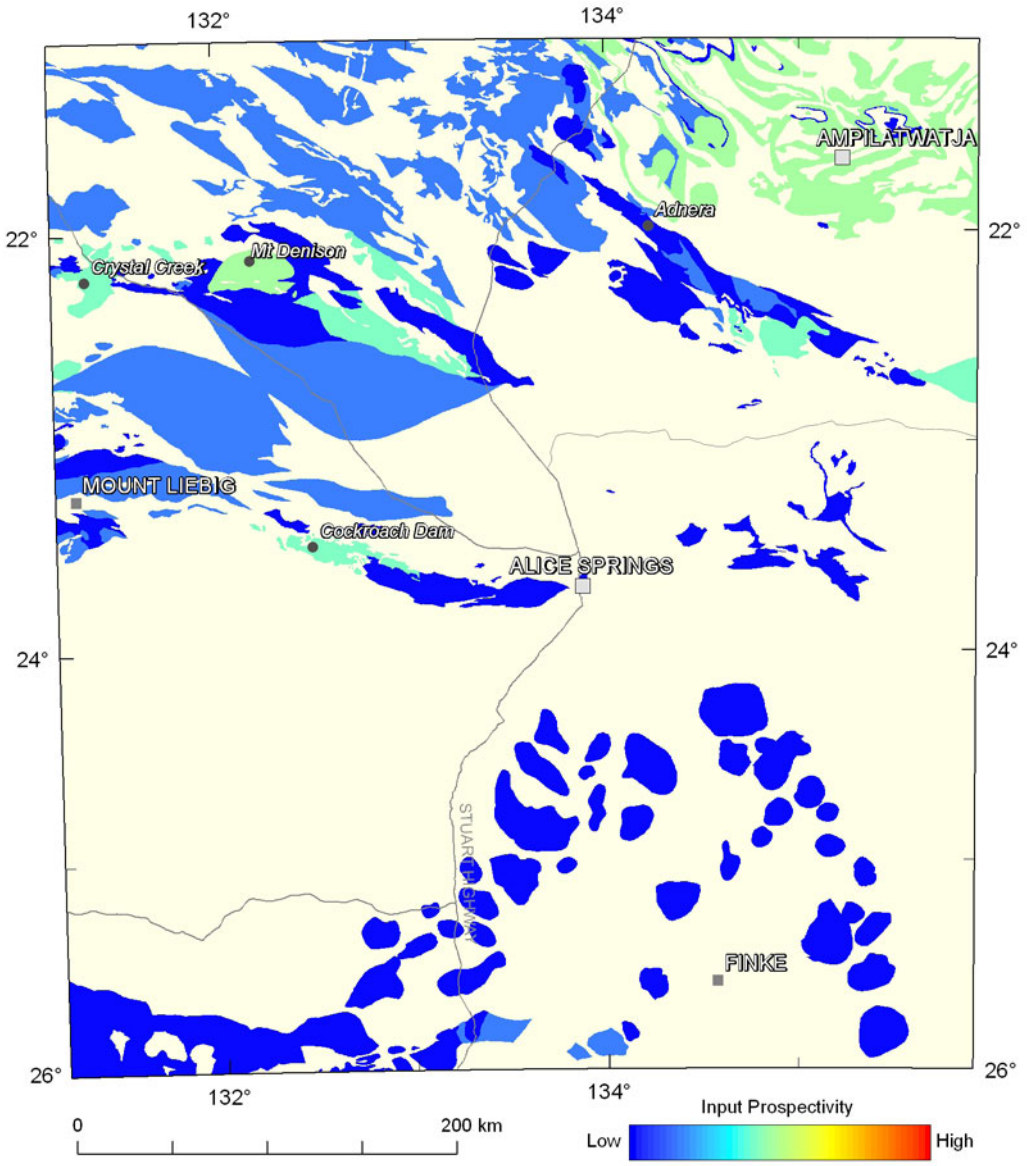

Figure 3.5.2: *Variation in the weightings for intrusive igneous rocks with elevated uranium content. The colour stretch for the mappable criteria used in the assessment for magmatic-related uranium systems uses a numerical range from the minimum to the maximum weighting of all criteria used (0.002 to 0.729; see Table 3.5.2), and utilises 20 equal-interval breaks.*

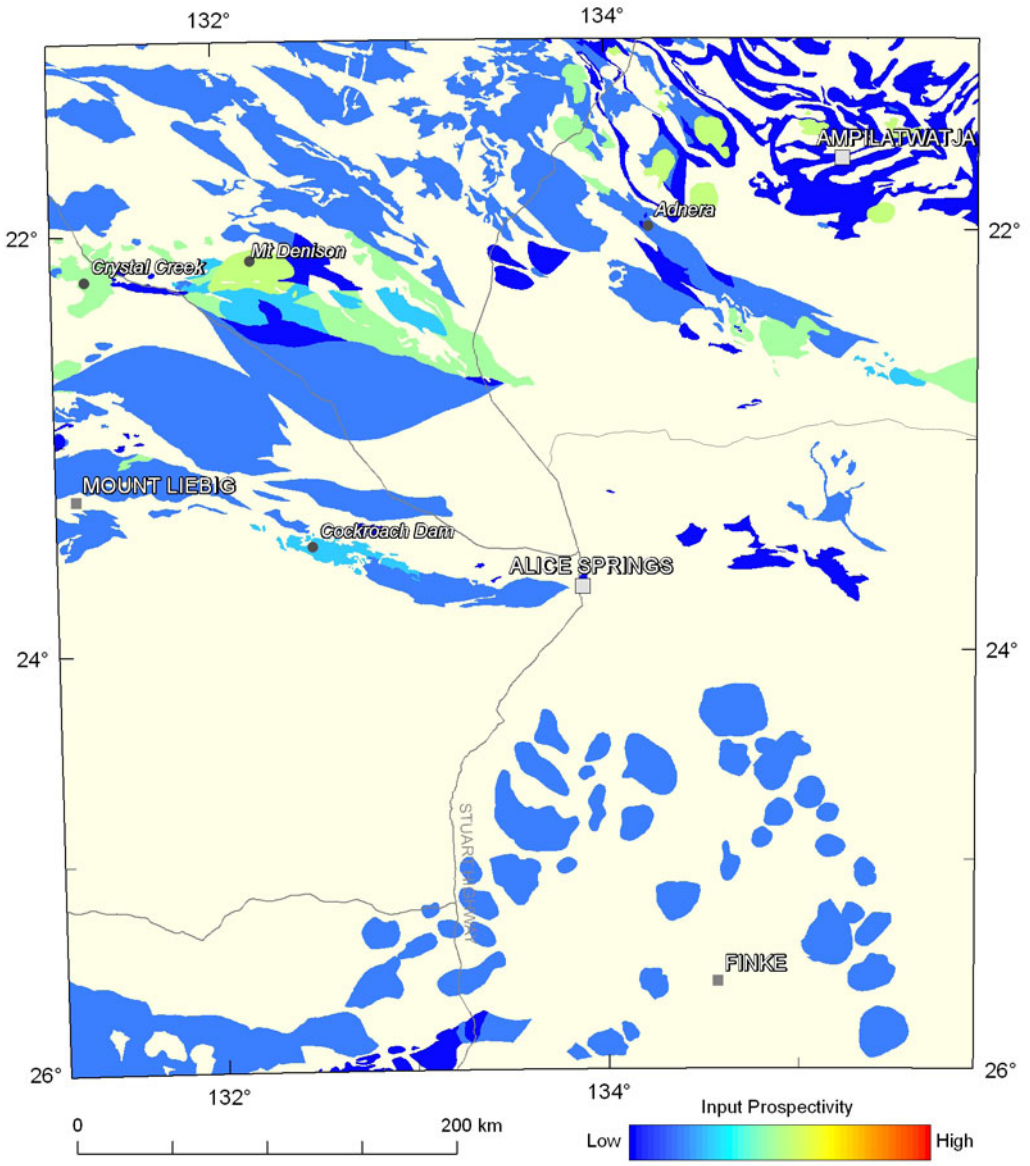

Figure 3.5.3: *Variation in the weightings for fractionated igneous rocks, representing magmatic-stage concentration of uranium. The colour stretch for the mappable criteria used in the assessment for magmatic-related uranium systems uses a numerical range from the minimum to the maximum weighting of all criteria used (0.002 to 0.729; see Table 3.5.2), and utilises 20 equal-interval breaks.*

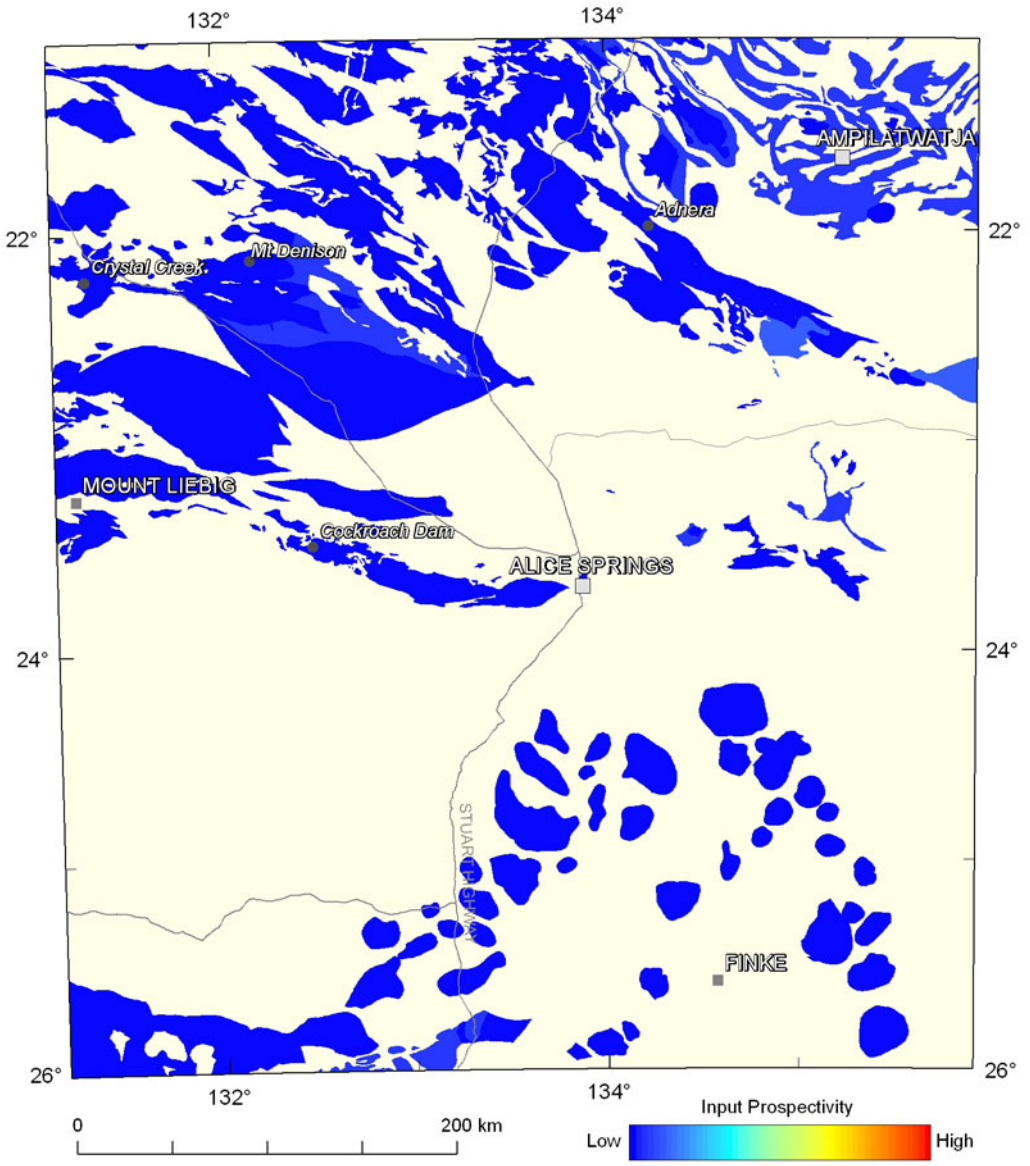

Figure 3.5.4: *Variation in the weightings for igneous rocks with high magmatic temperatures. The colour stretch for the mappable criteria used in the assessment for magmatic-related uranium systems uses a numerical range from the minimum to the maximum weighting of all criteria used (0.002 to 0.729; see Table 3.5.2), and utilises 20 equal-interval breaks.*

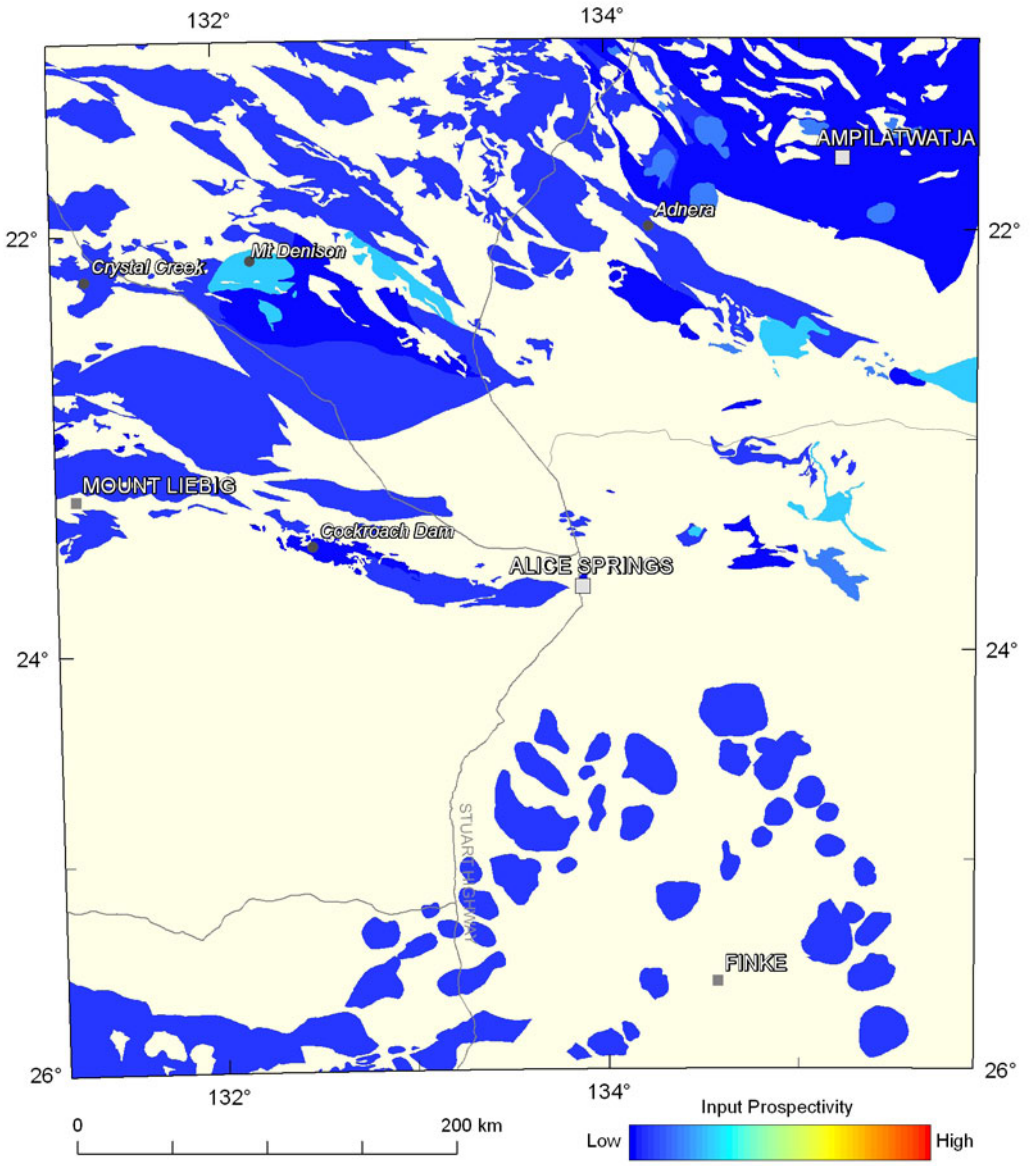

Figure 3.5.5: *Variation in the weightings for sources of favourable ligands, as represented by high fluorine contents. The colour stretch for the mappable criteria used in the assessment for magmatic-related uranium systems uses a numerical range from the minimum to the maximum weighting of all criteria used (0.002 to 0.729; see Table 3.5.2), and utilises 20 equal-interval breaks.*

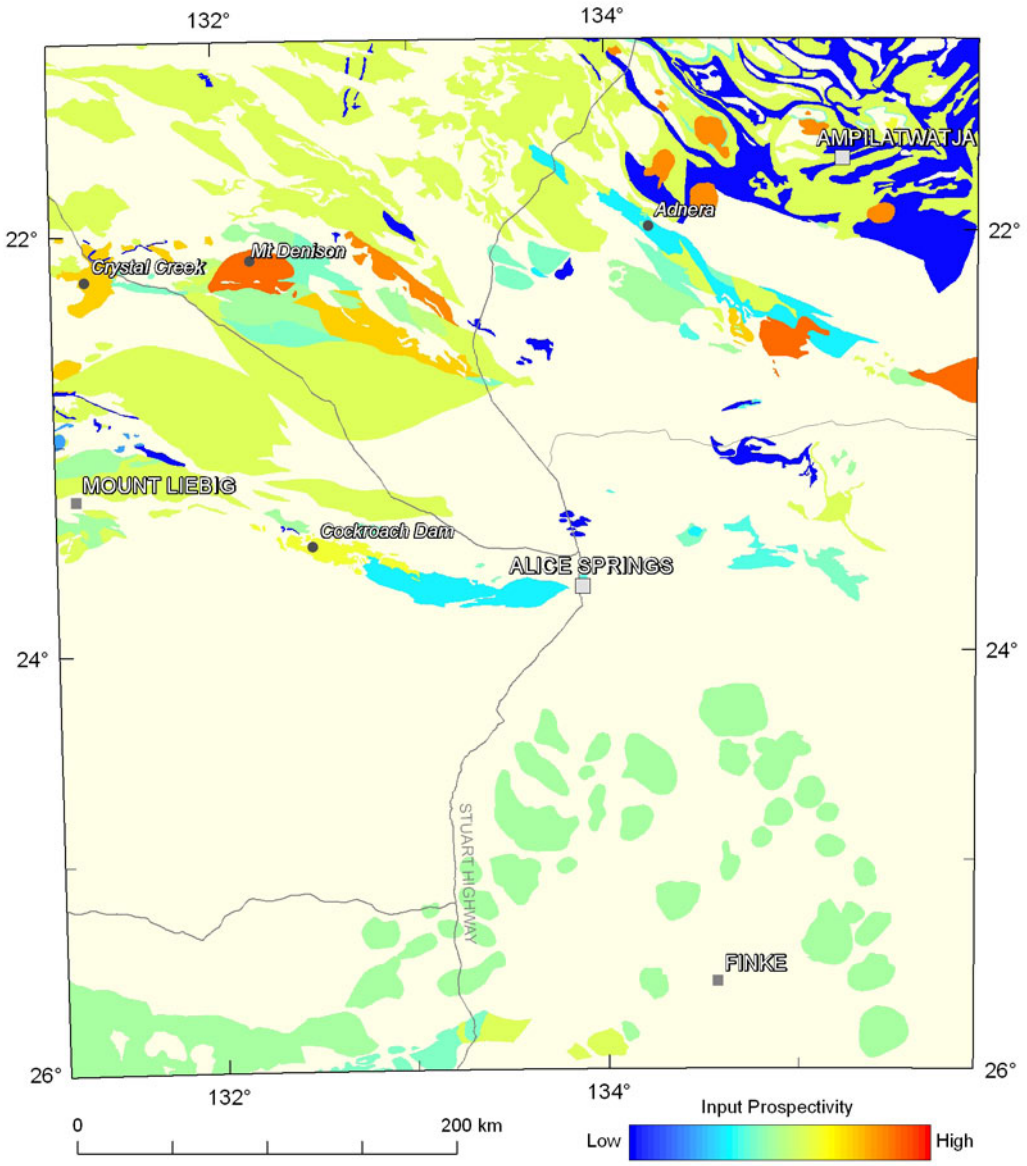

Figure 3.5.6: *Variation in the weightings for the source system component for magmatic-related uranium systems. The colour stretch for each mineral system component in the assessment for magmatic-related uranium systems uses a numerical range from the minimum to the maximum weighting for each of the system components (0.001 to 0.387), and utilises 20 equal-interval breaks.*

3.5.3.3 Drivers

Fluids involved in magmatic-related uranium systems may be derived from the igneous rocks themselves or from external sources. For this investigation, only magmatic-hydrothermal fluids are considered, as externally-sourced fluids more correctly belong to hybrid uranium systems (Figure 3.1.1). The fluid-flow driver criterion for the magmatic-related uranium assessment therefore involves processes whereby fluids are expelled from the magma. One criterion (Figure 3.5.7) has been used to map drivers of fluid flow:

- Fluid exsolution and volatile release.

The likelihood of fluid exsolution and volatile release occurring has been mapped using three strands of evidence, which have been assigned weightings accordingly (Table 3.5.2):

- Presence of textural features indicating fluid exsolution, indicated by the presence of miarolitic cavities;
- Inferred evidence of fluid exsolution, given by the presence of high-level granite intrusion as these are most likely to have exsolved a magmatic fluid. Depending on the certainty of evidence for high-level intrusion, three individual categories are recognised. Units with 'good' evidence of high-level intrusion have co-magmatic volcanic rocks, granophyric intergrowth, or high-level/subvolcanic descriptors. Units with 'moderate' evidence of high-level intrusion are porphyritic or have large contact aureoles. Units with 'poor' evidence show some evidence of high-level intrusion, but this cannot be applied confidently to the whole unit. These may be weakly porphyritic or only containing a porphyritic component; and
- Evidence for being volatile-rich or of volatile release, including the presence of pegmatites, veins, greisens, breccias and tourmaline.

Evidence was determined based on descriptions contained within the GA stratigraphic units database, in Budd *et al*. (2001) and provided by J. Whelan (*pers. comm.*).

Many of the same igneous rocks are highlighted by the driver system component as were identified by the source systems component (Figure 3.5.7). Particularly highlighted is the Wangala Granite in the central Aileron Province.

3.5.3.4 Fluid-flow pathways and architecture

The importance of fluid-flow pathways in magmatic-related uranium systems is suggested by the association of known mineralisation with zones of faulting, brecciation, fracturing and rheological contrasts (Campana and King, 1958; Thompson, 1982; Thompson *et al*., 1988; Wilson and Fairclough, 2009). Fluid-flow pathways, strictly speaking, are difficult to map, but may be approximated using the distribution of proxies for zones which may have experienced fluid flow. Two criteria have been used as proxies to map possible fluid-flow pathways for magmatic-hydrothermal systems:

- Fluid flow along faults; and
- Fluid flow along rheological contrasts.

Fluid flow along faults was mapped by buffering the faults within the basement solid geology dataset (see Appendix 1) to a subjectively chosen distance of 2.5 km (Figure 3.5.8). Rheological contrasts established due to lithological contacts or contact metamorphism have been used as the second criterion. In order to map these potential pathways, non-faulted intrusive contacts were extracted from the basement solid geology dataset (see Appendix 1). These were subsequently buffered to a subjectively chosen distance of 2.5 km (Figure 3.5.9). The final weightings for the fluid-flow pathways system component are shown in Figure 3.5.10.

3.5.3.5 Depositional mechanisms

Assuming uranium has been transported as a fluoride complex, uranium deposition may occur as a result of ligand destabilisation triggered by fluorite precipitation. Mechanisms for fluorite destabilisation include cooling, changes in pressure, dilution of ore fluids, fluid mixing and pH increase (Richardson and Holland 1979). Additionally, interaction with reactive rocks, principally those which are Ca-rich, may also cause ligand destabilisation. Based on these considerations, the following criteria have been used to map sites where uranium may be precipitated from a favourable magmatic-hydrothermal fluid:

- Distribution of potential chemical deposition sites; and
- Potential sites of ligand destabilisation.

Potential chemical deposition sites (Figure 3.5.11) were mapped using reactive host rocks. Three classes of reactive host rocks were recognised: Fe-rich rocks, carbonate-rich rocks and other Ca-rich rocks (e.g., calc-silicates, anorthosites). Using unit descriptions contained within the basement solid geology dataset (see Appendix 1), units were assessed for reactive lithologies and were classified as to whether the reactive component was major or minor. Units with a carbonate component are considered to be more favourable than Fe-rich rocks, which are in turn more favourable than other non-carbonate Ca-rich rocks.

Potential sites of ligand destabilisation (Figure 3.5.12) were mapped using units containing breccias and veins, which may act as sites where a uranium-bearing fluid may undergo physical and chemical modification, resulting in ore deposition. Ideally, these zones would be mapped using the distribution of the breccias and veins themselves; however, such data are presently not available. Evidence for this criterion was determined using descriptions contained within the GA stratigraphic units database, in Budd *et al*. (2001) and provided by J. Whelan (*pers. comm.*).

The third criterion used to map depositional mechanisms seeks to directly map areas of uranium enrichment (Figure 3.5.13). The following criterion has been used:

- Direct evidence of elevated uranium mapped from U^2/Th radiometric data. The process for developing this criterion is described in Section 3.2.

The final map of weightings for the depositional mechanisms system component emphasises locations where criteria used for mapping uranium precipitation mechanisms occur in conjunction with radiometric anomalies (Figure 3.5.14).

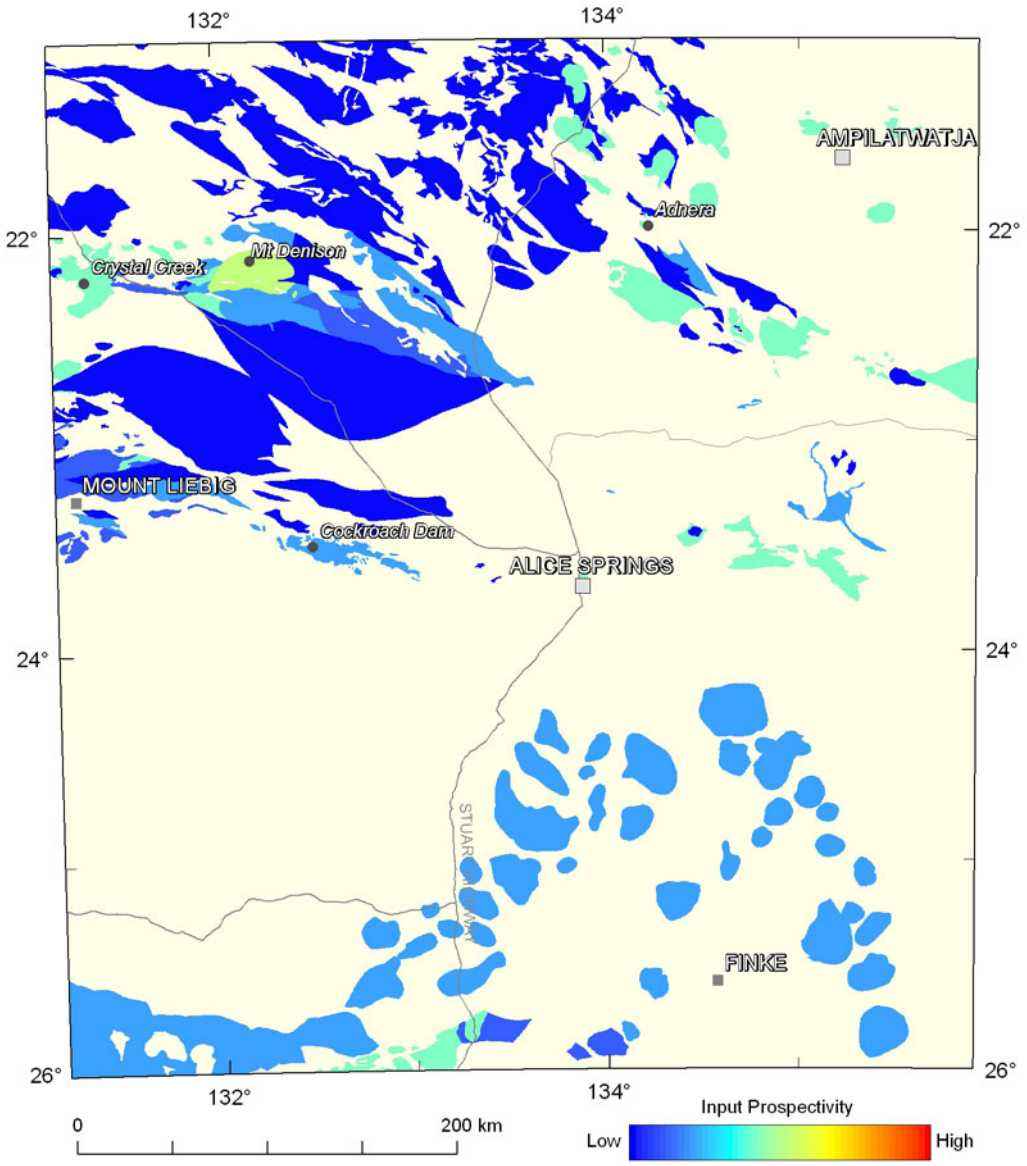

Figure 3.5.7: *Variation in the weightings for fluid exsolution and volatile release. This also represents the weightings for the driver system component, as it is the sole criterion used. The colour stretch for the mappable criteria used in the assessment for magmatic-related uranium systems uses a numerical range from the minimum to the maximum weighting of all criteria used (0.001 to 0.729; see Table 3.5.2), and utilises 20 equal-interval breaks.*

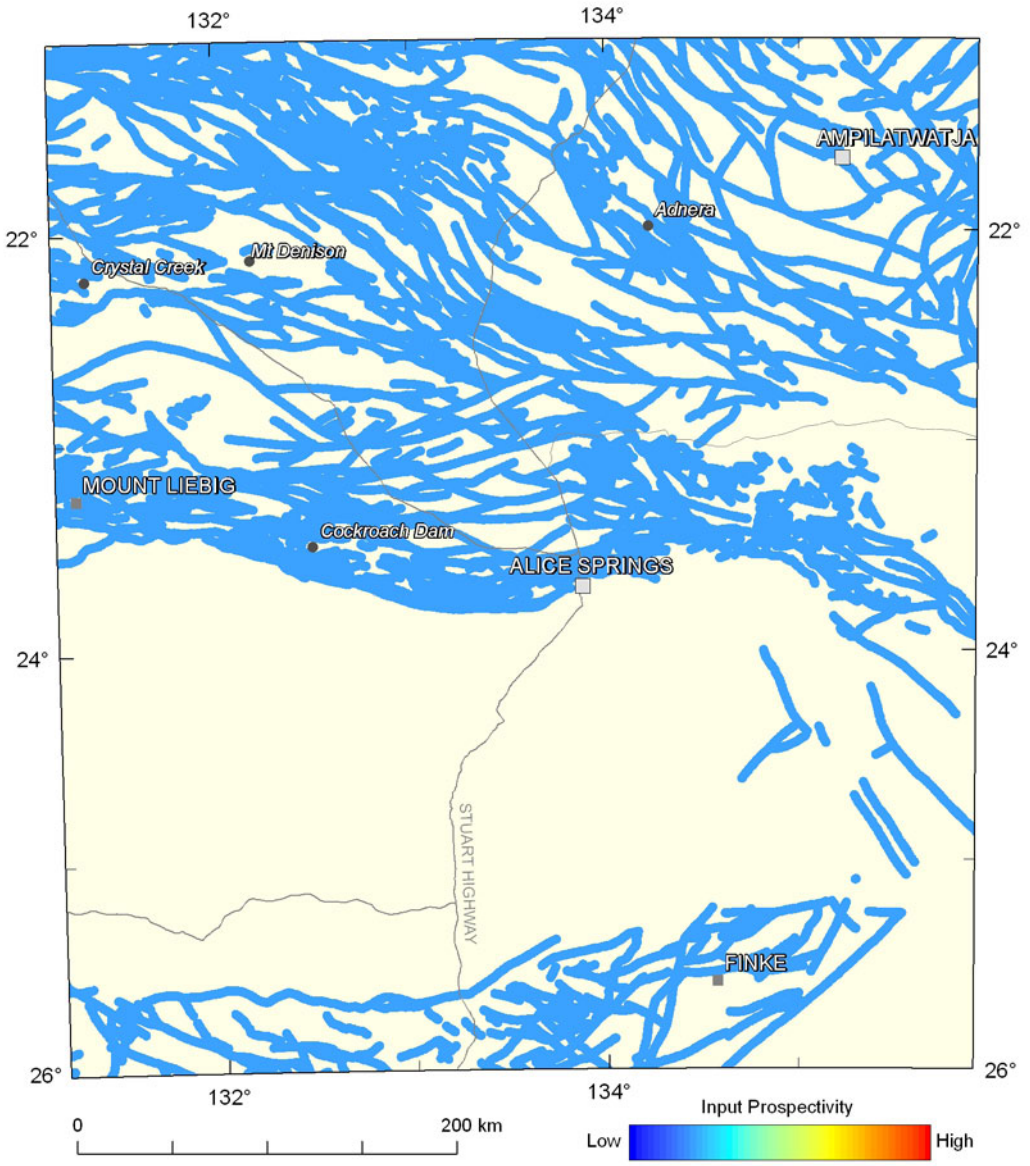

Figure 3.5.8: *Weighting for potential fluid-flow pathways, as represented by buffered faults. The colour stretch for the mappable criteria used in the assessment for magmatic-related uranium systems uses a numerical range from the minimum to the maximum weighting of all criteria used (0.002 to 0.729; see Table 3.5.2), and utilises 20 equal-interval breaks.*

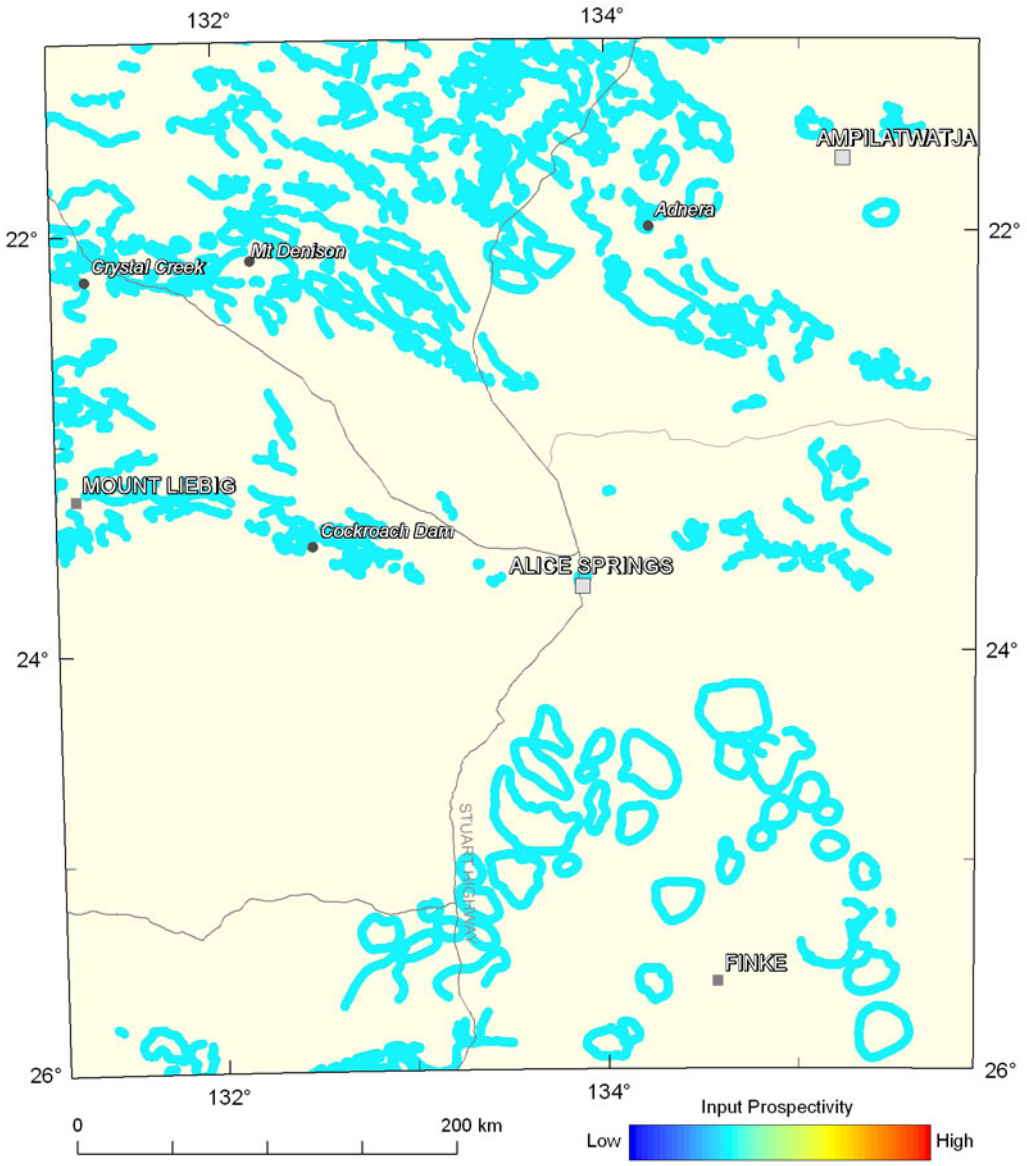

Figure 3.5.9: *Weighting for potential fluid flow along rheological contrasts. The colour stretch for the mappable criteria used in the assessment for magmatic-related uranium systems uses a numerical range from the minimum to the maximum weighting of all criteria used (0.002 to 0.729; see Table 3.5.2), and utilises 20 equal-interval breaks.*

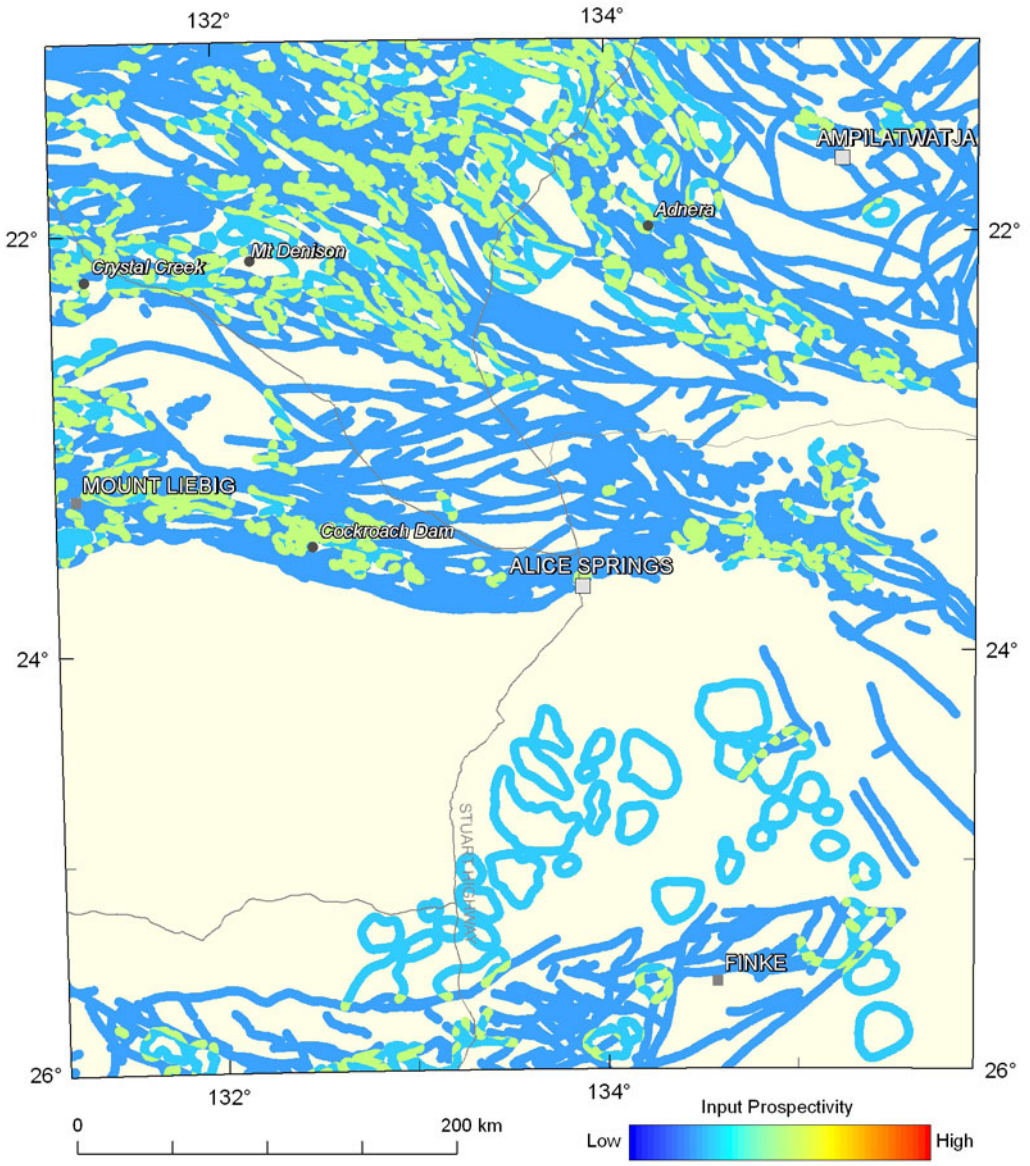

Figure 3.5.10: *Variation in the weightings for the fluid-flow pathways system component for magmatic-related uranium systems. The colour stretch for each mineral system component in the assessment for magmatic-related uranium systems uses a numerical range from the minimum to the maximum weighting for each of the system components (0.001 to 0.387), and utilises 20 equal-interval breaks.*

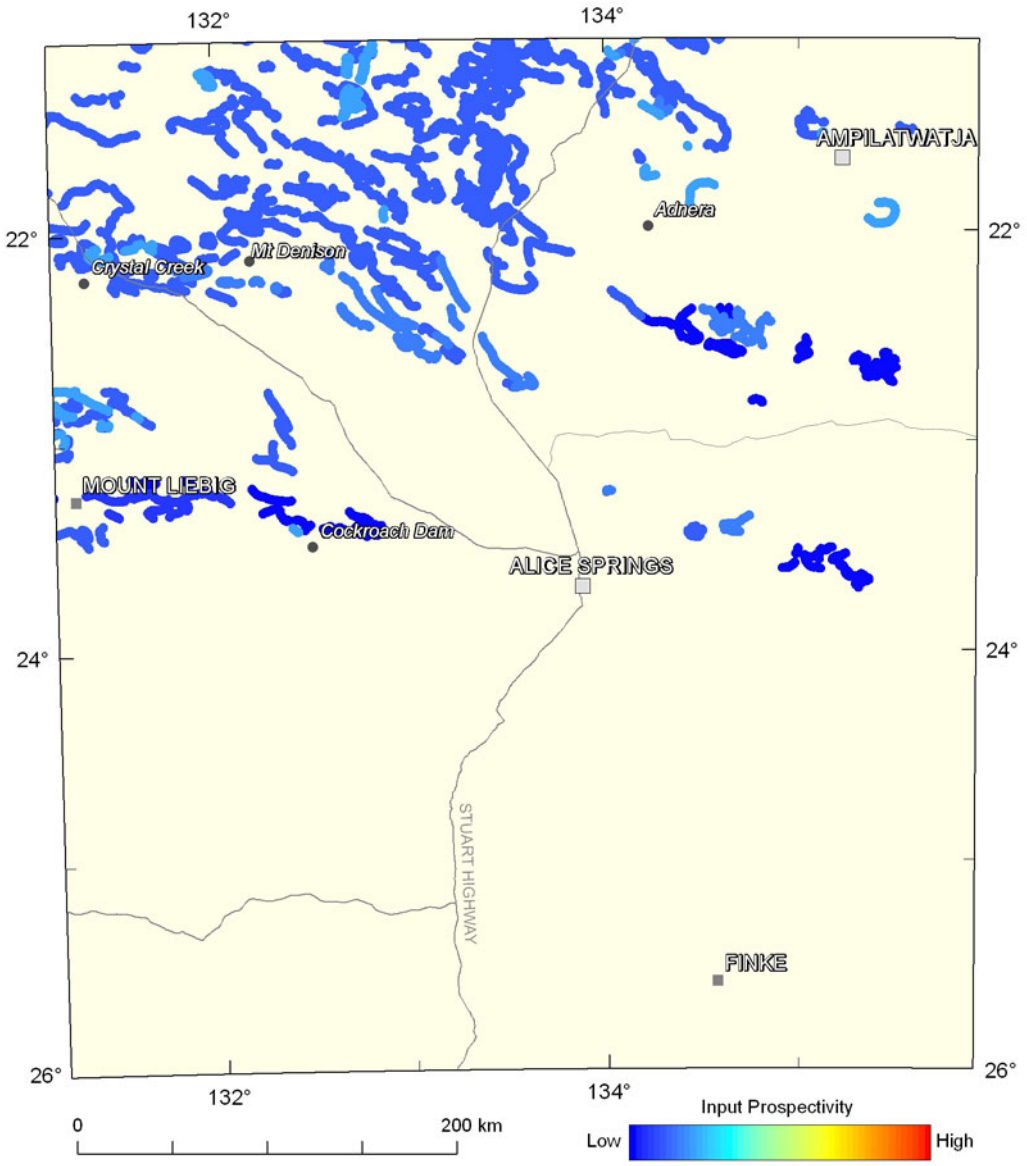

Figure 3.5.11: *Variation in the weightings for potential chemical depositional sites. The colour stretch for the mappable criteria used in the assessment for magmatic-related uranium systems uses a numerical range from the minimum to the maximum weighting of all criteria used (0.002 to 0.729; see Table 3.5.2), and utilises 20 equal-interval breaks.*

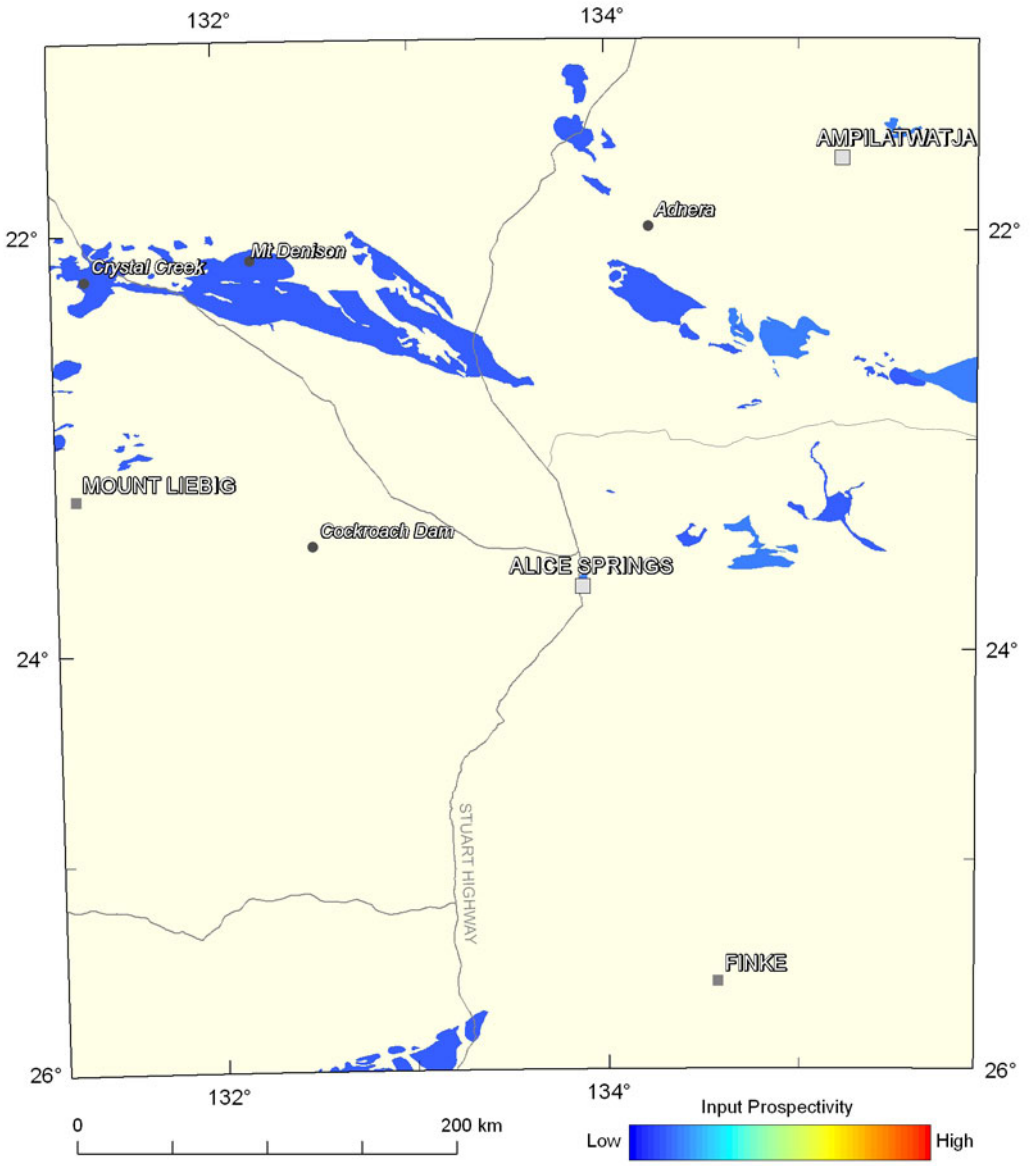

Figure 3.5.12: *Variation in the weightings for potential sites of ligand destabilisation. The colour stretch for the mappable criteria used in the assessment for magmatic-related uranium systems uses a numerical range from the minimum to the maximum weighting of all criteria used (0.002 to 0.729; see Table 3.5.2), and utilises 20 equal-interval breaks.*

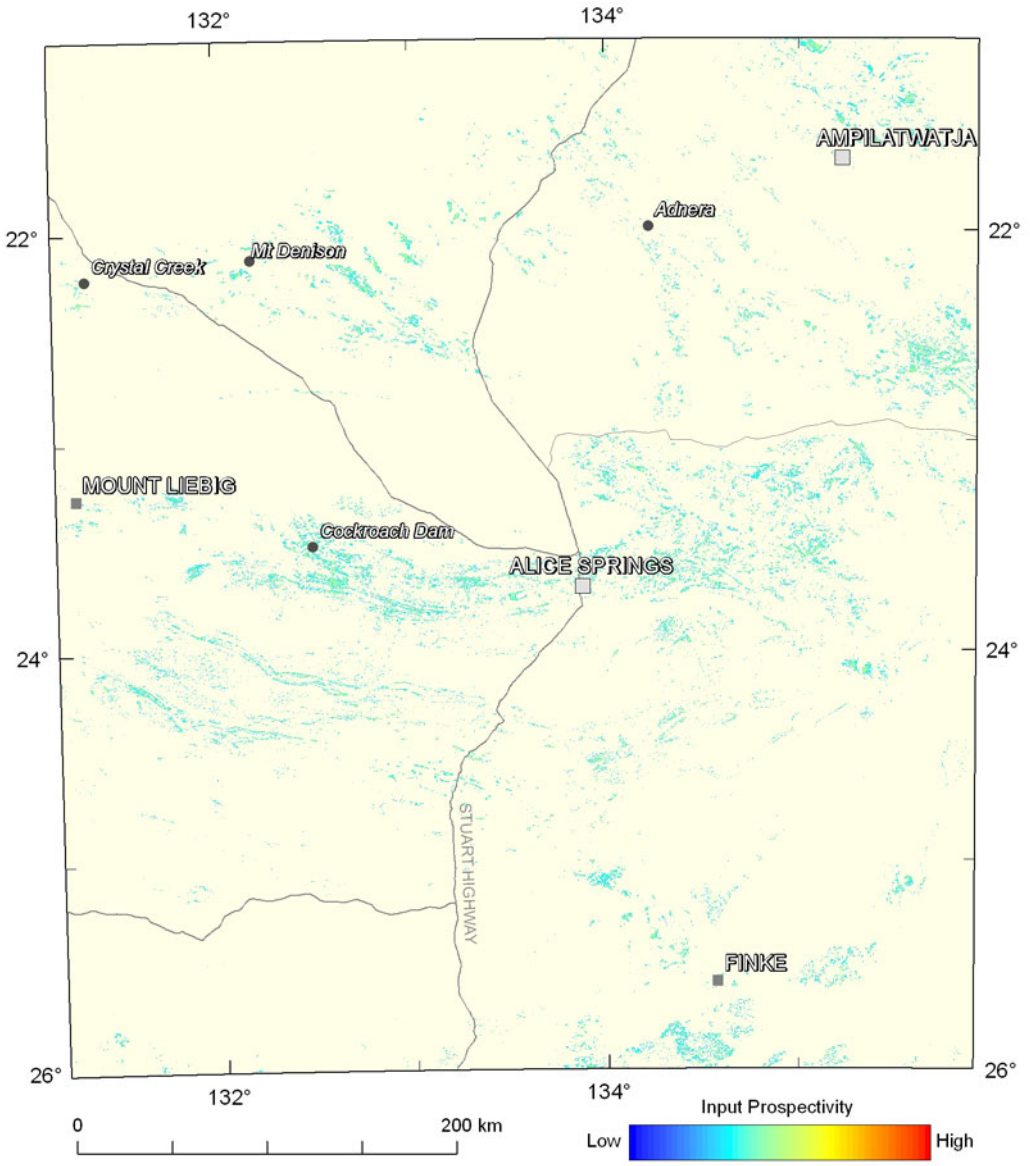

Figure 3.5.13: *Variation in the weightings for direct evidence of elevated uranium, as indicated by radiometric anomalies. The colour stretch for the mappable criteria used in the assessment for magmatic-related uranium systems uses a numerical range from the minimum to the maximum weighting of all criteria used (0.002 to 0.729; see Table 3.5.2), and utilises 20 equal-interval breaks.*

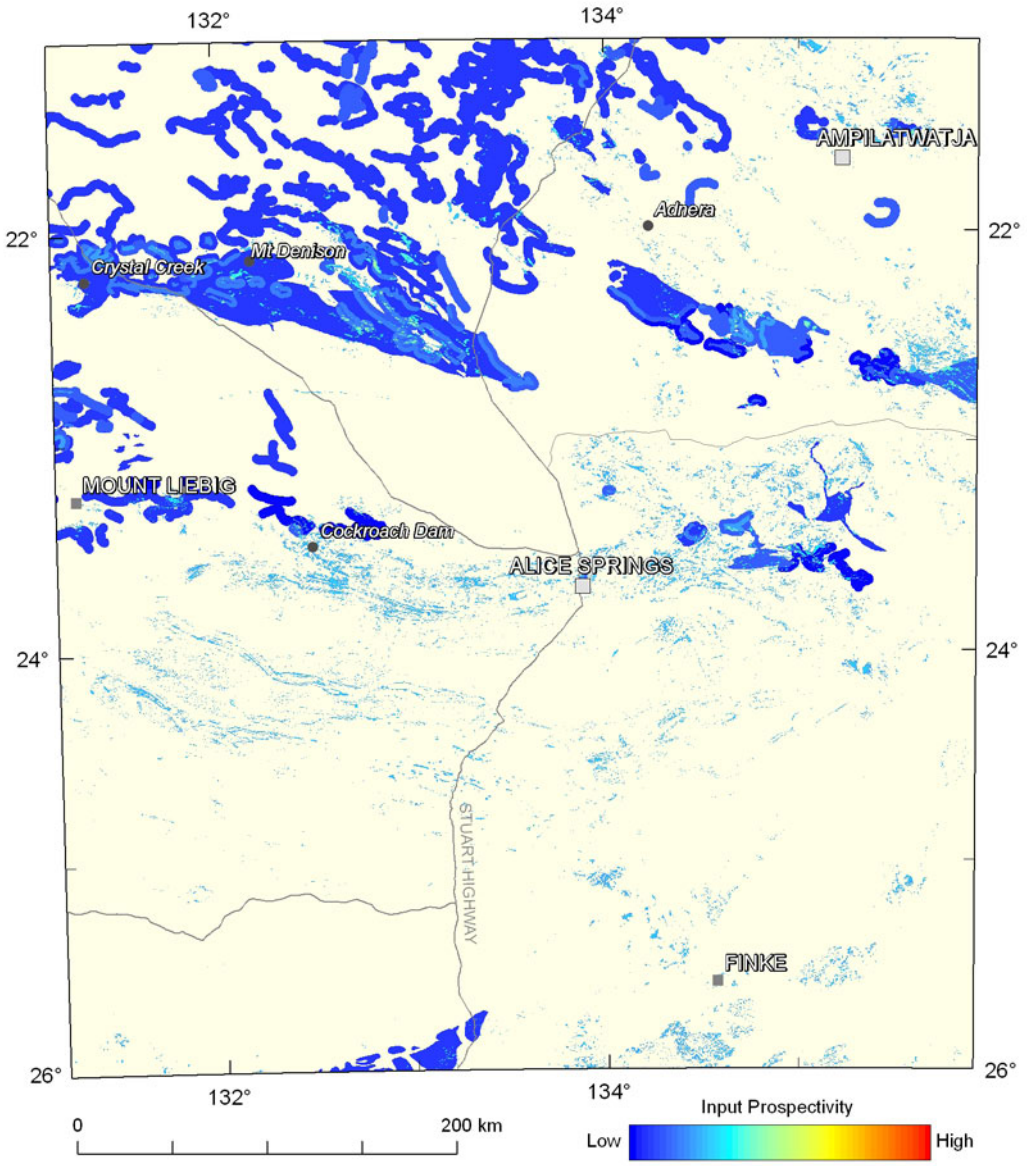

Figure 3.5.14: *Variation in the weightings for the depositional mechanisms system component for magmatic-related uranium systems. The colour stretch for each mineral system component in the assessment for magmatic-related uranium systems uses a numerical range from the minimum to the maximum weighting for each of the system components (0.001 to 0.387), and utilises 20 equal-interval breaks.*

3.5.4 Results

The results of the assessment for magmatic-related uranium systems are shown in Figure 3.5.15 and Plate 3.5. Intrusive igneous rocks exhibiting elevated potential are distributed throughout the study area. The majority of these are located within the Aileron Province, although zones of elevated potential also occur within the other basement provinces in the study area. The following specific regions have been identified:

- The highest modelled potential occurs in the Wangala Granite (A), the Mount Swan and Mount Ida granites (B) and the Jinka Granite (C). These occur in a rough east-west belt through the Aileron Province;
- The Southwark Suite (D_{1-3}) in the west of the study area, including the Yarunganyi Granite (D_2), which hosts the Crystal Creek prospect (Table 3.5.1);
- The Devils Suite in the Davenport Province (E_{1-5});
- A region on the northern margin of the Ngalia Basin consisting of several units, including the Anmatjira Orthogneiss, Boothby Orthogneiss and Yaloolgarrie Granite (F). Although not mapped in the solid geology dataset used, this area also includes the Ennugan Mountains Granite, which exhibits evidence of hydrothermal F-uranium-REE fluids (Beyer *et al*., 2012); and
- Several regions of lower potential occur (G-J), including the Teapot Granite Complex (I). The moderate potential of the Teapot Granite Complex is lower than what may be expected considering the presence of known low-grade uranium mineralisation (Table 3.5.1), and warrants further investigation.

Within these zones, the highest potential occurs at the margins of granitic bodies, especially where radiometric anomalies are present.

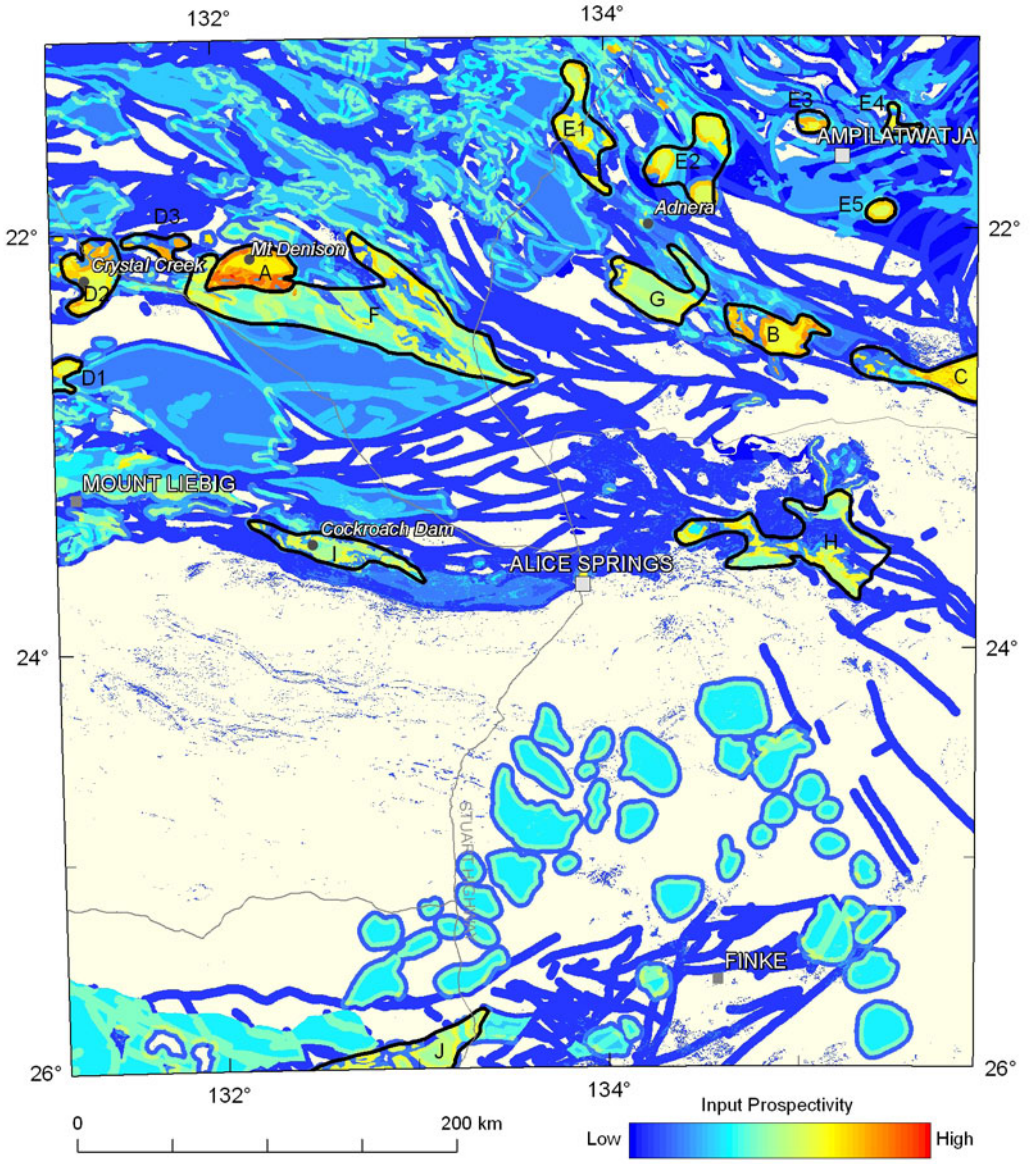

Figure 3.5.15: *Final modelled potential for magmatic-related uranium systems. The colour stretch used for this figure has a minimum value of 0.001 and a maximum value of 0.275, and utilises 20 equal-interval breaks. Areas outlined in black are discusses in Section 3.5.4.*

4. Geothermal systems

A. J. Meixner, E.J. Gerner, R.D. Weber, T. Brennan, B. Lewis and R.G. Gallagher

A geothermal energy system comprises three key components: (1) a heat source, (2) a fluid to transport the heat and (3) sufficient permeability to enable the fluid to circulate through the rock. Conventional (hydrothermal) geothermal systems are typically associated with active volcanism. In these systems, the three components of a geothermal energy system generally occur naturally. In areas distal to active volcanism, it is possible to artificially create a geothermal energy system. Of the three components listed above, a heat source is the only one required to occur naturally; fluids can be artificially injected into hot rocks and permeability can be chemically or hydraulically created.

Geothermal energy systems in Australia are generally either hot rock systems (also known as Engineered or Enhanced Geothermal Systems, EGS) or hot sedimentary aquifer systems (Figure 4.1). The heat sources for both geothermal systems are most commonly radiogenic basement rocks (typically granites) that are enriched in the radioactive elements uranium, Th and K. The decay of these three elements over time generates heat, and, if these high-heat producing rocks are buried beneath a sufficient thickness of insulating units (typically sediments), the heat is trapped and temperatures as high as 250°C can be found at depths of less than five kilometres depth. Only basement heat sources are considered in this geothermal assessment. The requirement for insulation (in the case of hot rock systems) and permeable stratigraphic formations (in the case of hot sedimentary aquifer resources) means that geothermal systems in Australia are more likely to be associated with sedimentary basins than areas of outcropping basement.

In areas where high-heat producing basement rocks are not known to occur, geothermal systems may still be present as temperature in any location generally increases with crustal depth. In addition, hot fluid can migrate away from the area in which it was initially heated, forming hot sedimentary aquifer systems with no immediately obvious heat source. However, geothermal systems remote from local sources of enhanced heat production are likely to be relatively low temperature systems (generally <150^{o}C).

There are a variety of applications for a geothermal resource, dependant on the temperature and volume of the available fluid. Higher temperature resources (more than 200°C) are ideal for generating electricity, although much lower temperatures can be suitable under the right circumstances. High temperature resources (e.g., 300°C) can have cycle conversion efficiencies up to 20% (Tester, 1982). In off-grid areas dependant on fuel oil for on-site power generation, lower temperatures may be used to economically generate power. Although possible, electricity generation from lower temperature resources is less efficient, with only about 6% of the thermal energy being converted into electrical energy. Low temperature geothermal resources (less than 150°C) can be used to provide heat for industrial or domestic processes. For these lower temperature resources, direct use is a more thermodynamically efficient use of the geothermal resource. Examples of potential applications where geothermal heat can be used directly are displayed in Figure 4.2.

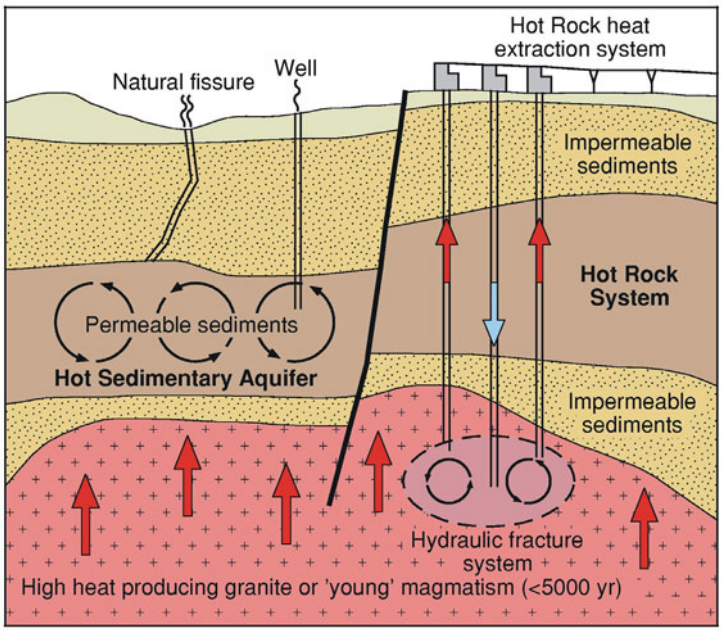

Figure 4.1: *Schematic diagram of styles of geothermal systems found in Australia.*

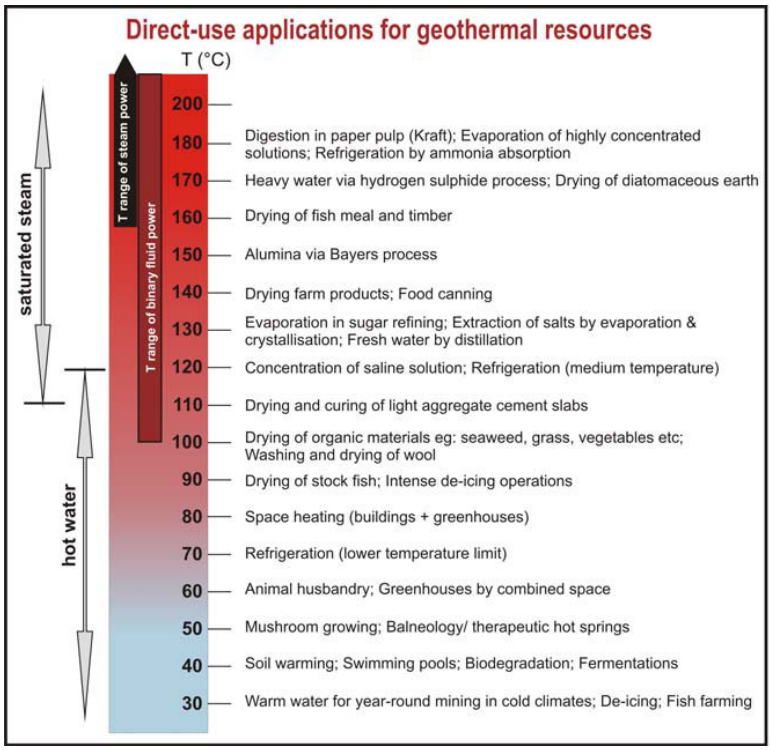

Figure 4.2: *The variety of applications for direct-use of geothermal heat, as a function of the resource temperature (modified from Lindal, 1973).*

Although Australia is yet to generate electricity from a hot rock geothermal system, a small binary power plant in Birdsville, southwest Queensland, has been generating electricity from a low temperature (about 100°C) hot sedimentary aquifer system in the Great Artesian Basin. The plant has been operating since the early 1990s and is currently generating about 80 kW_e net.

Assessments of hot rock and hot sedimentary aquifer geothermal potential have previously been undertaken in north Queensland and in east-central South Australia. The north Queensland study (Ayling and Lewis, 2010) employed a GIS-based approach similar to that used elsewhere (e.g., Noorollahi *et al*., 2007) to identify potential regional-scale geothermal resources. In comparison, the geothermal assessment of east-central South Australia (Meixner *et al*., 2011) was based on a constructed 3D geological map and subsequent 3D thermal modelling. The development of this modelling approach has formed the basis for the assessment presented here. The geothermal potential of the Northern Territory has also previously been assessed by Beardsmore (2007) using a qualitative approach to categorise each sedimentary basin within the Northern Territory based on the potential for heat production, insulating sediments and natural or artificial reservoirs.

4.1 PREDICTING TEMPERATURE AT DEPTH

Exploration for geothermal resources ultimately aims to locate commercially exploitable temperatures at economically viable depths. Ideally, this could be achieved by measuring temperature in deep drill holes distributed in a grid-like manner. On a continental scale, however, this is not economically or logistically feasible and, as result, other data and methods must be used to predict temperature at depth.

To predict temperature at depth, the transfer of heat in the crust must be considered. Heat flows within the earth by conduction or advection of fluids (Stüwe, 2007), and heat can be generated in the crust by radiogenic, chemical and mechanical heat sources. Gibson *et al.* (2008) suggest that, since the Australian continent is not subjected to active tectonism, there is minimal chemical or mechanical heat production, and at depths of interest for geothermal electricity generation the dominant mode of heat transfer is conduction.

The heat transfer process is described in the following equation (modified after Stüwe, 2007):

$$\frac{dT}{dt} = \kappa\left(\frac{d^2T}{dz^2}\right) + u\left(\frac{dT}{dz}\right) + (A)/(\rho c_p) \qquad (1)$$

Where κ = the thermal diffusivity and is given by $k/(\rho c_p)$, k = thermal conductivity, ρ = density, c_p = heat capacity, A = the heat production from radiogenic heat sources and u is the advection rate vector. This equation assumes that thermal conductivity does not vary with temperature. In reality, thermal conductivity does vary with temperature, with the usual pattern being a decrease with increasing temperature (Birch and Clark, 1940). Therefore, the temperatures predicted in this assessment are likely to be conservative.

Gibson *et al.* (2008) also proposed that, for the Australian crust, it is sufficient to consider only the case of the thermal steady-state based on the assumption that the crust has attained thermal equilibrium since the last period of tectonic or magmatic disturbance. For steady-state:

$$\frac{dT}{dt} = 0$$

The steady state equation for conductive heat flow can be expressed as:

$$Q_0 = Q_d + \int A(z)\partial z \qquad (2)$$

Where Q_0 = surface heat flow, Q_d = heat flow at depth d, $\int A(z)\partial z$ = the integral of volumetric heat generation from the surface to d, A = heat production and z = depth.

The heat flow at depth d can be calculated from the following relationship:

$$Q_d = \lambda_d \cdot \left[\frac{\Delta T}{\Delta z}\right]_d \qquad (3)$$

Where: λ_d = thermal conductivity at depth d and T = temperature.

From equations (2) and (3), it can be seen that the key datasets for calculating temperature at depth are: heat flow at the base of the crust, thermal conductivity, and heat production. The relationship between these variables is diagrammatically illustrated in Figure 4.3.

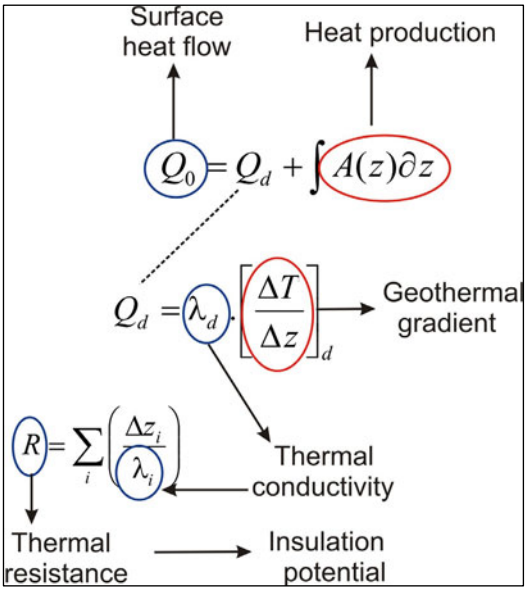

Figure 4.3: *Relationship between key physical parameters useful for geothermal resource exploration.*

4.2 3D THERMAL MODELLING USING GEOMODELLER

Temperatures were predicted using a 3D geological map constructed in GoCad[2] and thermal modelling undertaken using the 3D GeoModeller[3] software package. GeoModeller explicitly solves the following steady state equation for 3D temperature prediction (Stüwe, 2007):

$$\left(\frac{d\left(-k\frac{dT}{dx}\right)}{dx} + \frac{d\left(-k\frac{dT}{dy}\right)}{dy} + \frac{d\left(-k\frac{dT}{dz}\right)}{dz} \right) + \rho c_p \left(u_x \frac{dT}{dx} + u_y \frac{dT}{dy} + u_z \frac{dT}{dz} \right) = -A \qquad (4)$$

The above equation combines conduction and heat production terms as well as considering spatially varying thermal conductivity. The equation is discretised with an explicit finite difference scheme within GeoModeller utilising a voxelised grid. This finite difference approximation is iteratively solved with a Gauss-Seidel iteration scheme until the sum of the residual errors fall below a given threshold (Gibson *et al*., 2008).

Three boundary conditions were applied to the 3D temperature prediction equation:

- For the four vertical sides, Neumann-type boundary conditions were applied. where all lithologies and temperatures are mirrored beyond the model boundaries, thereby implying that no heat flows through the model boundaries;
- For the basal boundary, either a constant heat flow or temperature; and
- For the top boundary, a constant temperature, such as the mean annual surface temperature (Gibson *et al.*, 2008). The effects of topography were dealt with by applying the top boundary condition to a topographic surface (digital elevation model, DEM; Gibson *et al.*, 2008).

Once the boundary conditions and topography were set, thermal-conductivity and heat-production values were assigned to each lithology of a voxelised 3D geological map (Gibson *et al*., 2010). After all the inputs are assigned the number of iterations must be specified, with the number of iterations large enough that the model is able to reach thermal equilibrium. The GeoModeller solver then computes a 3D grid with modelled outputs (summarised in Table 4.1).

Table 4.1: Summary of outputs solved in 3D by the thermal modelling component of GeoModeller (from Gibson *et al*. 2010)

Temperature	In °C; solved for every cell/voxel centre by finite difference
Vertical heat flow	In mW/m^2; flow of heat measured in energy per time per unit area. Solved for each cell/voxel centre with respect to the centre of the cell immediately above
Vertical temperature gradient	In °C/km; change of temperature over distance. Solved for each cell/voxel centre with respect to the centre of the cell immediately above
Total horizontal temperature gradient	In °C/km; change of temperature over a distance of one cell to four neighbours in the horizontal plane. Equal to the square root of the sum of the squares of the horizontal temperature gradients in the x and y directions. (An expression of gradient strength with no expression of direction within the horizontal plane)

[2] http://www.gocad.org/
[3] http://www.geomodeller.com/geo/index.php?lang=EN&menu=homepage

4.3 HEAT-FLOW AND TEMPERATURE DATA

The assessment area lies within the broad region of elevated heat flow referred to as the Central Australian Heat-Flow Province by McLaren *et al*. (2003; Figure 2.2.3). However, measured Australian heat-flow data is scarce. There are only two measured heat-flow values in the study area (Figure 4.4), one in the northern Ngalia Basin of 55.8 mW/m^2 (CUL089 Yuendumu; Cull and Denham, 1979), and the other in the northern Amadeus Basin of 62 mW/m^2 (Alice 1; Hyndman, 1967). Both of these heat-flow values are above the global Proterozoic average of 49–54 mW/m^2, but are below the average Central Australian Heat-Flow Province value of 82 ± 25 mW/m^2 (McLaren *et al*., 2003), although the value from Alice 1 is within error.

The OZTemp[4] database stores temperature and geothermal gradients collected from drill holes around Australia, and is an updated and improved version of the AUSTHERM05 borehole temperature database previously described by Chopra and Holgate (2005). Using measured and estimated thermal gradients, surface temperature estimates, and depth to basement information, these temperatures have been vertically extrapolated to give interpreted temperatures at five kilometres depth. The interpreted temperatures were gridded to produce a map of crustal temperature across the Australian continent[5] (study area shown in Figure 4.4). The interpolation required to produce a continuous grid across such heterogeneously distributed data points invariably results in unreliable temperature predictions in areas of low data density.

Although an awareness of the limitations of the technique surrounding data distribution and reliability of the temperature extrapolation and interpolation needs to be maintained when viewing the temperature at five kilometres map (Figure 4.4), it is a valuable tool for visualising variations in the temperature field at depth near data locations. The map shows limited variation in the interpreted temperature at depth across the assessment area (primarily due to scarcity of data) with a few exceptions. The most dominant area of higher interpreted temperature is in the western portion of the assessment area. It can be seen that this anomaly is based on a single data point (East Mereenie 1) and is unconstrained by any other data to the west. Importantly this temperature was based on a single reported temperature gradient only and is therefore of low reliability. Note that wells with only a thermal gradient value in the database were not used in the 3D thermal modelling in this assessment; these data are only shown in Figure 4.4 for the sake of completeness and to provide the context of the temperature at five kilometres interpretation.

In the south-eastern corner of the assessment area there is a small positive anomaly reflecting data collected from wells just outside of the assessment area. These wells are predominantly petroleum wells drilled through the Eromanga Basin and into the Pedirka Basin beneath. The Eromanga Basin south of this area is known to have elevated heat flow (Beardsmore, 2004), although heat flow within the Eromanga Basin is unconstrained within the assessment area. Other more local-scale variations in the image are due to slight data inconsistencies that are highlighted by viewing a section of a continental dataset at this reduced scale.

[4] https://www.ga.gov.au/products/servlet/controller?event=GEOCAT_DETAILS&catno=70604
[5] https://www.ga.gov.au/products/servlet/controller?event=GEOCAT_DETAILS&catno=71143

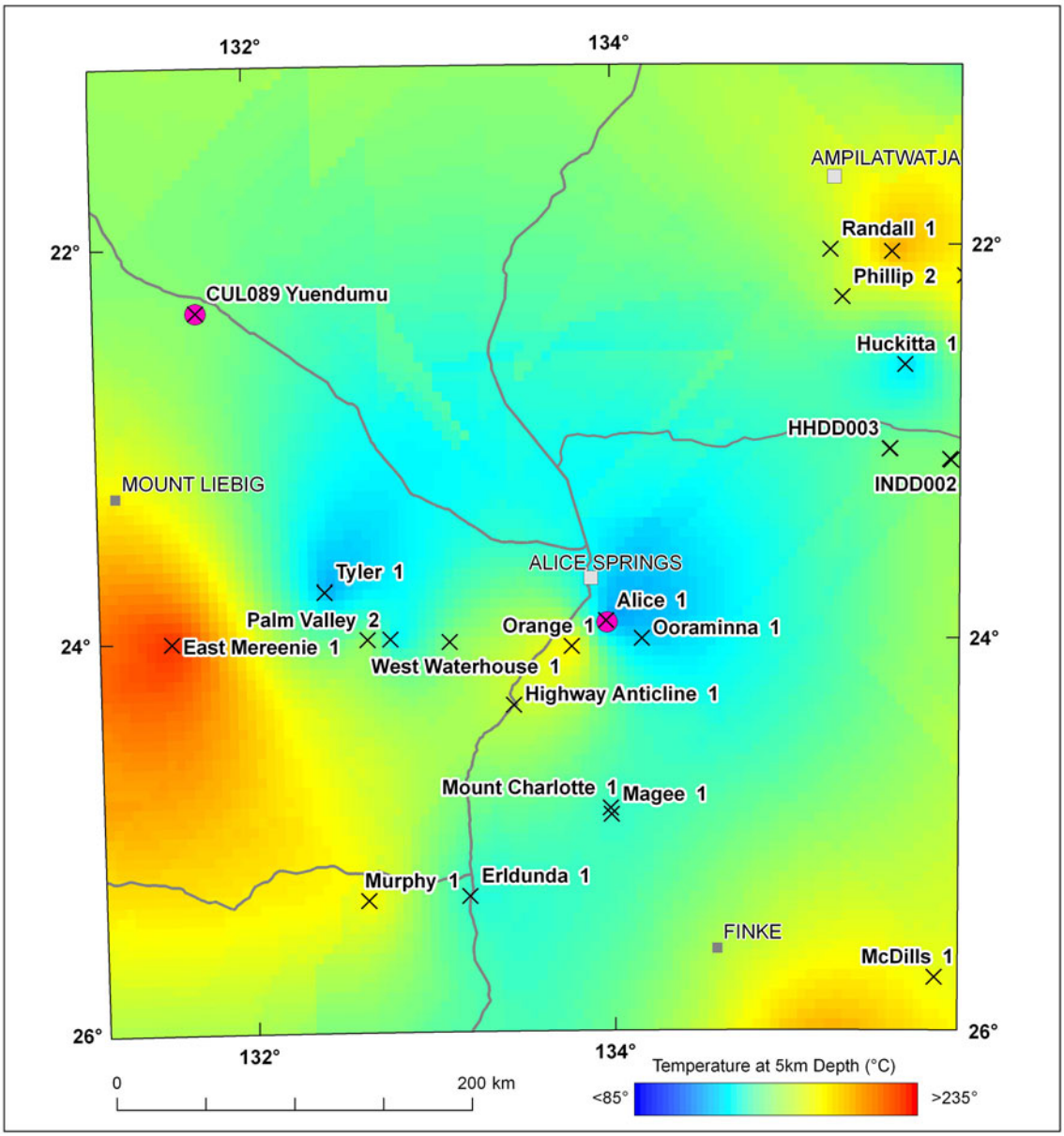

Figure 4.4: *Image of temperature at 5 km depth map generated from the OZTemp database. The locations of down-hole temperature measurements are shown (crosses – open-file bottom of hole temperature readings; pink circles – published heat-flow determinations). These temperature data were used to constrain the thermal properties of the 3D geological map during thermal modelling.*

4.4 THERMAL-CONDUCTIVITY DATA

Thermal conductivity is the measure of how well a rock conducts heat. For a geothermal resource, an overburden with a low thermal-conductivity value is desirable, as the insulating effect is greater and thus there is more potential for trapping heat (or elevating temperature) at depth. Thermal-conductivity data is very sparse in Australia and there are only a handful of publicly available values for the Northern Territory. As such, thermal-conductivity values needed for formations in the assessment area were estimated where required to enable the completion of the assessment.

For the purposes of thermal modelling, thermal-conductivity values were assigned to each basin in the assessment area. Thermal-conductivity values were also assigned separately to granites and the different basement terranes. Basin thermal-conductivity values were determined by assigning a value to each unit in a basin and a weighted harmonic mean was calculated for the basin. The spatial extent of six basins and the five basement provinces found in the study area is shown in Figure 4.5 (Lake Eyre Basin not shown). Of particular note are the stacked basins seen in the south-eastern corner of the study area. The distribution of felsic intrusive rocks is shown in Figure 2.1.1.

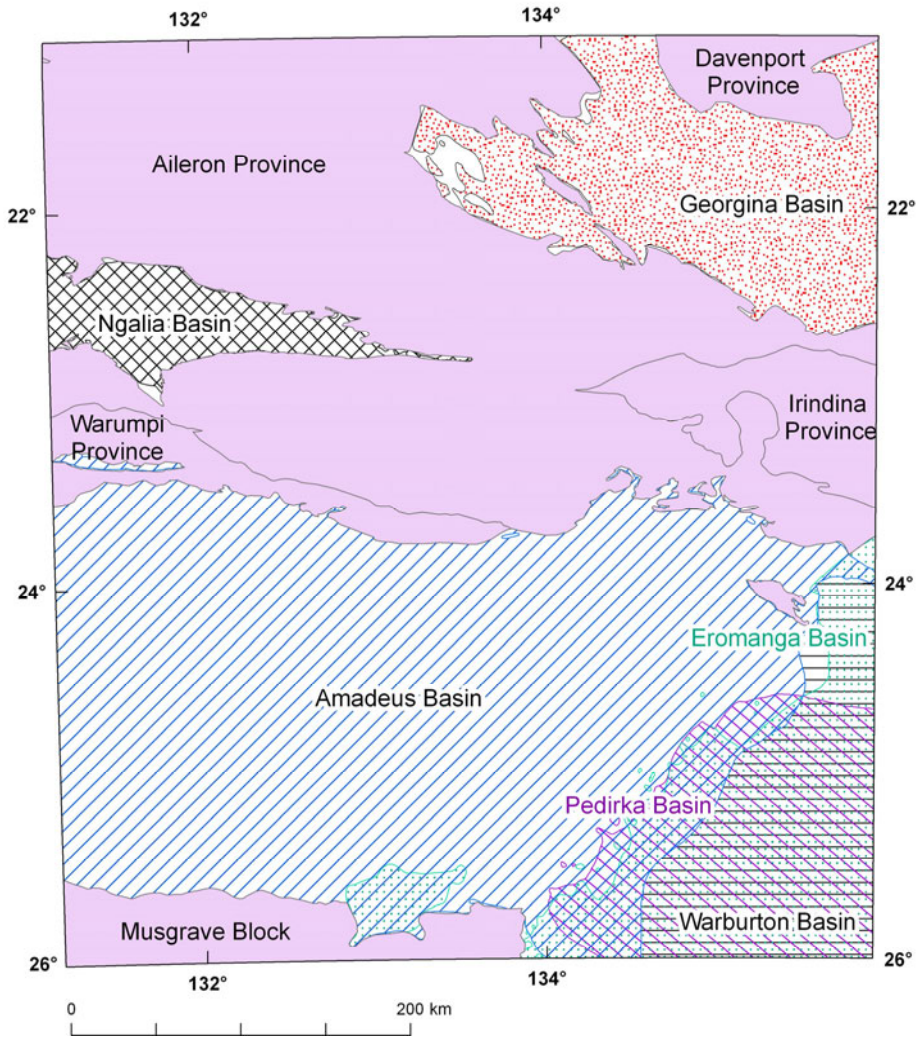

Figure 4.5: *Spatial extent of sedimentary basins (hashed and spotted), and basement provinces (pink) in the study area (Lake Eyre Basin not shown).*

Thermal-conductivity measurements for various formations were directly used where available. For formations where no published data exists, thermal-conductivity values were estimated by assessing available literature sources for information on lithology distribution within each formation. The percentage of each lithology present within each individual formation was then numerically estimated. For example, if the literature stated a formation was composed of majority sandstone and minor siltstone it was assumed that the formation was 80% sandstone and 20% siltstone (following Beardsmore, 2004). The thermal-conductivity values assigned to each lithology are summarised in Table 4.2.

Once thermal-conductivity values were calculated for each formation, an overall thermal-conductivity value for each basin was determined. Each of the formation values and the relative proportions of each formation in the basin were used to calculate a weighted harmonic mean. The error was calculated using a 5000 seed Monte Carlo simulation (Haynes, 2011). Where detailed stratigraphic information exists and the stratigraphy varies from one region to another (as in the Amadeus Basin), the thermal conductivity was estimated for more than one region in the basin. The values that were assigned to each basin in the model are shown in Table 4.3. The thermal-conductivity values used for the Warburton and Eromanga basins in this study are as calculated by Meixner *et al*. (2011) for the South Australia geothermal assessment. The Warburton and Pedirka basins were combined during 3D map construction, with the thermal-conductivity value assigned to the combined basin (Table 4.3) derived from the harmonic mean of the individual basins.

The thermal conductivities calculated for the older Georgina, Ngalia, Amadeus and Warburton basins are high and probably reflect the high quartz and/or carbonate content present in these basins. The high calculated thermal-conductivity values for these basins implies that these older basins will act as poor thermal insulators, while the younger Pedirka and Eromanga basins, with lower thermal conductivities, will provide better thermal insulation.

4.5 HEAT-PRODUCTION DATA

Heat-production values were calculated initially for cropping out geological units using radiometric data as outlined below (Section 4.5.1). These values were used to calculate sedimentary basin heat-production values (Section 4.5.2) and basement heat-production values (Section 4.5.3).

4.5.1 Heat production from radiometric data

Initial heat-production values for individual surficial geological units in this study were calculated by Goodwin and van der Wielen (*in prep.*); the methodology used to generate these values is outlined below. The values were calculated using the K, Th and uranium concentration grids from the radiometric map of Australia (Minty, 2010). Each grid was intersected with the 1:1 000 000 scale surface geology of Australia map (Raymond and Retter, 2010), and mean K, Th and uranium values assigned to each geological unit. Using these concentrations, heat-production values were calculated for each geological unit in the map. As the calculation of heat production requires a volume-mass conversion, density values were also required. Density values were applied to all geological units within the surface geology dataset based on lithological descriptions or actual measured values (approximately 5% of all units). Based on this information, heat-production values were calculated for each geological unit by grid unit, and the mean and standard deviation distributions for geological units across the whole coverage were compiled to give a final value and estimation of heat production variation for each geological unit.

Table 4.2: Common lithologies and thermal-conductivity values (Tc) compiled from a range of sources

LITHOLOGY	Tc (W/mK)	ERROR (W/mK)	# SAMPLES	REFERENCE(S)
Alluvium	1.3	0.1	3	Southern Methodist University (SMU)
Andesite	2.25	0.05	29	Cermak *et al*., 1982; Norden and Forster, 2006
Argillite	3.7	0.5	5	Davis *et al*., 2007
Basalt	2.17	0.17	65	Sass, 1964; Raznjevic, 1976; Skvarla *et al*., 1981; Cermak *et al*., 1982; Norden and Forster, 2006
Chert	2.3	0.4	14	GA; Skvarla *et al*., 1981; Cermak *et al*., 1982
Claystone	1.58	0.10	307	GA; SMU; Cermak *et al*., 1982
Coal	0.29	0.09	98	Raznjevic, 1976; Cermak *et al*.,1982
Conglomerate	2.67	0.19	119	GA; Cermak *et al*., 1982
Dacite	2.3	0.1	4	Norden and Forster, 2006
Diorite	2.93	0.08	180	SMU; Cermak *et al*., 1982
Dolerite	2.49	0.14	55	Sass, 1964; Cermak, 1982; Norden and Forster, 2006
Dolomite	3.31	0.10	385	Cermak *et al*., 1982; Beach, 1985; Carter *et al*., 1998
Dunite	4.4	0.1	7	Cermak *et al*., 1982
Gabbro	2.69	0.08	55	Sass, 1964; Cermak *et al*., 1982
Granite	3.00	0.15	316	GA; Cermak *et al*., 1982; Galson *et al*., 1987
Granodiorite	2.86	0.10	158	Cermak *et al*.,1982; Davis, 2007
Halite	3.92	0.17	67	Cermak *et al*.,1982
Limestone	2.39	0.57	1221	Cermak *et al*., 1982; Beach, 1985; Beardsmore, 1996; Davis, 2007
Marble	2.98			SMU
Marl	2.24	0.18	175	Kappelmeyer and Haenel, 1974; Hurtig and Schlosser, 1979; Cermak *et al*., 1982
Mudstone	1.9	0.3	6	GA
Quartz Monzonite	2.76	0.04	17	Davis, 2007
Quartzite	4.60	0.30	189	Cermak *et al*.,1982; Davis, 2007
Rhyolite	4.00	0.23	182	Cermak *et al*., 1982; Norden and Forster, 2006
Sandstone	3.60	0.10	450	GA; Beach, 1985; Carter *et al*., 1998; Davis, 2007
Schist	2.80	0.208	135	GA; Cermak *et al*.,1982
Shale	1.92	0.19	469	GA; Cermak *et al*.,1982; Beach, 1985; Carter *et al*., 1998
Siltstone	2.83	0.19	35	GA; Beardsmore, 1996
Trachyte	2.5	0.5	2	Norden and Forster, 2006
Tuff	2.01	1.14	47	SMU; Cermak *et al*.,1982
Unconsolidated Sediment	1.45	0.27	25	Raznjevic and Haenel, 1974; Cermak *et al*., 1982

Table 4.3: Thermal-conductivity values (T_C) assigned to each basin in the assessment area including the averaged value for the combined Warburton and Pedirka basins. STDEV is one standard deviation of data

BASIN	REGION	TC (W/mK)	STDEV (W/mK)	BASIN TC (W/mK)	BASIN TC STDEV (W/mK)
Georgina	East	2.6	0.4	2.8	0.3
	West	2.9	0.2		
Ngalia		3.1	0.2		
Amadeus	Southwest	3.1	0.1	3.0	0.1
	Central	3.0	0.1		
	Northeast	3.0	0.2		
Eromanga		2.4	0.4		
Warburton		3.2	0.2		
Pedirka		1.8	0.2		
Warburton/Pedirka				2.3	0.2

Following initial calculation of heat-production values, the data were corrected in order to overcome some of the limitations of using radiometric data. This was performed in two main steps:

1. A correction was applied to address systemic under-estimation of uranium concentrations in the radiometric data due to radon loss. This was corrected using an empirical factor of 1.4, such that corrected uranium concentration (Uc) = U x 1.4. (Goodwin and van der Wielen, *in prep*.); and
2. The second correction was applied to remove surficial effects, including the cropping out area of each unit and degree of weathering. Units as defined by the geological polygons of the surface geology dataset reflect, in reality, a mixture of outcrop and subcrop, as well as residual and transported regolith material, all with variably weathered overprints. As a result the element concentrations as determined by this methodology may not be true representations of each geological unit, but are instead indicative values that will vary with percentage of actual outcrop and degree of weathering. This is especially true for uranium and K, which are more geochemically mobile than Th. To overcome this deficiency, the data have been corrected by fixing the concentration of Th at the measured value and calculating the concentrations of uranium and K relative to Th concentration. Uranium concentration was recalculated based on the commonly occurring Th-uranium ratio of four as used by Taylor and McLennan (1985) and Rudnick and Gao (2003). Potassium concentration (in %) was recalculated as K = Th x 0.2667 (for further detail see Meixner *et al*., 2011).

Regression of original heat-production values against the values recalculated as described above gives a final correction factor of 1.24, as shown in Figure 4.6. All initial heat-production values calculated for basins (Table 4.4) were revised using this correction factor.

4.5.1.1 Limitations

The above methodology provides a consistent approach to calculating heat production for cropping out geological units. There are, however, some limitations to this approach that were not corrected for, as outlined below.

As heat-production values are assigned using K, Th and uranium radiometric data for cropping out units, geological units with little or no surficial expression may be misrepresented. For those geological units in the basins which do not crop out, heat-production values were assigned based on geochemically similar units that do crop out within the basin. For basins which have no surface expression, such as the Cooper Basin, heat-production values used were based on an average values for all of the sedimentary basin data compiled this study.

Assigned densities also may be inaccurate. However, given the density range for most crustal rocks is 2.6–3.0 g/cm^3, resultant errors in heat production arising from this methodological limitation are probably less than 10%.

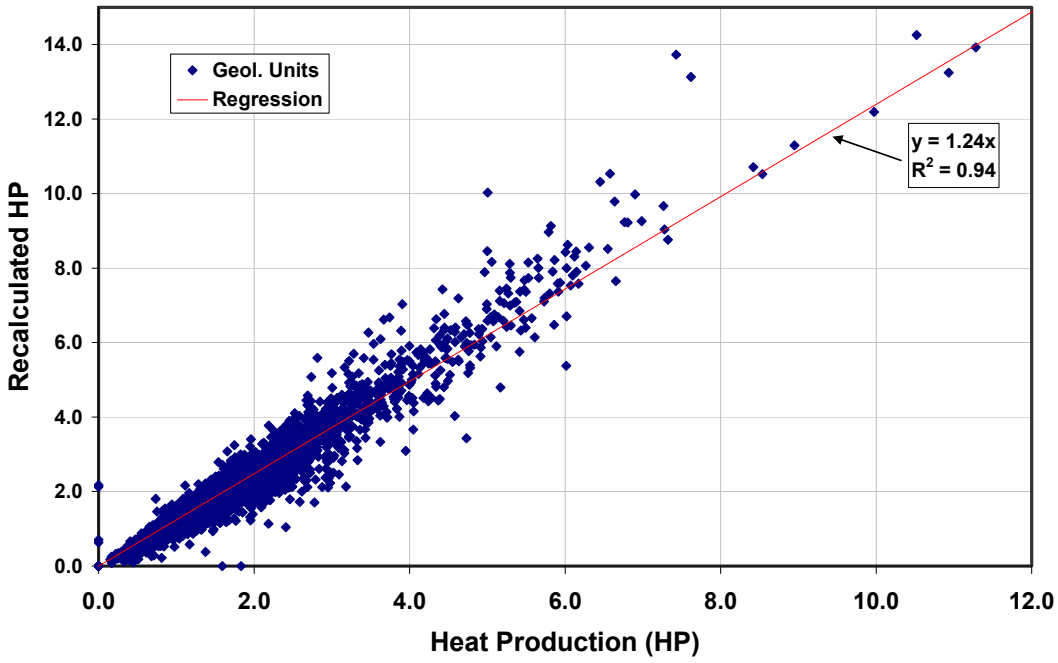

Figure 4.6: *Heat production (HP) data for Australian geological units (calculated from airborne radiometric data) versus recalculated heat-production values. Recalculation is based on adjusting uranium and K concentrations (see text for details). Linear regression gives a correction factor of 1.24.*

4.5.2 Sedimentary basin heat production

Heat-production values were calculated from radiometric data for the Ngalia, Georgina and Amadeus basins using the approach described in Section 4.5.1 (Table 4.4). The mean basin values have been weighted for unit thicknesses compiled using idealised stratigraphic sections (as used for thermal-conductivity calculations). Standard deviations for the heat-production values were calculated using a weighting system based on the relative thickness of each unit.

Heat-production values and standard deviations for the Warburton and Eromanga basins were assigned using values calculated for the South Australian geothermal assessment (Meixner *et al*., 2011). No heat-production data for individual geological units were available for the Pedirka Basin and, as such, the average value calculated for all sedimentary basins in the South Australia geothermal assessment (Meixner *et al*., 2011) was assigned. The Warburton and Pedirka basins were not differentiated in the 3D geological map (see Table 4.4 below).

Table 4.4: Heat-production values assigned to sedimentary basins in the 3D map. Heat production for each basin region and basin has been assigned (HP), where necessary multi-region basins have also been assigned a final basin-wide HP value (Basin HP). STDEV is one standard deviation of data

BASIN	REGION	HP (mW/m^2)	STDEV (mW/m^2)	BASIN HP (mW/m^2)	BASIN HP STDEV (mW/m^2)
Georgina	East	1.2	0.3	1.3	0.4
	West	1.3	0.4	-	-
Ngalia		1.5	0.4	1.5	0.4
Amadeus	Southwest	1.1	1.1	1.1	0.6
	Central	1.2	0.3	-	-
	Northeast	1.1	0.3	-	-
Eromanga		1.4	0.3	1.4	0.3
Warburton		1.6	0.5	-	-
Pedirka		1.7	0.8	-	-
Warburton/Pedirka		-	-	1.7	0.8

4.5.3 Basement heat production

The heat-production values calculated for individual surface geological units using the process described above (Section 4.5.1) were assigned to corresponding basement units in the basement solid geology (Figure 2.1.1; see Appendix 1 for detail). Where individual geological units were combined into a broader unit on the simplified solid geology map, the heat production of the individual geological units were combined using an area weighted mean.

In order to simplify the construction of the 3D map (see Section 4.6 below) and the subsequent thermal modelling process, it was necessary to combine solid geology units. This was achieved using heat-production values to group similar units together. This was achieved by creating a series of 'bins' or heat production categories into which the heat-production values obtained for each solid geology unit were sorted. The geological units in the 3D map were then grouped together according to these bins. The binned heat-production values are shown in Figure 4.7 and Table 4.6. The heat-production value assigned to the 3D map for each bin represents the median value for upper and lower bin range (Table 4.6). For a complete list of heat-production values for each geological unit see Appendix 2.

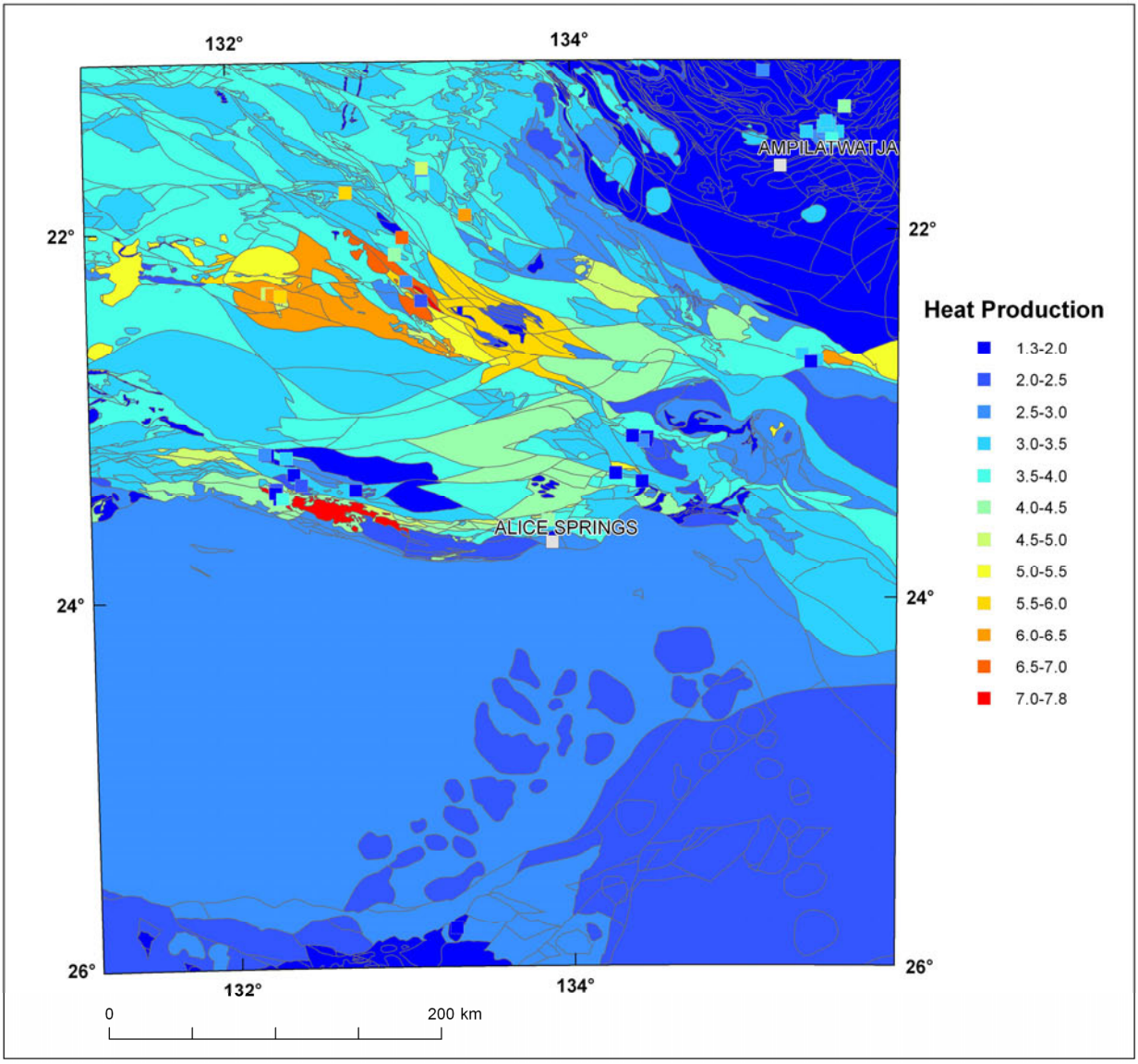

Figure 4.7: *Heat-production values assigned to the solid geology map. The heat-production values calculated from whole rock geochemistry data (squares) are also shown using the same colour scale for comparison. Heat production for both datasets in $\mu W/m^3$ coloured as per legend.*

In addition to the more generalised heat production calculation from radiometric data applied broadly across the study area, a number of point heat-production values were also calculated using whole rock geochemical data from Geoscience Australia's OZCHEM database for the purpose of validation (see Figure 4.7). The geochemical data largely correlate with the calculated heat production from radiometric data in areas where significant geological exposures occur (Figure 4.7). In areas dominated by regolith, such as in the northern Aileron Province, there is greater variability between the geochemical and radiometric data, as shown in Figure 4.7. Based on these results, it is considered that the radiometric data reasonably approximate true heat-production values.

Lithologies with the highest calculated point heat production (>5.0 $\mu W/m^3$) dominantly occur in the central-north of the study area within the Aileron Province. The Southwark Suite (5.3 $\mu W/m^3$) extends into the western part of the study area, and includes a number of associated granitic bodies interpreted beneath the Ngalia Basin. In the eastern part of the study area, the Marshall (6.3 $\mu W/m^3$) and Jinka (5.4 $\mu W/m^3$) granites have elevated heat production, and are interpreted to extend eastward beneath the Georgina Basin.

Heat production for the outcropping Davenport and Irindina provinces is low (mostly <3.5 $\mu W/m^3$). The hottest granites in the Davenport Province are represented by the Devils Suite and have a heat-production value of 3.2 $\mu W/m^3$. In the north of the Warumpi Province, the Teapot Granite Complex (7.3 $\mu W/m^3$) has elevated heat production. Heat-production values in the Musgrave Province are also low (<3.0 $\mu W/m^3$), including the extensive Pitjantjatjara Supersuite (2.4 $\mu W/m^3$) which extends north beneath the Amadeus Basin.

4.6 3D GEOLOGICAL MAP CONSTRUCTION

A 3D geological map of the study area was constructed using GoCad (version 2.6.0). The map delineates the two major components required for a geothermal play: the cover sequence, which provides sediments with potentially high thermal insulation properties, and basement, which is the source of potentially high-heat producing units. The 3D map dimensions based on a UTM Map Grid of Australia Zone 53 (Datum GDA94; Spheroid GRS 1980; central meridian 135°) consist of:

- 100 000 to 600 000 m Easting for an east-west width of 500 km;
- 7 670 000 to 7 100 000 m Northing for a north-south length of 570 km; and
- 2000 to -20 000 m (above sea level) for a depth of 22 km.

These dimensions approximate the following geographical extent:

- 131° 10' to 135° 55' longitude; and
- -26° 00' to -21° 5' latitude.

4.6.1 Cover sequences

The cover sequence consists of Neoproterozoic and younger cover sediments of the Amadeus, Georgina, Ngalia, Warburton, Pedirka and Eromanga basins. The top of the cover sequence is defined by the modelled DEM based on the 9 second DEM sourced from Geoscience Australia's Geophysical Archive Data Delivery System (GADDS)[6]. The base of the cover sequence is defined using a combination of a depth to magnetic basement map (Meixner and Haynes, 2012) and a previous study by Wellman (1991), who delineated the depth to the base of the Amadeus Basin.

The depth to magnetic basement map shows the interpreted depth to magnetic stratigraphy in metres below the topography (Figure 4.8). The map was constructed using depth to magnetic stratigraphy point values derived from drillhole and seismic data, and depth to magnetic source modelling methods. These points were combined with mapped geology (Raymond and Retter, 2010) to

[6] http://www.geoscience.gov.au/bin/mapserv36?map=/public/http/www/geoportal/gadds/gadds.map&mode=browse

delineate the outcropping magnetic basement and gridded using Intrepid Geophysics[7] variable density gridding routine using reduction factors of 3 and 3, and a cell size of 1000 m. Details of the compilation of the depth to magnetic basement map are found in Meixner and Haynes (2012).

The magnetic basement surface largely delineates the interface between Mesoproterozoic and older crystalline rocks from the overlying Neoproterozoic and younger cover sediments. The magnetic basement includes the Aileron, Warumpi, Davenport and Musgrave provinces. The non-magnetic cover consists of the Amadeus, Georgina, Ngalia, Warburton, Pedirka and Eromanga basins. The Harts Range Metamorphic Complex of the Neoproterozoic to Paleozoic Irindina Province has been included as basement due to the strong magnetic character of the highly metamorphosed units. The depth to magnetic basement 3D surface was generated by importing a grid of the depth to magnetic basement map (Meixner and Haynes, 2012) into GoCad. Topography was added to the depth values to change the relative depth values from metres below topography, to metres below sea level.

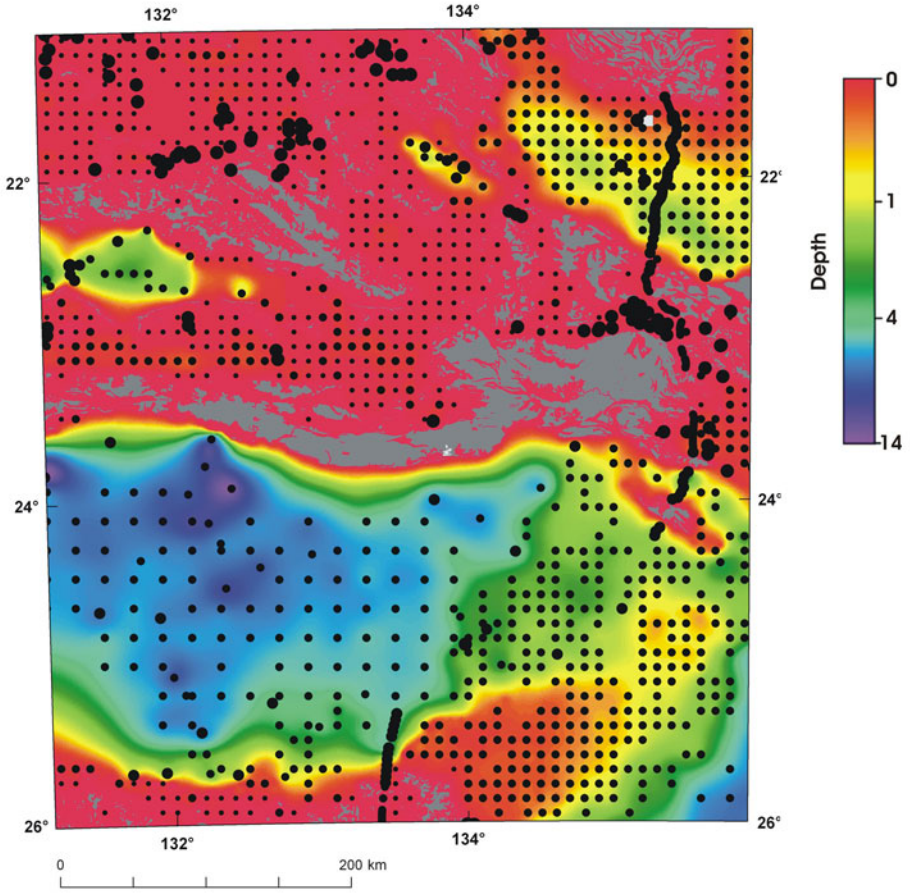

Figure 4.8: *Image of the depth to magnetic basement surface coloured by depth below topographic surface in km. Colour ramp legend at right. Grey polygons show cropping out basement. Points show locations of the depth delineating data used to constrain the basement surface. The size of the points indicates the level of confidence in the input data: large – high confidence; small – low confidence.*

[7] http://www.intrepid-geophysics.com/ig/index.php

Geological interpretations of the central portion of the Amadeus Basin (e.g., Wellman, 1991), indicate a shallowing of the basal contact to ~1460 m. This east-west trending shallow platform is also evident in interpretations of the seismic line L121-BMR85 (Shaw *et al*., 1991). The depths to the magnetic source in the same area are considerably deeper, with depth values reaching 7400 m. The larger magnetic depth estimates are evident in both the profile modelling and the spectral method results. This difference between the depth to the base of the Amadeus Basin and the depth to the top of the magnetic sources in the same area has been observed in previous depth to magnetic basement studies (Young and Shelley, 1966; Wells *et al*., 1970; Wellman 1991), and has been attributed to additional non-magnetic material above basement, an interpretation which is supported by Meixner and Haynes (2012). The depth estimates from the seismic data and the depth to magnetic source methods converge in the north and south of the basin suggesting that the base of the Amadeus Basin is coincident with the depths to the magnetic source and therefore, the magnetic basement.

The surface describing the base of the Amadeus Basin has been constructed using an amalgamation of two surfaces, together with the seismic data. The first surface, a contour map (Figure 2 of Wellman, 1991) delineating the depth to the base of the Amadeus Basin generated from mapping geological boundaries and formation thicknesses was imported into GoCad and converted into a 3D surface. This surface, where data exists, forms the base of the Amadeus Basin. Where it does not exist, the base of the Amadeus Basin has been defined by the depth to magnetic basement surface. Where the two surfaces meet, the magnetic basement surface has been modified to ensure a smooth transition between the two surfaces. This new surface describing the base of the Amadeus Basin has then been fitted to depth constraints from seismic line L121-BMR85 (Shaw *et al*., 1991). The eastern boundary of the Amadeus Basin sequence has been constrained by the Australian Geological Provinces dataset to separate the Amadeus Basin from the Warburton-Pedirka basin sequence. Figure 4.9 shows an oblique view of the base of the cover sequence surface.

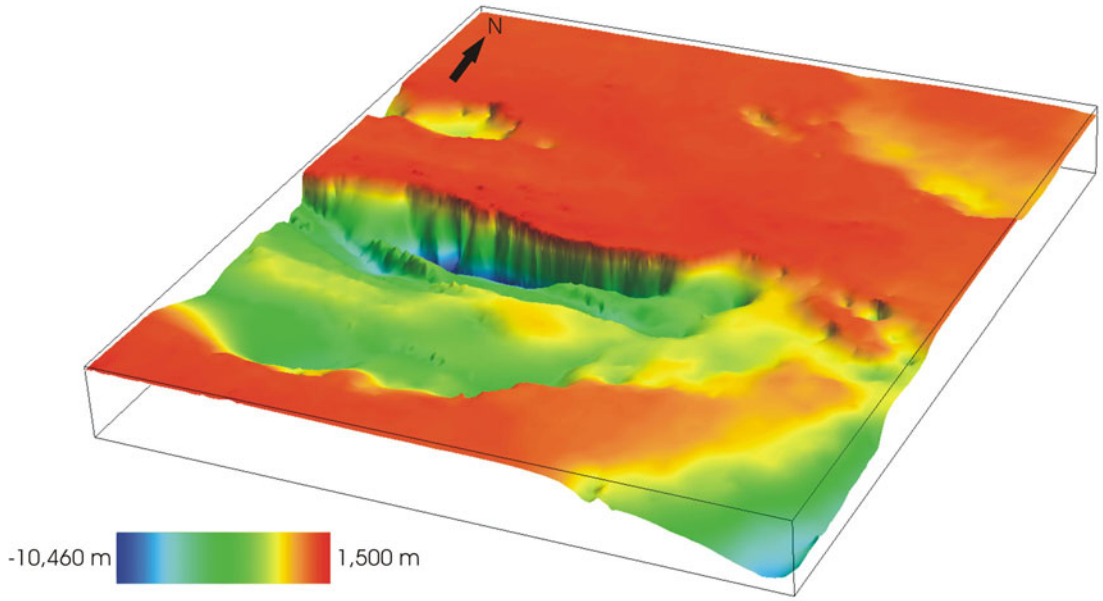

Figure 4.9: *Oblique plan view of the base of the cover sequence surface that separates the basement from Neoproterozoic and younger cover including the Amadeus, Ngalia, Georgina, Warburton, Pedirka and Eromanga basins. Depth above sea level given in metres, vertical exaggeration 5x.*

The base of the Pedirka Basin was constructed using the Australian Geological Provinces dataset to constrain its outcropping and subcropping extent. Depth information is from an interpreted cross-section from Ambrose *et al*. (2002). This surface separates the Pedirka Basin from the underlying Warburton Basin and was not incorporated in the 3D map for the thermal modelling. It was, however, used to define the basal temperature of the Pedirka Basin for the hot sedimentary aquifer prospectivity analysis (see Section 4.10). A portion of the Eromanga Basin overlying the Pedirka and Warburton basins in the south east of the assessment area, has been extracted from an existing larger Eromanga Basin study (van der Wielen *et al*., *in prep*.) and incorporated into the 3D map.

4.6.2 Basement

The basement portion of the 3D map consists of the Aileron, Warumpi, Davenport, Musgrave and Irindina provinces. The solid geology map boundaries were imported into GoCad and extrapolated downwards from the base of the cover sequence surface to approximate the base of the variable heat production layer (Figure 4.10). Eight 3D maps were constructed using different depths of extrapolation (3, 4, 5, 6, 7, 8, 9, and 10 km) in order to simulate the different possible depth extent of the variable heat production layer. Between the base of the variable heat production layer and the base of the model at 20 km depth, a flat horizontal layer has been added at 13 km depth to separate the low heat producing mid-crustal layer from an upper-crustal layer. The mid-crustal layer has been assigned a heat-production value of 1.0 $\mu W/m^3$ (Rudnick and Gao, 2003), while the upper-crustal layer has been assigned an average heat-production value of 1.7 $\mu W/m^3$ (Rudnick and Gao, 2003).

The model space was then voxelised, creating cells with the dimensions 4 km by 4 km by 200 m. The overall dimensions of the 3D map volume are 500 km by 570 km with a 22 km vertical extent. The 22 km vertical extent includes 20 km below sea level and two kilometres above sea level to accommodate surface topography. Regions within the 3D volume were created using the surfaces described above as bounding surfaces. Figure 4.10 shows a north-south section through the final model using the five kilometre thick variable heat production layer.

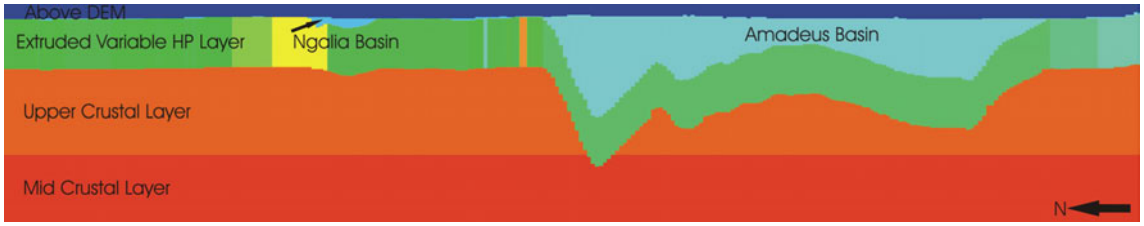

Figure 4.10: *North-south cross-section through the western portion of one of the eight 3D maps. The section shows the 5 km depth extrapolated variable heat production layer assigned from the solid geology map (oranges and yellows – high- heat producing lithologies; aquas and greens – low- heat producing lithologies). The cross-section transects a thin section of the Ngalia Basin, as well as a thick section of the Amadeus Basin. Beneath the extrapolated 5 km section lies the homogenous upper (solid orange) and mid crustal (solid red) layers. The dark blue layer shows the region of the model above the topography. Vertical exaggeration 5x.*

4.7 GEOTHERMAL PROSPECTIVITY RELATIVE CONFIDENCE MAP(S)

A relative confidence map has been constructed for the hot rock geothermal assessment, and is based on levels of certainty attributed to the geological and thermal properties used in the construction of the 3D geological and thermal models. This has been achieved by attributing 2D GIS representations of the depth to basement (see above) and solid geology (see Appendix 1) maps. Three GIS coverages were created to provide an indication of the relative confidence level for each dataset: (1) confidence in the geological data used, (2) confidence in the thermal conductivity, and (3) confidence in the heat-production data, in addition to temperature residual data (see Section 4.7 below). The confidence level in each coverage was normalised and used to create rasters that were then summed together to provide a combined indication of confidence in the input data. These additive rasters were coloured using the same continuous colour ramp for all three images for ease of comparison; in the simpler maps this is less apparent as less confidence intervals are present. In addition, the temperature residuals between the measured borehole temperatures and the final thermal model were used to define the confidence in the thermal model output.

4.7.1 3D geology relative confidence image

A raster that represents the relative confidence in the geological data used to construct the 3D geological model was generated (Figure 4.11). The primary input into the 3D geological model was the solid geology map (see Section 4.6 above). The confidence level attributed to each of the elements of the solid geology map was based directly on the depth of cover in each part of the map (Section 4.6.1).

Units in the surface geology of Australia map (Raymond and Retter, 2010) were attributed a high relative confidence level, those under shallow cover (<2000 m) a medium relative confidence level and those under deep cover (>2000 m) a low relative confidence level (Table 4.5). This reflects the confidence in the definition of lithologies and their distribution beneath cover. It also reflects the confidence in the distribution of the geological units within the sedimentary basins.

Table 4.5: The depth of cover from the depth to magnetic basement map (Meixner and Haynes, 2012) and the uncertainty value (low number – low relative confidence; high number – high relative confidence) assigned

DEPTH OF COVER	CONFIDENCE VALUE
Cropping out unit (1:1 000 000 surface geology)	3
Under shallow cover (<2000 m)	2
Under deep cover (>2000 m)	1

4.7.2 Thermal properties relative confidence images

The thermal modelling results that form the basis of the geothermal potential assessment are fundamentally influenced by the heat-production and thermal-conductivity values assigned to the thermal model. Uncertainty in these assigned values results in uncertainty in the surface heat flow and temperature at depth. As part of the construction of the thermal modelling relative confidence map, heat production and thermal conductivity confidence images were generated (Figure 4.12).

The confidence in the thermal properties at any point is a combination of the confidence in the geological attribution and also the variability of the thermal conductivity or heat production within that unit. The confidence levels attributed to each unit were therefore heavily influenced by the depth of cover (Table 4.5). The depth of cover value was therefore normalised and multiplied by the percentage error of each thermal property as described in Tables 4.3 and 4.4. As described in Sections 4.4 and 4.5, the errors in the heat production and the thermal conductivities are represented by the first standard deviation of the value calculated during the thermal property data compilation.

For areas of outcropping basement units, a single thermal-conductivity value with a uniform 10% error was estimated.

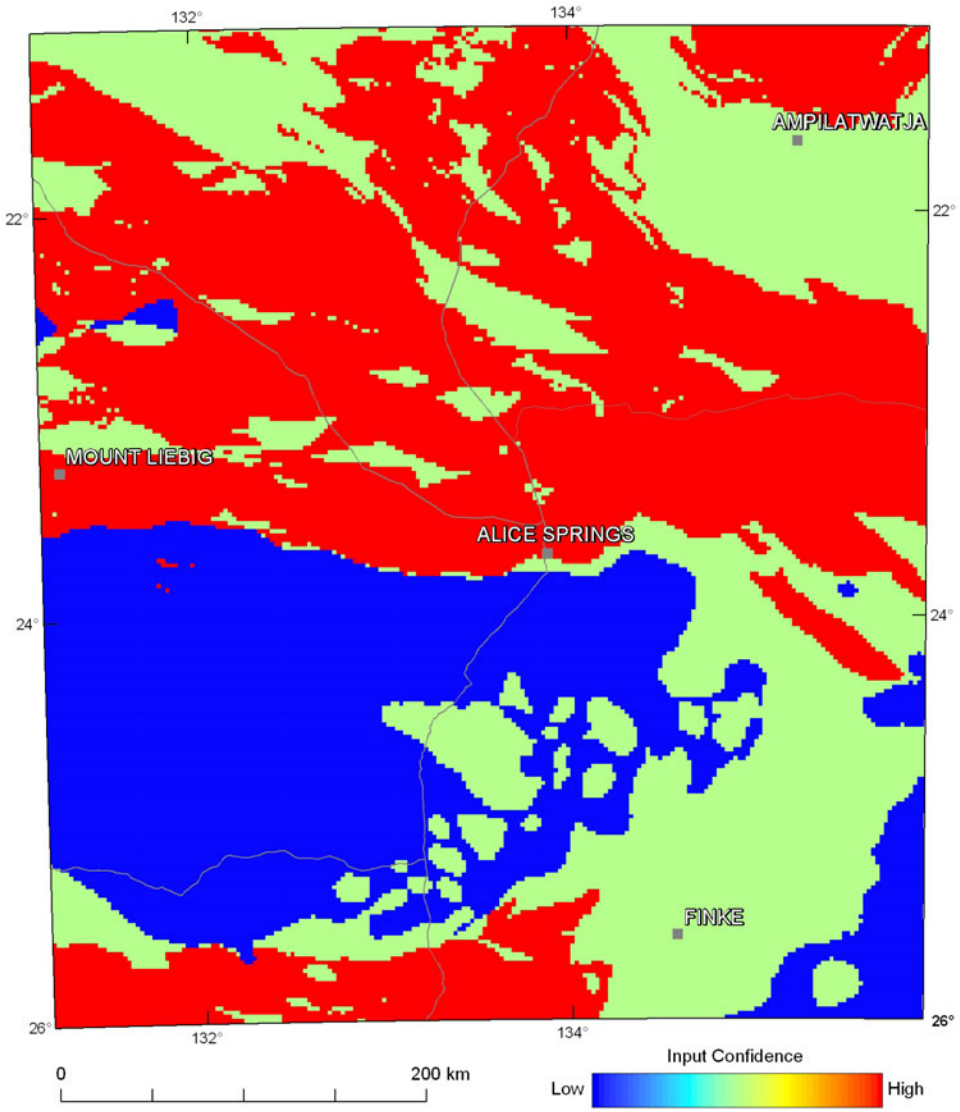

Figure 4.11: *3D geology relative confidence map. This is a 2D representation of the reliability and uncertainty in the data that has been used to produce the 3D geological map.*

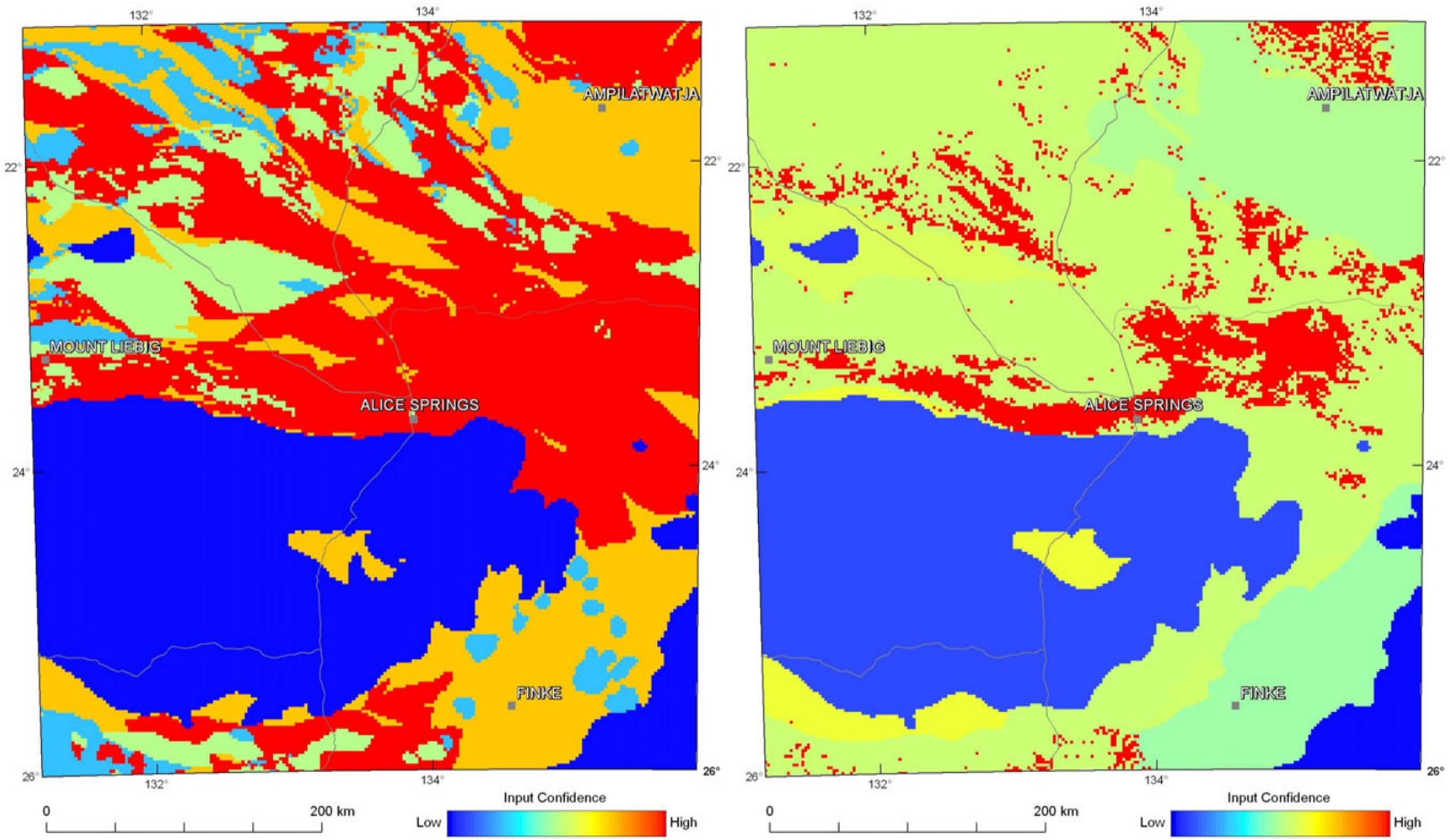

Figure 4.12: *Images of the relative thermal conductivity (left) and relative heat production (right) confidence maps.*

4.7.3 Modelled temperature residual

The difference between measured borehole temperatures and the final modelled temperatures at the same depth and location were extracted from the final 3D temperature model to give the temperature residual values. As described, only actual temperature measurements were used in the modelling, and drill holes with only temperature gradients were excluded. The locations of these are described in Section 4.3. A fit of ± 5°C was achieved in twelve of the twenty wells with temperature data. These twelve wells were attributed with positive confidence values. The remaining eight wells with higher residual temperatures had a negative confidence value attributed to them. The locations of the wells were then buffered with a 10 km radius (see Figure 4.13).

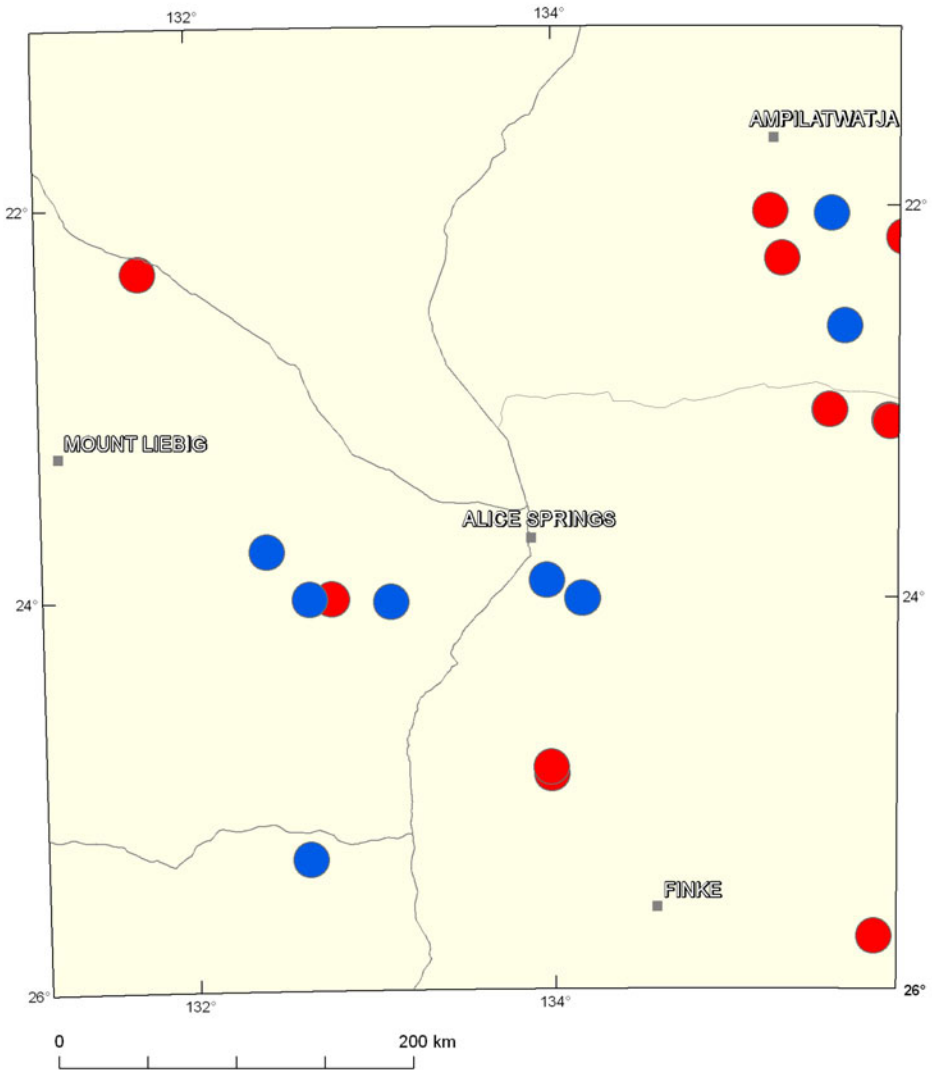

Figure 4.13: *Well locations buffered to 10 km with the residual between the recorded temperature and the modelled temperature. Red spots – wells with a temperature residual < 5°C above or below actual value ; blue spots – residual temperature > 5°C above or below actual value.*

4.7.4 Combined relative confidence image

The combined relative confidence map (Figure 4.14) incorporates the relative confidence values of the 3D geological map, heat production, and thermal conductivity confidence maps, in addition to point data of modelled temperature residual. The confidence values from these maps were normalised then combined using the following formula:

$$\text{Combined} = (\text{3Dmap} \times \text{HP}) + (\text{3Dmap} \times \text{Tc}) \quad (5)$$

Where: Combined = the combined relative confidence map; 3Dmap = the 3D geology confidence map; HP = the heat production relative confidence map; and Tc = the thermal conductivity relative confidence map.

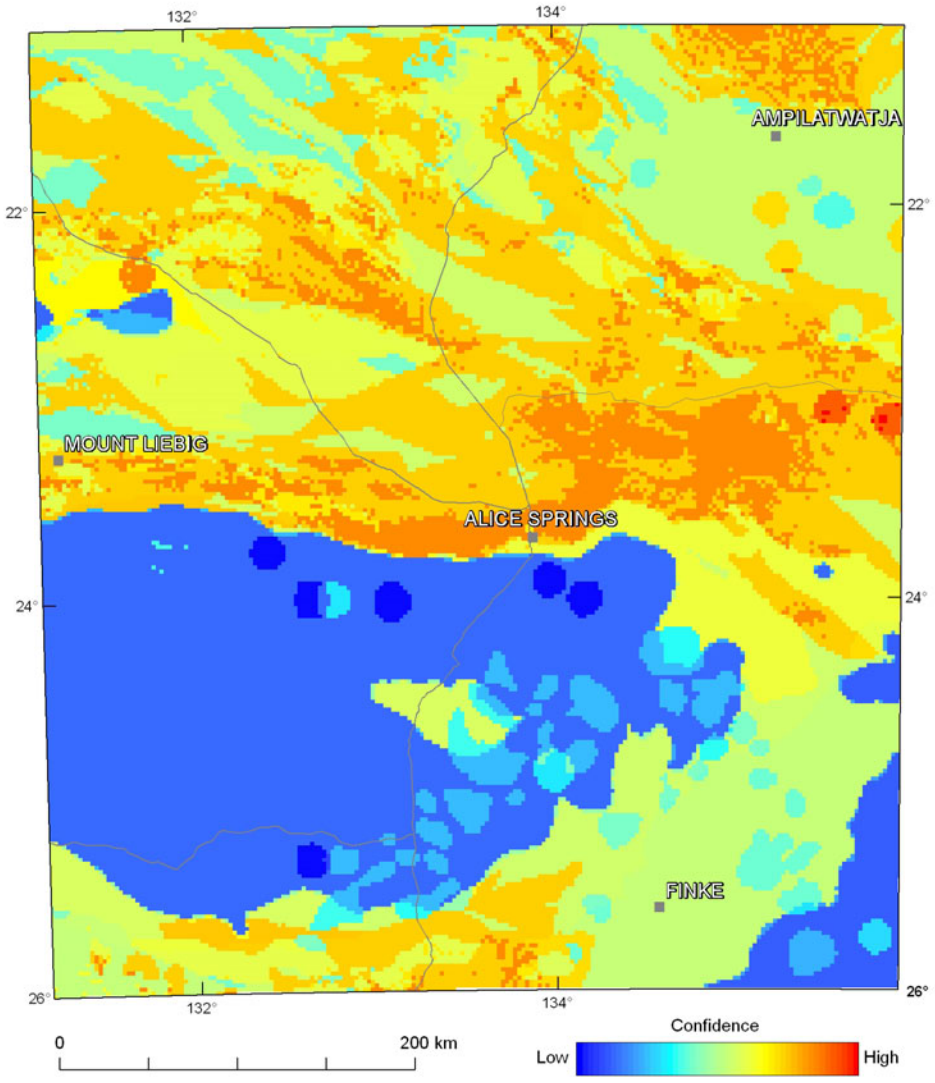

Figure 4.14: *Combined relative confidence map of the assessment area incorporating the data uncertainty from the 3D geological map, as well as the uncertainty in the heat-production and thermal-conductivity data and the residual between the measured temperature data and the final modelled results.*

4.8 THERMAL MODELLING

4.8.1 Thermal modelling workflow

Thermal properties were assigned to each geological unit of the 3D geological maps. The boundary conditions for all of the thermal model runs were set as follows:

- Cells in the 3D mesh coincident with the topographic surface were assigned a constant temperature of 25°C. This value was calculated based on the Bureau of Meteorology's[8] mean annual surface temperature approximated for the assessment area (22°C). Three degrees were added to this mean annual surface temperature to take into account the average soil temperature which is generally about 3°C higher than the average air temperature (Howard and Sass, 1964); and
- A constant heat-flow value of 33 mW/m^2 was applied to the base of the model at 20 km depth. This value was calculated by adding the heat flow contribution from the heat produced between the base of the model and the base of the crust, to the heat flow at the base of the crust. Rudnick and Gao (2003) estimate mid-crustal heat production (13 to 23 km depth) as 1.0 µW/m^3, and lower-crustal heat production (more than 23 km depth) as 0.19 µW/m^3. The averaged Moho depth in the region is approximately 47 km (Kennett *et al*., 2011). Based on these heat-production values and depth extents, the heat flow contribution between the Moho and the base of the model is 8 mW/m^2. Adding this value to 25 mW/m^2, the reduced heat flow calculated at the base of the crust from McLaren, *et al.* (2003), results in a heat-flow value of 33 mW/m^2 at the base of the model.

The thermal model runs were performed at the National Computational Infrastructure (NCI) [9] high-performance computing facility at the Australian National University. The thermal modelling component of the GeoModeller software was run via a batch script, which bypasses the GeoModeller Graphical User Interface (GUI) and allows the importation and computation of GoCad-format 3D geological maps. The batch script assigns the boundary conditions and thermal properties to the 3D map lithologies and also specifies the maximum number of iterations and the temperature residual. The temperature residual is the maximum temperature difference between the second last and last model iteration from all cells in the model. The modelling is complete once either the maximum number of iterations is completed, or the temperature residual drops below the value specified in the script. The temperature residual should be of a value low enough, and the number of iterations should be high enough, that the model approaches thermal equilibrium.

Initial forward model runs were conducted on the voxelised 3D geological maps at a reduced 6 km by 6 km by 200 m resolution to reduce computation time. The computation time for the 4 km by 4 km by 200 m cell size full resolution final model was approximately 18 hours on the NCI. The long computation time reflects the large number of cells (~2 million) and the number of iterations (~50 000) required for the model to approach thermal equilibrium. Thermal equilibrium was considered to have been reached once the final temperature residuals were less than 0.0001°C.

Following computation of the thermal models, the calculated vertical heat flow and temperature values were imported into GoCad for comparison with the available surface heat flow and down-hole temperature measurements. Residual values between the measured and modelled temperature and surface heat-flow values were computed. Mean residual values were then calculated for the assessment area. Mean temperature residuals were also calculated for specific regions in the model including the Amadeus, Ngalia, Eromanga and Georgina basins.

[8] http://www.bom.gov.au/jsp/ncc/climate_averages/temperature/index.jsp?maptype=6&period=an
[9] http://nci.org.au/

The median residuals for each model run were reduced by making adjustments to the input 3D map and thermal model properties. Adjustments were made in three stages. In the first stage, the optimum depth extent of the variable heat production layer required to produce a minimum in the mean temperature residuals for the entire assessment area was determined. In stage two, heat-production values for the variable heat production basement layer in the Amadeus, Ngalia, Eromanga and Georgina basins were modified to minimise the regional mean temperature residuals. Finally, in stage three, where further improvements to mean temperature residuals were deemed possible, adjustments were made to the thermal conductivities of the sedimentary basins.

Modifying the heat-production values of the basement prior to modifying thermal conductivities of the basins is justified considering the relative uncertainties. The heat-production values for the basement beneath the sedimentary basins have a higher degree of uncertainty due to the inherent uncertainty associated with the solid geology map in regions where basement is covered by thick sedimentary sequences. In addition, the initial heat-production values assigned to these mostly undifferentiated basement province units are averaged heat-production values for their respective provinces (see Appendix 2) thereby incorporating a further degree of uncertainty. The degree to which individual heat-production values were allowed to vary, however, was restricted to 1.1 $\mu W/m^3$ so that final heat-production values were not radically different to the initial values used. However, in the Ngalia Basin the basement heat production needed to be modified by 2.1 $\mu W/m^3$. Modification of thermal properties was spatially restricted to where the heat-flow measurements and all but two of the down-hole temperature measurements are located in the Amadeus, Ngalia, Eromanga and Georgina basins. The modelling process was considered completed once the mean absolute temperature residual (measured down-hole temperatures minus the modelled temperatures) for the entire assessment area and the individual basin regions was less than 2°C.

4.8.2 Forward modelling results

Initial forward thermal models were computed on eight 3D maps with depth of extrapolated variable heat production set at 3, 4, 5, 6, 7, 8, 9 and 10 km. The individual geological elements of the 3D maps were assigned initial thermal properties based on the thermal-conductivity (Tables 4.2 and 4.3) and heat-production (Table 4.4) data compilations. The thermal models were then computed. These values are shown in Table 4.6. The resulting heat-flow values and temperature residuals are shown in Table 4.7. The two measured surface heat-flow values have also been compared to the coinciding modelled values. The optimum depth of variable heat flow was determined using mean residual temperatures rather than heat flow residuals, as the number of temperature measurements available (22) far exceeds the number of heat flow measurements available (two). The initial thermal model that produced the smallest absolute mean temperature residual was based on the 3D map with the six kilometres depth extent of variable heat flow. As a result, all subsequent thermal modelling used the six kilometre variable heat flow depth extent 3D map. The modelled temperatures at four kilometre depth from the optimum initial forward model run and the temperature residuals are shown in Figure 4.15.

The initial model was then updated using the processes described in stages two and three in Section 4.8.1 to produce the final thermal model. The modelled temperatures from the final thermal model are shown in Figure 4.16. The mean temperature residuals are shown in Table 4.7, and the residual temperature values and modelled heat flow at the measurement locations are shown in Table 4.8.

Table 4.6: Thermal properties used in the initial and final thermal models. The initial model properties are from the data compilations (see Tables 4.2 to 4.4) unless otherwise stated. The uncertainty values were assigned from the data compilations unless otherwise stated

3D LITHOLOGICAL ELEMENT	HEAT PRODUCTION ($\mu W/m^3$)		THERMAL CONDUCTIVITY (W/mK)	
	INITIAL	FINAL	INITIAL	FINAL
Eromanga Basin	1.4	1.4	2.4	2.3
Warburton/Pedirka Basins	1.7	1.7	2.3	2.2
Georgina Basin	1.3	1.3	2.6	2.8
Ngalia Basin	1.5	1.5	3.1	2.8
Amadeus Basin	1.1	1.1	3.0	2.9
Basement (HP bin 1.3 – <2.0)	1.7	1.7	3.0[3]	3.0
Basement (HP bin 2.0 – <2.5)	2.3	2.3	3.0[3]	3.0
Basement (HP bin 2.5 – <3.0)	2.8	2.8	3.0[3]	3.0
Basement (HP bin 3.0 – <3.5)	3.3	3.3	3.0[3]	3.0
Basement (HP bin 3.5 – <4.0)	3.8	3.8	3.0[3]	3.0
Basement (HP bin 4.0 – <4.5)	4.3	4.3	3.0[3]	3.0
Basement (HP bin 4.5 – <5.0)	4.8	4.8	3.0[3]	3.0
Basement (HP bin 5.0 – <5.5)	5.3	5.3	3.0[3]	3.0
Basement (HP bin 5.5 – <6.0)	5.8	5.8	3.0[3]	3.0
Basement (HP bin 6.0 – <6.5)	6.3	6.3	3.0[3]	3.0
Basement (HP bin 6.5 – <7.0)	6.8	6.8	3.0[3]	3.0
Basement (HP bin 7.0 – ≤7.8)	7.4	7.4	3.0[3]	3.0
Upper Crust	1.7[1]	1.7	3.0[3]	3.0
Mid Crust	1.0[2]	1.0	2.0[4]	2.0

[1] Average heat production for upper crust (< 13 km depth) Rudnick and Gao (2003)
[2] Average heat production for mid crust (> 13 km depth) Rudnick and Gao (2003)
[3] Typical thermal-conductivity values for crystalline basement rock (Meixner *et al*., 2011)
[4] Typical thermal-conductivity values for crystalline basement rock at mid crustal levels (Meixner *et al*., 2011)

Table 4.7: Results of the initial forward thermal model runs using differing depths of variable heat production. The mean temperature residual is the measured down-hole temperature minus the modelled result. The measured (values shown in brackets after the well name) and modelled heat-flow values are also shown for the two wells in the assessment area

DEPTH OF VARIABLE HEAT PRODUCTION (km)	MEAN TEMPERATURE RESIDUAL (°C)	HEAT-FLOW VALUES (mW/m^2)	
		CUL089 YUENDUMU (56)	ALICE 1 (62)
3	3.8	65	60
4	2.5	68	63
5	1.1	72	66
6	-0.3	75	68
7	-1.6	79	71
8	-2.9	83	74
9	-4.2	86	76
10	-5.6	90	79

Table 4.8: Results of the initial and final thermal model runs on the 6 km variable heat production layer 3D map. The initial and final temperature residuals (measured down-hole temperatures minus the modelled values), for the entire assessment area as well as the individual basin regions are listed. The measured (values shown in brackets after the well name) and modelled heat-flow values are also shown for the two wells in the assessment area

	INITIAL	FINAL
SURFACE HEAT FLOW (mW/m^2)		
CUL089 Yuendumu (56)	75	65
Alice 1 (62)	68	61
MEAN TEMPERATURE RESIDUAL (°C)		
Entire assessment area	-0.3	0.2
Amadeus Basin	-2.3	0.3
Georgina Basin	3.2	1.8
Ngalia Basin	-3.4	-1.6
Eromanga Basin	5.9	1.7

The results of both the initial and final thermal models (Figures 4.15 and 4.16) show temperature at depth has a strong relationship with the heat-production values assigned to the solid geology map (Figure 4.7). This is a somewhat expected result, as higher heat production ultimately results in elevated temperatures. This relationship reflects the small relative differences in the thermal-conductivity values assigned to the older Georgina, Ngalia and Amadeus basins as compared to those assigned to the basement units (Table 4.6) and suggests that these older covering basins are not acting as good insulators. The younger sedimentary basins have lower thermal-conductivity values and hence provide more effective thermal insulation. This results in elevated temperatures in the southeast of the assessment area, even though the basement in this area was assigned a relatively low heat-production value.

The values of the temperature residuals (down-hole measured temperature minus modelled temperature) for the initial thermal model are all relatively small (Table 4.8). This indicates that the initial thermal model produces a relatively good temperature match, at least in the regions where there are down-hole temperature measurements. The largest residual value lies within the Eromanga Basin, where the initial model underestimates the measured temperature by about 6°C. Considering this temperature was measured at a depth of ~3 km, a ~2°C/km mismatch of the temperature gradient is considered acceptable. The difference between the measured and modelled heat-flow values for the Alice 1 and CUL089 Yuendumu wells, however, are of greater significance. The modelled heat flow for the Alice 1 well (68 mW/m^2) in the Amadeus Basin overestimates the measured value (62 mW/m^2) by a modest 6 mW/m^2, while the modelled value for the CUL089 Yuendumu well (75 mW/m^2) in the Ngalia Basin overestimates the measured heat flow (56 mW/m^2) by 19 mW/m^2. These overestimations of the heat flow indicate that the heat production beneath the measurement locations and/or the basal heat flow of the model is too high.

The major difference between the initial and final thermal models is the heat-production values assigned to the basement underlying the Amadeus, Georgina and Ngalia basins. The geometry of the basement units under these basins were based on the solid geology map units (Figure 2.1.1) and consist of largely undivided units. These undivided units were assigned averaged heat-production values for their respective provinces. These averaged heat-production values were, at least in the locations of temperature measurements, too high for both the Warumpi Province, which underlies the Amadeus Basin, and the Aileron Province, which underlies the Ngalia Basin. These elevated heat-production values have produced the negative temperature residuals in Table 4.8. In contrast, the heat-production values were too low in the Georgina Basin, where the heat production assigned to the underlying Davenport Province resulted in positive temperature residuals. Decreasing the heat production assigned to the Warumpi and Aileron provinces to 1.7 μW/m^3, and increasing the heat production for the Davenport Province to 2.8 μW/m^3 resulted in smaller temperature residuals. The

lowering of basement heat production beneath the Ngalia and Amadeus basins has also produced a better fit between measured and modelled heat-flow values (Table 4.8). The final modelled heat flow in the CUL089 Yuendumu well was 65 mW/m^2 as compared to the measured value of 56 mW/m^2, despite basement heat production being revised in the vicinity of the well. This high modelled heat flow is the result of one or more of the following model properties being too high: basal heat flow; heat production of mid crust; heat production of lower crust; heat production of basement beneath the CUL089 Yuendumu well; depth extent of extruded basement; and heat production of the Ngalia Basin. Without additional heat-flow measurements it is not possible to determine which single property, or properties, are the cause of this increased modelled heat flow.

Further minimisation of temperature residuals was achieved by modifying the thermal conductivities assigned to the sedimentary basins. Thermal conductivities were reduced for the Eromanga, Warburton/Pedirka, Ngalia and Amadeus basins, and increased for the Georgina Basin, as seen in Table 4.6. A small number of individual temperature residuals greater than 10°C remain (Figure 4.16). It was not possible to minimise these temperature residuals further due to the simplicity of the 3D map.

The changes to heat-production and thermal-conductivity values between the initial and final thermal model runs resulted in a modest change in the 3D temperature distribution (Figures 4.15 and 4.16). These thermal property changes have minimised temperature residuals and improved the fit between modelled and measured data, through the lowering of temperature at depth in the Amadeus and Ngalia basins, and increasing temperature at depth in the Georgina and Eromanga basins.

4.9 RELATIVE HOT ROCK GEOTHERMAL POTENTIAL

The predicted temperatures at the four kilometres depth slice through the thermal model (Figure 4.16; Plate 4.1) can be used to identify areas that have a higher hot rock geothermal potential. The four kilometre depth slice image has temperatures ranging from 103–134°C and indicates hot rock geothermal potential ranges from low to moderate.

The highest relative potential is found to the north of the Ngalia Basin and on the northern edge of the Amadeus Basin. These regions of relatively elevated potential are related to the spatial distribution of high-heat producing lithologies (>6 $\mu W/m^3$; Figure 4.7). These are mostly granites of the Aileron and Warumpi provinces. The lack of thermally-insulating sediments over these high-heat producing lithologies has resulted in only moderate temperatures and, therefore, moderate hot rock geothermal potential.

The only granites identified on the solid geology map that are high-heat producing occur beneath the southern Ngalia Basin on the western edge of the assessment area. The final thermal conductivity assigned to Ngalia Basin, however, is relatively high (2.8 W/mK), resulting in only limited thermal insulation. The potential in this region is, therefore, low to moderate.

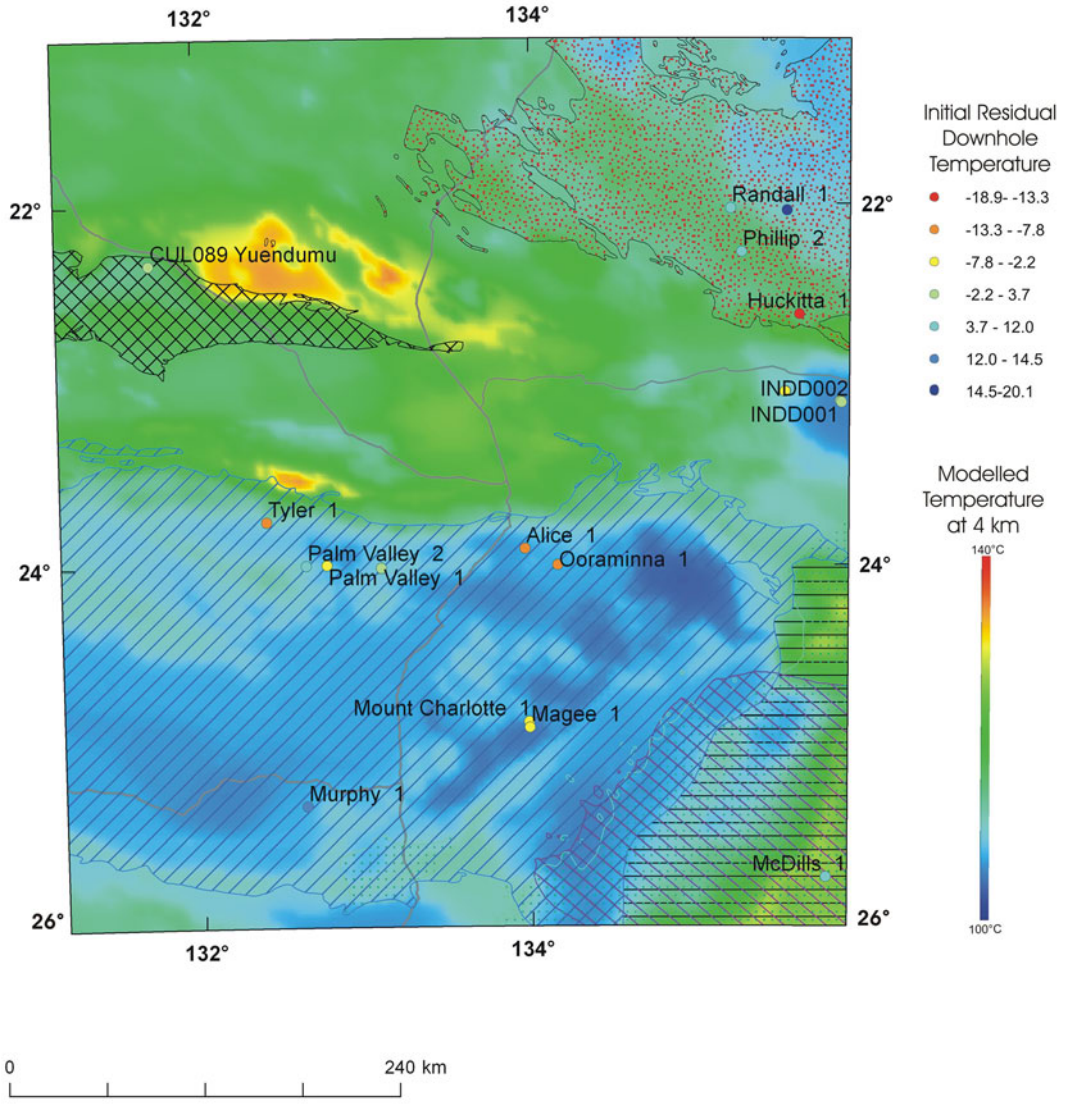

Figure 4.15: *Results of the initial thermal model run showing modelled temperature for the 4 km depth slice (i.e., 4 km below topography). Modelled using the 6 km variable heat production layer 3D map; continuous colour ramp at right shows temperature range in ˚C. Temperature residuals (measured down-hole temperatures minus the modelled values) are shown as labelled point values for comparison; refer to legend in ˚C at top right of image. Basin extents and major roads shown for reference; Amadeus – blue diagonal hash, Eromanga – green spotted, Georgina – red spotted, Ngalia – black cross hatch, Pedirka – purple diagonal hash, Warburton – black horizontal stripes. Roads are represented by grey solid lines.*

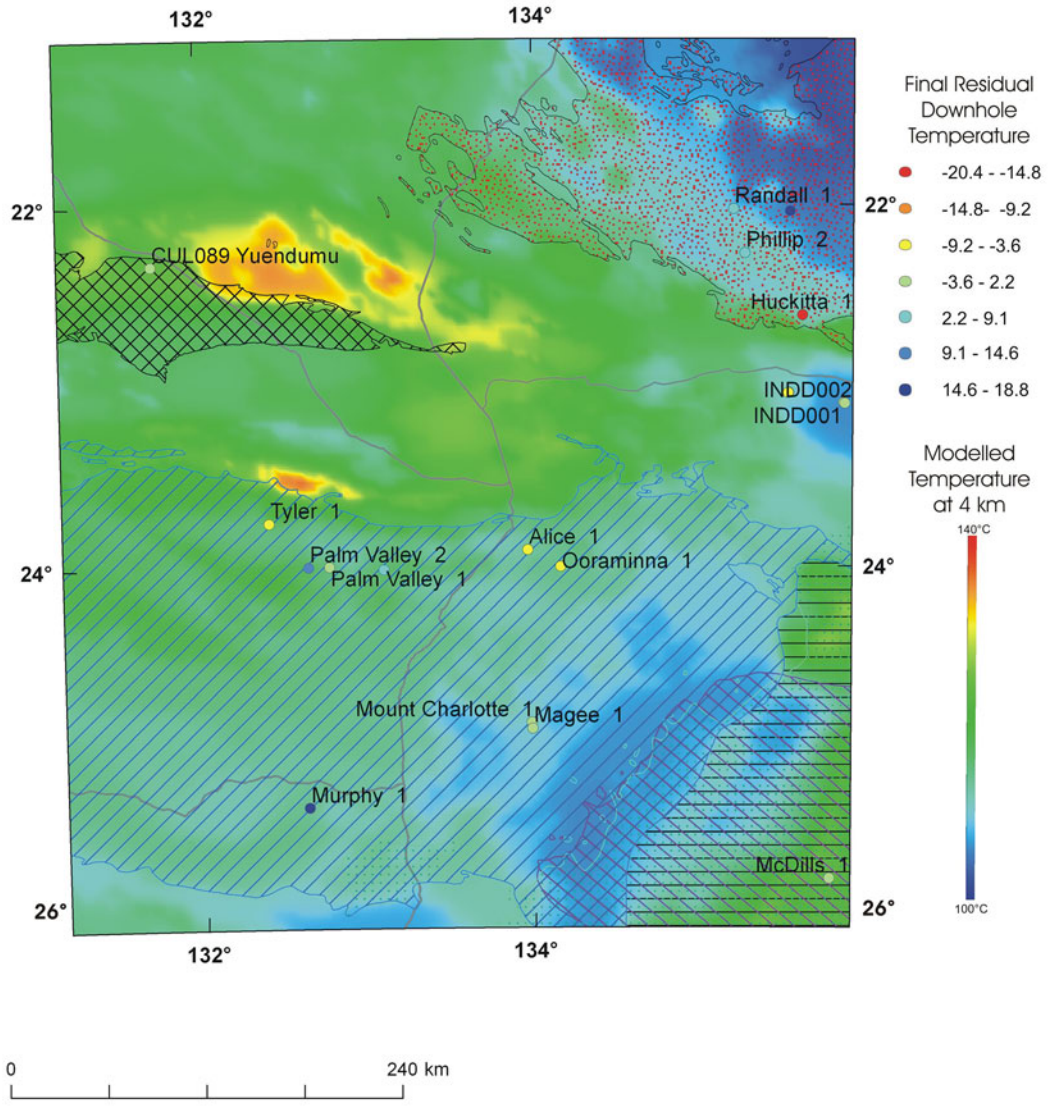

Figure 4.16: *Results of the final thermal model run showing modelled temperature for the 4 km depth slice (i.e., 4 km below topography). Modelled using the 6 km variable heat production layer 3D map. The continuous colour ramp at right shows temperature range in ˚C. Temperature residuals (measured down-hole temperatures minus the modelled values) are shown as labelled point values for comparison (refer to legend in ˚C at top right of image). Basin extents and major roads are shown for reference.*

The region of the assessment area that is blanketed with insulating sediments occurs in the southeast where up to 8 km of low thermal conductivity Eromanga and Warburton/Pedirka basin sediments (2.3 and 2.2 W/mK respectively) overlie basement. The basement in this region consists of undivided Musgrave Province, which has been assigned a low heat-production value. The maximum temperature reached at 4 km in this region is 127°C resulting in a low to moderate potential.

Hot rock potential is heavily affected by the reliability of the solid geology map (Figure 4.11) and the reliability of the heat-production values assigned to these geological units (Figures 4.7 and 4.12). Beneath regions of thick cover, the reliability of both these inputs is significantly reduced (Figures 4.11 and 4.12). Beneath cover, the solid geology units are generally undivided sequences, with heat-production values assigned based on the averaged heat production of the individual units within these sequences. This approach, although simplistic, is the best that can be achieved based on the available geological and geophysical data. This is reflected in the relative confidence analysis, which shows lower relative confidence in the above regions (Figure 4.14). Final outputs from the thermal modelling reflect the limitations in areas where temperature residuals from wells vary by ± 20°C (Figure 4.16), indicating the model is over- or underestimating temperatures. Where the thermal modelling is underestimating temperature (positive residuals), it may indicate that there are high-heat producing bodies in the basement that are unaccounted for.

The paucity of down-hole temperature and heat-flow measurements severely limits the ability to predict regions of high-heat production within the basement. If these predictions were better constrained by additional data, and hence with more confidence, these interpreted high-heat producing regions could be incorporated into the 3D map and the resultant temperatures predicted through thermal modelling. Acquisition of additional down-hole temperature and heat-flow measurements would significantly improve the ability to predict the locations of high-heat producing regions, and therefore the reliability of the hot rock geothermal energy assessment.

4.10 RELATIVE HOT SEDIMENTARY AQUIFER POTENTIAL

The prerequisite for an economically viable hot sedimentary aquifer resource is the presence of a suitably permeable aquifer at a sufficiently high temperature. There are limited data available on the presence of aquifers in the assessment area. Available porosity and permeability data for basins in the southeast of the study area, compiled as part of the assessment for hot sedimentary aquifer geothermal systems in South Australia (Meixner *et al*., 2011), are summarised in Table 4.9. Where measured data are unavailable, general comments about basin lithologies from published sources have been included in the table. The Warburton Basin, although listed, is not considered to have hot sedimentary aquifer potential as, while the Pando Formation and Mooracoochie Volcanics have high porosities, it is considered that both units would require additional fracturing to produce adequate permeability. Porosity and permeability data have not been compiled for the older Amadeus, Georgina, and Ngalia basins. However, these basins may have potential for hot sedimentary aquifer geothermal systems if sufficient porosity and permeability is present in aquifer units.

Table 4.9: Summary of basins in assessment area that have units potentially suitable for hot sedimentary aquifer resources

BASIN	UNIT	POROSITY	PERMEABILITY	REFERENCE
Eromanga Basin	Murta Formation		21 mD in some places up to 661 mD	PIRSA 2010b
	Namur Sandstone		601 mD and in some places up to 4300 mD	PIRSA 2010b
	Birkhead Formation		200 mD and in some places up to 4950 mD	PIRSA 2010b
	Hutton Sandstone		897 mD and in some places up to 5130 mD	PIRSA 2010b
	Poolowanna Formation	porosity 18%	364 mD and in some places up to 1917 mD	PIRSA 2010b
	Algebuckina Sandstone	Major artesian aquifer, porosity >20%		PIRSA 2010b
Pedirka Basin	Purni Formation	6-12%	Fair to good permeability	PIRSA
	Crown Point Formation	20-25%,	300-2000 mD	PIRSA
Warburton Basin	Pando Formation	5-20%	Needs fractures for permeability	PIRSA 2010a
	Mooracoochie Volcanics	Up to 17%	Needs fractures for permeability	PIRSA 2010a

Temperatures derived from the thermal modelling at the basal contact of the basins that contain high permeability units are shown in Figure 4.17. The maximum predicted temperature at the base of the Eromanga Basin (~1700 m below ground level) is 76°C, and therefore the Eromanga Basin is considered to have a low to moderate hot sedimentary aquifer potential within the assessment area. The Eromanga Basin thickens to the south and east (van der Wielen *et al.*, *in prep.*) and is considered to have higher hot sedimentary aquifer potential beyond the limits of the assessment area. The Pedirka Basin, which is situated beneath the Eromanga Basin, has a maximum temperature at its base (~2900 m below ground level) of 111°C indicating moderate to high hot sedimentary aquifer potential.

Hot sedimentary aquifer potential is also heavily affected by the reliability of the solid geology map and the reliability of the heat-production values assigned to these geological units beneath the Eromanga, Pedirka and Warburton basins (Figure 4.7). This is reflected in the relative confidence analysis, which shows lower relative confidence in the above regions (Figure 4.14).

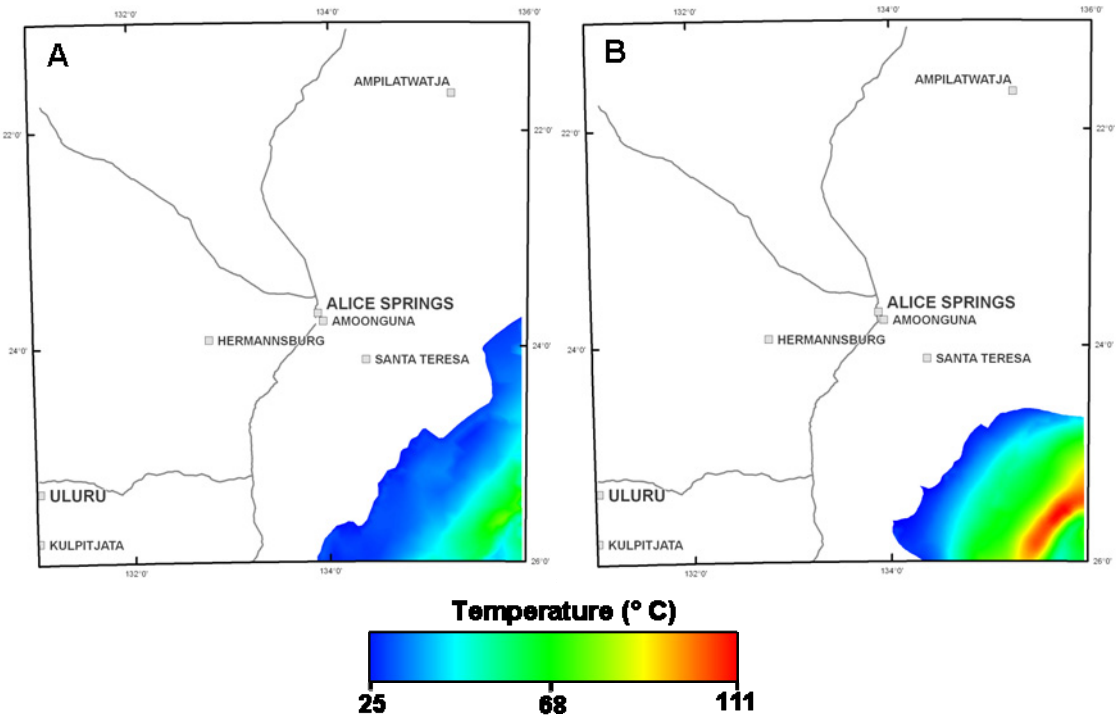

Figure 4.17: *Temperatures derived from the thermal model at the basal contact of the Eromanga Basin (a) and at the base of the Pedirka Basin (b).*

5. Summary and conclusions

The southern region of the Northern Territory has a long-lived and diverse geological history, giving rise to a number of favourable geological features for both uranium and geothermal energy systems. Within the southern Northern Territory, assessments have been undertaken on four individual uranium systems using a GIS-based approach: sandstone-hosted, uranium-rich IOCG, unconformity-related and magmatic-related systems. The potential for two geothermal systems has been investigated using 3D thermal modelling: hot rock geothermal and hot sedimentary aquifer.

5.1 RESULTS

5.1.1 Uranium systems

Potential for sandstone-hosted uranium systems is highest in the Amadeus and Ngalia basins. Almost the entire Ngalia Basin is highlighted as prospective, owing to the distribution of the Mount Eclipse Sandstone. In the Amadeus Basin, the highest potential occurs in an east-west trending belt along the northern margin of the basin. The overall high potential of this belt is owing to favourable uranium sources on the northern margin of the basin, which is interpreted to have been uplifted during the Alice Springs Orogeny, thus driving fluid flow. Further evidence of this is seen in the distribution of syn-orogenic sedimentary units in the northern Amadeus Basin. In addition, the northern Amadeus Basin also hosts potentially favourable aquifers and has several reducing units and hydrocarbon shows. The portion of the Georgina Basin within the study area has lower potential than the Amadeus and Ngalia basins. However, two regions of elevated potential are noted along the southern and western margin of the basin. Although not assessed for, Cenozoic basins within the study area are also thought to have high potential for recent sandstone-hosted uranium systems similar to those in the Frome Embayment.

Mineral potential modelling for uranium-rich IOCG mineral systems has identified six areas as having potential. The most significant area is an extensive area along the southern margin of the Aileron Province. The recently-discovered Austin, Powers and Bigglesworth prospects and the Johnnies Reward deposit are located in this zone which likely extends westward to prospects in the western Aileron Province, including the Te Anau and Manapouri prospects in the Northern Territory and the Pokali and nearby prospects in Western Australia. The analysis also highlights areas in the southern Davenport region, which may extend to the Rover and Tennant Creek districts to the north. The analysis identified other smaller areas, including the area that contains the Jervois district.

A belt of high potential for Precambrian unconformity-related uranium potential extends approximately east-west along the northern Amadeus Basin. This belt coincides with the Albarta and Tourmaline Gorge prospects, which may be unconformity-related systems. Additional potential for Precambrian systems occurs in the Georgina Basin in the northeast of the study area and in the northern part of the Ngalia Basin, where suitable source rocks and thick basin cover sequences occur. Potential for unconformity-related uranium systems in the Phanerozoic is highest in the southern Davenport Province, extending into the Georgina Basin. In the southeast of the study area, potential is elevated near the margin of the Eromanga Basin. The northern margin of the Amadeus Basin also shows elevated potential for Phanerozoic-aged unconformity uranium systems.

A number of small magmatic-related uranium prospects occur within the study area. Generally speaking, igneous rocks hosting these prospects have also been identified as having potential for magmatic-related uranium systems in this study. Igneous units with high potential are distributed throughout the study area, although granites on the northern margin of the Ngalia Basin form a concentration of high potential. Elevated potential also occurs along the southern margin of the Aileron Province and into the Warumpi Province, as well as in the Davenport Province. The Aileron Province appears to be more favourable for magmatic-related uranium systems.

5.1.2 Hot rock geothermal systems

Modelled temperatures at four kilometres depth range from 103 to 134°C and indicates hot rock geothermal potential in the study area ranges from low to moderate. The highest potential is found to the north of the Ngalia Basin and on the northern edge of the Amadeus Basin. These regions of elevated potential are related to the spatial distribution of high-heat producing lithologies, in particular the granites of the Aileron and Warumpi provinces. High-heat producing granites also occur beneath the southern Ngalia Basin on the western edge of the assessment area. However, thermal conductivity in the Ngalia Basin is relatively high, resulting in only a modest degree of thermal insulation, and thus potential in this region is low to moderate.

In the southeast of the study area up to eight kilometres of low thermal conductivity sediments of the Eromanga and Warburton/Pedirka basins overlie undivided Musgrave Province, which is interpreted to have relatively low heat production. The good insulation potential, but relatively lower heat production capacity of this area results in a maximum temperature reached of 127°C in this region and an overall low to moderate hot rock geothermal potential.

5.1.3 Hot sedimentary aquifer geothermal systems

Potential for hot sedimentary aquifer geothermal systems has only been assessed for basins in the southeastern study area. The porosity and permeability characteristics of the Eromanga and Pedirka basins indicate potentially viable aquifer systems. The predicted temperature at the base of the Eromanga Basin is 76°C and is considered to have a low to moderate hot sedimentary aquifer potential within the assessment area. The Eromanga Basin does thicken to the south and east however (van der Wielen *et al*., *in prep*.), and is considered to have higher hot sedimentary aquifer potential beyond the limits of the assessment area. The Pedirka Basin, which is situated beneath the Eromanga Basin, has a maximum basal temperature of 111°C indicating moderate to high hot sedimentary aquifer prospectivity.

5.2 DIRECTIONS FOR FUTURE WORK

5.2.1 Sandstone-hosted uranium systems

While this assessment has highlighted a number of units exhibiting high potential for sandstone-hosted uranium (including the hosts to the Bigrlyi and Angela/Pamela deposits), additional criteria are required to further narrow the search space. Examples of such data include the distribution of sedimentary facies (as suggested by Schmid *et al*, 2012) and the distribution of reductants within sedimentary units. This analysis may be performed in 3D using the methodology of van der Wielen and Britt (2009). The role of uranium sourced from detrital components within sedimentary aquifers also should be examined, and should focus particularly on the presence of leachable detrital phases within the identified prospective units. Further constraint on the locations and timing of uplift would also be beneficial. This could be achieved with strategic acquisition of Ar isotopic data.

5.2.2 Unconformity-related uranium systems

Unconformities are obviously a critical aspect of unconformity-related uranium systems and, although the unconformities in the basins are relatively well documented, there is little information about unconformities within the basement. Future assessments would benefit from further constraints on these. Reduced lithologies are also important for locating depositional sites. At present there is only limited information on reduced lithologies (mostly associated with petroleum studies of the basins). More work is needed on identifying carbonaceous and Fe^{2+}-rich minerals by either mineral mapping or more extensive geochemical programs. Additional work is also required for identifying fluid-flow pathways. The aquifers and aquitards within basins are relatively well documented but the distribution of faults and their relative timings are poorly known in this area. Ideally, 3D geological models and 3D geochemical/fluid flow models would greatly enhance our understanding of mineral systems and depositional mechanisms as well.

5.2.3 Uranium-rich iron oxide-copper-gold systems

The analysis indicates that, in several places, potential extends outside of the study area, suggesting that areas to the west and north of the study area require analysis. Although tentatively identified as IOCG deposits in this and previous studies, the origin of prospects in the study area is uncertain. Additional geological, geochemical and geochronological data are required to verify an IOCG origin for these deposits. If such a link could be proved, the prospectivity of the southern Aileron Province as a potential IOCG province would be enhanced.

5.2.4 Magmatic-related uranium systems

Magmatic-related uranium systems remain poorly understood relative to the other systems examined in this investigation. The most favourable zones for magmatic-related uranium mineralisation are those which have been the locus of magmatic-hydrothermal fluid flow. The most likely zones are the apical parts of intrusions or variations in granite topography. An understanding of these may be achieved using 3D geophysical modelling. In addition, further acquisition of geochemical data will assist in constraining the possible uranium concentration processes and hydrothermal histories of favourable intrusions.

5.2.5 Geothermal energy systems

Geothermal energy is a relatively new concept in Australia, and relevant data for assessing the potential for geothermal energy systems is scarce. Improving the data density of the input datasets used in the assessments for hot rock and hot sedimentary aquifer geothermal systems will assist in developing a better understanding of the geothermal energy potential of the study area. Six key areas will assist in enhancing the reliability of the temperature modelling:

- Detailed solid geology datasets to better represent lithological distribution;
- Sampling to improve constraints on the thermal properties, especially heat production;
- Acquisition of down-hole temperature and heat-flow measurements;
- Quantitative assessment of the uncertainty in the modelled temperatures;
- Consideration of temperature dependence on thermal conductivity; and
- Increased density and porosity/permeability data to better characterise potential aquifers.

6. Acknowledgements

This assessment of the uranium and geothermal potential of the southern Northern Territory was only made possible by the contribution of many. In particular, Geoff Fraser, Terry Brennan, Ollie Raymond, Alistair Stewart, Songfa Liu and Richard Chopping are thanked for their assistance in compiling the base geological datasets (solid geology and geological provinces) necessary for undertaking the assessments. Staff from the Northern Territory Geological Survey are also acknowledged for their input into the compilation of these datasets, particularly Dot Close, Ian Scrimgeour and Jo Whelan. This report was improved thanks to the thoughtful reviews provided by Geoff Fraser, Allison Britt, Roger Skirrow, David Huston, David Champion, Bridget Ayling, Allison Kirkby, Richard Blewett and Narelle Neumann (Geoscience Australia), and Dot Close, Jo Whelan, Christine Edgoose, and Eloise Beyer (Northern Territory Geological Survey). Finally, great appreciation goes to the Minerals and Natural Hazards Division GIS team for their hard (and often frustrating work) throughout.

7. References

Ahmad, M. and Munson, T.J. (compilers), *in press*. Geology and mineral resources of the Northern Territory. *Northern Territory Geological Survey, Special Publication 5*.

Ahmad, M. and Wygralak, A.S., 1990. Murphy Inlier and environs — regional geology and mineralisation. *Australasian Institute of Mining and Metallurgy Monograph,* **14**, 819-826.

Ahmad, M., Wygralak, A.S. and Ferenczi, P.A., 2009. Gold deposits of the Northern Territory (second edition). *Northern Territory Geological Survey Report 11*.

Allen, A.R. and Stubbs, D., 1982. An $^{40}Ar/^{39}Ar$ study of a polymetamorphic complex in the Arunta Block, central Australia. *Contributions to Mineralogy and Petrology*, **79**, 319-332.

Alley, N.F., 1998. Cainozoic stratigraphy, palaeoenvironments and geological evolution of the Lake Eyre Basin. *Palaeogeography, Palaeoclimatology, Palaeoecology*, **144**, 239-263.

Ambrose, G., 2006a. The Amadeus Basin. In: Ambrose, G. (ed.), Northern Territory of Australia, onshore hydrocarbon potential, 2006. *Northern Territory Geological Survey, Record* **2006-003**, 1-19.

Ambrose, G., 2006b. The Pedirka/Simpson Desert/Eromanga Basins. In: Ambrose, G. (ed.), Northern Territory of Australia, onshore hydrocarbon potential, 2006. *Northern Territory Geological Survey, Record* **2006-003**, 1-19.

Ambrose, G.J., Liu, K., Deighton, I., Eadington, P.J. and Boreham, C.J., 2002. New petroleum models in the Pedirka Basin, Northern Territory, Australia. *APPEA Journal*, **42**, 250-286.

Ambrose, G. and Putnam, P., 2006. The Georgina Basin. In: Ambrose, G. (ed.), Northern Territory of Australia, onshore hydrocarbon potential, 2006. *Northern Territory Geological Survey,* **Record 2006-003**, 1-22.

Ashley, P.M., 1984. Sodic granitoids and felsic gneisses associated with uranium-thorium mineralisation, Crockers Well, South Australia. *Mineralium Deposita,* **19**, 7-18.

Ayling B. and Lewis, B., 2010. Geothermal systems. In: Huston, D.L. (ed.), An assessment of the uranium and geothermal potential of north Queensland. *Geoscience Australia Record*, **2010/14**, 68-91.

Bailey, J.C., Gwodz, R., Rose-Hansen, J. and Sørensen, H., 2001. Geochemical overview of the Ilímaussaq alkaline complex, South Greenland. *Geology of Greenland Survey Bulletin,* **190**, 35-53.

Bastrakov, E., Jaireth, S. and Mernagh, T.P., 2010. Solubility of uranium in hydrothermal fluids at 25° to 300°C: Implication for the formation of uranium deposits. *Geoscience Australia Record,* **2010/29**, 91pp.

Beach, R., 1985. Sedimentary heat flow in the $\Delta Q = 0$ region of Alberta, Unpublished M.Sc. Thesis, University of Alberta, Edmonton, Alberta.

Beardsmore, G., 1996. Thermal history of the Browse Basin and its implications for petroleum exploration. Unpublished PhD thesis, Monash University.

Beardsmore, G., 2004. The influence of basement on surface heat flow in the Cooper Basin, *Exploration Geophysics*, **35**, 223-225.

Beardsmore, G.R., 2007. Geothermal potential of the Northern Territory. *Northern Territory Geological Survey, Record* **2007-004**.

Betts, P.G. and Giles, D., 2006. The 1800-1100 Ma tectonic evolution of Australia. *Precambrian Research*, **144**, 92-125.

Beyer, E.E., Edgoose, C.J., Vandenberg, L.C., Webb, G. and Bodorkos, S., 2010. Regional geology and prospectivity of the Aileron Province in the Alcoota 1:250 000 mapsheet area. In: *Annual Geoscience Exploration Seminar (AGES) 2010, record of abstracts. Northern Territory Geological Survey, Record* **2010-003**, 32-37.

Beyer, E.E., Kositcin, N. and Dunkley, D.J., 2012. Prospectivity of high-heat producing granites of the central Arunta Region, Northern Territory. In: *Annual Geoscience Exploration Seminar (AGES) 2012, record of abstracts. Northern Territory Geological Survey, Record* **2012-002**, 25-30.

Biermeier, C., Stüwe, K., Foster, D.A. and Finger, F., 2003. Thermal evolution of the Redbank thrust system, central Australia: geochronological and phase-equilibrium constraints. *Tectonics*, **22**, 1-23.

Birch, F. and Clark, H., 1940. The thermal conductivity of rocks and its dependence upon temperature and composition. *American Journal of Science*, **238**, 529-558.

Black, L.P. and Gulson, B.L., 1978. The age of the Mud Tank Carbonatite, Strangways Range, Northern Territory. *BMR Journal of Australian Geology and Geophysics*, **3**, 227-232

Blewett, R.S., Czarnota, K. and Henson, P.A., 2010. Structural-event framework for the eastern Yilgarn Craton, Western Australia, and its implications for orogenic gold. *Precambrian Research*, **183**, 203-229.

Bonham-Carter, G.F., 1994. Geographic information systems for geoscientists: modelling with GIS. Pergamum Press, New York, 398p.

Borshoff, J. and Faris, I., 1990. Angela and Pamela uranium deposits. In: Hughes, F.E. (ed.), Geology of the mineral deposits of Australia and Papua New Guinea, *The Australasian Institute of Mining and Metallurgy*, Melbourne, 1139-1142.

Budd, A.R., Wyborn, L.A.I. and Bastrakova, I.V., 2001. The metallogenic potential of Australian Proterozoic granites. *Geoscience Australia Record,* **2001/12**, 152pp.

Campana, B. and King, D., 1958. Regional geology and mineral resources of the Olary Province. *Geological Survey of South Australia Bulletin*, **34**, 133pp.

Candela, P. A., 1997. A review of shallow, ore-related granites: textures, volatiles and ore metals. *Journal of Petrology,* **38**, 1619-1633.

Carter, J. D., 1982. Mortimer Hills pegmatite uranium prospect: a Rossing-style uranium deposit in the Gascoyne Province. *Geological Survey of Western Australia Professional Paper,* **12**, 27-31.

Carter, L.S., Kelly, S.A., Blackwell, D.D. and Naeser, N.D., 1998. Heat flow and thermal history of the Anadarko Basin, Oklahoma, *American Association of Petroleum Geologists Bulletin*, **82,** 291-316.

Cartwright, I., Buick, I.S., Foster, D.A. and Lambert, D.D., 1999. Alice Springs age shear zones from the southeastern Reynolds Range, central Australia. *Australian Journal of Earth Sciences*, **46**, 355-363.

Cawood, P.A. and Korsch, R.J., 2008. Assembling Australia: Proterozoic building of a continent. *Precambrian Research*, **166**, 1-38.

Cermak, V., Huckenholz, H.G., Rybach, L., Schmid, R., Schopper, J. R., Schuch, M., Stoffler, D. and Wohlenberg, J., 1982. Thermal conductivity and specific heat of minerals and rocks. In: Angenheister, G. (ed.), Physical Properties of Rocks, Springer-Verlag Berlin, New York, 30-370.

Chappell, B.W., White, A.J.R., Williams, I.S., Wyborn, D. and Wyborn, L.A.I., 2000. Lachlan Fold Belt granites revisited: high- and low-temperature granites and their implications. *Australian Journal of Earth Sciences*, **47**, 123-138.

Chopping, R. and van der Wielen, S.E., 2009. Querying potential field inversions for signatures of chemical alteration: an example from Cobar, NSW. Australian Society of Exploration Geophysicists, *Preview*, **138**, Proceedings of the 20th International Geophysical Conference and Exhibition, Adelaide.

Chopping, R. and van der Wielen, S.E., 2011. Mapping the footprint of ore deposits in 3D using geophysical data. *AusGeo News*, **101**, 3-7.

Chopra, P.N. and Holgate, F., 2005. A GIS analysis of temperature in the Australian crust, *Proceedings of the World Geothermal Congress*, Anatalya, Turkey, 1-7.

Chuck, R.G., 1984. Annual report, Exploration Licence 3026, NT for the period 25/5/1984 to 24/5/1985 and final report for project. Unpublished Alcoa of Australia Limited Exploration Department Report.

Claoué-Long, J., 2007. Time-space evolution of the southern North Australia Craton. In: Neumann, N.L. and Fraser, G.L. (eds.): Geochronological synthesis and time-space plots for Proterozoic Australia. *Geoscience Australia Record*, **2007/06**, 88-102.

Claoué-Long, J. and Hoatson, D., 2005. Proterozoic mafic–ultramafic intrusions in the Arunta Region, central Australia: Part 2: Event chronology and regional correlations. *Precambrian Research*, **142**, 134-158.

Close, D. and Scrimgeour, I., 2009. Deep seated structures and mineralisation in the Arunta Region. In: *Annual Geoscience Exploration Seminar (AGES) 2009, record of abstracts. Northern Territory Geological Survey, Record* **2009-002**, 44-45.

Close, D.F., Scrimgeour, I.R., Edgoose, C.J., Claoué-Long, J., Kinny, P. and Meixner, A.J., 2003. Redefining the Warumpi Province. In: *Annual Geoscience Exploration Seminar (AGES) 2003, record of abstracts. Northern Territory Geological Survey, Record* **2003-001**.

Close, D.F., Scrimgeour, I.R., Edgoose, C.J., Wingate, M.T.D. and Selway, K., 2005. Late Palaeoproterozoic oblique accretion of a 1690-1660 Ma magmatic arc onto the North Australian Craton. *Geological Society of Australia, Abstracts*, **81**, 36.

Compston, D. M., 1994. The Geochronology of the Tennant Creek Inlier, N.T. Unpublished PhD thesis, Australian National University.

Compston, D. M., 1995. Time constraints on the evolution of the Tennant Creek Block, northern Australia. *Precambrian Research*, **71**, 107-129.

Compston, D. M. and McDougall, I., 1994. $^{40}Ar/^{39}Ar$ and K-Ar age constraints on the Early Proterozoic Tennant Creek Block, northern Australia, and the age of its gold deposits. *Australian Journal of Earth Sciences*, **41,** 609-616.

Cook, P.J., 1988. Palaeogeographic atlas of Australia: Volume 1, Cambrian. *Australian Government Publishing Service, Canberra*.

Cross, A.J., 2009. SHRIMP U-Pb xenotime geochronology and its application to dating mineralisation, sediment deposition and metamorphism. Unpublished PhD thesis, Australian National University, 298p.

Cull, J.P., 1982. An appraisal of Australian heat-flow data. *BMR Journal of Australian Geology and Geophysics*, **7**, 11-21.

Cull, J.P. and Denham, D., 1979. Regional variations in Australian heat flow. *BMR Journal of Australian Geology and Geophysics*, **4**, 1-13.

Cuney, M., 2005. World-class unconformity-related uranium deposits; key factors for their genesis. *Proceedings of the Biennial SGA (Society for Geology Applied to Mineral Deposits) Meeting 8*, 245-248.

Cuney, M., 2009. The extreme diversity of uranium deposits. *Mineralium Deposita*, **44**, 3-9.

Cuney, M., 2010. Evolution of uranium fractionation processes through time: driving the secular variation of uranium deposit types. *Economic Geology*, **105**, 553-569.

Cuney, M. and Kyser, K., 2008. Recent and not-so-recent developments in uranium deposits and implications for exploration. *Mineralogical Association of Canada Shortcourse Series,* **39**, 258p.

Cuney, M., Brouand, M., Cathelineau, M., Derome, D., Frieberger, R., Hecht, L., Kister, P., Lobaev, V., Lorilleux, G., Peiffert, C. and Bastoul, A.M., 2003. What parameters control the high-grade-large tonnage of the Proterozoic unconformity related uranium deposits? Uranium Geochemistry 2003: Proceedings of Uranium Geochemistry 2003, Nancy, France, 123-126.

Davis, M.G., Chapman, D.S., Van Wagoner, T.M. and Armstrong, P.A., 2007. Thermal conductivity anisotropy of metasedimentary and igneous rocks, *Journal of Geophysical Research,* **112**, B05216.

De Vries, S.T., Fry, N. and Pryer, L., 2006. OZ SEEBASE™ Proterozoic basins study. Report to Geoscience Australia and consortium partners by FrOG Tech Pty Ltd. Public domain GIS and report, available from www.frogtech.com.au.

Derome, D., Cathelineau, M., Cuney, M., Fabre, C. and Lhomme, T., 2005. Mixing of sodic and calcic brines and uranium deposition at McArthur River, Saskatchewan, Canada. *Economic Geology,* **100**, 1529-1545.

Donnellan, N., Hussey, K.J. and Morrison, R.S., 1995. Flynn and Tennant Creek, Northern Territory. 1:100 000 geological map series explanatory notes, 5759 and 5758. Northern Territory Geological Survey, Darwin and Alice Springs.

Donnellan, N. and Johnstone, A., 2004. Mapped and interpreted geology of the Tennant Region. 1:500 000 scale. Northern Territory Geological Survey, Darwin and Alice Springs.

Drexel, J. F., 2008. Review of the Burra mine project, 1980-2008 a progress report. *Primary Industry and Resources, South Australia Report Book,* **2008/16**, 76 pp.

Drummond, B., Lyons, P., Goleby, B. and Jones, L., 2006. Constraining models of the tectonic setting of the giant Olympic Dam iron oxide-copper-gold deposit, South Australia, using deep seismic reflection data. *Tectonophysics*, **420**, 91-103.

Dunster, J.N., Kruse, P.D., Duffett, M.L. and Ambrose, G.J., 2007. Geology and resource potential of the southern Georgina Basin. *Northern Territory Geological Survey DIP 007*.

Edgoose, C.J., Scrimgeour, I.R. and Close, D.F., 2004. Geology of the Musgrave Block, Northern Territory. *Northern Territory Geological Survey, Report*, ***15***, 44p.

El Bouseilly, A. M. and El Sokkary, A. A., 1975. The relation between Rb, Ba and Sr in granitic rocks. *Chemical Geology,* **16**, 207-219.

Farquhar, J., Wu, N., Canfield, D.E. and Oduro, H., 2010. Connections between sulfur cycle evolution, sulfur isotopes, sediments, and base metal sulfide deposits. *Economic Geology,* **105**, 509-533.

Ferenczi, P.A., 2005. Low-profile basemetal deposits in the Northern Territory. In: *Annual Geoscience Exploration Seminar (AGES) 2005, record of abstracts. Northern Territory Geological Survey, Record* **2005-001***, 23-25*.

Fidler, R.W., Pope. G.J. and Ivanac, J.F., 1990. Bigrlyi uranium deposit. In: Hughes, F.E. (ed.), Geology of the mineral deposits of Australia and Papua New Guinea, *The Australasian Institute of Mining and Metallurgy*, Melbourne, 1135-1138.

Foden, J.D., Buick, I.S. and Mortimer, G.E., 1988. The petrology and geochemistry of granitic gneisses from the east Arunta Inlier, central Australia: implications for Proterozoic crustal development. *Precambrian Research*, **40/41**, 233–259.

Fraser, G., Huston, D., Bagas, L., Hussey, K., Claoué-Long, J., Cross, A., Vandenberg, L., Wygralak, A., Donnellan, N. and Crispe, A., 2006. $^{40}Ar/^{39}Ar$ constraints on the episodic history of mineralisation and tectonism in the southern North Australian Craton. In: Lyons, P. and Huston, D.L. (eds.): Evolution and metallogenesis of the North Australian Craton. *Geoscience Australia Record*, **2006/16**, 13-14.

Fraser, G.L., Hussey, K. and Compston, D.M., 2008. Timing of Palaeoproterozoic Au–Cu–Bi and W-mineralization in the Tennant Creek region, northern Australia: Improved constraints via intercalibration of $^{40}Ar/^{39}Ar$ and U–Pb ages. *Precambrian Research*, **164**, 50–65.

Frater, M., 2006. New insights into the Jervois mineral field. In: *Annual Geoscience Exploration Seminar (AGES) 2006, record of abstracts. Northern Territory Geological Survey, Record* **2006-002**, 18-20.

Fricke, C., 2008. Definitions of Mesoproterozoic igneous rocks of the Curnamona Province: The Ninnerie Supersuite. *Primary Industry and Resources, South Australia Report Book,* **2008/4**, 86pp.

Fricke, C. and Conor, C.H.H., 2010. Building granite plutons in the Olary Domain, South Australia: a ring dyke model. *Primary Industry and Resources, South Australia Report Book,* **2010/11**, 55pp.

Galson, D.A., Wilson, N.P., Scharli, U. and Rybach, L., 1987. A comparison of the divided-bar and QTM methods of measuring thermal conductivity. *Geothermics*, **16,** 215-222.

Gauci G., 1997. The Kintyre Advancement Program. Twenty-second Annual Symposium, Uranium Institute, London; 1-6.

Gerner, E. and Holgate, F.L., 2010. OZTemp – Interpreted temperature at 5 km depth image. Geoscience Australia (https://www.ga.gov.au/products/servlet/controller?event=GEOCAT_DETAILS&catno=71143).

Gibson, H., Seikel, R., and Meixner, T., 2010. Characterising uncertainty when solving for 3D temperature: New tools for the Australian geothermal energy exploration sector. *21st Australian Society of Exploration Geophysicists Conference,* Extended Abstracts.

Gibson, H., Stüwe, K., Seikel, R., FitzGerald, D., Calcagno, P., Argast, S., McInerney, P. and Budd, A., 2008. Forward prediction of spatial temperature variation from 3D geology models. PESA *Eastern Australian Basins Symposium III*. Sydney 14-17 September 2008.

Goldfarb, R.J., Baker, T., Dubé, B., Groves, D.I., Hart, C.J.R. and Gosslein, P., 2005. Distribution, character and genesis of gold deposits in metamorphic terranes. *Economic Geology 100th Anniversary Volume*, 561-608.

Goleby, B.R., Huston, D.L., Lyons, P., Vandenberg, L., Bagas, L., Davies, B.M., Jones, L.E.A., Gebre-Mariam, M., Johnson, W., Smith, T. and English, L., 2009. The Tanami deep seismic reflection experiment: an insight into gold mineralisation and Paleoproterozoic collision in the North Australian Craton. *Tectonophysics*, **427**, 169-182.

Goodwin, J.A. and van der Wielen, S.E., *in prep.* A national assessment of radioelement (uranium, thorium, potassium) enrichment using radiometrics, geochemistry, and surface geology.

Groves, D.I., Bierlein, F.P., Meinert, L.D. and Hitzman, M.W., 2010. Iron oxide copper-gold (IOCG) deposits through Earth history: implications for origin, lithospheric setting, and distinction from other epigenetic iron oxide deposits. *Economic Geology,* **105**, 641-654.

Haas, J.R., Everett L. Shock, E.L. and Sassani, D.C., 2000. Rare earth elements in hydrothermal systems: Estimates of standard partial molal thermodynamic properties of aqueous complexes of the rare earth elements at high pressures and temperatures. *Geochimica et Cosmochimica Acta*, **59**, 4329–4350.

Haigh, J.E., 1971. Strangways Range geophysical survey, Northern Territory, 1967. *BMR Record*, **1971/018**.

Haines, P.W., Hand, M. and Sandiford, M., 2001. Palaeozoic synorogenic sedimentation in central and northern Australia: a review of distribution and timing with implications for the evolution of intracontinental orogens. *Australian Journal of Earth Sciences*, **48**, 911-928.

Haynes, M., 2011. Geothermal potential in the Clarence-Morton Basin, New South Wales: a case study in reducing uncertainties in geothermal modelling. Unpublished BSc Honours thesis.

Hayward, N. and Skirrow, R.G., 2010. Geodynamic setting and controls on iron oxide Cu-Au (±U) ore in the Gawler Craton, South Australia. In: Porter, T.M. (ed.)*, Hydrothermal Iron Oxide Copper-Gold and Related Deposits: A Global Perspective*, **3**. *PGC Publishing*, Adelaide, 600p.

Hickman, A.H. and Clarke, G.L., 1994. Geology of the Broadhurst 1:100 000 sheet, Western Australia. Western Australia Geological Survey.

Hitzman, M.W., 2000. Iron oxide-Cu-Au deposits: what, where, when and why. In: Porter, T.M. (ed.), Hydrothermal iron oxide copper-gold and related deposits — a global perspective. Adelaide, Australian Mineral Foundation, 9-26.

Hitzman, M.W. and Valenta, R.K., 2005. Uranium in iron oxide-copper-gold (IOCG) systems. *Economic Geology,* **100**, 1657-1661.

Hitzman, M.W., Oreskes, N. and Einaudi, M.T., 1992. Geological characteristics and tectonic setting of Proterozoic iron oxide (Cu-U-Au-LREE) deposits. *Precambrian Research,* **58**, 241–287.

Hoatson, D.M., Sun, S.-S. and Claoué-Long, J., 2005. Proterozoic mafic-ultramafic intrusions in the Arunta Region, central Australia: Part 1: Geological setting and mineral potential. *Precambrian Research*, **142**, 93-133.

Hoeve, J., Sibbald, T.I.I., Ramakers, P. and Lewry, J.F., 1980. Athabasca Basin unconformity-type uranium: a special type of sandstone-type deposits? In: Ferguson, J. and Goleby, A. B. (eds.), Uranium in the Pine Creek Geosyncline. *International Atomic Energy Agency*, Vienna, p. 575-594.

Hollis, J.A. and Glass, L.M., 2012. Howship and Oenpelli, Northern Territory. 1:100 000 geological map series explanatory notes, 5572, 5573. Northern Territory Geological Survey, Darwin.

Howard, L.E. and Sass, J.H., 1964. Terrestrial heat flow in Australia. *Journal of Geophysical Research*, **69**, 1617-26.

Hurtig, E. and Schlosser, P., 1979. Vertical changes of heat flow in boreholes in the north German sedimentary basin. *KAPG Geophysical Monograph*, Budapest, Akademiai Kiado, 398-401.

Hussey, K.J., 2003. Rare earth element mineralisation in the eastern Arunta region. *Northern Territory Geological Survey Record* **2003-004**.

Hussey, K.J., Huston, D.L. and Claoué-Long, J.C., 2005. Geology and origin of some Cu-Pb-Zn (-Au-Ag) deposits in the Strangways Metamorphic Complex, Arunta Region, Northern Territory. *Northern Territory Geological Survey Report 17*.

Hussey, K.J., 2008. Report on NBDH37, a cored diamond drillhole at Nolans Bore P-REE-Th-U deposit, Reynolds Range, Arunta Region *Northern Territory Geological Survey Record* **2008-005**.

Huston, D.L. (ed.), 2010. An assessment of the uranium and geothermal potential of north Queensland. *Geoscience Australia Record,* **2010/14**, 108pp.

Huston, D.L., Blewett, R.S. and Champion, D.C., 2012. Australia through time: a summary of its tectonic and metallogenic evolution. *Episodes*, **35**, *in press*.

Huston, D.L., Bolger, C. and Cozens, G., 1993. A comparison of mineral deposits at the Gecko and White Devil deposits: implications for ore genesis in the Tennant Creek district, Northern Territory, Australia. *Economic Geology*, **88**, 1198-1225.

Huston, D.L., Czarnota, K., Jaireth, S., Williams, N.C., Maidment, D., Cassidy, K.F., Duerden, P. and Miggins, D., 2010. Mineral systems of the Paterson region. *Geoscience Australia Record*, **2010/12**, 155-218.

Huston, D., Maas, R., Fraser, G. and Hussey, K., 2011a. Nolans Bore REE-U-Th deposit, Northern Territory. In: Skirrow, R.G. (ed.), Uranium mineralisation events in Australia: geochronology of the Nolans Bore, Kintyre, Oasis, Mt Gee-Armchair, and Maureen deposits. Geoscience Australia Record **2011/11**, 9-20.

Huston, D.L., Maas, R. and Hussey, K.J., 2011b. The Nolans Bore rare earth element-phosphorous-uranium-thorium deposit: geology, age and origin. In: Barra, F. *et al*. (eds.), Let's talk ore deposits, Proceedings of the Eleventh Biennial SGA Meeting, Antofagasta, 2011, 127-129.

Huston, D.L. and van der Wielen, S.E. (eds.), 2011. An assessment of the uranium and geothermal prospectivity of east-central South Australia. *Geoscience Australia Record,* **2011/34**, 229pp.

Huston, D.L., Whelan, J.A., Jaireth, S., Kirkby, A., Gerner, E., Close, D.F., Blewett, R., Scrimgeour, I.R. and Korsch, R.J., 2011c. Implications of the Georgina-Arunta seismic survey to energy and mineral systems. In: *Annual Geoscience Exploration Seminar (AGES) 2011, record of abstracts. Northern Territory Geological Survey, Record* **2011-003**, 86-93.

Hyndman, R.D., 1967. Heat flow in Queensland and the Northern Territory, Australia. *Journal of Geophysical Research*, **72**, 527-539.

Idnurm, M., 2000. Towards a high resolution late Paleoproterozoic-earliest Mesoproterozoic apparent polar wander path for northern Australia. *Australian Journal of Earth Sciences,* **47**, 405-429.

Ivanac, J.F., 1954. The geology and mineral deposits of the Tennant Creek gold-field, Northern Territory. Bureau of Mineral Resources, Geology and Geophysics Bulletin, **22**.

Jackson, D.J. and Andrew, R.L., 1990. Kintyre uranium deposit. In: Hughes, F.E. (ed.), *Geology of the Mineral Deposits of Australia and Papua New Guinea*. The Australasian Institute of Mining and Metallurgy, 653-658.

Jaireth, S., 2009. Uranium deposits of the Lake Frome region. In: Skirrow, R.G. (ed.), Uranium ore-forming systems of the Lake Frome region, South Australia: regional controls and exploration criteria. *Geoscience Australia Record,* **2009/40,** 57-66.

Jaireth, S., McKay, A., Lambert, I., 2008. Association of large sandstone uranium deposits with hydrocarbons. *AusGeo News,* **89**, 8-12.

Johnston, J.D., 1984. Structural evolution of the Pine Creek Orogen and mineralisation therein, Northern Territory, Australia: Melbourne, Monash University. 335pp.

Kappelmeyer, O. and Haenel, R., 1974. Geothermics with special reference to practical application, *Geoexploration Monographs,* **1**. Borntraeger, Berlin, 238pp.

Kennett, B., Salmon, M., Saygin, E. and AusMoho Working Group, 2011. AusMoho: the variation of Moho depth in Australia. *Geophysical Journal International*, **187**, 946-958.

Keppler, H. and Wyllie, P.J., 1990. Role of fluids in transport and fractionation of uranium and thorium in magmatic processes. *Nature*, **348**, 531-533.

Keppler, H. and Wyllie, P.J., 1991. Partitioning of Cu, Sn, Mo, W, U, and Th between melt and aqueous fluid in the system haplogranite-H_2O-HCl and haplogranite-H_2O-HF. *Contributions to Mineralogy and Petrology*, **109**, 139-150.

King, D., 1954. Geology of the Crockers Well uranium deposits. *Geological Survey of South Australia Bulletin,* **30**, 70-78.

Kinnaird, J.A. and Nex, P.A.M., 2007. A review of geological controls on uranium mineralisation in sheeted leucogranites within the Damara Orogen, Namibia. *Institute of Mining and Metallurgy Transactions, Section B, Applied Earth Sciences,* **B116**, 68-85.

Knox-Robinson, C.M. and Wyborn, L.A.I., 1997. Towards a holistic exploration strategy: using geographic information systems as a tool to enhance exploration. *Australian Journal of Earth Sciences,* **44**, 453-463.

Kositcin, N., Magee, C., Whelan, J. and Champion, D.C., 2011. New SHRIMP geochronology from the Arunta Region: 2009–2010. *Geoscience Australia Record*, **2011/14**.

Korsch, R.J., Blewett, R.S., Close, D.F., Scrimgeour, I.R., Huston, D.L., Kositcin, N., Whelan J.A., Carr, L.K. and Duan, J., 2011. Geological interpretation and geodynamic implications for the deep seismic reflection and magnetotelluric line 09GA-GA1: Georgina Basin-Arunta Region, Northern Territory. In: *Annual Geoscience Exploration Seminar (AGES) 2011, record of abstracts. Northern Territory Geological Survey, Record* **2011-003**, 67-76.

Korsch, R.J., Henson, P.A., Champion, D.C., Blewett, R.S., Huston, D.L., Withnall, I.W., Hutton, L.J., Henderson, R.A., Fergusson, C.L. and Collins, W.J., 2009a. Geodynamic implications of the deep seismic reflection profiles in north Queensland. *AIG Bulletin*, **49**, 181-183.

Korsch, R., Henson, P., Huston, D., Whitaker, A., Carson, C.J., Maas, R. and Hussey, K., 2009b. Geoscience Australia's Onshore Energy Security Program in the Northern Territory: current results and future directions. In: *Annual Geoscience Exploration Seminar (AGES) 2009, record of abstracts. Northern Territory Geological Survey, Record* **2009-002**, 11-14.

Korsch, R.J. and Kositcin, N. (eds.), 2010. GOMA (Gawler Craton-Officer Basin-Musgrave Province-Amadeus Basin) seismic and MT workshop 2010. *Geoscience Australia Record,* **2010/39**, 162 pp.

Korsch, R.J., Kositcin, N., Blewett, R.S., Fraser, G.L., Baines, G., Kennett, B.L.N., Neumann, N.L., Reid, A.J., Preiss, W.V., Giles, D., Armit, R. and Betts, P.G., 2010. Geodynamic implications of the deep seismic reflection line 08GA-OM1: Gawler Craton-Officer Basin-Musgrave Province-Amadeus Basin (GOMA), South Australia and Northern Territory. In: Korsch, R.J. and Kositcin, N. (eds.) 2010. GOMA (Gawler Craton-Officer Basin-Musgrave Province-Amadeus Basin) seismic and MT workshop 2010. *Geoscience Australia Record,* **2010/39**, 138-151.

Korsch, R.J. and Lindsay, J.F., 1989. Relationships between deformation and basin evolution in the intracratonic Amadeus Basin, central Australia. *Tectonophysics*, **158**, 5-22.

Kyser, T. K., 2007. Fluids, basin analysis, and mineral deposits. *Geofluids,* **7**, 238-257.

Kyser, K., Hiatt, E., Renac, C., Durocher, K., Holk, G. and Deckart, K., 2000. Diagenetic fluids in Paleo- and Meso-Proterozoic sedimentary basins and their implications for long protracted fluid histories. *Mineralogical Association of Canada, Short Course* 28, 225-262.

Lally, J.H. and Bajwah, Z.U., 2006. Uranium deposits of the Northern Territory. *Northern Territory Geological Survey Report*, **20**, 87 pp.

Lambert, I., Jaireth, S., McKay, A. and Meizitis, Y., 2005. Why Australia has so much uranium, *AusGeo News,* **80**, 7-10.

Large, R.R., 1975. Zonation of hydrothermal minerals at the Juno mine, Tennant Creek goldfield, central Australia. *Economic Geology*, **70**, 1387–1413.

Le Messurier, P., Williams, B. T. and Blake, D. H., 1990. Tennant Creek inlier - Regional geology and mineralisation. *Australasian Institute of Mining and Metallurgy Monograph*, **14**, 829-838.

Leach, D.L., Sangster, D.F., Kelley, K.D., Large, R.R., Garven, G., Allen, C.R., Gutzmer, J. and Walters, S., 2005. Sediment-hosted zinc deposits: a global perspective. *Economic Geology, 100th Anniversary Volume*, 561-608.

Li, Y. and Oldenburg, D.W., 1996. 3-D inversion of magnetic data. *Geophysics*, **61**, 394-408.

Li, Y. and Oldenburg, D.W., 1998. 3-D inversion of gravity data. *Geophysics*, **63**, 109-119.

Lindal, B., 1973. Industrial and other applications of geothermal energy. Geothermal Energy: Review of Research and Development, LC No. 72-97138. Paris, UNESCO, 135-148.

Lindsay. J.F. (ed.), 1993. Geological atlas of the Amadeus Basin. Australian Geological Survey Organisation, Canberra.

Ludwig, K.R. and Cooper, J.A., 1984. Geochronology of Precambrian granites and associated U-Ti-Th mineralization, northern Olary province, South Australia. *Contributions to Mineralogy and Petrology,* **86**, 298-308.

Lyons, P. and Huston, D.L. (eds.), 2006. Evolution and metallogenesis of the North Australian Craton, Conference Abstracts. *Geoscience Australia Record*, **2006/16**.

Maas, R., 1989. Nd-Sr isotope constraints on the age and origin of unconformity-type uranium deposits in the Alligator Rivers uranium field, Northern Territory, Australia. *Economic Geology,* **84**, 64-90.

Maas, R., Huston, D. and Hussey, K., 2009. Isotopic constraints on the genesis of world-class REE-P-U-Th mineralization, Nolan Bore, Central Australia. *Geochimica et Cosmochimica Acta*, **73**, A809.

Mackie, A.M., 1984. Geology of the Green Parrot and Reward silver-lead deposits, Jervois Range, Northern Territory. *Proceedings of the Australasian Institute of Mining and Metallurgy Conference*, Darwin, 323-327.

Mackie, A.W., 2002. Final Report, Johnnies Reward-The Pinnacles prospects, Strangways Range N.T. (EL8489) for 6 years to 20 October 2001. Unpublished Flinders Diamonds Ltd Report.

Maidment, D., Lambeck, L., Huston, D. and Donnellan, N., 2006. New geochronological data from the Tennant region. In: *Annual Geoscience Exploration Seminar (AGES) 2006, record of abstracts. Northern Territory Geological Survey, Record* **2006-002**, 32-35.

Maidment, D.W., Williams, I.S. and Hand, M., 2007. Testing long-term patterns of basin sedimentation by detrital zircon geochronology, Centralian Superbasin, Australia. *Basin Research*, **19**, 335-360.

Maidment, D.W., Lambeck, A., Huston, D. and Donnellan, N., *in prep*. Constraints on the timing of the Tennant Event and associated Au-Cu-Bi mineralisation in the Tennant Region, Northern Territory.

Mawby, J., Hand, M. and Foden, J., 1999. Sm-Nd evidence for high-grade Ordovician metamorphism in the Arunta Block, central Australia. *Journal of Metamorphic Geology*, **17**, 653-668.

Mawby, J., 2000. Metamorphic and geochronologic constraints on Palaeozoic tectonism in the eastern Arunta Inlier. Unpublished PhD thesis, University of Adelaide.

Mayer, T.E., Thompson, A. and Burdett, M., 2009. Johnnies Reward Project, Northern Territory, EL 23592, Annual Technical Report for the period 12 February 2008 – 11 February 2009, ALICE SPRINGS 1:250 000 Map Sheet. Unpublished Minotaur Exploration Ltd. Report, 09/13.

McCuaig, T.C., Beresford, S. and Hronsky, J., 2010. Translating the mineral systems approach into an effective exploration targeting system. *Ore Geology Reviews*, **38**, 128-138.

McDermott, F., Harris, N.B.W. and Hawkesworth, C.J., 1996. Geochemical constraints on crustal anatexis: a case study from the Pan-African Damara granitoids of Namibia. *Contributions to Mineralogy and Petrology,* **123**, 406-423.

McKay, A.D. and Miezitis, Y., 2001. Australia's uranium resources, geology and development of deposits. *AGSO-Geoscience Australia Mineral Resource Report,* **1**, 184p.

McKinnon-Matthews, J., 2010. Blackadder meets Basil, more copper and nickel sulfides in the Irindina. In: *Annual Geoscience Exploration Seminar (AGES) 2010, record of abstracts. Northern Territory Geological Survey, Record* **2010-002**, 27-29.

McLaren, S., Sandiford, M., Hand, M., Neumann, N., Wyborn, L., and Bastrakova, I., 2003. Chapter 12-The hot southern continent: heat flow and heat production in Australian Proterozoic terranes. *Geological Society of Australia Special Publication*, **22**, 151-161.

McLaren, S., Sandiford, M., Dunlap, W.J., Scrimgeour, I., Close, D. and Edgoose, C., 2009. Distribution of Palaeozoic reworking in the western Arunta Region and northwestern Amadeus Basin from $^{40}Ar/^{39}Ar$ thermochronology: implications for the evolution of intracratonic basins. *Basin Research*, **21**, 315-334.

McPhie, J., 1993. A syn-sedimentary rhyolitic sill with peperite margins: the Tennant Creek porphyry. *Australian Journal of Earth Sciences*, **40**, 545-558.

Meixner, A.J. and Haynes, M.W., 2012. Depth to magnetic basement of the Arunta-Georgina-Amadeus-Musgrave region (first edition), 1:1 000 000 scale. Geoscience Australia, Canberra.

Meixner, A.J., Kirkby, A., Champion, D.C., Weber, R., Connolly, D. and Gerner, E., 2011. Geothermal systems. In: Huston, D.L. and van der Wielen, S.E. (eds.), An assessment of the uranium and geothermal prospectivity of east-central South Australia. *Geoscience Australia Record,* **2011/34**, 166-207.

Mernagh, T.P., Heinrich, C.A., Leckie, J.F., Carville, D.P ., Gilbert, D.J., Valenta, R.K. and Wyborn, L.A.I., 1994. Chemistry of the low-temperature hydrothermal gold, platinum, and palladium (± uranium) mineralization at Coronation Hill, Northern Territory, Australia. *Economic Geology,* **89**, 1053-1073.

Mernagh, T.P., Wyborn, L.A.I. and Jagodzinski, E.A., 1998. "Unconformity-related" U ± Au ± platinum-group-element deposits. *AGSO Journal,* **17**, 197-205.

Meyer, M. and Brooker, J., 1991. Eliciting and analysing expert judgement: a practical guide. London, Academic Press.

Miller, J.A., Cartwright, I. and Buick, I.S., 1997. Granulite facies metamorphism in the Mallee Bore area, northern Harts Range; implications for thermal evolution of the eastern Arunta Inlier, central Australia. *Journal of Metamorphic Geology*, **15**, 613-629.

Milligan, P.R., Franklin, R., Minty, B.R.S., Richardson, L.M. and Percival, P.J., 2010. Magnetic anomaly map of Australia (fifth edition). Geoscience Australia, Canberra.

Minty, B.R.S., Franklin, R., Milligan, P.R., Richardson, L.M. and Wilford, J., 2010. Radiometric Map of Australia (Second Edition), 1:5 000 000 scale. Geoscience Australia, Canberra.

Nex, P.A.M., Kinnaird, J. and Oliver, G.J.H., 2001. Petrology, geochemistry and uranium mineralisation of post-collisional magmatism around Goanikontes, southern Central Zone, Damaran Orogen, Namibia. *Journal of African Earth Sciences,* **33**, 481-502.

Nex, P., Herd, D. and Kinnaird, J., 2002. Fluid extraction from quartz in sheeted leucogranites as a monitor to styles of uranium mineralization: an example from the Rössing area, Namibia. *Geochemistry: Exploration, Environment, Analysis*, **2**, 83-96.

Noorollahi, Y., Itoi, R., Fujii, H. and Tanaka, T., 2007. GIS model for geothermal resources exploration in Akita and Iwate Prefecture, northern Japan. *Computers and Geosciences,* **33** 1008-1021.

Norden, B. and Forster, A., 2006. Thermal conductivity and radiogenic heat production of sedimentary and magmatic rocks in the Northeast German Basin. *American Association of Petroleum Geologists Bulletin,* **90**, 939-962.

OECD Nuclear Energy Agency, 2008. Uranium 2007 - Resources, production and demand. Organisation for Economic Cooperation and Development Publishing, Paris. 420p.

Oliver, N.H.S., Butera, K.M., Rubenach, M.J., Marshall, L.J., Cleverley, J.S., Mark, G., Tullemans, F. and Esser, D., 2008. The protracted hydrothermal evolution of the Mount Isa Eastern Succession: A review and tectonic implications. *Precambrian Research*, **163**, 108-130.

Oreskes, N. and Einaudi, M.T., 1992. Origin of hydrothermal fluids at Olympic Dam: Preliminary results from fluid inclusions and stable isotopes. *Economic Geology,* **87**, 64-90.

OZ SEEBASE™ Study, 2005. Public Domain Report to Shell Development Australia by FrOG Tech Pty Ltd., 182 p.

Pegum, D.M., 1997. An introduction to the petroleum geology of the Northern Territory of Australia. Northern Territory Geological Survey, 46p.

Peiffert, C., Cuney, M. and Nguyen-Trung, C., 1994. Uranium in granitic magmas: Part 1. Experimental determination of uranium solubility and fluid-melt partition coefficients in the uranium oxide-haplogranite-H_2O-Na_2CO_3 system at 720-770°C, 2 kbar. *Geochimica et Cosmochimica Acta*, **58**, 2495-2507.

Peiffert, C., Nguyen-Trung, C. and Cuney, M., 1996. Uranium in granitic magmas: Part 2. Experimental determination of uranium solubility and fluid-melt partition coefficients in the uranium oxide-haplogranite-H_2O-NaX (X = Cl, F) system at 770°C, 2 kbar. *Geochimica et Cosmochimica Acta,* **60**, 1615-1529.

Pidgeon, R.T., 1977. U-Pb isotopic analysis and age determination of uranium ore samples submitted by Central Pacific Minerals NL. Unpublished report prepared for Central Pacific Minerals NL.

PIRSA, Petroleum and geothermal in South Australia: Pedirka Basin. http://www.pir.sa.gov.au/__data/assets/pdf_file/0014/34142/prospectivity_pedirka.pdf (accessed April 2012)

PIRSA, 2010a. Petroleum and Geothermal in South Australia 2010, data package DVD.

PIRSA, 2010b. Petroleum – Basin and Province Information, http://www.pir.sa.gov.au/petroleum/prospectivity/basin_and_province_information (accessed March 2011).

Plant, J.A., Simpson, P.R., Smith, B. and Windley, B.F., 1999. Uranium ore deposits: products of the radioactive earth. *Reviews in Mineralogy and Geochemistry,* **38**, 255-319.

Polito, P.A., Kyser, T.K. and Jackson, M.J., 2006. The role of sandstone diagenesis and aquifer evolution in the formation of uranium and zinc-lead deposits, southern McArthur Basin, Northern Territory, Australia. *Economic Geology,* **101**, 1189-1209.

Polito, P.A., Kyser, T.K., Rheinberger, G. and Southgate, P.N., 2005a. A Paragenetic and Isotopic Study of the Proterozoic Westmoreland Uranium Deposits, Southern McArthur Basin, Northern Territory, Australia. *Economic Geology,* **100**, 1243-1260.

Polito, P.A., Kyser, T.K., Thomas, D., Marlatt, J. and Drever, G., 2005b. Re-evaluation of the petrogenesis of the Proterozoic Jabiluka unconformity-related uranium deposit, Northern Territory, Australia. *Mineralium Deposita,* **40**, 257-288.

Polito, P.A., Kyser T.K., Marlatt J., Alexandre P., Bajwah Z.U. and Drever D., 2004. Significance of alteration assemblages for the origin and evolution of the Proterozoic Nabarlek unconformity-related uranium deposit, Northern Territory, Australia. *Economic Geology*, **99**, 113–139.

Questa Australia Pty Ltd., 1989. Petroleum Basin study – Ngalia Basin, 76p.

Radke, B.M., Ferguson, J., Cresswell, R.G., Ransley, T.R. and Haberbehl, M.A., 2000. Hydrochemistry and implied hydrodynamics of the Cadna-owie Hooray Aquifer, Great Artesian Basin, Australia. Bureau of Rural Sciences, Canberra, 229p.

Rattenbury, M.S., 1992. Stratigraphic and structural controls on ironstone mineralization in the Tennant Creek goldfield, Northern Territory, Australia. *Australian Journal of Earth Sciences*, **39**, 591–602.

Raymond, O.L. and Retter, A., 2010. Surface geology of Australia 1:1 000 000 scale, 2010 edition [Digital Dataset]. Geoscience Australia, Canberra. http://www.ga.gov.au.

Raznjevic, K., 1976. Handbook of Thermodynamic Tables and Charts, Washington DC: Hemisphere Publishing Corporation.

Richardson, C.K. and Holland, H.D., 1979. Fluorite deposition in hydrothermal systems. *Geochimica et Cosmochimica Acta*, **43**, 1327-1335.

Rheinberger, G.M., Hallenstein, C. and Stegman, C.L., 1998. Westmoreland uranium deposits. In: Berkman, D.A. and Mackenzie, D.H. (eds.), *Geology of Australian and Papua New Guinean mineral deposits*. Australasian Institute of Mining and Metallurgy, Melbourne, 807-814.

Root, J.C. and Robertson, W.J., 1994. Geophysical signature of the Kintyre uranium deposit, Western Australia. In: Dentith, M.C., Frankcombe, K.F., Ho, S E., Shepherd, J.M., Groves, D.I. and Trench, A. (eds.), *Geophysical signatures of Western Australian mineral deposits*. Geology and Geophysics Department (Key Centre) and UWA Extension, The University of Western Australia, Publication 26 and the Australian Society of Exploration Geophysicists, Special Publication 7, 371-382.

Rudnick, R.L. and Gao, S., 2003. Composition of the Continental Crust. *Treatise on Geochemistry,* **3**, 1–64.

Ruzicka, V., 1993. Unconformity-associated uranium deposits. *Geological Association of Canada Special Paper,* **40**, 125-149.

Sass, J. H., 1964. Heat-flow values from the Precambrian Shield of Western Australia. *Journal of Geophysical Research,* **69**, 299-308.

Sass, J.H. and Lachenbruch, A.H., 1979. Thermal regime of the Australian continental crust. In: McElhinny, M.W. (ed.), *The Earth — its Origin, Structure and Evolution*, 301-351.

Sawka, W.N. and Chappell, B.W., 1986. The distribution of radioactive heat production in I- and S-type granites and residual source regions: implications for high heat flow areas in the Lachlan Fold Belt, Australia. *Australian Journal of Earth Sciences*, **33**, 107-118.

Schmid, S. and Cleverley, J., 2011. Characterisation of uranium-vanadium mineralisation at Bigrlyi, Ngalia Basin, Australia. In: Barra, F. *et al*. (eds.), Let's talk ore deposits, Proceedings of the Eleventh Biennial SGA Meeting, Antofagasta, 2011, 950-952.

Schmid, S., Foss, C., Hill, J., Quigley, M., Schaubs, P., Cleverley, J. and Robinson, J., 2012. JSU Ngalia Basin uranium mineral system project. *Northern Territory Geological Survey, Record* **2012-003**.

Schofield, A., 2009. Uranium content of igneous rocks of Australia 1:5 000 000 maps: explanatory notes and discussion. *Geoscience Australia Record,* **2009/17**, 20p.

Schofield, A., 2010. Potential for magmatic-related uranium mineral systems in Australia. *Geoscience Australia Record*, **2010/20**, 56pp.

Schofield, A., 2011. Uranium systems processes in the Crocker Well Suite, South Australia. *Geoscience Australia Record,* **2011/45**, 39p.

Schofield, A. and Connolly, D., 2011. Magmatic-related uranium mineral systems. In: Huston, D.L. and van der Wielen, S.E. (eds.), An assessment of the uranium and geothermal prospectivity of east-central South Australia. *Geoscience Australia Record,* **2011/34**, 92-118.

Schofield, A. and Huston, D., 2010. Magmatic-related uranium systems. In: Huston, D.L. (ed.), An assessment of the uranium and geothermal potential of north Queensland. *Geoscience Australia Record,* **2010/14**, 54-67.

Scrimgeour, I.R., 2003. Developing a revised framework for the Arunta Region. In: *Annual Geoscience Exploration Seminar (AGES) 2003, record of abstracts. Northern Territory Geological Survey, Record* **2003-001**.

Scrimgeour, I.R., *in press* a. Aileron Province. In: Ahmad, M. and Munson, T.J. (compilers), *in press*, Geology and mineral resources of the Northern Territory. *Northern Territory Geological Survey, Special Publication 5*.

Scrimgeour, I.R., *in press* b. Warumpi Province. In: Ahmad, M. and Munson, T.J. (compilers), *in press*, Geology and mineral resources of the Northern Territory. *Northern Territory Geological Survey, Special Publication 5*.

Scrimgeour, I.R., *in press* c. Irindina Province. In: Ahmad, M. and Munson, T.J. (compilers), *in press*, Geology and mineral resources of the Northern Territory. *Northern Territory Geological Survey, Special Publication 5*.

Scrimgeour, I.R. and Close, D.F., 2011. Overview of the geology and tectonics along the Georgina-Arunta seismic traverse. In: *Annual Geoscience Exploration Seminar (AGES) 2011, record of abstracts. Northern Territory Geological Survey, Record* **2011-002**, 57-62.

Scrimgeour, I.R., Kinny, P.D., Close, D.F. and Edgoose, C.J., 2005. High-T granulites and polymetamorphism in the southern Arunta Region, central Australia: evidence for a 1.64 Ga accretional event. *Precambrian Research*, **142**, 1-27.

Scrimgeour, I. and Raith, J., 2001. Tectonic and thermal events in the northeastern Arunta Province. *Northern Territory Geological Survey, Report 12*, 45p.

Senior, B.R., Truswell, E.M., Idnurm, M., Shaw, R.D. and Warren, R.G., 1995. Cenozoic sedimentary basins in the eastern Arunta Block, Alice Springs region, central Australia. *AGSO Journal of Australian Geology and Geophysics*, **15**, 421-444.

Shaw, R.D. and Black, L.P., 1991. The history and tectonic implications of the Redbank Thrust Zone, central Australia, based on structural, metamorphic and Rb-Sr isotopic evidence. *Australian Journal of Earth Sciences*, **38**, 307-332.

Shaw, R.D., Korsch, R.J., Goleby, B.R. and Wright, C., 1991. The BMR regional seismic line across the Amadeus Basin, central Australia: implications for tectonics of the basin for hydrocarbon exploration. *Exploration Geophysics*, **22**, 345-352.

Shaw, R.D., Zeitler, P.K., McDougall, I. and Tingate, P.R., 1992. The Palaeozoic history of an unusual intracratonic thrust belt in central Australia based on ^{40}Ar-^{39}Ar, K-Ar and fission track dating. *Journal of the Geological Society of London*, **149**, 937-954.

Skirrow, R.G. (ed.), 2009. Uranium ore-forming systems of the Lake Frome region, South Australia: regional spatial controls and exploration criteria. *Geoscience Australia Record,* **2009/40**, 151p.

Skirrow, R.G., 2010. 'Hematite-group' IOCG ± U ore systems: tectonic settings, hydrothermal characteristics, and Cu-Au and U mineralizing processes. In: Corriveau, L. and Mumin, H. (eds.), Exploring for Iron Oxide Copper-Gold Deposits: Canada and Global Analogues. *Geological Association of Canada Shortcourse Notes*, **20**, 39-58.

Skirrow, R.G., 2011. Controls on uranium in iron oxide copper-gold systems: insights from Proterozoic and Paleozoic deposits in southern Australia. *Proceedings of Society for the*

Geology Applied to Ore Deposits 11th Biennial Meeting, Antofagasta, Chile, 26-29th September 2011, 482-484.

Skirrow, R. and Huston, D., 2010. Uranium-rich iron oxide-copper-gold systems. In: Huston, D.L. (ed.), 2010. An assessment of the uranium and geothermal potential of north Queensland. *Geoscience Australia Record*, **2010/14**, 42-54.

Skirrow, R.G., Jaireth, S., Huston, D.L., Bastrakov, E.N., Schofield, A., van der Wielen, S.E. and Barnicoat, A.C., 2009. Uranium mineral systems: Processes, exploration criteria, and a new deposit framework. *Geoscience Australia* Record **2009/20**.

Skirrow, R.G., Schofield, A. and Connolly, D., 2011. Uranium-rich iron oxide-copper-gold. In: Huston, D.L. and van der Wielen, S.E. (eds.), An assessment of the uranium and geothermal prospectivity of east-central South Australia. *Geoscience Australia Record,* **2011/34**, 37-68.

Skirrow, R.G. and Walshe, J.L., 2002. Reduced and oxidized Au-Cu-Bi iron oxide deposits of the Tennant Creek Inlier, Australia: an integrated geologic and chemical model. *Economic Geology*, **97**, 1167-1202.

Skvarla, M.J., Vandersande, J.W., Linvill, M.L., and Pohl, R.O., 1981. Thermal conductivity of selected repository minerals. *Scientific Basis for Nuclear Waste Management,* **3**, 43–50.

Smith, K.G., 1972. Stratigraphy of the Georgina Basin. BMR Bulletin 111, 156p.

Smith, J., 2001. Summary of Results, Joint NTGS – AGSO Age Determination Program, 1999 - 2001. *Northern Territory Geological Survey, Record*, **2001/007**, 53 p.

Southern Methodist University (SMU) geothermal database, accessed at http://www.smu.edu/geothermal/georesou/alldata.csv.

Sørensen, H., 2001. Brief introduction to the geology of the Ilímaussaq alkaline complex, south Greenland, and its exploration history. *Geology Survey of Greenland Bulletin,* **190**, 7-23.

Spirakis, C.S., 1996. The roles of organic matter in the formation of uranium deposits in sedimentary rocks. *Ore Geology Reviews*, **11**, 53-59.

Staatz, M.H., 1978. I and L uranium and thorium vein system, Bokan Mountain, southeastern Alaska. *Economic Geology,* **73**, 512-523.

Stüwe, K., 2007. Geodynamics of the Lithosphere. An Introduction. 2nd edition. Springer Verlag, 493 p.

Taylor, S.R., and McLennan, S.M., 1985. The Continental Crust: Its Composition and Evolution. Blackwell, Oxford.

Tester, J.W., 1982. Energy Conversion and Economic Issues for Geothermal Energy. Handbook of Geothermal Energy. Gulf Publishing Co., Houston, Texas. 471-586.

Thompson, T.B., 1988. Geology and uranium-thorium mineral deposits of the Bokan Mountain granite complex, southeastern Alaska. *Ore Geology Reviews,* **3**, 193-210.

Thompson, T.B., Pierson, J.R. and Lyttle, T., 1982. Petrology and petrogenesis of the Bokan Granite Complex, southeastern Alaska. *Geological Survey of America Bulletin,* **93**, 898-908.

Tipper, D.B., 1966. Strangways Range detailed aeromagnetic survey, Northern Territory. *Bureau of Mineral Resources, Australia, Report*, **136**.

van der Wielen, S., 2010. Sandstone-hosted uranium systems. In: Huston, D.L. (ed.), An assessment of the uranium and geothermal potential of north Queensland. *Geoscience Australia Record,* **2010/14**, 10-17.

van der Wielen, S.E. and Britt, A., 2009. Uranium depositional gradients and chemical architecture. In: Skirrow, R. G. (ed.), 2009, Uranium ore-forming systems of the Lake Frome region, South Australia: regional spatial controls and exploration criteria. *Geoscience Australia Record,* **2009/40**, 42-56.

van der Wielen, S.E., Huston, D.L. and Connolly, D., 2011. Sandstone-hosted uranium systems. In: Huston, D.L. and van der Wielen, S.E. (eds.), An assessment of the uranium and geothermal prospectivity of east-central South Australia. *Geoscience Australia Record,* **2011/34**, 21-36.

van der Wielen, S.E., Kirkby, A., Britt, A.F., Nicoll, M.G., and Skirrow, R., *in prep.* An integrated 3D map for the greater Eromanga Basin, Australia.

Wade, B.P., Barovich, K.M., Hand, M., Scrimgeour, I.R. and Close, D.F., 2006. Evidence for early Mesoproterozoic arc magmatism in the Musgrave Block, central Australia: implications for Proterozoic crustal growth and tectonic reconstructions of Australia. *Journal of Geology*, **114**, 43-63.

Walter, M.R., Veevers, J.J., Calver, C.R., and Gray, K., 1995. Neoproterozoic stratigraphy of the Centralian Superbasin, Australia. *Precambrian Research,* **73**, 173-195.

Warren, R.G., 1980. Summary of the mineral deposits in the Alice Springs 1:250 000 sheet area. *Bureau of Mineral Resources, Australia, Record*, **1980/44**.

Warren, R.G., 1989. Geochemical sampling in the Arunta Block, 1980–1988. *Bureau of Mineral Resources, Australia, Record*, **1989/54**.

Warren, R.G. and Shaw, R.D., 1985. Volcanogenic Cu-Pb-Zn bodies in granulites of the central Arunta Block, central Australia. *Journal of Metamorphic Geology*, **3**, 481-499.

Watson, E.B. and Harrison, T.M., 1983. Zircon saturation revisited: temperature and composition effects in a variety of crustal magma types. *Earth and Planetary Science Letters,* **64**, 295-304.

Wedekind, M.R., Large, R.R., Williams, B.T., 1989. Controls on high-grade gold mineralization at Tennant Creek, Northern Territory, Australia. *Economic Geology Monograph*, **6**, 168-179.

Wedepohl, K.H., 1974a. Copper. 29-E. Abundance in common igneous rock types; crustal abundances. *Handbook of Geochemistry,* 29-E-1 to 29-E-13.

Wedepohl, K.H., 1974b. Copper. 29-K. Abundance in common sediments and sedimentary rocks. *Handbook of Geochemistry,* 29-K-1 to 29-E-10.

Wellman, P., 1991. Amadeus Basin, Northern Territory, structure from gravity and magnetic anomalies. In: Korsch, R.J. and Kennard, M. (eds.), Geological and geophysical studies in the Amadeus Basin, central Australia. *Bureau of Mineral Resources, Australia, Bulletin*, **236**, 594p.

Wells, A.T., Forman, D.J., Ranford, L.C. and Cook, P.J., 1970. Geology of the Amadeus Basin, central Australia. *Bureau of Mineral Resources Bulletin*, **100**, 222p.

Wells, A.T. and Moss, F.J., 1983. The Ngalia Basin, Northern Territory: stratigraphy and structure. BMR Bulletin 212, 88p.

Whelan, J., Close, D., Carson, C. and Baker, M., 2008. Overview of the geology and mineral potential of the Entia Dome, eastern Arunta Region. In: *Annual Geoscience Exploration Seminar (AGES) 2008, record of abstracts. Northern Territory Geological Survey, Record* **2008-002**, 8-10.

Whelan, J.A., Close, D.F., Scrimgeour, I.R. and Hallett, L., 2009a. Magmatism and mineralisation in the eastern Arunta Region, central Australia. In: Williams, P. J. *et al*. (eds.), Smart science for exploration and mining, Record of abstracts. *Proceedings of the 10th Biennial Society for Geology Applied to Mineral Deposits (SGA), Townsville, Australia*

Whelan, J.A., Hallett, L. and Close, D.F., 2009b. Magmatism in the eastern Arunta Region: implications for Ni, Cu and Au mineralisation. In: *Annual Geoscience Exploration Seminar (AGES) 2009, record of abstracts. Northern Territory Geological Survey, Record* **2009-002**, 37-40.

Whelan, J.A., Webb, G., Close, D.F., Kositcin, N., Bodorkos, S., Huston, D.L., Armstrong, R. and Allen, C., 2011. New geochronological and geochemical data from the Limbla 1:100 000 map area: implications for mineralisation in the eastern Arunta Region. In: *Annual Geoscience Exploration Seminar (AGES) 2011, record of abstracts. Northern Territory Geological Survey, Record* **2011-002**, 40-43.

Whelan, J., Webb, G., Close, D., Kositcin, N., Bodorkos, S. and Maas, R., 2012. New copper-gold discoveries in the eastern Arunta Region: implications for Cu-Au mineralisation in the Arunta. In: *Annual Geoscience Exploration Seminar (AGES) 2012, record of abstracts. Northern Territory Geological Survey, Record* **2012-002**, 38-42.

Whittle, A.W.G., 1954. Petrology of Crockers Well uranium deposit. *Geological Survey of South Australia Bulletin,* **30**, 79-83.

Wilde, A.R. and Wall, V.J., 1987. Geology of the Nabarlek uranium deposit, Northern Territory, Australia. *Economic Geology*, **82**, 1152–1168.

Wilford, J., Worrall, L. and Minty, B., 2009. Radiometric map of Australia provides new insights into uranium prospectivity. *AusGeo News,* **95**, 7-10.

Williams, P.J., Barton, M.D., Johnson, D.A., Fontboté, L., De Haller, A., Mark, G., Oliver, N.H. S. and Marschik, R. 2005. Iron Oxide Copper-Gold Deposits: Geology, Space-Time Distribution, and Possible Modes of Origin. *Economic Geology 100th Anniversary Volume,* 371-405.

Wilson, T. and Fairclough, M., 2009. Uranium and uranium mineral systems in South Australia. *Primary Industry and Resources, South Australia Report Book,* **2009/14**, 182pp.

World Nuclear Association, 2010. Geology of Uranium Deposits, World Nuclear Association. http://www.world-nuclear.org/info/inf26.html

Wyborn, L., 2001. The metallogenic potential of Australian Proterozoic granites: Tennant Creek/Davenport synthesis. Geoscience Australia. https://www.ga.gov.au/image_cache/GA17686.pdf.

Wyborn, L., Bastrakova, I., Hensley, C. and Budd, A., 2001. The metallogenic potential of Australian Proterozoic granites: Mount Isa Inlier synthesis. Geoscience Australia. https://www.ga.gov.au/image_cache/GA17692.pdf.

Wygralak, A.S. and Mernagh, T.P., 2005. Regional characteristics of fluids in the Tanami and Arunta region. In: *Annual Geoscience Exploration Seminar (AGES) 2005, record of abstracts. Northern Territory Geological Survey, Record* **2005-001**.

Young, G.A. and Shelley, E.P., 1966. Amadeus Basin airborne magnetic and radiometric survey, Northern Territory, 1965. *Bureau of Mineral Resources, Australia, Record*, **1966/230**.

Ypma, P.J., de Boorder, H., Van Gils, H., Kehrens, R., Ormsby, W. and Peters, M., 1984. Geology and mineralization of the Jervois Range, NT. *Proceedings of the Australasian Institute of Mining and Metallurgy Conference*, Darwin, 319-321.

Zhao, J. and McCulloch, M.T., 1995. Geochemical and Nd isotopic systematics of granites from the Arunta Inlier, central Australia: implications for Proterozoic crustal evolution. *Precambrian Research*, **71**, 265-299.

Appendix 1: Solid geology compilation

The Northern Territory Geological Survey (NTGS) has produced a state-wide geological map at a scale of 1:2 500 000 (Ahmad and Scrimgeour, 2006), as well as a number of regional products at smaller (1:500 000 to 1:100 000) scales. While the value of these datasets is recognised, the requirements of this study has led to the compilation of two original solid geology datasets (basement and overlying sedimentary basins) to be used in the assessment for uranium and geothermal energy systems. There are four key requirements of the solid geology datasets for use in the southern Northern Territory energy assessment:

- The solid geology should be seamless across the entire study area;
- The dataset should be developed at a suitable scale. A nominal display scale of 1:1 000 000 was selected in accordance with Geoscience Australia's (GA) 1:1 000 000 surface geology of Australia dataset (Raymond and Retter, 2010);
- Each geological unit should be attributed with a single stratigraphic unit number, enabling attribution from the Australian stratigraphic units database (http://dbforms.ga.gov.au/www/geodx.strat_units.int); and
- Datasets for basement and sedimentary basins solid geology should be compiled separately to preserve information on the geology at depth beneath sedimentary cover. This is particularly relevant for the assessment for geothermal energy systems. In order to accomplish this, solid geology was compiled within province boundaries found within the GA provinces database.

DATASETS USED

To compile the solid geology datasets, five key input datasets were used. These are briefly described below.

Existing Northern Territory Geological Survey solid geology coverages

A number of NTGS solid geology datasets are available within the study area, ranging in scale from 1:500 000 to 1:250 000. Datasets utilised at a scale of 1:500 000 were:

- Musgrave Block interpreted geology special (Slater, 2004);
- Mapped and interpreted geology of the Tennant region (Donnellan and Johnstone, 2004); and
- Northern Arunta interpreted geology special (Vandenberg *et al*., 2004).

Datasets utilised at a scale of 1:250 000 were:

- Mount Doreen interpreted geology (Goldberg *et al*., 2005);
- Mount Liebig interpreted geology (Meixner *et al*., 2004); and
- Alcoota 1:250 000 preliminary interpreted geology (*in prep.*).

Where available, these datasets were directly utilised with only minor modification in order to edge-match individual datasets and generalise where necessary. In a small number of cases, the identities of some units were changed based on interpretations of the other available datasets, particularly the GA 1:1 000 000 surface geology.

Surface geology

Geoscience Australia's 1:1 000 000 surface geology of Australia map (Raymond and Retter, 2010) was used as a fundamental layer in both the basement and basin solid geology interpretations. This dataset was produced using existing 1:250 000 geological mapping by the NTGS and GA (and its predecessors). The geology of the study area is obscured by a large amount of cover; therefore the surface geology dataset was combined with additional datasets in order to constrain the distribution of geological units.

Geophysical data

Magnetic and gravity geophysical data were used to assist in interpreting beneath cover. Magnetic data from the magnetic anomaly map of Australia (Milligan *et al*., 2010) were extracted for the study area. These data were processed to generate images of total magnetic intensity (reduced to pole) and the first vertical derivative of the total magnetic intensity. Gravity data stations for the study area are generally broadly spaced (Bacchin *et al*., 2008). Gravity data were extracted for the study area from the gravity map of Australia and images generated of the region. An image of the high-pass filter gravity was also produced to eliminate broad, large-scale geological features.

Geological provinces dataset

As mentioned above, both the basement and basin solid geology coverages were compiled within discrete boundaries defined by geological provinces. These were modified from GA's provinces database (Raymond and Totterdell, 2004) on the basis of geological and geophysical evidence.

SOLID GEOLOGY DATASETS PRODUCED

Solid geology compiled for basement geological provinces was combined to generate the basement solid geology layer (Figure 2.1.1). The basins solid geology dataset was compiled from solid geology interpretations within the major sedimentary basin provinces present within the study area (Figure 2.1.2), and is built strongly on interpretations produced previously by Songfa Liu of GA. The latter of these datasets applies only to the assessments for sandstone-hosted and unconformity-related uranium potential.

REFERENCES

Ahmad, M. and Scrimgeour, I.R., 2006. Geological map of the Northern Territory, 1:2 500 000 scale. Northern Territory Geological Survey, Darwin.

Bacchin, M., Milligan, P.R., Wynne, P. and Tracey, R., 2008. Gravity anomaly map of the Australian region (third edition). Geoscience Australia, Canberra.

Donnellan, N. and Johnstone, A., 2004. Mapped and interpreted geology of the Tennant region, 1:500 000 scale. Northern Territory Geological Survey, Darwin and Alice Springs.

Goldberg, A., Meixner, A.J. and Edgoose, C.J., 2005. Mount Doreen, Northern Territory (first edition). 1:250 000 interpreted geological map series, SF 52-12. Northern Territory.

Meixner, T., Scrimgeour, I.R., Close, D.F. and Edgoose, C.J., 2004. Mount Liebig, Northern Territory (second edition). 1:250 000 interpreted geological map series, SF 52-16. Northern Territory Geological Survey.

Milligan, P.R., Franklin, R., Minty, B.R.S., Richardson, L.M. and Percival, P.J., 2010. Magnetic anomaly map of Australia (fifth edition). Geoscience Australia, Canberra.

Raymond, O.L. and Retter, A.J. (editors), 2010. Surface geology of Australia 1:1 000 000 scale, 2010 edition (digital dataset). Geoscience Australia, Canberra.

Raymond, O.L. and Totterdell, J. (custodians), 2004. Australian geological provinces database. Geoscience Australia, Canberra.

Slater, K.R., 2004. Musgrave Block Special, Northern Territory, integrated interpretation of geophysics and geology, 1:500 000-scale map. Northern Territory Geological Survey, Darwin and Alice Springs.

Vandenberg, L.C., Johnstone, A., Donnellan, N., Green, M.G. and Crispe, A., 2004. Northern Arunta region integrated interpretation of geophysics and geology, Northern Territory (first edition), 1:500 000-scale map. Northern Territory Geological Survey, Alice Springs.

Appendix 2: Heat-production values

This table lists lithological units in the solid geology map (at the time of running the models) and their assigned heat-production (HP) values calculated from radiometric data (see text for details). AWM - area weighted mean. StDev represents one standard deviation in the HP data

Lithological name	**HP** ($\mu W/m^3$)	**StDev** ($\mu W/m^3$)	**Comments**
Harts Range Group	2.4	0.6	
Brady Gneiss	3.5	0.8	
Irindina Gneiss	2.7	0.9	
Naringa Calcareous Member	2.9	0.8	
Riddock Amphibolite Member	1.5	0.8	
Stanovos Gneiss Member	3.0	1.0	
mafic intrusives 72360	1.9	0.9	
felsic intrusives 72645	3.5	2.7	
Atnarpa Igneous Complex	2.2	0.8	
Atneequa Granitic Complex	2.8	0.6	
Alice Springs Granite	1.9	0.4	
Barrow Creek granite complex	2.4	1.1	
Copia Granite	3.7	0.8	
Anmatjira Granite	7.0	2.3	
Huckitta Granodiorite	2.4	0.7	
Mount Ida Granite	3.6	0.8	
Inkamulla Granodiorite	2.5	0.7	
Jinka Granite	5.4	2.1	
Crooked Hole Granite	3.1	0.4	
Marshall Granite	6.3	2.7	
Mount Swan Granite	4.2	2.3	
Mount Zeil Granite	2.5	0.8	
Wangala Granite	5.4	1.7	
Uldirra Porphyry	5.0	1.0	
Queenie Flat Granite	3.3	0.7	
Redhackle Granite	3.9	0.9	
Woodgreen Granite Complex	5.0	1.7	
high grade metamorphic rocks 72653	3.6	1.2	
Ankala Gneiss	3.5	0.8	
Aileron Metamorphics	5.6	1.8	
Aloolya Gneiss	7.8	1.7	
Bruna Gneiss	2.9	0.8	
Delmore Metamorphics	3.0	0.6	
Delny Gneiss	3.2	0.4	
Entia Gneiss	2.6	0.8	
Jessie Gap Gneiss	2.9	0.7	
Forty Five Augen Gneiss	2.2	0.5	
Hillsoak Bore Metamorphics	4.2	1.2	
Mount Airy Orthogneiss	2.7	1.5	
Yaningidjara Orthogneiss	6.7	0.9	

Lithological name	HP ($\mu W/m^3$)	StDev ($\mu W/m^3$)	Comments
Illyabba Metamorphics	4.3	1.1	
Charles River Gneiss	3.4	0.7	
Mulga Creek Granitic Gneiss	1.9	0.9	
Jennings Granitic Gneiss	4.3	1.6	
Randall Peak Metamorphics	3.4	0.8	
Sliding Rock Metamorphics	4.2	1.0	
Langford Gneiss	3.3	1.7	
Mendip Metamorphics	3.9	1.3	
Bunghara Metamorphics	3.2	1.3	
Nolans Dam Metamorphics	5.3	0.7	
Mount Hay Granulite	1.5	0.5	
Narwietooma Metamorphic Complex	2.7	0.2	
Old Hamilton Downs Gneiss	3.2	0.9	
Boothby Orthogneiss	5.5	1.9	
Ngalurbindi Orthogneiss	6.3	1.6	
Napperby Gneiss	6.4	1.8	
Adla Granulite	3.8	1.0	
Mount Bleechmore Granulite	4.2	1.1	
Chiripee Gneiss	4.3	1.0	
Cadney Metamorphics	3.5	1.2	
Erontonga Metamorphics	5.5	1.3	
Bungitina metamorphics	3.5	0.8	
Harry Anorthositic Gabbro	2.7	1.0	
Johannsen Metagabbro	3.7	2.1	
Kanandra Granulite	3.9	1.0	
Mapata Gneiss	3.9	0.7	
Ongeva Granulite	2.5	1.3	
Albarta Metamorphics	3.1	0.8	
Enbra Granulite	3.6	1.1	
Strangways Metamorphic Complex	3.2	1.1	
Yambah Granulite	4.1	1.2	
Tyson Creek granulite	4.2	1.6	
Wickstead Creek beds	3.4	1.0	
Weldon Metamorphics	5.6	2.2	
Woolla Gneiss	2.6	0.4	
Patmungala beds	2.8	0.5	
Waldrons Hill Complex	3.7		AWM Aileron Province
Cackleberry Metamorphics	3.8	0.9	
Sadadeen Range Gneiss	2.9	0.6	
Madderns Yard Metamorphic Complex	4.4	0.8	
Lizard Schist	2.2	1.0	
Ledan Schist	2.6	0.5	
Mount Freeling Schist	4.6	1.0	
Putardi Quartzite	1.4	0.2	
Reynolds Range Group	3.6	1.0	

Lithological name	HP ($\mu W/m^3$)	StDev ($\mu W/m^3$)	Comments
Utopia Quartzite	2.2	0.3	
Teapot Granite Complex	7.3	2.5	
Yaloolgarrie Granite	3.6	1.0	
Mordor Igneous Complex	2.7	1.3	
Bitter Springs Formation	1.7	0.5	
Heavitree Quartzite	1.5	0.6	
Undivided Aileron Province	3.7		AWM Aileron Province
Andrew Young Igneous Complex	1.5	0.3	
Undivided Davenport Province	1.7		AWM Davenport Province
Dashwood Gabbro Complex	4.7	1.1	
Undivided Proterozoic granite	3.1		AWM all assigned granites
Pitjantjatjara Supersuite	2.4	1.4	
Mantarrur Granite Suite	2.4		Assigned Pitjantjatjara Suite value
Kulpitjata Suite	3.8	1.8	
Ayers Rock Granite and Kulgera Granite	1.5	0.2	
Umbeara granites	3.0	0.7	
Geophysically intepreted Pitjantjatjara Supersuite (magnetic)	2.4	1.4	
Belt Granite	3.1		AWM all assigned granites
Michell Nob Granite and Nulchara Charnockite	1.3	0.1	
Carrington Suite	2.5	0.8	
Devils Suite	3.2	0.9	
Elkedra Granite	2.8	0.6	
Ehrenberg Granite	5.0	1.3	
Warumpi Granite	5.0	1.3	
Yulyupunyu Granitic Gneiss	5.6	1.9	
Moderately magnetic granite	3.1		AWM all assigned granites
Non-magnetic granite in the northern Arunta area	3.1		AWM all assigned granites
Southwark Suite	5.3	2.6	
Talipata Granite	3.3	1.6	
Udor Granite	1.9	0.8	
Tjungkubu Granodiorite	3.4	0.8	
Kakalyi Gneiss	3.4	0.8	
Larrie Granodiorite	3.4	0.8	
Mollie Granite Complex	3.1		AWM all assigned granites
Russell Charnockite	3.4	0.8	
Talyi-Talyi Charnockite	3.4	0.8	
unnamed dioritic to rhyolitic granophyre	3.5		
Hatches Creek Group	1.3	0.5	
Hanlon Subgroup	1.3	0.4	
Wauchope Subgroup, Lower	1.8	0.9	
Wauchope Subgroup, Upper	1.4	0.4	
Ikuntji Metamorphics	2.6	0.7	
Iwupataka Metamorphic Complex	2.2	0.4	

Lithological name	HP ($\mu W/m^3$)	StDev ($\mu W/m^3$)	Comments
Bullion Schist	2.8	0.4	
Aileron Metamorphics - gneissic mafic granulite, amphibolite and felsic granulite (paragneiss)	3.0		AWM all assigned lithologies
Lander Rock Formation	3.8	1.1	
Undivided Musgrave Province	2.4		AWM Musgrave Province
Musgravian Gneiss - amphibolite facies	2.7	0.5	
Musgravian Gneiss - granulite facies	1.9	0.3	
Nicker beds	2.9	0.7	
Napperby Suite	6.4	1.8	
Ooradidgee Group	1.9	0.5	
Taragan Sandstone	1.3	0.5	
Edmirringee Volcanics	1.4	0.4	
Mia Mia Volcanics	3.1	1.1	
Kurinelli Sandstone	1.6	0.5	
Rooneys Formation	2.7	0.6	
Treasure Volcanics	2.4	1.2	
Dead Bullock Formation	2.0	0.6	
Morphett Creek Formation	1.5	0.5	
Peculiar Complex	2.1	0.6	
Undivided Warumpi Province	3.0		AWM Warumpi Province
Yaya Metamorphic Complex	3.1	1.1	
Inyalinga Granulite	3.2	0.8	
retrograde schist zones 72682	3.8	1.4	
Redbank Deformed Zone	4.6	1.2	

SOUTHERN NORTHERN TERRITORY ENERGY SYSTEMS ASSESSMENT

SANDSTONE-HOSTED URANIUM PROSPECTIVITY

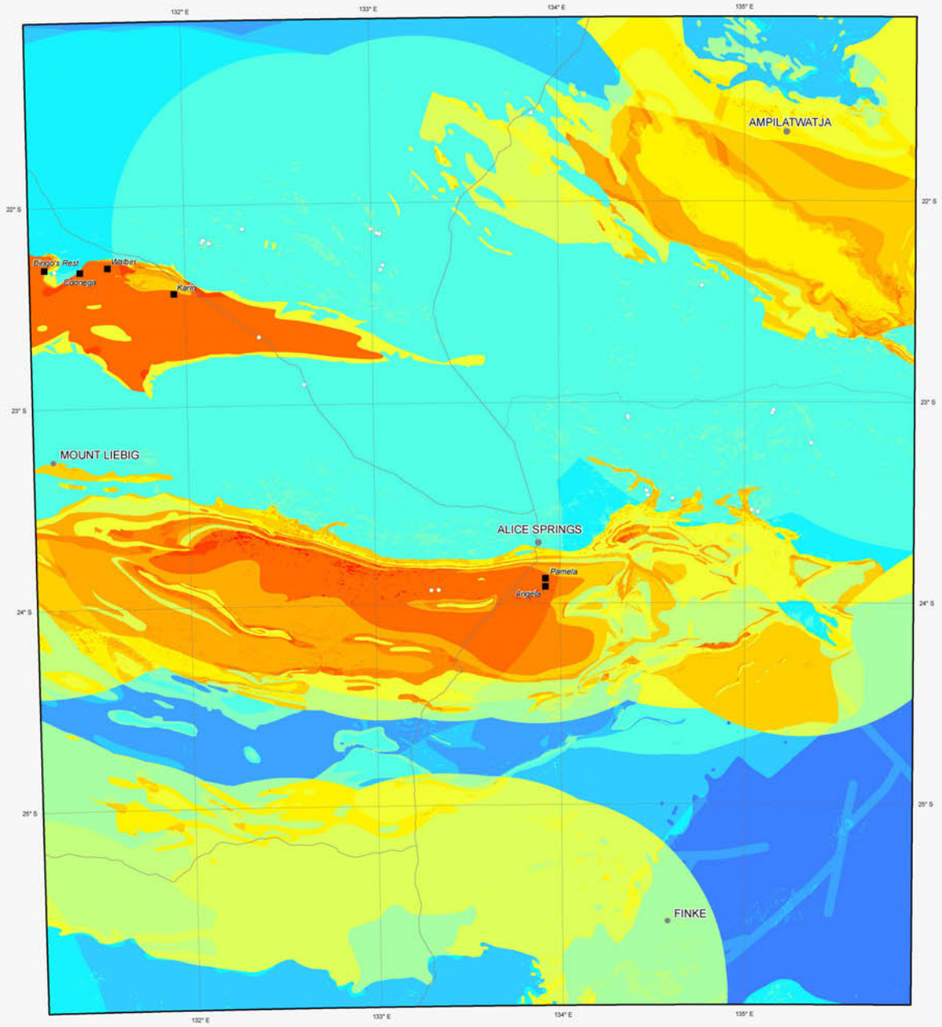

Sandstone-hosted Uranium Prospectivity

Low — High

Potential for uranium deposits based on summation and normalisation of mineral system components shown in inserts. See text for more information and references.

0 100 200 km

Universal Transverse Mercator Projection Zone 53, Geocentric Datum of Australia (GDA94)

■ *Sandstone-hosted uranium deposit or prospect*

Uranium occurrence

Source

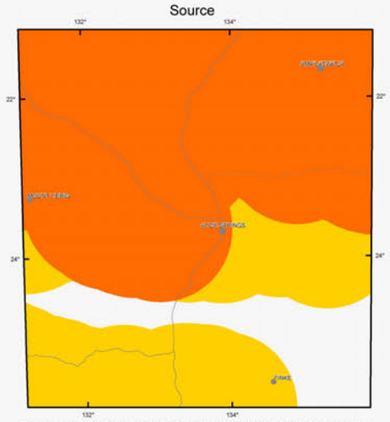

Prospectivity based on sources of uranium, mineralising fluids and other components needed for ore transport.

Source Prospectivity

0 200 km Low — High

Driver

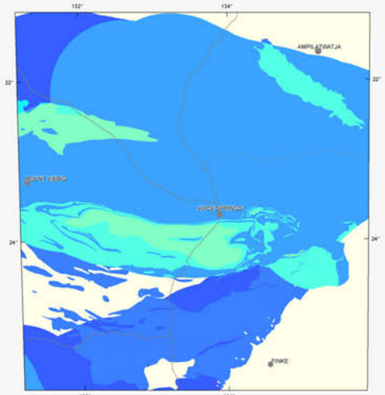

Prospectivity based on energy gradients that will mobilise sufficient quantities of ore-bearing fluids to the site of deposition.

Driver Prospectivity

0 200 km Low — High

Fluid Pathway/Architecture

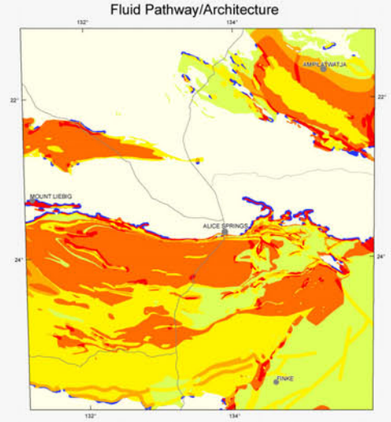

Prospectivity based on favourable lithologies and structures that will enable movement of fluids to the site of ore deposition.

Fluid Pathway/Architecture Prospectivity

0 200 km Low — High

Depositional Mechanism

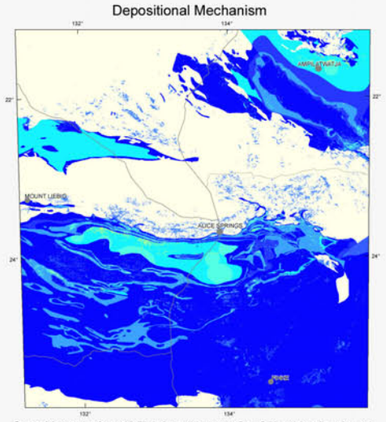

Prospectivity based on favourable lithologies and structures to focus fluids and deposit uranium and other metals via physical and/or chemical processes.

Depositional Mechanism Prospectivity

0 200 km Low — High

Prospectivity Assessment Workflow

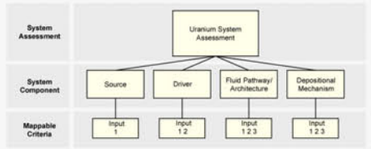

Energy Assessment Prospectivity

The uranium system assessment has been undertaken using a mineral systems framework. This framework consists of four key mineral system components: 1) sources, 2) fluid-flow drivers, 3) fluid-flow pathways and architecture, and 4) depositional sites and mechanisms. Using this framework, prospectivity criteria have been developed which are interpreted to reflect mineralising processes. Each mineral system component is comprised of a varying number of inputs specific to the targeted uranium system, and represents the sum of the weightings for the input mappable criteria normalised by the number of criteria. Weightings for the criteria are assigned subjectively based on the interpretation of the importance of the criterion, the validity of the mappable proxy used and the confidence in the data source.

Each mineral system component shown on this map has been scaled using an identical colour stretch based on the maximum weighting across the four components. The colour stretch used on the main map of uranium prospectivity is unique to that map.

Source
Potential for sources of uranium and other metals, mineralising fluids and other components needed for ore transport. The source weighting is calculated by combining the constituent mappable criteria listed below and normalised to the total number of mappable criteria. The input data are:

1) Presence of igneous uranium sources in basement

Driver
Prospectivity based on energy gradients that will mobilise sufficient quantities of ore-bearing fluids to the site of deposition. The driver weighting is calculated by combining the constituent mappable criteria listed below and normalised to the total number of mappable criteria. The input data are:

1) (Paleo)topographic-driven fluid flow
2) Presence of sediments generated during uplift of hinterland regions

Fluid Pathway/Architecture
Potential for favourable lithologies and structures that will enable movement of fluids to the site of ore deposition. The fluid pathway/architecture weighting is calculated by combining the constituent mappable criteria listed below and normalised to the total number of mappable criteria. The input data are:

1) Distribution of sedimentary basins
2) Location of favourable fluid-flow aquifers
3) Location of fluid pathways for reductants at depth in basin

Depositional Mechanism
Potential for favourable lithologies and structures to focus fluids and deposit uranium and other metals via physical and/or chemical processes. The depositional mechanism weighting is calculated by combining the constituent mappable criteria listed below and normalised to the total number of mappable criteria. The input data are:

1) Distribution of reduced units within basin
2) Sources of reducing fluids
3) Direct evidence of elevated uranium determined from radiometric data

Location of Study Area

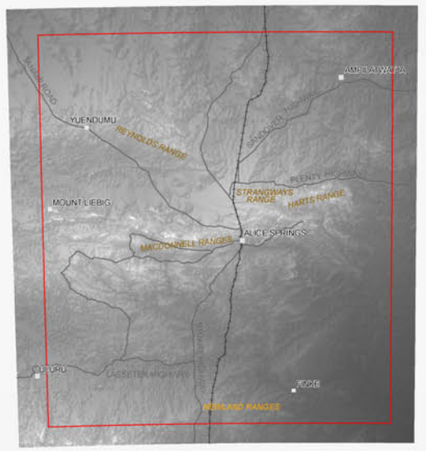

MAP LOCALITY

Compiled by A. Schofield, Geoscience Australia
Data analysis by A. Schofield
Geoprocessing and Cartography by R.G. Gallagher

Produced by GIS Group, Information Services Section,
Minerals and Natural Hazards Division, Geoscience Australia.

It is recommended that this map be referred to as:
Schofield, A. and Gallagher, R.G., 2012. *Sandstone-hosted Uranium Prospectivity*. In: Schofield, A. (ed.), 2012. An assessment of the uranium and geothermal prospectivity of the southern Northern Territory. Geoscience Australia Record, 2012/51.
Geocat # 74118.

ISSN 1448-2177
ISBN 978-1-922103-53-6 (web)
978-1-922103-54-3 (DVD)
978-1-922103-55-0 (print)

Published by Geoscience Australia, Department of Resources, Energy and Tourism, Canberra, Australia. Issued under the authority of the Minister for Resources, Energy and Tourism.

Copies of the GA Record containing this map can be downloaded from the Geoscience Australia internet site at: *http://www.ga.gov.au* or by contacting:

Sales Centre, Geoscience Australia
GPO Box 378
Canberra ACT 2601
Phone (02) 6249 9966, Facsimile (02) 6249 9960
Email: sales@ga.gov.au

Australian Government
Geoscience Australia

Northern Territory Government

SOUTHERN NORTHERN TERRITORY ENERGY SYSTEMS ASSESSMENT

SANDSTONE-HOSTED URANIUM PROSPECTIVITY

JULY 2012

PLATE 3.2

SOUTHERN NORTHERN TERRITORY ENERGY SYSTEMS ASSESSMENT

IRON OXIDE-COPPER-GOLD-URANIUM PROSPECTIVITY

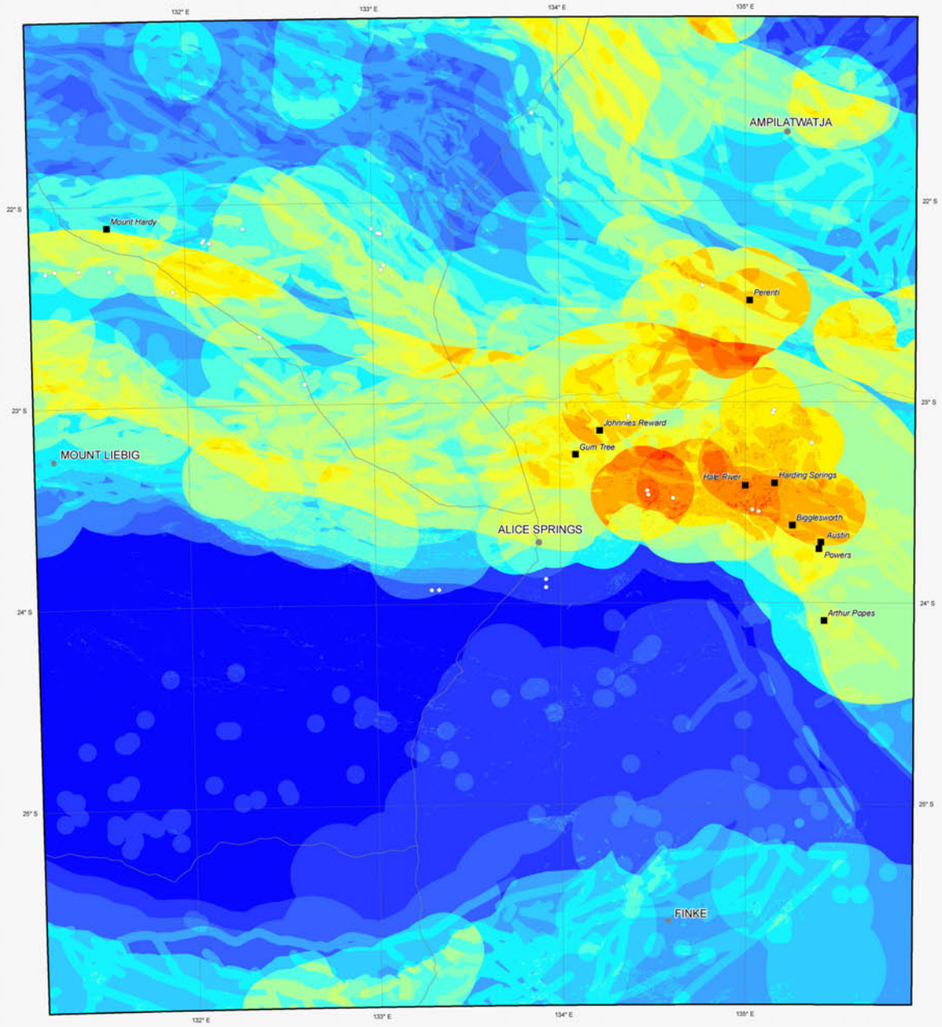

Iron Oxide-Copper-Gold-Uranium Prospectivity

Low — High

Potential for uranium deposits based on summation and normalisation of mineral system components shown in inserts. See text for more information and references.

0 100 200 km

Universal Transverse Mercator Projection Zone 53; Geocentric Datum of Australia (GDA94)

■ *Iron oxide-copper-gold-uranium deposit or prospect*

Uranium occurrence

Source

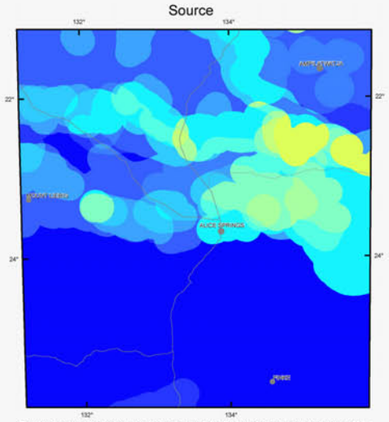

Prospectivity based on sources of uranium, mineralising fluids and other components needed for ore transport.

0 200 km Low — Source Prospectivity — High

Driver

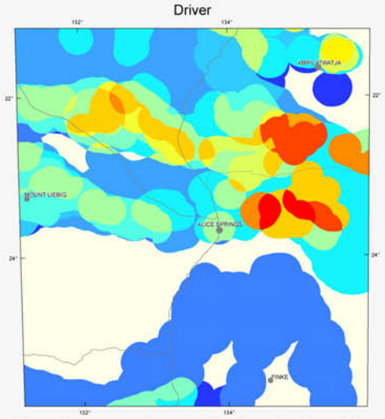

Prospectivity based on energy gradients that will mobilise sufficient quantities of ore-bearing fluids to the site of deposition.

0 200 km Low — Driver Prospectivity — High

Fluid Pathway/Architecture

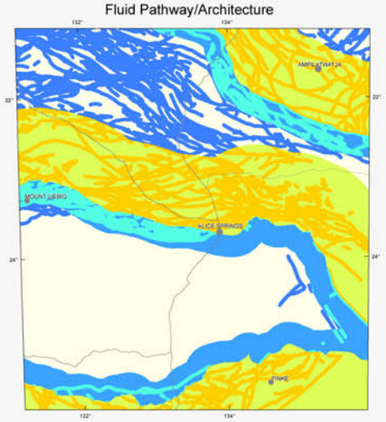

Prospectivity based on favourable lithologies and structures that will enable movement of fluids to the site of ore deposition.

0 200 km Low — Fluid Pathway/Architecture Prospectivity — High

Depositional Mechanism

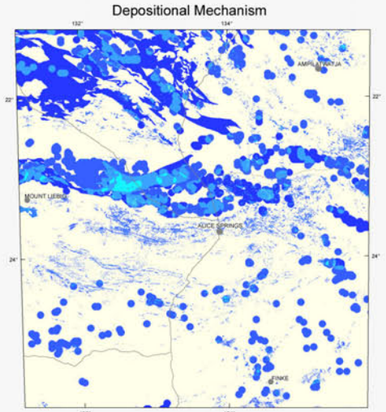

Prospectivity based on favourable lithologies and structures to focus fluids and deposit uranium and other metals via physical and/or chemical processes.

0 200 km Low — Depositional Mechanism Prospectivity — High

Prospectivity Assessment Workflow

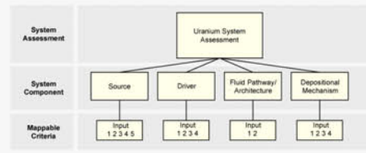

Energy Assessment Prospectivity
The uranium system assessment has been undertaken using a mineral systems framework. This framework consists of four key mineral system components: 1) sources, 2) fluid-flow drivers, 3) fluid-flow pathways and architecture, and 4) depositional sites and mechanisms. Using this framework, prospectivity criteria have been developed which are interpreted to reflect mineralising processes. Each mineral system component is comprised of a varying number of inputs specific to the targeted uranium system, and represents the sum of the weightings for the input mappable criteria normalised by the number of criteria. Weightings for the criteria are assigned subjectively based on the interpretation of the importance of the criterion, the validity of the mappable proxy used and the confidence in the data source.

Each mineral system component shown on this map has been scaled using an identical colour stretch based on the maximum weighting across the four components. The colour stretch used on the main map of uranium prospectivity is unique to that map.

Source
Potential for sources of uranium and other metals, mineralising fluids and other components needed for ore transport. The source weighting is calculated by combining the constituent mappable criteria listed below and normalised to the total number of mappable criteria. The input data are:

1) Presence of extensional basins as a source of iron, brines and sulfur
2) Presence of igneous rocks with high uranium content
3) Presence of igneous rocks with high zircon saturation temperature
4) Presence of mafic or ultramafic intrusions and volcanics
5) Presence of volatile-rich igneous rocks as indicated by high fluorine

Driver
Prospectivity based on energy gradients that will mobilise sufficient quantities of ore-bearing fluids to the site of deposition. The driver weighting is calculated by combining the constituent mappable criteria listed below and normalised to the total number of mappable criteria. The input data are:

1) Evidence of high paleo-geothermal gradient as indicated by high-level granite intrusions
2) Presence of breccias in intrusive rocks
3) Presence of large-volume high-temperature crustal melts
4) Location of mafic and ultramafic intrusions and volcanics, indicative of metasomatised mantle melts

Fluid Pathway/Architecture
Potential for favourable lithologies and structures that will enable movement of fluids to the site of ore deposition. The fluid pathway/architecture weighting is calculated by combining the constituent mappable criteria listed below and normalised to the total number of mappable criteria. The input data are:

1) Distribution of potential zones of fluid flow as indicated by basement fault and shear zones
2) Location of crustal domain boundaries

Depositional Mechanism
Potential for favourable lithologies and structures to focus fluids and deposit uranium and other metals via physical and/or chemical processes. The depositional mechanism weighting is calculated by combining the constituent mappable criteria listed below and normalised to the total number of mappable criteria. The input data are:

1) Direct evidence of elevated uranium determined from radiometric data
2) Presence of magnetite as indicated from inversion modelling of magnetic and gravity data
3) Presence of hematite as indicated from inversion modelling of magnetic and gravity data
4) Presence of ironstones and iron formations

Location of Study Area

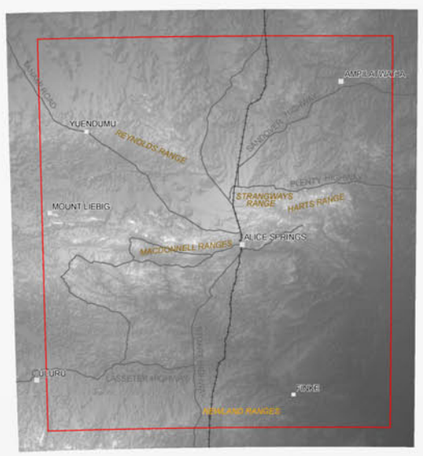

MAP LOCALITY

Australian Government
Geoscience Australia

Northern Territory Government

Compiled by D.L. Huston, A. Schofield and R.G. Gallagher, Geoscience Australia
Data analysis by D.L. Huston, A. Schofield (Geoscience Australia) and
J.A. Whelan (Northern Territory Geological Survey)
Geoprocessing and Cartography by R.G. Gallagher

Produced by GIS Group, Information Services Section,
Minerals and Natural Hazards Division, Geoscience Australia.

It is recommended that this map be referred to as: Huston, D.L., Whelan, J.A., Schofield, A., Chopping, R.G. and Gallagher, R.G., 2012. *Iron Oxide-Copper-Gold-Uranium Prospectivity*. In: Schofield, A. (ed.), 2012. An assessment of the uranium and geothermal prospectivity of the southern Northern Territory. Geoscience Australia Record 2012/51. Geocat # 74118.

ISSN 1448-2177
ISBN 978-1-922103-53-6 (web)
978-1-922103-54-3 (DVD)
978-1-922103-55-0 (print)

Published by Geoscience Australia, Department of Resources, Energy and Tourism, Canberra, Australia. Issued under the authority of the Minister for Resources, Energy and Tourism.

Copies of the GA Record containing this map can be downloaded from the Geoscience Australia internet site at: *http://www.ga.gov.au* or by contacting:

Sales Centre, Geoscience Australia
GPO Box 378
Canberra ACT 2601
Phone (02) 6249 9966, Facsimile (02) 6249 9960
Email: sales@ga.gov.au

SOUTHERN NORTHERN TERRITORY ENERGY SYSTEMS ASSESSMENT

IRON OXIDE-COPPER-GOLD-URANIUM PROSPECTIVITY

JULY 2012

PLATE 3.3

SOUTHERN NORTHERN TERRITORY ENERGY SYSTEMS ASSESSMENT

PRECAMBRIAN UNCONFORMITY-RELATED URANIUM PROSPECTIVITY

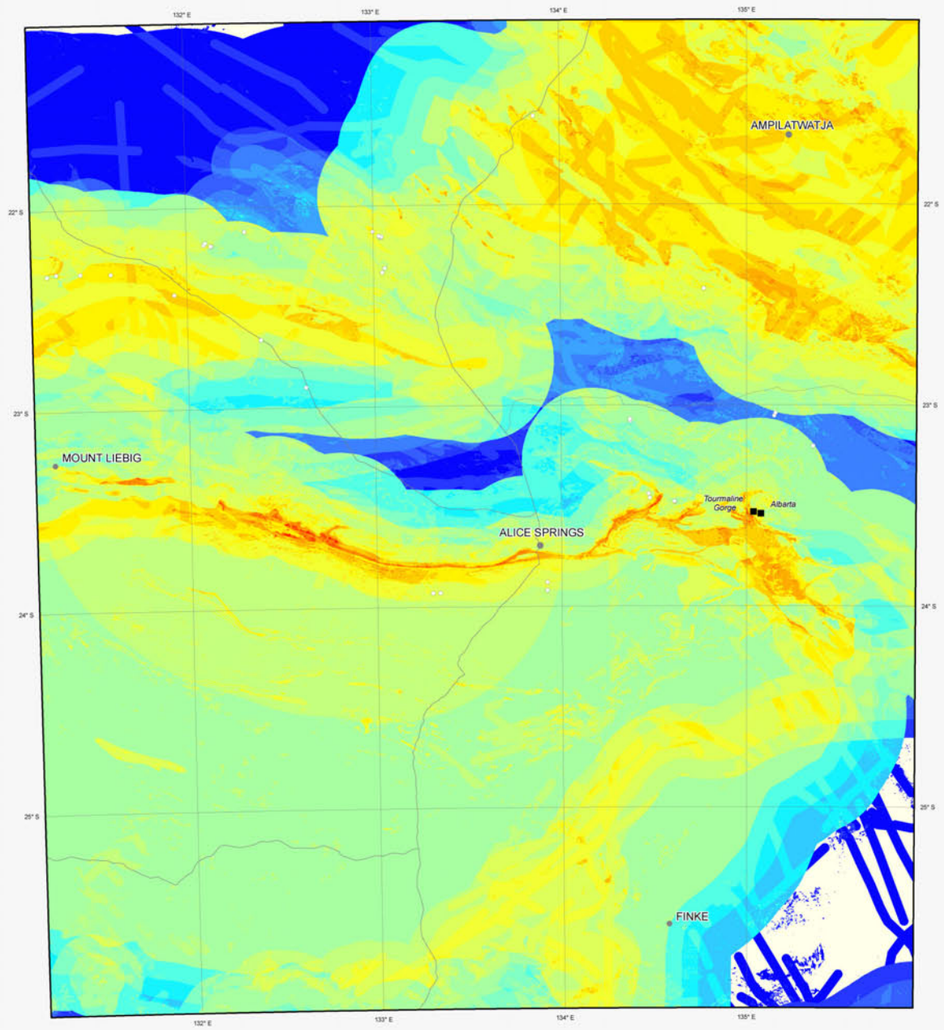

Precambrian Unconformity-related Uranium Prospectivity

Low — High

Potential for uranium deposits based on summation and normalisation of mineral system components shown in inserts. See text for more information and references.

0 100 200 km

Universal Transverse Mercator Projection Zone 53; Geocentric Datum of Australia (GDA94)

■ *Unconformity-related uranium deposit or prospect*

Uranium occurrence

Source

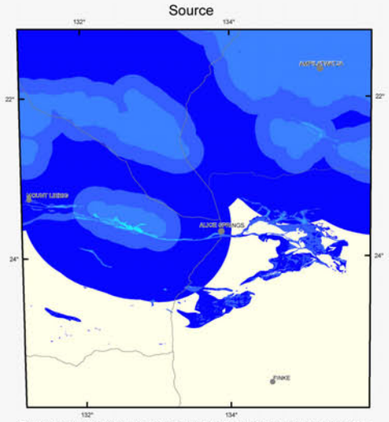

Prospectivity based on sources of uranium, mineralising fluids and other components needed for ore transport.

0 200 km

Source Prospectivity

Low — High

Driver

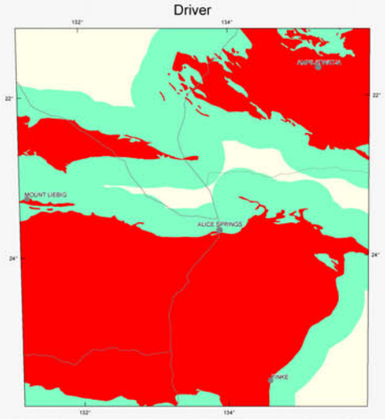

Prospectivity based on energy gradients that will mobilise sufficient quantities of ore-bearing fluids to the site of deposition.

0 200 km

Driver Prospectivity

Low — High

Fluid Pathway/Architecture

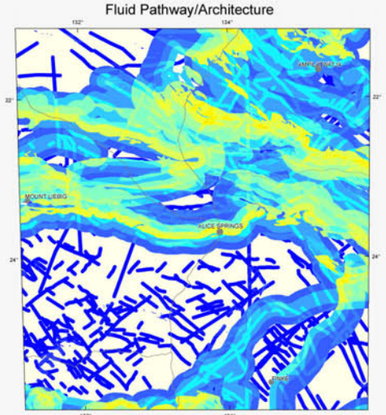

Prospectivity based on favourable lithologies and structures that will enable movement of fluids to the site of ore deposition.

0 200 km

Fluid Pathway/Architecture Prospectivity

Low — High

Depositional Mechanism

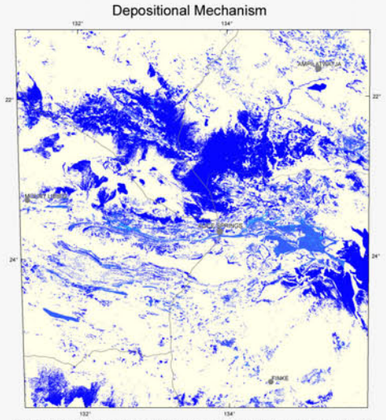

Prospectivity based on favourable lithologies and structures to focus fluids and deposit uranium and other metals via physical and/or chemical processes.

0 200 km

Depositional Mechanism Prospectivity

Low — High

Location of Study Area

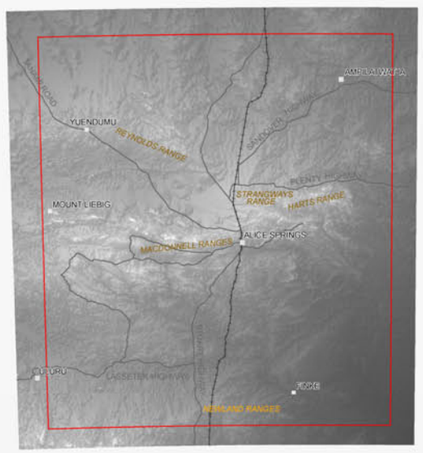

MAP LOCALITY

Prospectivity Assessment Workflow

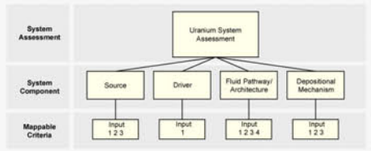

Energy Assessment Prospectivity
The uranium system assessment has been undertaken using a mineral systems framework. This framework consists of four key mineral system components: 1) sources, 2) fluid-flow drivers, 3) fluid-flow pathways and architecture, and 4) depositional sites and mechanisms. Using this framework, prospectivity criteria have been developed which are interpreted to reflect mineralising processes. Each mineral system component is comprised of a varying number of inputs specific to the targeted uranium system, and represents the sum of the weightings for the input mappable criteria normalised by the number of criteria. Weightings for the criteria are assigned subjectively based on the interpretation of the importance of the criterion, the validity of the mappable proxy used and the confidence in the data source.

Each mineral system component shown on this map has been scaled using an identical colour stretch based on the maximum weighting across the four components. The colour stretch used on the main map of uranium prospectivity is unique to that map.

Source
Potential for sources of uranium and other metals, mineralising fluids and other components needed for ore transport. The source weighting is calculated by combining the constituent mappable criteria listed below and normalised to the total number of mappable criteria. The input data are:

1) Presence of igneous rocks with uranium concentration above the 75th percentile (intrusive and volcanic)
2) Presence of sedimentary rocks with above average uranium concentration
3) Distribution of evaporite-bearing or shallow water units that may act as a source of basinal brines

Driver
Prospectivity based on energy gradients that will mobilise sufficient quantities of ore-bearing fluids to the site of deposition. The driver weighting is calculated by combining the constituent mappable criteria listed below and normalised to the total number of mappable criteria. The input data are:

1) Distribution of the Amadeus, Ngalia and Georgina basins

Fluid Pathway/Architecture
Potential for favourable lithologies and structures that will enable movement of fluids to the site of ore deposition. The fluid pathway/architecture weighting is calculated by combining the constituent mappable criteria listed below and normalised to the total number of mappable criteria. The input data are:

1) Presence of basal unconformity
2) Presence of unconformities in the sedimentary basins
3) Distribution of extensional faults which may act as fluid-flow conduits
4) Presence of demagnetised zones in the magnetics providing evidence for oxidised fluid flow

Depositional Mechanism
Potential for favourable lithologies and structures to focus fluids and deposit uranium and other metals via physical and/or chemical processes. The depositional mechanism weighting is calculated by combining the constituent mappable criteria listed below and normalised to the total number of mappable criteria. The input data are:

1) Direct evidence of elevated uranium determined from radiometric data
2) Evidence of above average thorium concentration determined from radiometric data
3) Presence of carbonaceous rocks that provide redox gradients favourable for deposition

Australian Government
Geoscience Australia

Northern Territory Government

Compiled by T.P. Mernagh, A. Schofield and R.G. Gallagher, Geoscience Australia
Data analysis by T.P. Mernagh
Geoprocessing and Cartography by R.G. Gallagher

Produced by GIS Group, Information Services Section,
Minerals and Natural Hazards Division, Geoscience Australia.

It is recommended that this map be referred to as:
Mernagh, T.P. and Gallagher, R.G., 2012. *Precambrian Unconformity-related Uranium Prospectivity*. In: Schofield, A. (ed.), 2012. An assessment of the uranium and geothermal prospectivity of the southern Northern Territory. Geoscience Australia Record, 2012/51.
Geocat # 74118.

ISSN 1448-2177
ISBN 978-1-922103-53-6 (web)
978-1-922103-54-3 (DVD)
978-1-922103-55-0 (print)

Published by Geoscience Australia, Department of Resources, Energy and Tourism, Canberra, Australia. Issued under the authority of the Minister for Resources, Energy and Tourism.

Copies of the GA Record containing this map can be downloaded from the Geoscience Australia internet site at: *http://www.ga.gov.au* or by contacting:

Sales Centre, Geoscience Australia
GPO Box 378
Canberra ACT 2601
Phone (02) 6249 9966, Facsimile (02) 6249 9960
Email: sales@ga.gov.au

SOUTHERN NORTHERN TERRITORY ENERGY SYSTEMS ASSESSMENT

PRECAMBRIAN UNCONFORMITY-RELATED URANIUM PROSPECTIVITY

JULY 2012

PLATE 3.4.1

SOUTHER NORTHERN TERRITORY ENERGY SYSTEMS ASSESSMENT

PHANEROZOIC UNCONFORMITY-RELATED URANIUM PROSPECTIVITY

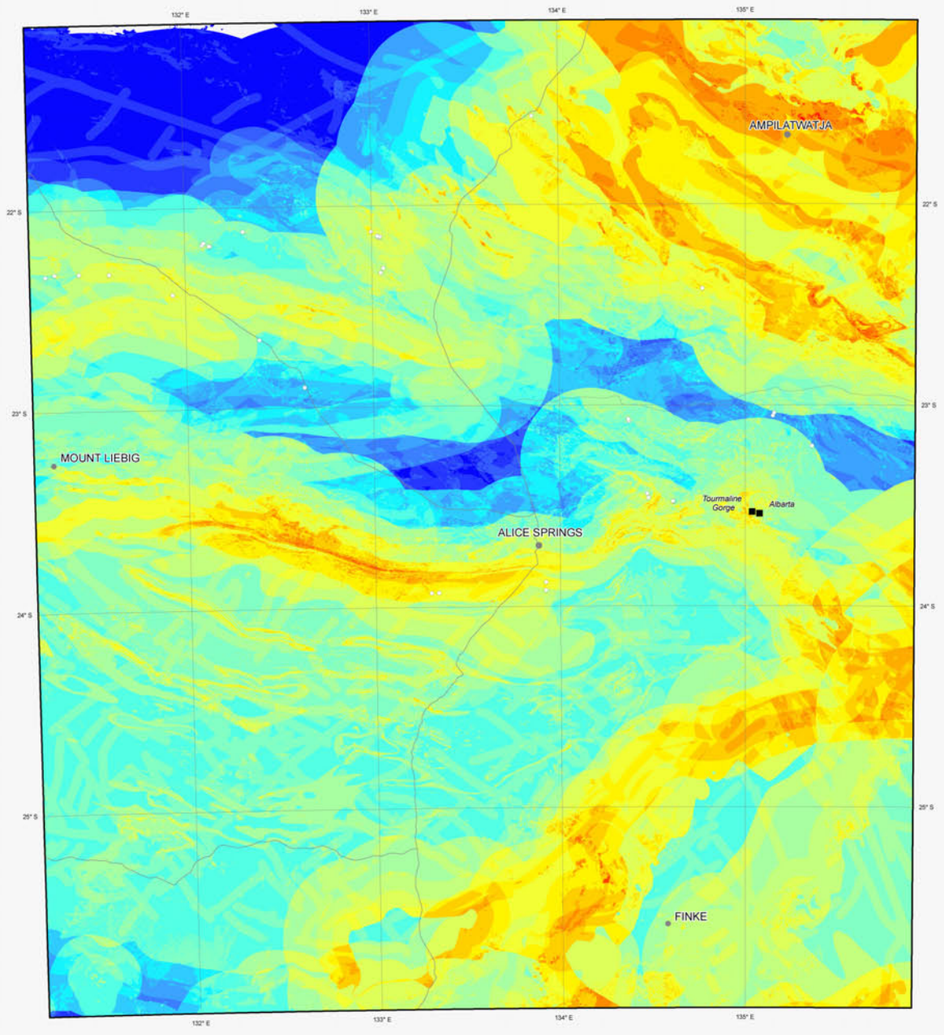

Phanerozoic Unconformity-related Uranium Prospectivity

Low — High

Potential for uranium deposits based on summation and normalisation of mineral system components shown in inserts. See text for more information and references.

0 100 200 km

Universal Transverse Mercator Projection Zone 53; Geocentric Datum of Australia (GDA94)

■ *Unconformity-related uranium deposit or prospect*

Uranium occurrence

Source

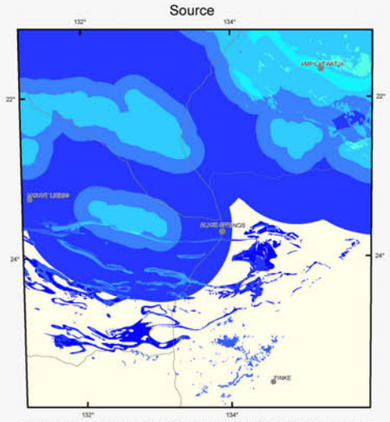

Prospectivity based on sources of uranium, mineralising fluids and other components needed for ore transport.

0 200 km

Source Prospectivity: Low — High

Driver

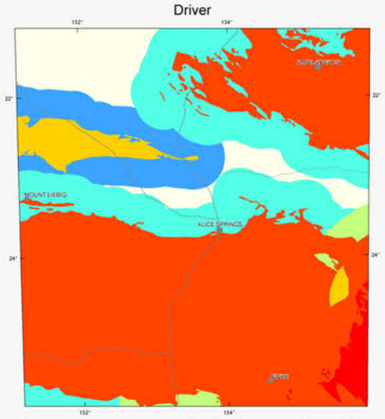

Prospectivity based on energy gradients that will mobilise sufficient quantities of ore-bearing fluids to the site of deposition.

0 200 km

Driver Prospectivity: Low — High

Fluid Pathway/Architecture

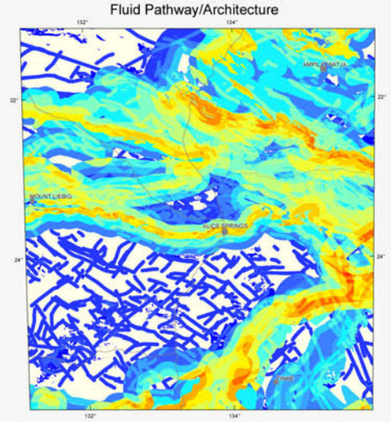

Prospectivity based on favourable lithologies and structures that will enable movement of fluids to the site of ore deposition.

0 200 km

Fluid Pathway/Architecture Prospectivity: Low — High

Depositional Mechanism

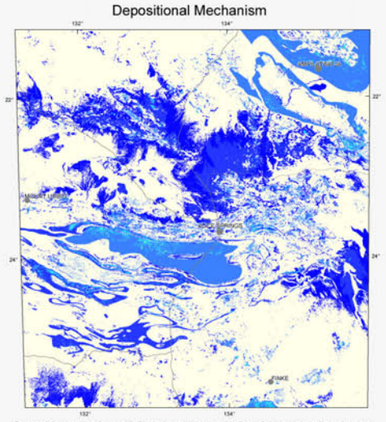

Prospectivity based on favourable lithologies and structures to focus fluids and deposit uranium and other metals via physical and/or chemical processes.

0 200 km

Depositional Mechanism Prospectivity: Low — High

Prospectivity Assessment Workflow

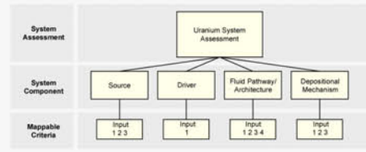

Energy Assessment Prospectivity
The uranium system assessment has been undertaken using a mineral systems framework. This framework consists of four key mineral system components: 1) sources, 2) fluid-flow drivers, 3) fluid-flow pathways and architecture, and 4) depositional sites and mechanisms. Using this framework, prospectivity criteria have been developed which are interpreted to reflect mineralising processes. Each mineral system component is comprised of a varying number of inputs specific to the targeted uranium system, and represents the sum of the weightings for the input mappable criteria normalised by the number of criteria. Weightings for the criteria are assigned subjectively based on the interpretation of the importance of the criterion, the validity of the mappable proxy used and the confidence in the data source.

Each mineral system component shown on this map has been scaled using an identical colour stretch based on the maximum weighting across the four components. The colour stretch used on the main map of uranium prospectivity is unique to that map.

Source
Potential for sources of uranium and other metals, mineralising fluids and other components needed for ore transport. The source weighting is calculated by combining the constituent mappable criteria listed below and normalised to the total number of mappable criteria. The input data are:

1) Presence of igneous rocks with uranium concentration above the 75th percentile (intrusive and volcanic)
2) Presence of sedimentary rocks with above average uranium concentration
3) Distribution of evaporite-bearing or shallow water units that may act as a source of basinal brines

Driver
Prospectivity based on energy gradients that will mobilise sufficient quantities of ore-bearing fluids to the site of deposition. The driver weighting is calculated by combining the constituent mappable criteria listed below and normalised to the total number of mappable criteria. The input data are:

1) Distribution of the Amadeus, Ngalia, Georgina, Eromanga, Lake Eyre and Warburton basins

Fluid Pathway/Architecture
Potential for favourable lithologies and structures that will enable movement of fluids to the site of ore deposition. The fluid pathway/architecture weighting is calculated by combining the constituent mappable criteria listed below and normalised to the total number of mappable criteria. The input data are:

1) Presence of basal unconformity
2) Presence of unconformities in the sedimentary basins
3) Distribution of extensional faults which may act as fluid-flow conduits
4) Presence of demagnetised zones in the magnetics providing evidence for oxidised fluid flow

Depositional Mechanism
Potential for favourable lithologies and structures to focus fluids and deposit uranium and other metals via physical and/or chemical processes. The depositional mechanism weighting is calculated by combining the constituent mappable criteria listed below and normalised to the total number of mappable criteria. The input data are:

1) Direct evidence of elevated uranium determined from radiometric data
2) Evidence of above average thorium concentration determined from radiometric data
3) Presence of carbonaceous rocks that provide redox gradients favourable for deposition

Location of Study Area

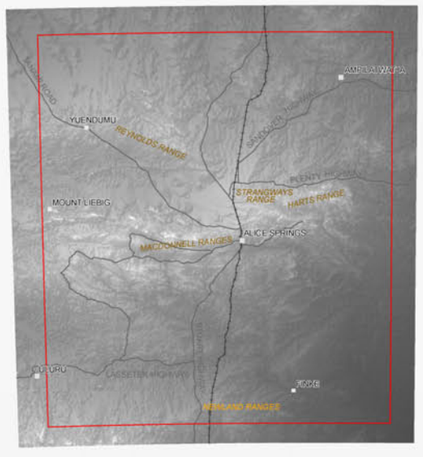

MAP LOCALITY

Compiled by T.P. Mernagh, A. Schofield and R.G. Gallagher, Geoscience Australia
Data analysis by T.P. Mernagh
Geoprocessing and Cartography by R.G. Gallagher

Produced by GIS Group, Information Services Section,
Minerals and Natural Hazards Division, Geoscience Australia.

It is recommended that this map be referred to as:
Mernagh, T.P. and Gallagher, R.G., 2012. *Phanerozoic Unconformity-related Uranium Prospectivity*. In: Schofield, A. (ed.), 2012. An assessment of the uranium and geothermal prospectivity of the southern Northern Territory. Geoscience Australia Record, 2012/51.
Geocat # 74118.

ISSN 1448-2177
ISBN 978-1-922103-53-6 (web)
978-1-922103-54-3 (DVD)
978-1-922103-55-0 (print)

Published by Geoscience Australia, Department of Resources, Energy and Tourism, Canberra, Australia. Issued under the authority of the Minister for Resources, Energy and Tourism.

Copies of the GA Record containing this map can be downloaded from the Geoscience Australia internet site at: *http://www.ga.gov.au* or by contacting:

Sales Centre, Geoscience Australia
GPO Box 378
Canberra ACT 2601
Phone (02) 6249 9966, Facsimile (02) 6249 9960
Email: sales@ga.gov.au

Australian Government
Geoscience Australia

Northern Territory Government

SOUTHERN NORTHERN TERRITORY ENERGY SYSTEMS ASSESSMENT

PHANEROZOIC UNCONFORMITY-RELATED URANIUM PROSPECTIVITY

JULY 2012

PLATE 3.4.2

SOUTHERN NORTHERN TERRITORY ENERGY SYSTEMS ASSESSMENT

MAGMATIC-RELATED URANIUM PROSPECTIVITY

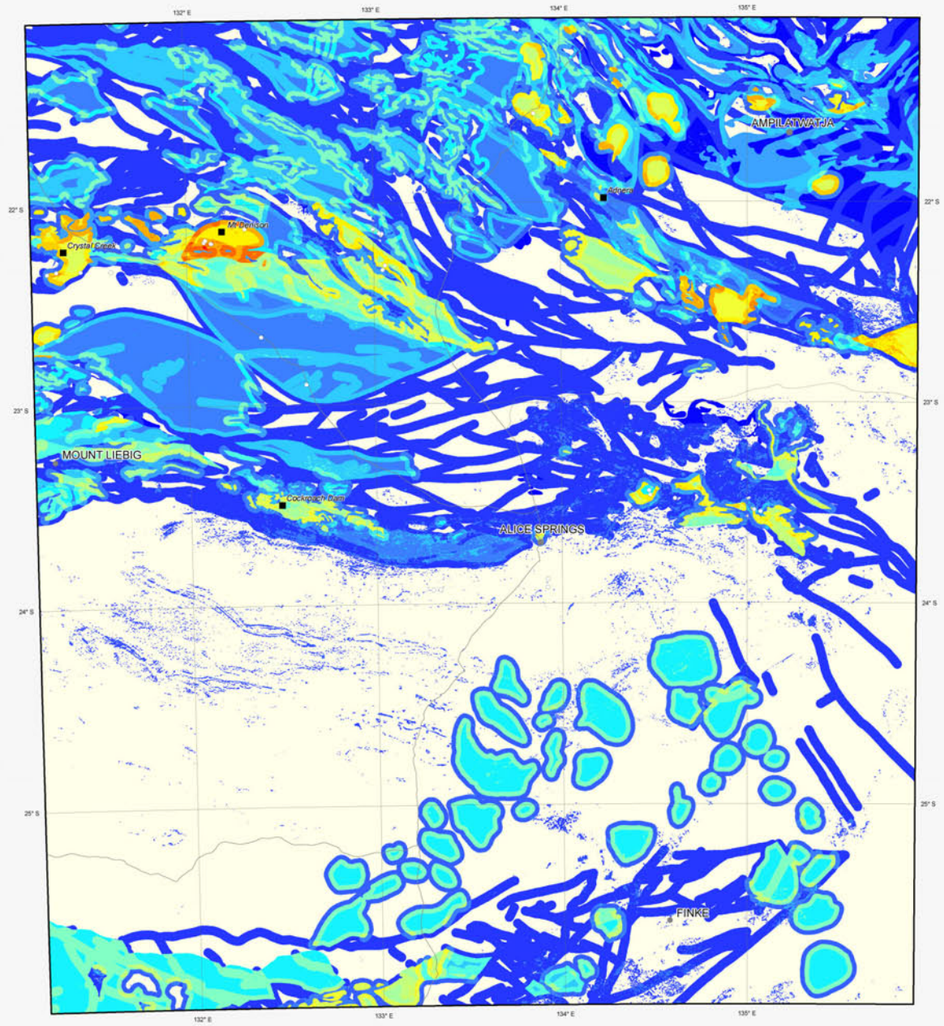

Magmatic-related Uranium Prospectivity

Low — High

Potential for uranium deposits based on summation and normalisation of mineral system components shown in inserts. See text for more information and references.

0 — 100 — 200 km

Universal Transverse Mercator Projection Zone 53; Geocentric Datum of Australia (GDA94)

■ *Magmatic-related uranium deposit or prospect*

Uranium occurrence

Source

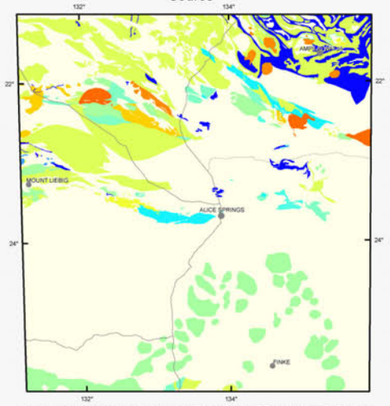

Prospectivity based on sources of uranium, mineralising fluids and other components needed for ore transport.

0 — 200 km — Low — High — Source Prospectivity

Driver

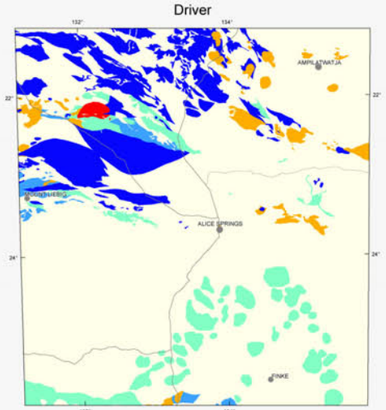

Prospectivity based on energy gradients that will mobilise sufficient quantities of ore-bearing fluids to the site of deposition.

0 — 200 km — Low — High — Driver Prospectivity

Fluid Pathway/Architecture

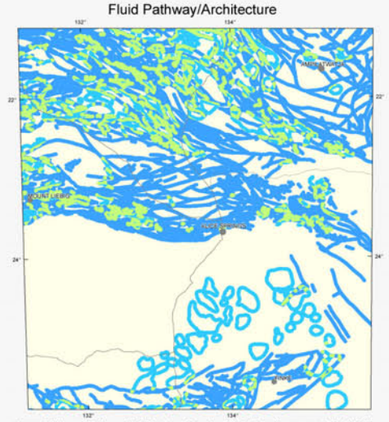

Prospectivity based on favourable lithologies and structures that will enable movement of fluids to the site of ore deposition.

0 — 200 km — Low — High — Fluid Pathway/Architecture Prospectivity

Depositional Mechanism

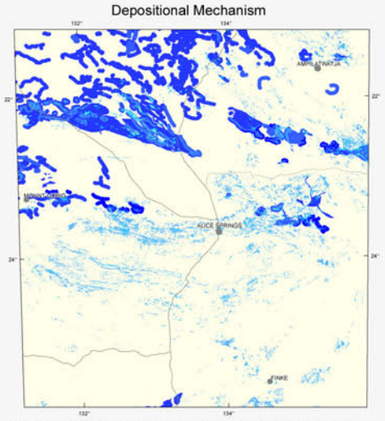

Prospectivity based on favourable lithologies and structures to focus fluids and deposit uranium and other metals via physical and/or chemical processes.

0 — 200 km — Low — High — Depositional Mechanism Prospectivity

Prospectivity Assessment Workflow

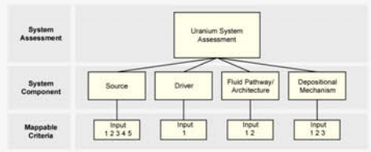

Energy Assessment Prospectivity

The uranium system assessment has been undertaken using a mineral systems framework. This framework consists of four key mineral system components: 1) sources, 2) fluid-flow drivers, 3) fluid-flow pathways and architecture, and 4) depositional sites and mechanisms. Using this framework, prospectivity criteria have been developed which are interpreted to reflect mineralising processes. Each mineral system component is comprised of a varying number of inputs specific to the targeted uranium system, and represents the sum of the weightings for the input mappable criteria normalised by the number of criteria. Weightings for the criteria are assigned subjectively based on the interpretation of the importance of the criterion, the validity of the mappable proxy used and the confidence in the data source.

Each mineral system component shown on this map has been scaled using an identical colour stretch based on the maximum weighting across the four components. The colour stretch used on the main map of uranium prospectivity is unique to that map.

Source
Potential for sources of uranium and other metals, mineralising fluids and other components needed for ore transport. The source weighting is calculated by combining the constituent mappable criteria listed below and normalised to the total number of mappable criteria. The input data are:

1) Presence of broadly felsic igneous rocks
2) Presence of uranium-enriched igneous rocks
3) Presence of fractionated igneous rocks
4) Distribution of high-temperature igneous rocks
5) Presence of igneous rocks with high fluorine

Driver
Prospectivity based on energy gradients that will mobilise sufficient quantities of ore-bearing fluids to the site of deposition. The driver weighting is calculated by combining the constituent mappable criteria listed below and normalised to the total number of mappable criteria. The input data are:

1) Presence of high-level and volatile-rich igneous rocks

Fluid Pathway/Architecture
Potential for favourable lithologies and structures that will enable movement of fluids to the site of ore deposition. The fluid pathway/architecture weighting is calculated by combining the constituent mappable criteria listed below and normalised to the total number of mappable criteria. The input data are:

1) Distribution of potential zones of fluid flow as indicated by basement fault and shear zones
2) Fluid flow along rheological contrasts

Depositional Mechanism
Potential for favourable lithologies and structures to focus fluids and deposit uranium and other metals via physical and/or chemical processes. The depositional mechanism weighting is calculated by combining the constituent mappable criteria listed below and normalised to the total number of mappable criteria. The input data are:

1) Chemical deposition sites
2) Potential sites of ligand destabilisation
3) Direct evidence of elevated uranium determined from radiometric data

Location of Study Area

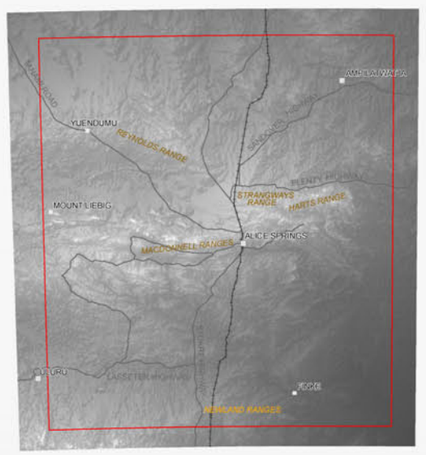

MAP LOCALITY

Compiled by A. Schofield, Geoscience Australia
Data analysis by A. Schofield
Geoprocessing and Cartography by R.G. Gallagher

Produced by GIS Group, Information Services Section,
Minerals and Natural Hazards Division, Geoscience Australia.

It is recommended that this map be referred to as:
Schofield, A. and Gallagher, R.G., 2012. *Magmatic-related Uranium Prospectivity*. In: Schofield, A. (ed.), 2012. An assessment of the uranium and geothermal prospectivity of the southern Northern Territory. Geoscience Australia Record, 2012/51. Geocat # 74118.

ISSN 1448-2177
ISBN 978-1-922103-53-6 (web)
978-1-922103-54-3 (DVD)
978-1-922103-55-0 (print)

Published by Geoscience Australia, Department of Resources, Energy and Tourism, Canberra, Australia. Issued under the authority of the Minister for Resources, Energy and Tourism.

Australian Government
Geoscience Australia

Northern Territory Government

SOUTHERN NORTHERN TERRITORY ENERGY SYSTEMS ASSESSMENT
MAGMATIC-RELATED URANIUM PROSPECTIVITY

JULY 2012

PLATE 3.5

SOUTHERN NORTHERN TERRITORY ENERGY SYSTEMS ASSESSMENT

HOT ROCK GEOTHERMAL PROSPECTIVITY

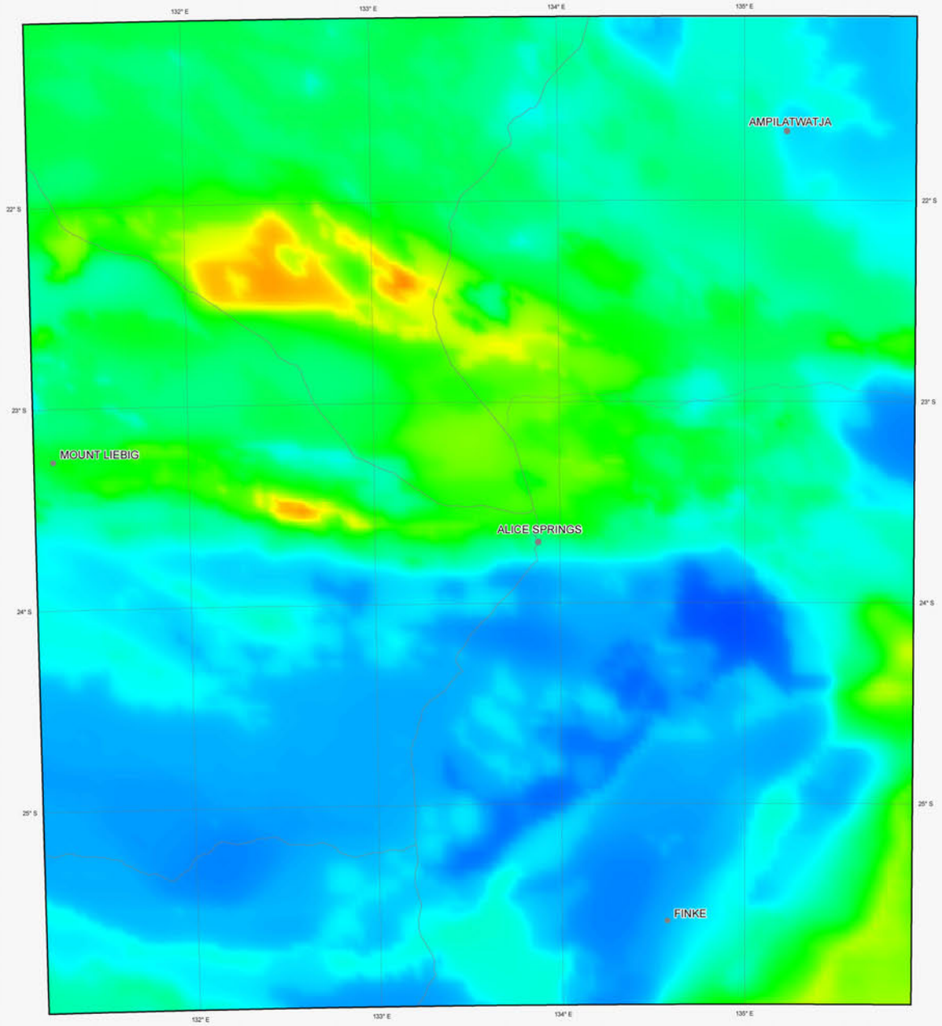

Temperature (°C)
103 118 134

Depth slice at four kilometres showing modelled temperature.

0 100 200 km

Universal Transverse Mercator Projection Zone 53; Geocentric Datum of Australia (GDA94)

Modelled Heat Flow at Surface

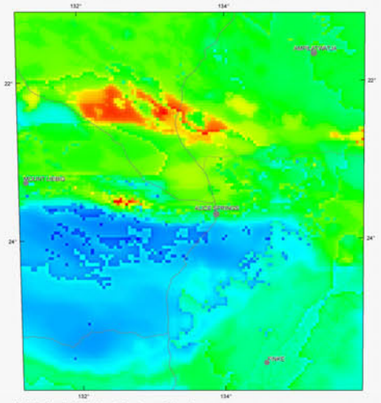

Modelled vertical heat flow at the topographic surface.

0 200 km

Surface Heat Flow mW/m^2
54 87

Heat Production

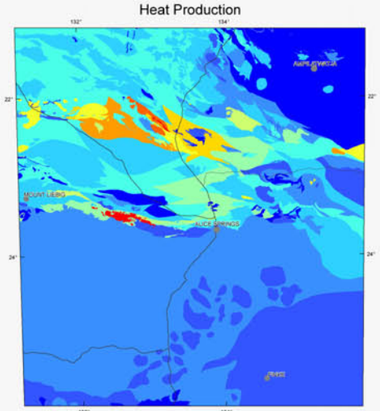

Heat-production values attributed to geological units in the 3D model.

0 200 km

Heat Production

1.3-2.0	3.0-3.5	4.5-5.0	6.0-6.5
2.0-2.5	3.5-4.0	5.0-5.5	6.5-7.0
2.5-3.0	4.0-4.5	5.5-6.0	7.0-7.8

Depth of Cover

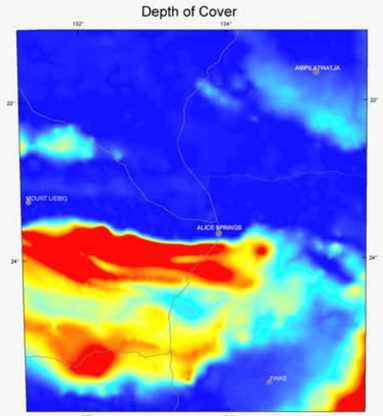

The interpretation of the depth of the sedimentary cover used in the 3D geological model.

0 200 km

Depth of Cover (m)
0 -10400 metres

Combined Relative Confidence

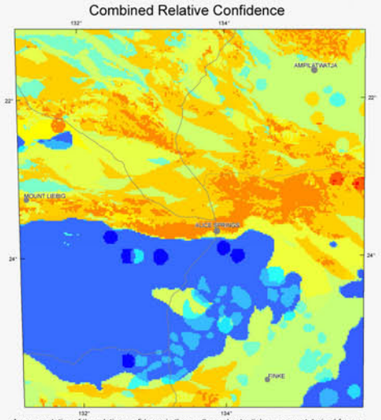

A representation of the relative confidence in the geothermal potential assessment derived from a combination of the certainty of each of the component layers: geology, thermal properties, depth of cover, and thermal modelling residual (measured minus modelled values).

0 200 km

Relative Confidence
Low High

Location of Study Area

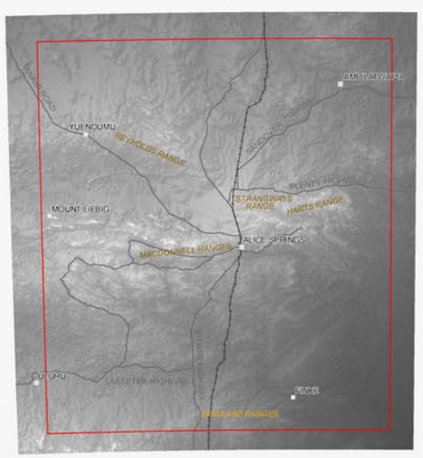

MAP LOCALITY

Hot Rock Geothermal Prospectivity Assessment Notes

Hot rock geothermal prospectivity is derived from the **Modelled Temperature at Four Kilometres**[1] depth slice extracted from a 3D thermal model. Higher temperatures equate to higher relative hot rock geothermal prospectivity. The thermal modelling was performed using a 3D geological map. The 3D map was constructed from geological and geophysical data to a depth of 15 km.

The 3D map delineates the two major components required for a geothermal play: 1) the cover sequence, which encompasses sedimentary sequences with potentially thermally insulating properties, and 2) the basement, with potentially high-heat producing lithologies.

The 3D map incorporates geological elements which were assigned heat-production and thermal-conductivity values, both of which influence hot rock geothermal prospectivity. For each unit of the 3D model, heat-production values were established using radiometric data and the small amount of geochemical data available. Thermal-conductivity values were sourced from published measurements or estimated from descriptions of the lithology.

The **Heat Production**[2] attributed to the geological units in the 3D model is the primary driver for variations seen in the **Modelled Heat Flow at the Surface**[3]. The **Depth of Cover**[4] (with associated variations in thermal conductivity) and the **Heat Production**[2], both directly influence the **Modelled Temperature at Four Kilometres**[1].

Thermal forward models were computed and the modelled temperature and heat flow results were compared to heat flow determinations and measured down-hole temperatures. Some heat-production and thermal-conductivity values were iteratively adjusted as necessary in order to produce an acceptable fit with thermal data.

Relative confidence maps have been generated and, in conjunction with the temperature and heat flow residuals (the difference between the measured and modelled thermal data), provide an indication of the reliability of the prospectivity assessment. Confidence levels were defined for each of the inputs into the thermal modelling: geological confidence, thermal properties and the modelled temperature residuals. These layers were normalised and combined to produce the **Combined Relative Confidence**[5] map.

[1]**Modelled Temperature at Four Kilometres (main map)**
Depth slice at four kilometres showing the modelled temperatures.

[2]**Heat Production**
Heat-production values attributed to the geological units of the 3D model when performing the surface thermal modelling.

[3]**Modelled Heat Flow at Surface**
Modelled vertical heat flow at the topographic surface.

[4]**Depth of Cover**
Depth of the sedimentary cover used in constructing the 3D geological model.

[5]**Combined Relative Confidence**
Combined relative confidence map which incorporates the uncertainty in the data used in the 3D geological map, as well as the uncertainty in the heat-production and thermal conductivity data, and the temperature residuals (measured minus modelled values).

Geothermal Systems

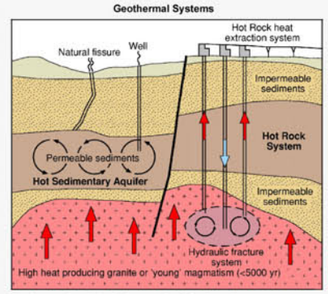

The above schematic describes two styles of geothermal system.
The hot sedimentary aquifer system (shown on the left) and the hot rock system (shown on the right). Hot sedimentary aquifer systems require naturally occuring permeability and fluid, while hot rock systems may require artificially enhanced permeability and potentially an introduced fluid.

Compiled by A.J. Meixner, E.J. Gerner, R.D. Weber and T. Brennan, Geoscience Australia
Data analysis by A.J. Meixner and E.J. Gerner
Geoprocessing and Cartography by A. Clive and E.J. Gerner

Produced by GIS Group, Information Services Section,
Minerals and Natural Hazards Division, Geoscience Australia.

It is recommended that this map be referred to as: Meixner, A.J., Gerner, E.J., Weber, R.D., Brennan, T., Lewis, B. and Gallagher, R.G., 2012. *Hot Rock Geothermal Prospectivity*. In: Schofield, A. (ed.), 2012. An assessment of the uranium and geothermal prospectivity of the southern Northern Territory. Geoscience Australia Record, 2012/51. Geocat # 74118.

ISSN 1448-2177
ISBN 978-1-922103-53-6 (web)
978-1-922103-54-3 (DVD)
978-1-922103-55-0 (print)

Published by Geoscience Australia, Department of Resources, Energy and Tourism, Canberra, Australia. Issued under the authority of the Minister for Resources, Energy and Tourism.

Copies of the GA Record containing this map can be downloaded from the Geoscience Australia internet site at: *http://www.ga.gov.au* or by contacting:

Sales Centre, Geoscience Australia
GPO Box 378
Canberra ACT 2601
Phone (02) 6249 9966, Facsimile (02) 6249 9960
Email: sales@ga.gov.au

Australian Government
Geoscience Australia

Northern Territory Government

SOUTHERN NORTHERN TERRITORY ENERGY SYSTEMS ASSESSMENT
HOT ROCK GEOTHERMAL PROSPECTIVITY
JULY 2012
PLATE 4.1